Developing targeted photodynamic therapy using glyconanoparticles

Brydie Anne Moore

This thesis is submitted in fulfilment of the requirements of the degree of
Doctor of Philosophy at the University of East Anglia

Department of Biological Chemistry

John Innes Centre

September 2019

Declaration

I declare that the work contained in this thesis submitted by myself for the Degree of Doctor of Philosophy is my work, except where due reference is made to other authors, and has not previously been submitted by me for a degree at this or any other university.

Brydie Anne Moore

Abstract

Current antibiotics are losing efficacy due to the rapid rise and spread of drug-resistant bacteria; and conventional cancer treatments can present many nasty side effects. Consequently, we urgently need to find alternative therapies to develop effective treatments and improve patient outcomes. One such approach is targeted photodynamic therapy (PDT), which uses a non-toxic dye (photosensitiser) that releases cytotoxic reactive oxygen species on activation with specific wavelengths of light. Here, glycan-modified 16 nm gold nanoparticles (glycoAuNPs) were explored for their use in targeted PDT, whereby the dye was localised to the target cell through selective glycan-lectin interactions.

Two novel glycan ligands were synthesised by Cu(I)-catalysed Huisgen azide-alkyne cycloaddition 'click chemistry', and used to modify AuNPs. By exploiting the unique colorimetric properties of AuNPs, detection of glycan-lectin interactions was possible. Target pathogen *Pseudomonas aeruginosa* lectin: LecA, was detected at 64 nM, by UV-Vis spectroscopy-based studies. Through a new filtration method that was developed in collaboration with Iceni Diagnostics, binding of different bacterial species was observed by the modified AuNPs. Finally, differential glycan binding by breast cancer and non-cancer cell lines was assessed to identify a glycan to selectively target overexpressed glycan-binding proteins on breast cancer cells. AuNPs were modified with photosensitiser and glycan (glycan-/ce6-AuNPs), and targeted cell killing of breast cancer cells was achieved, showing a ca 46% reduction in cell viability upon light treatment.

The findings demonstrate the versatility of using glycoAuNPs for selective binding to different cellular targets (bacterial and cancer cells), through glycan-lectin interactions. The selective cell killing of breast cancer cells demonstrates the potential of using this approach for targeted PDT.

Contents

List of Figures

List of Tables

List of Abbreviations

δ	Chemical shift
$[\alpha]_D$	Specific rotation at 589 nm
$CaCl_2$	Calcium chloride
E. coli	*Escherichia coli*
Ex_{678}	Extinction at 678 nm.
P. aeruginosa	*Pseudomonas aeruginosa*
c	Concentration
ABMA	9,10-anthracenediyl-bis(methylene)dimalonic acid
Ac-galactose-PEG$_3$-SAc	S-10-(1-(2,3,4,6-Tetra-O-acetyl-β-D-galactopyranosyl)-1H-1,2,3-triazol-4-yl)-3,6,9-trioxadecyl ethanethioate
Ac-mannose-PEG$_6$-SH	S-10-(1-(8-(2,3,4,6-Tetra-O-acetyl-α-D-mannopyranosyloxy)--3,6-dioxaoctyl)-1H-[1,2,3]-triazol-4-yl)-3,6,9-trioxadecyl ethanethioate
AF488-st	Fluorescent, Alexa Fluor 488 streptavidin conjugate
AuNPs	Gold nanoparticles
CF	Cystic Fibrosis
CHCl$_3$	Chloroform
ConA	Concanavalin A
CRD	Carbohydate recognition domain

CuAAC	Copper(I)-catalysed azide-alkyne cycloaddition
$CuSO_4$	Copper sulphate
d	Doublet
DCM	Dichloromethane
dd	Doublet of doublets
DIC	Differential interference contrast image
DMF	Dimethylformamide
DMSO	Dimethyl sulfoxide
ECDC	European Centre for Disease Prevention and Control
EDC	*N*-(3-Dimethylaminopropyl)-*N'*-ethylcarbodiimide
Eqv	Equivalents
ESI-MS	Electrospray ionization mass spectrometry
EtOAc	Ethyl acetate
Gal-/ce6-AuNPs	Galactose and chlorin e6 modified AuNPs
Gal-AuNPs	AuNPs functionalised with galactose-PEG_3-SH ligand
Galactose-PEG_3-SH	10-(1-(β-D-Galactopyranosyl)-1H-1,2,3-triazol-4-yl)-3,6,9-trioxadecylthiol
Glycan-/ce6-AuNPs	Glycan-/chlorin e6-PEG_4-AuNPs, 3: 1
GlycoAuNPs	Glycan functionalised gold nanoparticles
Glycocalyx	Cell-surface glycan coat that surrounds the outer membrane of cells
GPC	Gel permeation chromatography
Hex	Hexane
HIV	Human immunodeficiency virus type-1
HR ESI-MS	High resolution electrospray mass spectrometry

Inhibitor	(1-(β-D-Galactopyranosyl)-1H-1,2,3-triazol-4-yl)methanol
LB media	Luria-Bertani media
m	Multiplet
m/z	Mass-to-charge ratio
MALDI-TOF MS	Matrix-assisted laser desorption ionisation time of flight mass spectrometry
Man-/ce6-AuNPs	Mannose and chlorin e6 modified AuNPs
Mannose-PEG$_6$-SH	10-(1-(8-(α-D-Mannopyranosyloxy)-3,6-dioxaoctyl)-1H--[1,2,3]-triazol-4-yl)-3,6,9-trioxadecylthiol
MEBM	Mammary Epithelial Basal Medium
MeOH	Methanol
MgSO$_4$	Magnesium sulphate
MHz	Megahertz
MQ H$_2$O	MilliQ water
NaAsc	Sodium ascorbate
NMR	Nuclear magnetic resonance
PAA-glycan	Polyacrylamide functionalised with biotin and glycan
Pc	Zinc phthalocyanine
PEG$_3$-/ce6-AuNPs	PEG$_3$ and chlorin e6 modified AuNPs
PEG$_3$-AuNPs	PEG$_3$-SH functionalised AuNPs
ppm	Parts per million
PS	Photosensitiser
ROS	Reactive oxygen species
s	Singlet
SGLT	sodium-dependent glucose cotransporter

st	Staurosporine
t	Triplet
THPTA	Tris(3-hydroxypropyltriazolylmethyl)amine
TLC	Thin layer chromatography
TMAC	*N,N,N*-trimethyl-(11-mercaptoundecyl)ammonium chloride
WHO	World Health Organisation

Chapter 1

Introduction

The need for alternative, targeted therapeutics is well-documented, with current antibiotics losing efficacy due to drug-resistance[1]; and conventional anticancer therapeutics have many nasty side effects[2], arising from drugs that are non-selective. Finding effective strategies to selectively eradicate these cells is critical to lowering spread of drug-resistance and side effects[3], and improving patient outcomes[4]. Although cancer and drug-resistant bacteria may appear two seemingly disparate research areas, one common ground between them is that they both require glycans to function and survive, and coupled with glycan diversity and selectivity, glycans offer huge potential in the use of targeted drug delivery.

1.1   Cell-surface glycan interactions

Glycans, including glycolipids and glycoproteins, form a cell-surface glycan coating around the outermost membrane of a cell, known as the 'glycocalyx'[5]. The glycocalyx can be found surrounding both mammalian and bacterial cells. Cell-surface glycans allow cells to interact with one another and their environment, including cellular attachment, recognition, signalling, embryonic development, growth, metastasis and differentiation[6]. The varied biological roles

of glycans are only possible as a result of glycan diversity; a product of their: stereochemistry, generating different stereoisomers, configurations and glycosidic linkages; chemical substitutions, such as acetyl or amine groups; ability of a monosaccharide to form multiple linkages, generating linear or branched structures; and ability to form linkages with non-glycan structures, such as glycolipids and glycoproteins[7]. These surface glycans are 'read' by proteins expressed by cells, and this glycan-protein interaction facilitates the biological function of glycans (see Figure 1.1).
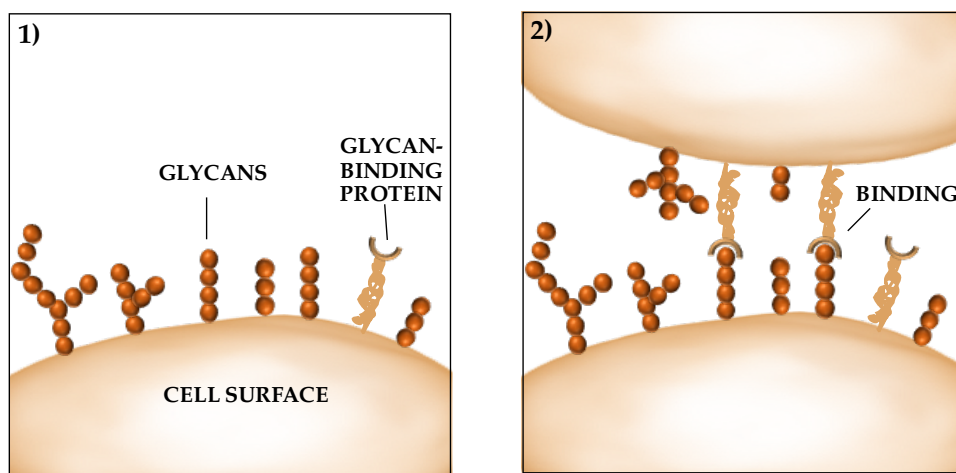
Figure 1.1: Cell-surface glycan binding by proteins: 1) glycan and glycan-binding proteins expressed on the cell surface; and 2) cell-surface glycan-protein interactions.

Glycan-lectin interactions

A predominant group of the glycan-binding proteins are 'lectins'[8]. Lectins differ from other glycan-binding proteins, as they do not modify saccharide residues (enzymes) nor are they a product of an immune response (antibodies). The glycan-lectin interaction is highly selective for saccharides, similar in selectivity as antibody-antigen and enzyme-substrate interactions[9]. As mentioned previously, the glycome is diverse, and yet lectins are able to accommodate

for this versatility, presenting a diverse group of proteins that can be highly selective towards specific glycan moieties.

Lectins rely on a module in the protein for glycan binding, called the carbohydrate recognition domain (CRD). The glycan-lectin interaction is relatively weak, with an association constant usually under 10^6 M^{-1} [10]. This interaction can be strengthened through multivalent binding by the lectin, which results in a strengthened interaction due to a 'cluster glycoside effect' (Figure 1.2a) [11]. Consequently, lectins can often exhibit multiple CRDs [12], which can also allow for agglutination of the glycoconjugate or cell[6].

a)

BINDING STRENGTH

b)

BINDING STRENGTH

LECTIN

CRD

MONOMERIC LECTIN

MULTIMERIC LECTIN

MONOSACCHARIDE

OLIGOSACCHARIDE
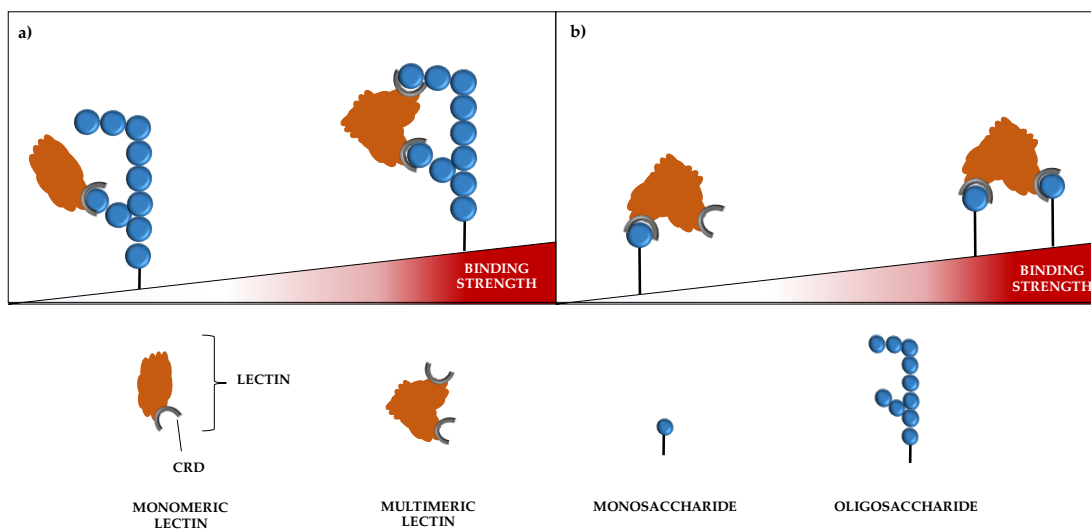
Figure 1.2: Glycan-lectin interactions strengthened by multivalency, known as the cluster glycoside effect. Multivalency can be achieved through multimeric lectins (a) or multivalent saccharide presentation (b).

Even though cell-surface glycans are often part of larger glycoconjugates, lectins tend to recognise small chains, *i.e.*, less than 10 saccharide residues[13]. Consequently, the natural ligands for lectins tend to be glycans with multivalent presentation (Figure 1.2). Multivalency not only provides stabilising and strengthening effects on the glycan-lectin interaction [14], but it also results in the high specificity of the glycan-lectin interaction, as glycan presentation is important. Consequently, discrimination between different linkages and stereochemical configurations are enabled, meaning lectins can have high specificity

for glycans[15].

The binding between a lectin and carbohydrate includes a number of different non-covalent interactions, including hydrogen bonding; salt-bridges; metal ion coordination; and hydrophobic stacking (Figure 1.3)[16][17].
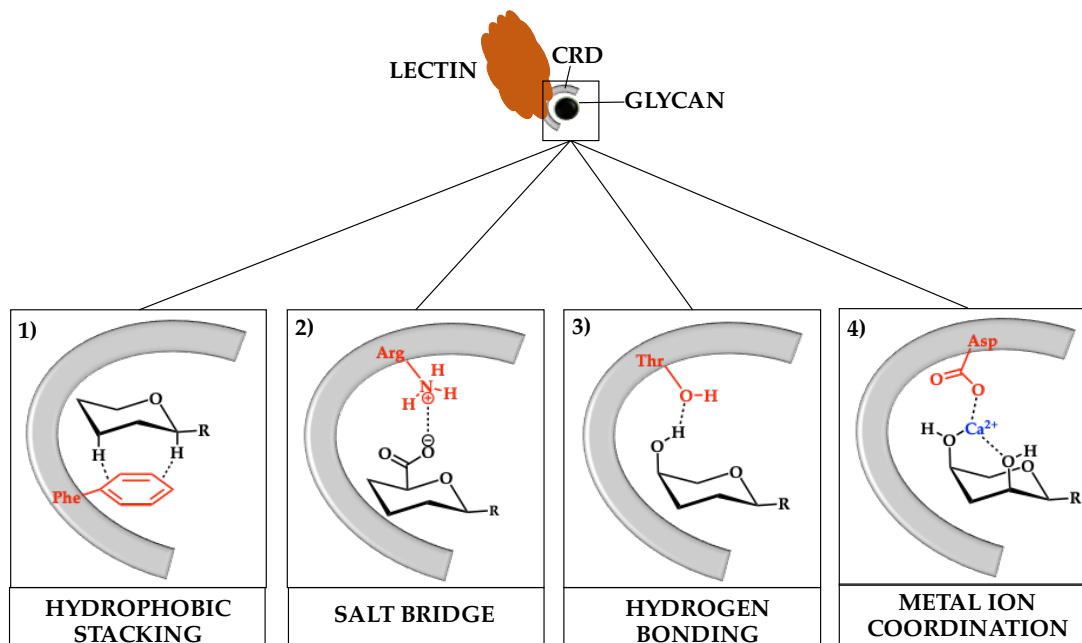
Figure 1.3: Non-covalent glycan-lectin interactions: 1) hydrophobic stacking, by glycan hydrophobic patches and aromatic amino acids; 2) salt bridges between charged glycans and oppositely charged amino acids; 3) hydrogen bonding between amino acids and glycan hydroxyl or amino groups; and 4) metal ion coordination by glycan hydroxyls and negatively charged amino acids. Phe = phenylalanine, Arg = arginine, Thr = threonine, Asp = aspartate.

Hydrogen bonding by hydroxyl groups act as the main interaction between the glycan and lectin, with further hydrogen bonding facilitated by water molecules[16]. The glycan hydroxyl groups form hydrogen bonds with polar amino acids, such as glutamine and serine[17]. The glycan hydroxyl groups can also participate in cooperative hydrogen bonding, where the hydroxyl is both the acceptor and donor. Further hydrogen bonding can occur between lectin and hydroxyl substitutes found on glycans, such as amines.

Although most glycans are neutral, salt-bridges can form between charged glycans and oppositely charged amino acid residues, such as sialic acid (negatively charged sugar) and lysine (positively charged amino acid). Some lectins

4

also require divalent metal ions, such as Ca^{2+}, for glycan binding[12]. The cation is coordinated between glycan hydroxyls and negatively charged amino acids[17].

Saccharides also contain hydrophobic and hydrophilic areas in their structure. Therefore, hydrophobic stacking can occur between hydrophobic regions of the saccharide (CH groups) and amino acids, such as the aromatic phenylalanine, tryptophan and tyrosine residues, in the lectin[16]. These hydrophobic interactions, along with hydrogen bonding and van der Waals interactions, are the main interactions that contribute to glycan selectivity by the lectin[18].

1.1.1   Cell-surface lectins in bacterial infection

Glycan-lectin interactions play a key role in bacterial pathogenesis, involved in both attachment and invasiveness. To establish an infection, pathogenic bacteria must adhere to the host cell surface. Without attachment, bacteria are at risk from clearance by the immune system. To facilitate adhesion, bacteria can use cell-surface lectins to bind to host cell surface glycans. Lectins used for adhesion (adhesins) may be found as part of protein appendages, such as fimbriae or pili (fimbrial adhesins); or on the outer membrane (non-fimbrial adhesins)[19]. Once adhered, the bacteria are able to colonise the host, and may become invasive, where they enter host cells and can spread to other tissues; or form biofilms (see Figure 1.4).
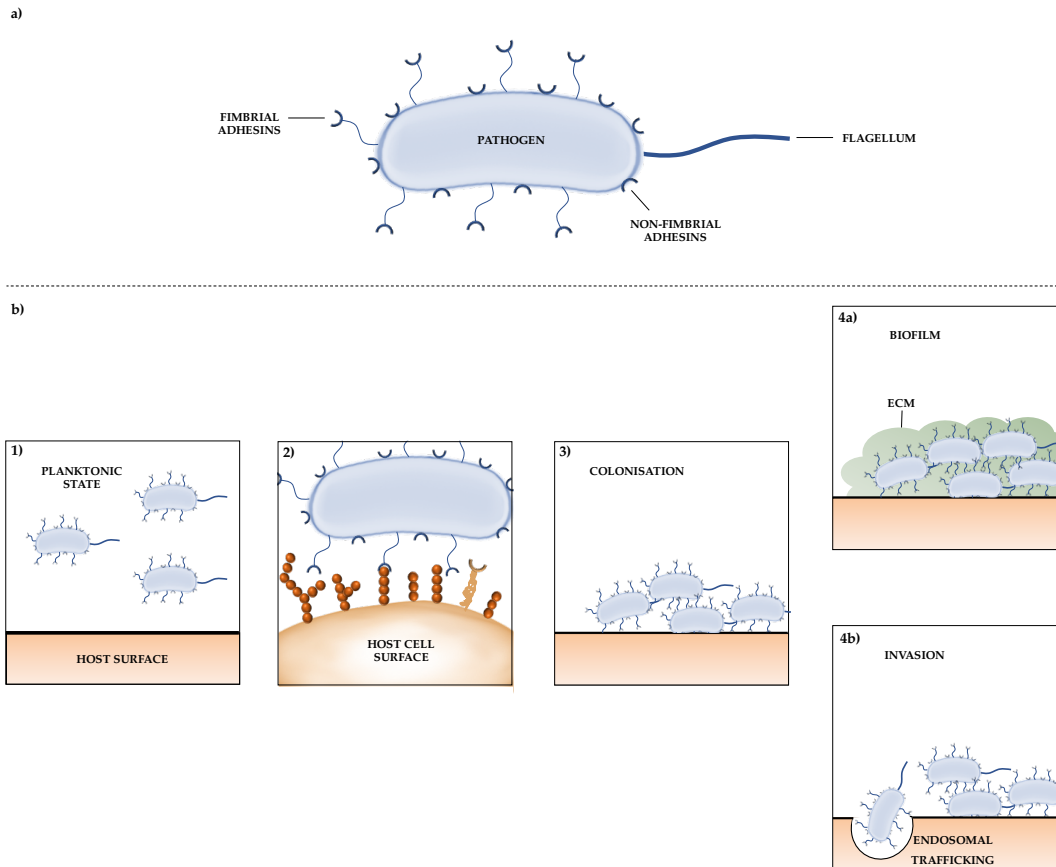
Figure 1.4: A) Bacterial lectins used for adhesion may be found localised on protein appendages (fimbrial adhesins) or on the outer membrane (non-fimbrial adhesins). B) Adhesion is a prerequisite for infection: 1) planktonic bacteria gain entry to host; 2) attachment to host cell surface through glycan-lectin interactions; 3) irreversible attachment leads to growth and colonisation; 4a) established colonies may form biofilms; or 4b) attachment may lead to invasion through endosomal trafficking.

The bacterial lectins used in attachment can be highly selective, and limit their pathogenesis to a single species, or to a particular location within a species, such as *Escherichia coli* (*E. coli*). Although many of these glycan-lectin interactions have not been characterised for human pathogens, one of the most well-studied is a mannose-binding lectin (FimH) found on uropathogenic *E. coli* (UPEC)[20]. FimH is a fimbrial lectin, located at the tip of type I fimbriae (Figure 1.5). FimH recognises monomannosyl and trimannosyl residues. UPEC must express FimH in order to cause a urinary tract infection (UTI), as they use FimH to bind to mannose-containing glycoproteins (uroplankin Ia and Ib) that are expressed on cells of the urinary tract lining (Figure 1.5). Interestingly,

many *E. coli* isolates can express FimH, but the lectin is not associated with pathogenesis elsewhere in the body. In fact, *E. coli* isolates differentially express a variety of different lectins that they use for attachment and invasion, which is dependent on their location[21].
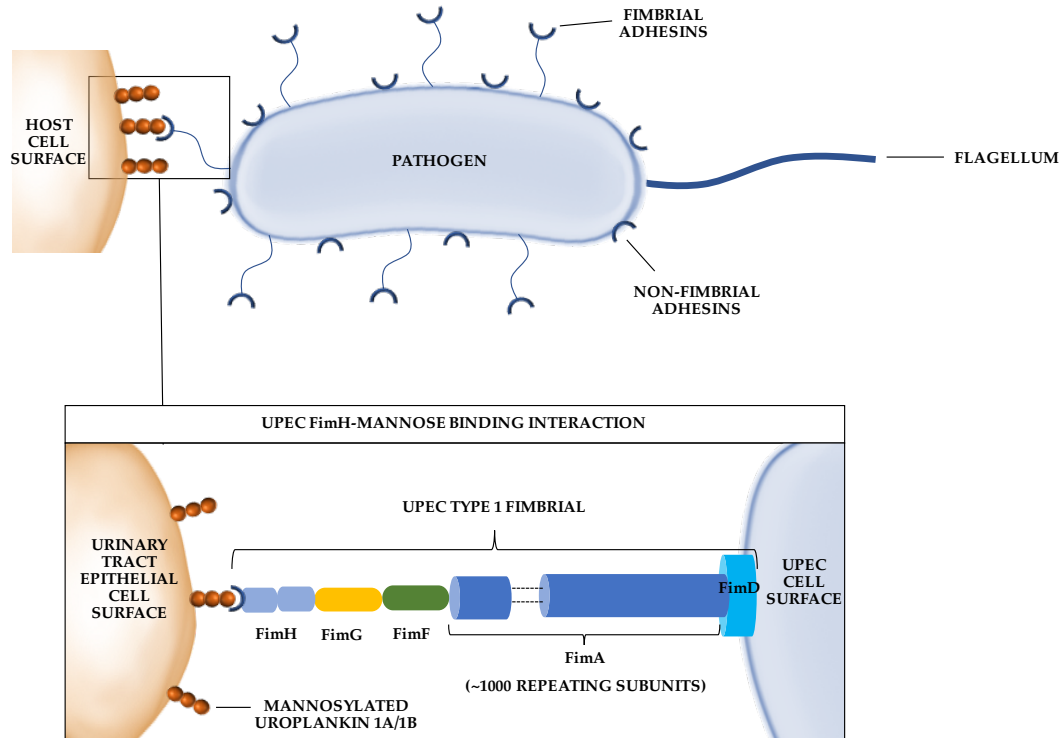
Figure 1.5: Uropathogenic *E. coli* (UPEC) lectin: FimH, binding to mannose found on uroplankins (Ia and Ib) on the urinary tract lining.

As mentioned previously, when bacteria colonise a host, they can form biofilms. Glycan-lectin interactions are also involved in biofilm formation and modulation. Biofilms are an adhered community of microorganisms, embedded in an extracellular polymeric substance (EPS) that largely consists of polysaccharides [22], DNA and proteins [23]. Biofilms present a major problem from a therapeutic standpoint. They account for 80% of all infections[24] and are much harder to treat than their planktonic counterparts. They provide protection against the environment, including the immune system and antimicrobial drugs. The EPS acts as a physical barrier, restricting access of drugs and

host defences from reaching the target site of action on, or inside, the bacteria. Components of the EPS, such as extracellular DNA and polysaccharides, can interact and sequester antibiotics through electrostatic interactions[25]. The EPS may also contain enzymes, such as β-lactamases, that degrade antibiotics before they can reach the bacterial cells[26]. In a biofilm context, the effectiveness of antimicrobial drugs can be reduced 1000-fold; often rendering the drug ineffective, or requiring doses unattainable for safe clinical use[27]. The increased antibiotic tolerance by biofilms is also thought to be linked to some of the bacterial cells existing in a low metabolic state. The bacterial cells closer to the surface have greater access to oxygen and other nutrients. Consequently, a nutrient gradient within the biofilm exists, with lower nutrient availability at deeper depths. In oxygen deprived conditions, bacterial cells are associated with low metabolic activity, and a slow-growing state. The low metabolic active cells are more tolerant to antibiotics, as many classes of antibiotics target fast-growing cells[25].

As well as using lectins for host surface attachment, these cell surface lectins can be critical for biofilm formation, for example, in the opportunistic pathogen *Pseudomonas aeruginosa* (*P. aeruginosa*). *P. aeruginosa* are Gram-negative bacteria that are associated with multi-drug resistance and hardy infections. As an opportunistic pathogen, *P. aeruginosa* can reside in healthy individuals without causing an infection. However, *P. aeruginosa* can cause life-threatening infections in individuals with compromised or low immunity, such as those with Cystic Fibrosis[28]. As well as using a plethora of virulence factors, *P. aeruginosa* also readily form biofilms, which contribute to the severity of the infection as well as the difficulty in clearance[29]. *P. aeruginosa* can express the cell surface lectins: LecA and LecB, that recognise galactosides and fucosides, respectively. The exact role in biofilm formation has not be determined, but it is thought that the lectins bind to exopolysaccharides and other bacteria, forming cross-linkages necessary for biofilm formation[30]. Consequently, lectins have potential to be used in drug targeting against both planktonic and biofilm bacterial

infections. Further discussion on *P. aeruginosa* can be found in Chapter 4.

1.1.2 Cell-surface lectins in cancer

As stated previously, glycan-lectin interactions are involved in diverse roles in the human body, and lectin expression can be altered in diseased-state cells, such as cancer. The type of lectins and their relative abundance, very much depends on the stage and location of the cancer. Differential lectin expression can result in many protumourigenic processes, such as promoting angiogenesis, metastasis and neoplastic transformation; as well as demonstrating anti-apoptotic effects; and aid evasion of immune surveillance[31]. Lectins that have received the most attention in their role in cancer modulation, belong to the galectin[32], siglec and C-type[33] lectin families[34].

Galectins recognise β-galactosides that can be classified as proto-, chimera, or tandem repeat-type galectins, dependent on their structure (Figure 1.6) and is discussed further in Chapter 5. Galectins can be found intracellularly, cell surface associated, or secreted[35]. Consequently, their roles are diverse as they can interact intracellularly and extracellularly. Differential galectin expression has been observed in many different cancers (breast, lung, colon, bladder and pancreas)[36]. In particular, much research has focused on overexpression of extracellular galectin-1 (proto-type galectin), which has been associated with promoting metastasis and angiogenesis, and exerting anti-apoptotic effects[37].
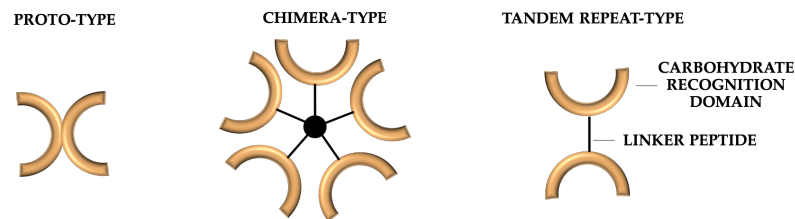
Figure 1.6: Illustration of three structural types of galectins: proto-type, chimera-type, and tandem repeat-type galectins (left to right). Adapted from Cagnoni *et al.*[34]

.

The siglecs (sialic acid-binding immunoglobulin-like lectin) are transmem-

brane receptors that recognise sialic acid derivatives, and play a key role in normal immune functioning [38]. Siglecs can have inhibitory effects on immune modulation, such as siglec-7 and -9 (Figure 1.7) that can be found on a type of immune cell called natural killer cells, which are involved in malignant cancer cell clearance[39]. As many cancers are hypersialyated, this increased sialic acid-siglec binding can aid immune evasion by the hypersialyated cancer cells[40]. Siglec overexpression has also been associated with cancers, such as siglec-2 (CD22, Figure 1.7), which has been shown to be overexpressed on B-cell lymphomas[41].
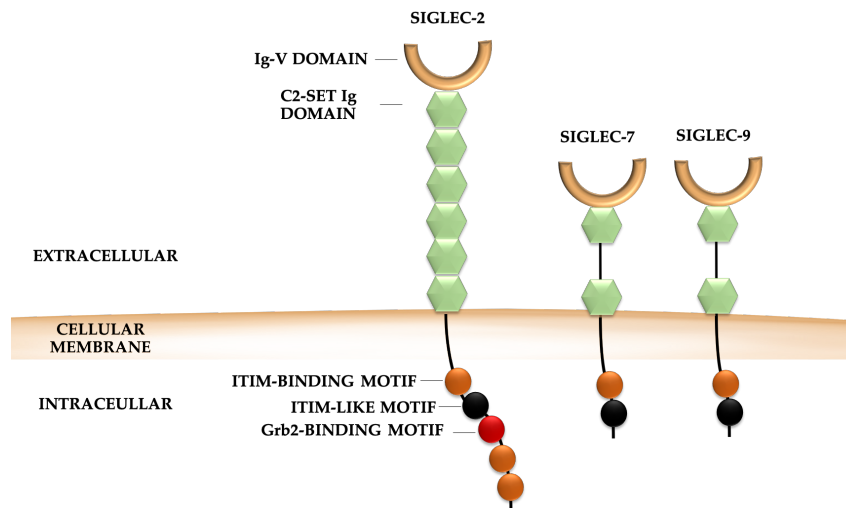
Figure 1.7: Illustration of key siglec structures involved in cancer. From left to right: siglec-2 (CD22), siglec-7, and siglec-9. Adapted from Cagnoni *et al.*[34].

C-type lectins are a large family of predominantly transmembrane proteins, with some secreted proteins, such as mannose-binding lectin. All C-type lectins share structural homologous CRDs. C-type lectins usually require calcium ions for binding and their glycan selectivity is more varied between family members, compared to other lectin families. The C-type lectins have demonstrated roles in promoting metastasis[42], and of particular interest in cancer progression, are the selectins and mannose receptor (Figure 1.8). The selectins recognise sialyated and fucosylated derivatives; whereas, mannose receptor recognises

mannosylated derivatives. Selectins have demonstrated a protumourgenic role in colon, lung and skin cancers[43], and overexpression in the tumour microenvironment, promoting metastasis[44]. Mannose receptor has been detected to be overexpressed in gastric [45] and breast cancer[46], and high expression is associated with poor prognosis[45].
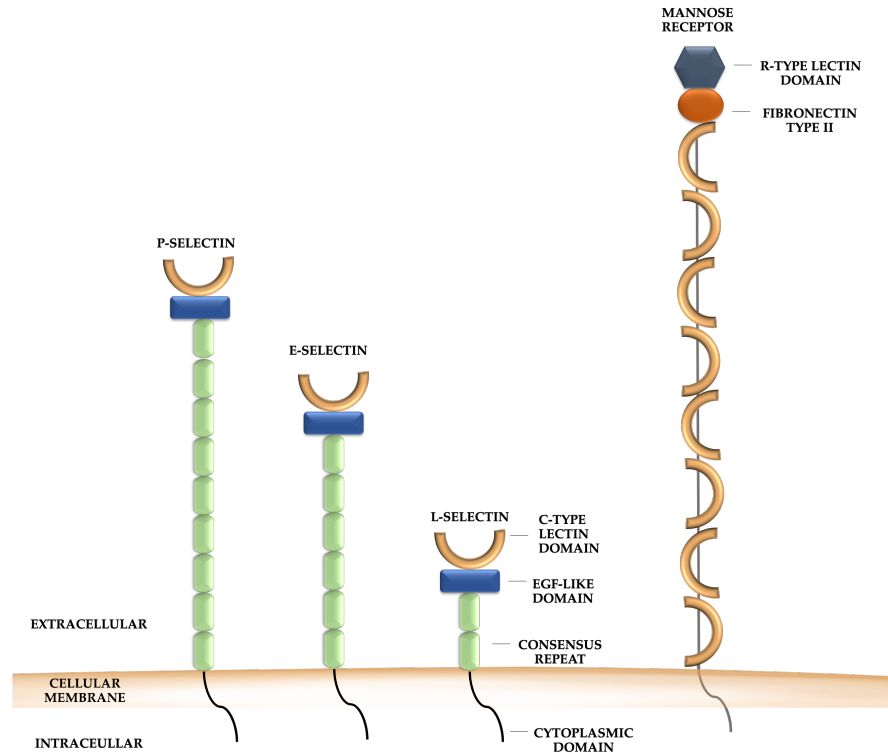
Figure 1.8: Illustration of key C-type lectin structures involved in cancer. From left to right: P-selectin, E-selectin, L-selectin, and mannose receptor. Adapted from Cagnoni *et al.*[34] and van Die *et al.*[47].

1.2 Targeted drug delivery: cell targeting

1.2.1 Overview of glycan-lectin targeting

Targeted binding by glycans to lectins may be split into two groups: 1) direct lectin binding, where glycans are used to target endogenous lectins; or 2) reverse lectin binding, where exogenous lectins are used to target glycans expressed on the cell-surface[9] (Figure 1.9).

11
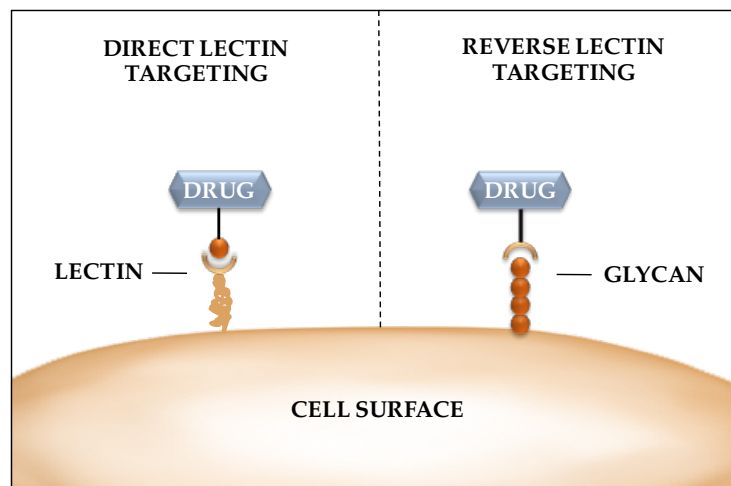
Figure 1.9: Illustration of direct (left) and reverse (right) lectin targeting.

Direct binding provides advantages as glycans offer solubility, stability and biocompatibility[48], which are important aspects when considering drug delivery applications and detection systems. It is also easier to obtain pure glycans, through chemical or enzymatic synthesis. Lectins can themselves be glycosylated, where they can present different glycoforms, and so high purity lectin is often hard to obtain[49]. Lectins can also present toxicity, and elicit an immune response[50]. Consequently, this PhD research uses direct lectin binding, using synthesised glycans for targeting lectins on cancer or bacterial cells.

1.3 Targeted drug delivery: drug carrier

The use of drug delivery systems can enhance safety and efficacy of the therapeutic [51], as they aim to carry the drug to the diseased or infected area at a controlled rate [52]. In order to combine targeting and eradication elements, a 'carrier' is often used. In glycan targeting, multivalent presentation of the glycan is necessary for strong binding, and carriers are one method of achieving this.

1.3.1 Nanoparticles as carriers

There are many different carriers that have been developed for drug delivery systems over the past thirty years [51], and in particular, 'nanoparticles' have gained large interest. Nanoparticles (NPs) are defined as particles with a size between 1 and 1000 nm [53]. NPs are available in a range of shapes, structures, sizes and materials, each contributing to various advantages and disadvantages dependent on their application. Generally, NPs are advantageous over larger drug carriers as they often exhibit high 'loading capacity' of a ligand/drug due to their high surface area to volume ratio. NPs also often have unique chemical and physical properties compared to the bulk material, such as optical and magnetic properties [54].

1.3.2 Gold nanoparticles

Although there are many different types of NPs, one of the most common ways to categorise NPs is based on their material, such as organic (carbon, polymeric, lipid-based) and inorganic (silica, semiconductor, magnetic) [54]. In this PhD research, inorganic gold NPs were used as the carrier, and will be given focus from herein.

Gold NPs (AuNPs) have been studied in great detail over the past two decades. Compared to organic carriers, AuNPs offer superior control over NP size and shape, and consequently monodispersity[55]. The relative ease of AuNP surface modification, along with their unique optical properties, has amplified interest in the potential of AuNPs as drug carriers, as well as in cellular imaging and sensing [56].

AuNPs for glycan-based detection

By coating the AuNP surface with glycans (glycoAuNPs), binding to their corresponding lectin can be observed through colour changes, detected by eye or

by UV-Vis spectrometry. This is a result of multivalent glycoAuNPs binding to multimeric lectin, creating an 'aggregate' of particles (see Figure 1.10).
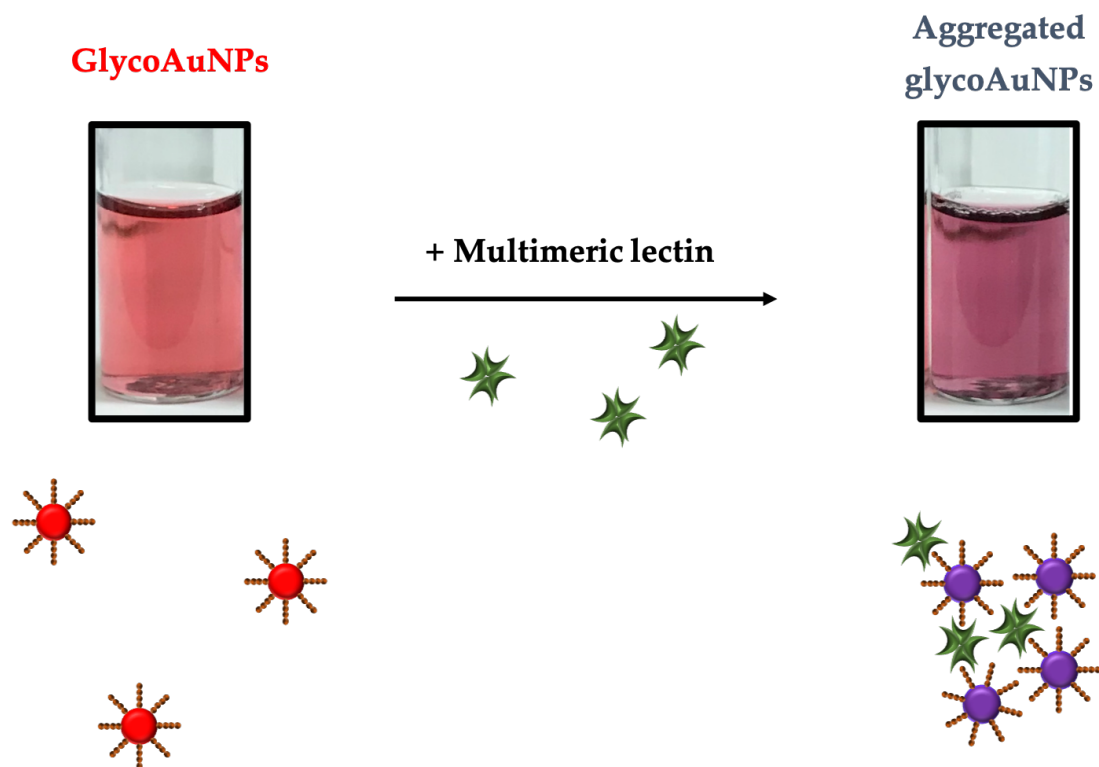
Figure 1.10: Image demonstrating aggregates formed between glycoAuNPs in the presence of multimeric lectin, leading to a colour change from red to purple/blue.

This concept has been explored for detection of soluble lectins[57]; toxins[58]; bacterial cells[59]; and viruses[60]. For example, in 2013, Marin *et al.*[60] were able to discriminate between human and avian influenza virus using a sialic acid α-2,6-galactose derivative to functionalise 16 nm AuNPs. The glycoAuNPs demonstrated preferential binding to human influenza, observed through changes in the UV-Vis extinction spectra. Consequently 16 nm AuNPs are particularly useful in developing glycan-lectin targeted antimicrobial therapeutics, as their color changes can be used to monitor cell surface glycan-lectin interactions.

AuNPs for drug delivery

AuNPs are also a good drug delivery candidate as their size, shape and surface (ligand/s, ligand density, charge) can all be easily controlled during preparation. All these properties affect cellular uptake, and so depending on the cellular target, manipulating these factors can improve uptake and binding interactions. However, the optimal conditions for cellular uptake is multifactoral and can become quite complex. Consideration should be given to factors such as the ligand/s used for surface functionalisation (charge, density, receptor target); the cell type; the concentration; site of action; and incubation time. As shown in Kumar *et al.*[61], where the study assessed cellular uptake by three different ovarian cancer cell lines (OVCAR5, OVCAR98 and SKOV3), assessing effects from particle size (18-80 nm), particle concentration, and incubation time (6-24 hours), using citrate-stabilised AuNPs (negatively charged). The study showed that all cell lines had highest levels of gold when incubated for longer incubation times (24 hours). When it came to size dependency of cellular uptake, the results were more complex. The highest levels of cellular gold (μg) for OVCAR8 was with 18 and 80 nm AuNPs; OVCAR5 was with 18 nm AuNPs; and SKOV3 was with 18, 60 and 80 nm. Highlighting that the optimal conditions should be assessed for the given drug delivery system, biological setting, and cellular target.

AuNPs for glycan-based drug delivery

As AuNPs can be functionalised with different ligands to create heterogeneous monolayers, a multicomponent system can be achieved, providing a way of combining targeting and cell eradication elements (Figure 1.11). For glycan targeting, multivalency and presentation are key for strong binding interactions with lectins. The AuNP aims to mimic the multivalency from biological glycoconjugates that are a lectin's natural ligand. The AuNP scaffold also offers a method of controlling glycan presentation by: the ligand tether, allowing

alterations such as hydrophobicity, charge and flexibility; and ligand density, by altering ligand concentrations for surface functionalisation or diluting with 'spacer' ligands, such as ethylene glycol derivatives.
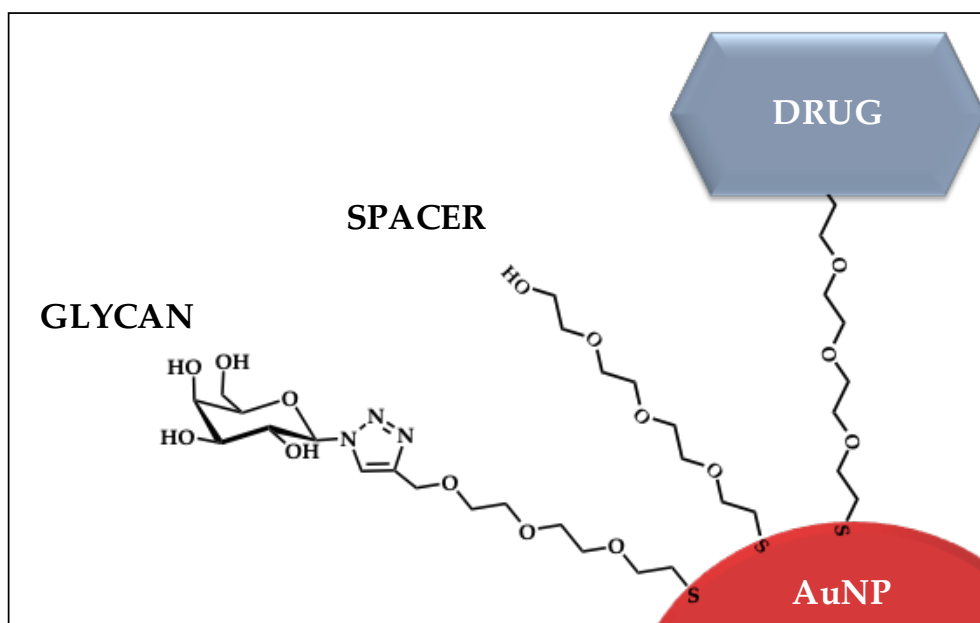
Figure 1.11: Illustration of heterogeneous surface modification of AuNPs, providing a method of combining targeting (glycan) and cell eradication (drug) elements. Glycan presentation can be optimised by including ligands (spacer) that control density of glycan on the AuNP surface.

Poly(ethylene glycol) is commonly used for modifying proteins for therapeutic use, through a method often termed 'PEGylation'. This PEGylation of the compound can improve stability, solubility, circulation time and reduce immunogenecity [52]. Pathogens generally have hydrophobic coatings that attracts serum proteins for attachment. Phagocytic cells recognise the bound serum proteins, and aim to internalise and eliminate the structure through a process called opsonisation. Therefore, hydrophobic drug molecules may have low circulation times in the body. Thus, PEGylation of the drug can increase the hydrophilicity of the compound. Consequently, ethylene glycol tethers were incorporated into the ligands for AuNP functionalisation used in this PhD research.

1.4 Targeted drug delivery: cell killing

1.4.1 Glycan-based AuNPs in cell killing

Glycan based AuNPs (glycoAuNPs) have been explored in therapeutic applications by: coupling glycans with known drugs to the surface, aiming to improve delivery and efficacy of a licensed drug; or coupling glycans with new eradication methods. The former is an approach taken to improve or prolong the effectiveness, and reduce side effects, in current treatments. Whereas new cell eradication mechanisms provide different strategies in hope of bypassing already ineffective cell death pathways and reduce side effects from current treatments.

Some systems use polysacchride coated AuNPs, before further conjugation to conventional drugs. For example, the anti-cancer drug doxorubicin can present cardiotoxicity in a dose-dependent manner[62]. Jang *et al.* demonstrated improved delivery of doxorubicin by coating the AuNP surface with dextran[1], and then conjugating doxorubicin to the dextran coat. The results showed high toxicity of HeLa cells at low concentrations of doxorubicin conjugate particles, in comparison to the unconjugated doxorubicin [64]. Note that in this study, the authors focus on dextran being used to improve biocompatibility, such as improved stability (pH and salt) and improved solubility, rather than for selective targeting of a glycan receptor. A similar approach was taken for targeted drug delivery to bacteria too. Mu *et al.* generated chitosan[2] conjugated to the antibiotic streptomycin (CS) to coat the surface of AuNPs (CS AuNPs). The group demonstrated increased inhibition and destruction of Gram-positive and Gram-negative biofilms with the CS AuNP, compared to the CS or streptomycin alone. The authors showed that the improved response was due to better biofilm penetration, with greater exposure to the streptomycin[66].

---

[1]Dextran is a polysaccharide consisting of glucose residues, with linear chain linkages of α-1,6, and branched chain linkages of α-1,3[63].

[2]Chitosan is a linear polysaccharide with β-1,4 glucosamine and *N*-acetyl-glucosamine, though randomly dispersed throughout the macromolecule[65].

Aswell as polysaccharides, groups have used glycan functionalised polymers (glycopolymers) for targeting. Adokoh *et al.* demonstrated glucose- and galactose-based polymer functionalised AuNPs, that were also co-functionalised with an anti-cancer agent: gold(I) phosphine. The galactose-based particles showed higher toxicity against HepG2 liver cancer cells, compared to conventional anti-cancer drugs (cisplatin and cytarabine). Yuan *et al.* also used polymer-based eradication agents but to target *E. coli*. The group used a glucose-based polymer (poly[2-(methacrylamido)glucopyranose], pMAG) that selectively binds FimH lectin on *E. coli*, and a positively charged polymer (poly[2-(methacryloyloxy)ethyl trimethylammonium iodide], pMETAI) that is normally used as a fungicide, which affects membrane permeability and metabolism. Higher toxicity was observed when the pMAG was present, and there was also a reduction in cell toxicity when mannose was present. Mannose is the preferential monosaccharide for FimH, and so both of these results suggested a specific binding event[67].

Monosaccharides have also been used for targeted drug delivery systems on AuNPs. Conde *et al.* used a multicomponent system for AuNP functionalisation, involving glucose; siRNA, targeting a gene involved in modulating apoptosis and proliferation (*c-Myc*); PEG; and fluorophore[68]. The study showed promising results against lung cancer *in vitro* and *in vivo* (mice), with an 80% reduction in tumour size *in vivo*. Also through glucose targeting, Chiodo *et al.* used glucose functionalised AuNPs, along with two antiretroviral drugs (abacavir and lamivudine), to target HIV-1. The AuNPs inhibited viral replication at a similar level to that of the free drug. However, current anti-HIV treatment needs a cocktail of antiretroviral drugs that can present host cell toxicity and drug resistance, and so the study demonstrated a proof-of-concept, with authors speculating on future prospects of using a similar approach but with different drugs to improve effectiveness[69].

1.4.2 Photodynamic therapy as an effective therapy against different cell types

Photodynamic therapy (PDT) relies on a non-toxic dye, termed a 'photosensitiser' (PS). Upon light activation, the PS releases reactive oxygen species (ROS) that causes irreversible damage to cells where the PS is localised[70]. The cell killing mechanism by PDT allows the therapy to be effective against a wide range of cell types, including cancer and bacteria, *i.e.* the drug target is not cell-specific. Further advantages of PDT are that the drug is only activated upon irradiation with light, consequently reducing side effects from uptake of the drug from surrounding tissues. The localised effects of PDT reduce healthy human cell cytotoxicity and tissue damage. Singlet oxygen has been demonstrated to have a lifetime of ~3 µs [71], in which time the singlet oxygen can only diffuse short distances of around 0.1 µm [72]. This makes the effects of PDT highly localised, further reducing host cell toxicity.

Photodynamic therapy mode of action

To induce cytotoxicity, the PS must first be activated by absorbing energy from an appropriate wavelength of light, which excites the molecule to a higher energy state [70]. There are two types of reaction that can produce reactive oxygen species (ROS). A Type I reaction involves electron or hydrogen transfer, and produces superoxide anions, hydroxyl radicals and hydrogen peroxides; whereas, a Type II reaction involves the transfer of energy to an oxygen molecule that generates singlet oxygen (see Figure 1.12)[73].
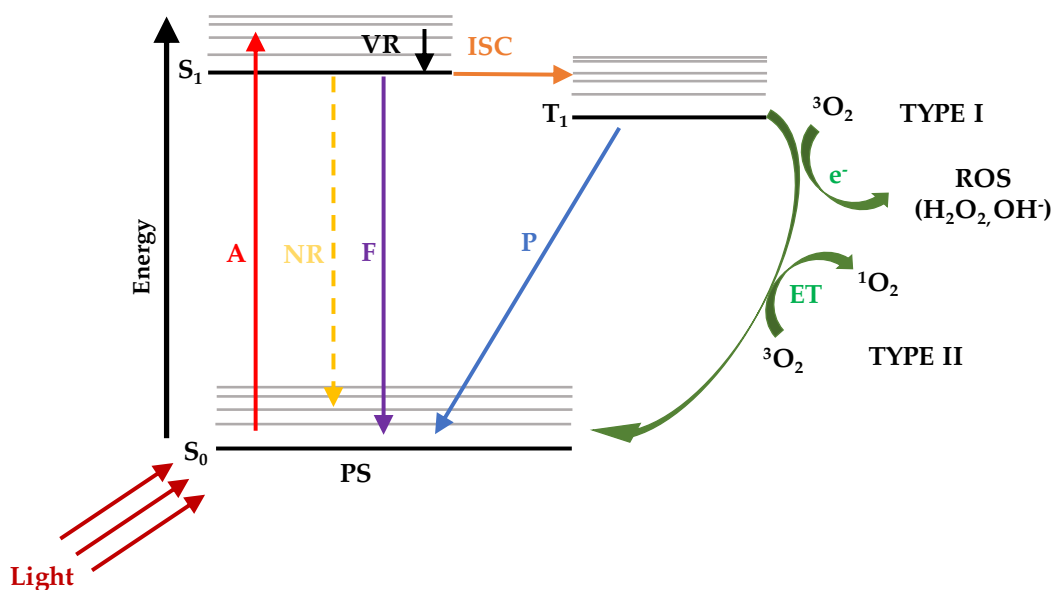
Figure 1.12: A Jablonski diagram demonstrating the principles of PDT, adapted from Dai *et al.*[74]. PS = photosensitiser; A = absorbance; VR = vibrational relaxation; ISC = intersystem crossing; NR = non-radiative; F = fluorescence; P = phosphorescence; e⁻ = electron transfer; ET = energy transfer.

Generally, molecules exist at a singlet ground state, which refers to paired electrons that have antiparallel spin in the lowest energy level. However, oxygen occupies a triplet state, which means paired electrons have parallel spin. Upon irradiation of light, the PS becomes excited to a higher energy singlet state, and after a short period the molecule returns to the singlet ground state *via* radiative (fluorescence) or non-radiative (heat) processes. Alternatively, the excited molecules can undergo spin conversion through intersystem crossing to the triplet state. At this stage, generation of Type I reactive oxygen species can be formed through the transfer of electrons or hydrogen to surrounding molecules [70]. The photoactive compound may also transfer energy to an oxygen molecule to generate singlet oxygen [75]. As oxygen exists in a triplet state, when oxygen absorbs the energy from an excited molecule, *i.e.,* the PS, the oxygen is excited to the lowest excited energy level that is a singlet state (see Figure 1.12).

Photosensitisers

PSs may be classified as first, second or third generation. First generation PSs are derivatives of hematoporphyrin. Hematoporphyrin is composed of a mixture of porphyrin-based compounds, and isolation of oligomers of the mixture led to the first commercially available PS: Photofrin®[76].The first generation PSs had a variety of disadvantages, such as long photosensitivity after treatment; low purity; and low light tissue penetration from a short PS activation wavelength.

Next, a series of second generation PSs were generated, both porphyrin (chlorin, bacteriochlorin, phthalocyanine) and non-porphyrin (phenothiazinium, xanthene, dipyrromethene), designed to overcome the problems from the first generation PSs. The aim of second generation PS was to improve purity; lower dark toxicity (activation without light); longer activation wavelengths for deeper light penetration; improve target cell selectivity; and improve singlet oxygen quantum yield through PS structural changes[77]. So far, only first and second generation PSs are approved for clinical use, including: Photofrin®, porfirmer sodium; Levulan, 5-aminolevulinic acid (ALA, precursor for protoporhyrin IX); Metvix, ALA-methyl derivative; Photosense, sulphonated aluminium phthalocyanine; Radachlorin, chlorophyll a derivatives; Laserphyrin, chlorin e6-L-aspartic acid conjugate; and Verteporfin, benzoporphyrin derivative[78]. For a summary of first and second generation PS classification see Figure 1.13.
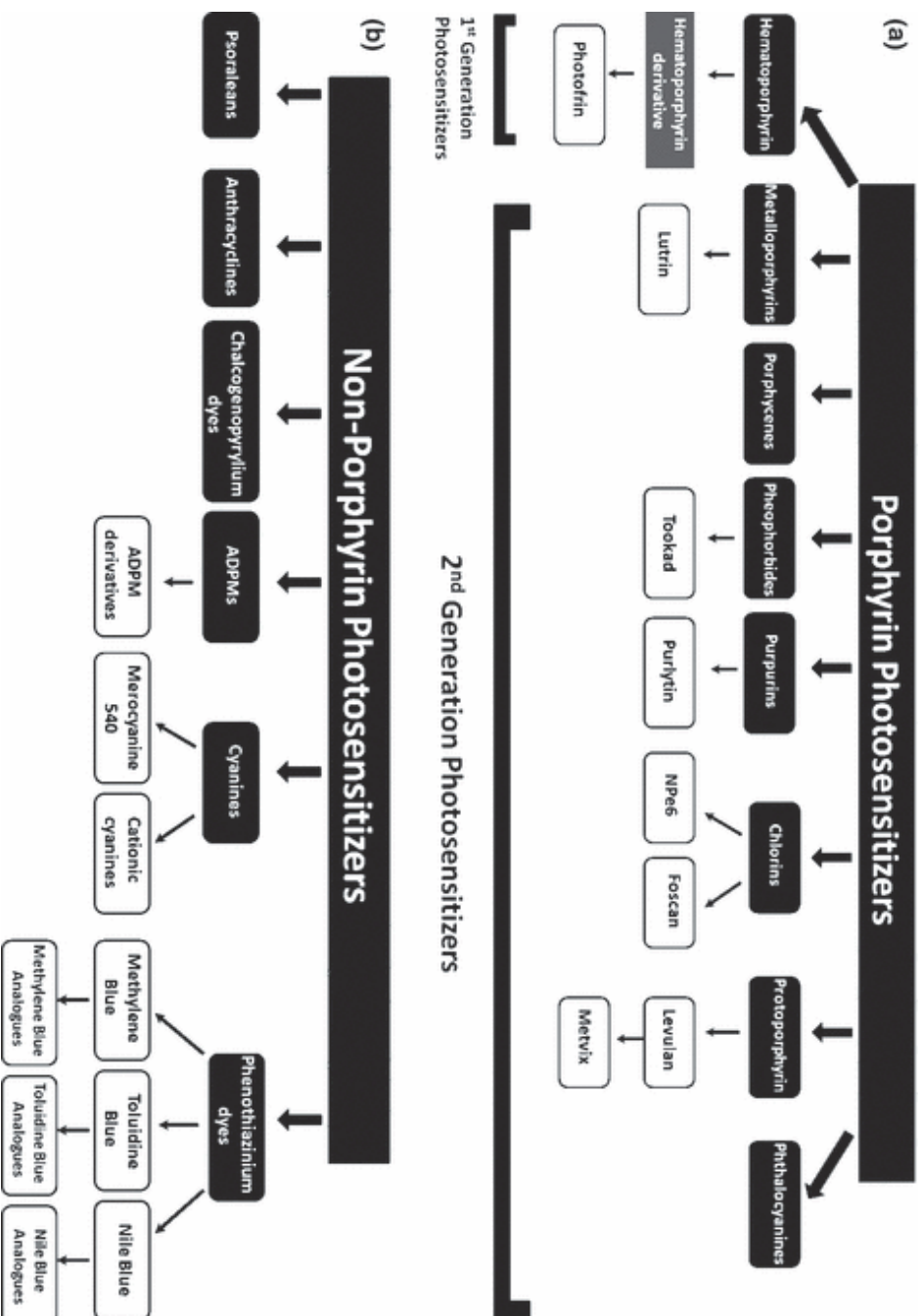
Figure 1.13: Summary of first and second generation PSs. Republished with permission of John Wiley and Sons, from A. E. O'Connor, W. M. Gallagher, and A. T. Byrne, "Porphyrin and nonporphyrin photosensitizers in oncology: Preclinical and clinical advances in photodynamic therapy," *Photochemistry and Photobiology*, vol. 85, no. 5, pp. 1053–1074, Sep. 2009, doi: 10.1111/j.1751-1097.2009.00585.x; permission conveyed through Copyright Clearance Center, Inc. ©2009 The Authors. Journal Compilation. The American Society of Photobiology 0031-8655/09.

Third generation PSs aim to incorporate targeted elements. This may be through the PS conjugated to targeting structures, such as antibodies[79][80], peptides[81], aptamers[82], fullerenes[83], bacteriophages[84], folic acid[85] and glycans (reviewed within). The use of PS conjugated to NPs (inorganic or organic) are also third generation PS, as nanomaterials have shown improved uptake and localisation to tumours[86] and infections[87]. As PSs tend to be hydrophobic, then can aggregate in biological media which reduces their uptake and effectiveness. NPs can improve solubility of the PS, and their high surface to volume ratio means large amounts of drug can be carried to the target cell; a process known as passive targeting (discussed further in Section 1.4.2). Alternatively, targeting structures and nanomaterials may be combined, and are classified as active targeting[86].

Photodynamic therapy against bacteria

PDT was observed to be effective against microorganisms over 100 years ago, but the discovery of antibiotics halted the focus of PDT as a clinical antimicrobial treatment[88]. Instead, focus was placed on PDT as an anti-cancer treatment. However, with drug-resistance and the lack of new antibiotics coming through to the clinics, PDT has started to gather momentum for the treatment of infections over the past three decades[89]. The main ways PDT causes cell death in bacteria intracellularly is by the ROS oxidising nucleic acid and damaging antioxidant enzymes (catalase, peroxidase); and extracellularly, ROS oxidises lipids and proteins in the membrane, and can cause cross-linking of membrane proteins (Figure 1.14).
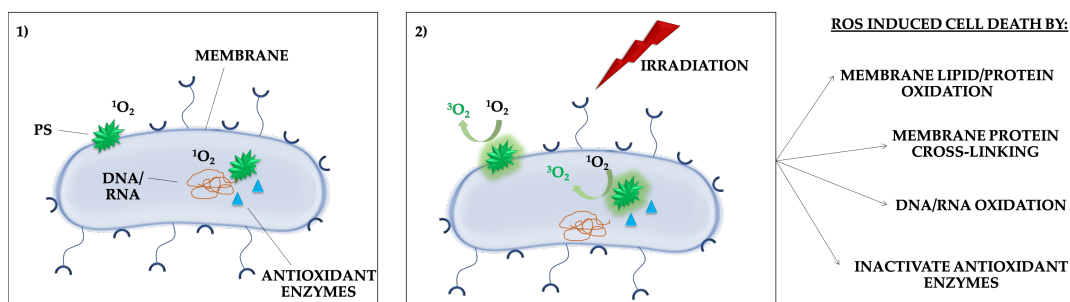
Figure 1.14: Mechanisms of ROS induced cytotoxicity against bacteria *via* PDT: 1) PS localises to cell membrane or intracellularly; 2) PS is activated upon irradiation, generating ROS; and 3) methods of cell death.

There are many advantages of PDT for antibacterial treatment. Firstly, PDT has already been shown to successfully eradicate a range of microorganisms [90], and also has been successful at killing multi-drug resistant bacteria [91]. Upon degradation, bacteria can release virulence factors such as LPS and proteases, which can stimulate proinflammatory cytokine production. Using toluidine blue O, PDT has been shown to 'detoxify' these products from *E. coli* and *P. aeruginosa*, and thus reducing an inflammatory response [92]. PDT is also faster acting than conventional antibiotics. Evidence also suggests that bacteria will develop resistance at a much slower rate to PDT than to current antimicrobial drugs, as damage is wide spread across the cell [93]. Bacteria may develop resistance to PDT by upregulating antioxidant enzymes against type I generated ROS. However, no bacterial defensive antioxidant enzymes against singlet oxygen (type II generated ROS) are known. Bacteria may also increase efflux pump expression to remove PS from the cell. However, the phenothiazinium dyes are the only PSs that have been shown to be removed by bacterial efflux pumps, even though many different types of PS have been assessed[94].

Photodynamic therapy against cancer

As mentioned above, cancer had been the predominant focus of PDT research. These efforts have resulted in PDT available in the clinics for treatment against a range of different cancers, such as skin, oesophageal, mouth, lung, and breast.

Singlet oxygen is thought to provide the largest contribution to the cytotoxicity that arises from PDT [75]. The reactive oxygen species are cytotoxic through necrosis or apoptosis [95], primarily damaging the DNA and cytoplasmic membrane [22]. PDT can also result in cancer treatment through indirect methods too.

PDT has notably three methods of tumour destruction, through direct and indirect damage. Firstly, as outlined in Section 1.4.2, there is the direct killing of the cancer cells by ROS (see Figure 1.15). This direct killing of the tumour cells can also generate indirect tumour damage through stimulating an immune response. The direct cell killing through apoptosis or necrosis results in inflammatory mediators and antigens being released from the cells, which triggers inflammation. This localised, acute inflammation subsequently results in an adaptive immune response that is tumour specific. Lastly, PDT can damage the surrounding tumour vasculature, starving the tumour of nutrients.
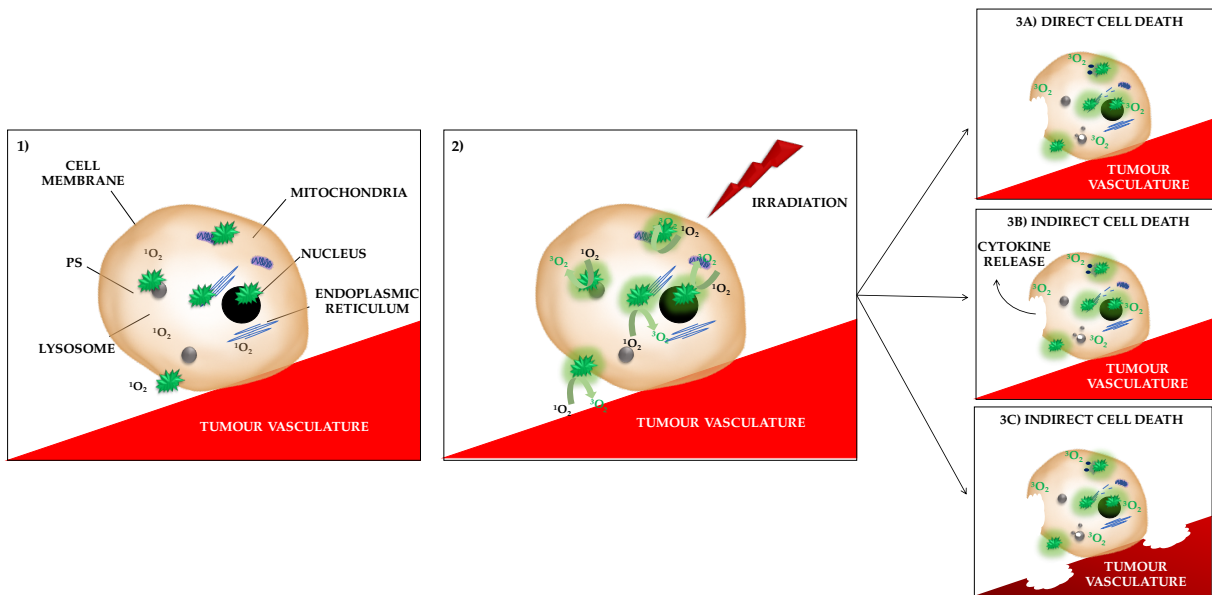
Figure 1.15: Mechanisms of ROS induced cytotoxicity against cancer cells *via* PDT: 1) PS localises to cell membrane or intracellularly; 2) PS is activated upon irradiation, generating ROS; 3a) oxidation of proteins, lipids, DNA; 3b) immune stimulation by cytokine release from dead cell; and 3c) destruction of surrounding vasculature by ROS.

Cancer cells are associated with their unregulated and rapid growth, which

results in stimulation of new vasculature to meet the the high oxygen and nutrient demand. Cancer cells release abnormal vasculature growth signals, which makes their surrounding vasculature disorganised, erratic and more permeable, as gaps form between endothelial cells in the blood vessel barrier[96]. Consequently, tumour vasculature is often described as 'leaky', as larger particulates (such as NPs) can move across the endothelial barrier; whereas, in normal vasculature, movement is restricted to smaller molecules. Tumours can also lack a functioning lymphatic drainage system, which is responsible for the removal of compounds from the tumour environment. NPs can therefore preferentially accumulate in tumours over healthy cells, which is known as the enhanced permeability retention effect (EPR)[97].

Limitations of photodynamic therapy

PDT relies on light being able to reach and activate the PS, and sufficient oxygen availability within the PS environment. Current PSs are activated by wavelengths of light that can travel a maximum of 1 cm through the skin[89]. Consequently, PDT treatment is limited by location and size of the target. For example in cancer, the unregulated and rapid growth often leads to lack of nutrients in the depths of large tumours; creating hypoxic conditions. Therefore, PDT is most effective against infections or cancers that are localised close to the skin or mucosal surfaces, and relatively low density or small in size. These limitations can only be solved by improving methods of light delivery, or developing PSs that can be activated by light that can penetrate further depths.

In the clinics, one of the major side effects from PDT is photosensitisation of the skin and eyes. This is a result of the low selectivity of current PSs, where large doses are needed to achieve efficient toxicity. By improving PS delivery, lower doses would be administered; which in turn, could reduce photosensitisation side effects[98]

1.4.3 Glycan targeted photodynamic therapy

Not only is targeted delivery of the PS important for lowering side effects, it is also critical for successful application as the singlet oxygen must be localised to the target cell to cause effective cytotoxicity; especially considering the short lifetime of singlet oxygen[99]. The hydrophobicity of PSs means that they often show poor solubility *in vivo*, and can form aggregates that lower their efficiency, or lead to quenching. Glycans offer hydrophilicity when conjugated to compounds, and so there has been much research into glycan-PS conjugates for biocompatibility, as well as targeting.

Through direct conjugation of glycans to PSs, the aim is to improve solubility and targeted uptake by the target cells. There has been much research using this approach, with focus on galactose-, glucose-, mannose-, and lactose-based PS conjugates[100]–[106], and extensive reviews of glyco-modified PSs have been published[107][108]. Although glycan modification can improve stability and biocompatibility of the PS for targeting purposes, multivalent presentation improves lectin binding. Consequently, multivalent presentation of glycans in conjugation with PSs has been explored too.

In 2015, Lu *et al.*[109] demonstrated a galactose functionalised polymer (2-(dimethylamino)ethyl meth-acrylate or 'DMAEMA') that was coupled to the macromolecular PS core: 4,4-difluoro-4-bora-3a,4a-diaza-s-indacene (BOD-IPY). The functionalised PS was shown to inhibit bacterial growth at a dose concentration of 0.3 nM. After investigation, the specificity was not linked to the glycan-lectin interaction. Although this study does show a potential method for conjugating a successful antimicrobial PS to a carbohydrate functionalised polymer.
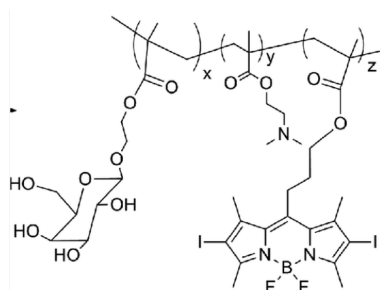
Figure 1.16: Structure of galactose-based polymer BODIPY conjugate used in Lu *et al.*[109]. Republished with permission of Royal Society of Chemistry, from Z. Lu, X. Zhang, Y. Zhao, *et al.*, "BODIPY-based macromolecular photosensitizer with cation-enhanced antibacterial activity," *Polymer Chemistry*, vol. 6, no. 2, pp. 302–310, Dec. 2015. DOI: 10.1039/C4PY00715H; permission conveyed through Copyright Clearance Center, Inc.

Silva *et al.*[110] synthesised galactose-based dendrimer PS conjugates (Figure 1.17). In 2014, the group demonstrated targeted anti-cancer PDT using the phthalocyanine derivative[111]. The dendrimer phthalocyanine conjugate was selectively taken up by two bladder cancer cell lines, through glycan-binding proteins (galectin-1 and GLUT1 receptor). This was demonstrated through siRNA to inhibit galectin-1 and GLUT1 expression, which reduced uptake and effective phototoxicity by PDT. However, to demonstrate effectiveness as a therapeutic, further work is needed to show either *in vitro* selectivity with a non-cancer cell line as a control, or *in vivo* studies to assess cancer targeting in a complex, biological context.
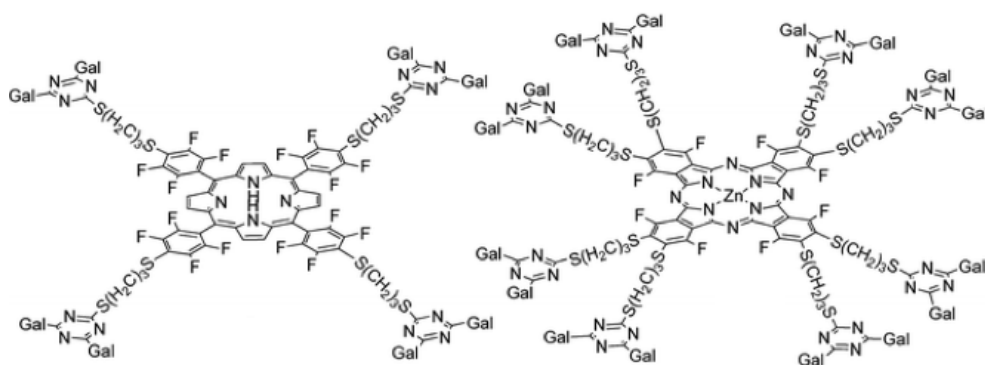
Figure 1.17: Galactose dendrimer porphyrin (left) and phthalocyanine (right) conjugates, synthesised in Silva *et al.*[110]. The phthalocyanine derivative is used in Pereira *et al.*[111]. Used with permission of Royal Society of Chemistry, from S. Silva, P. M. Pereira, P. Silva, *et al.*, "Porphyrin and phthalocyanine glycodendritic conjugates: Synthesis, photophysical and photochemical properties," *Chemical Communications*, vol. 48, no. 30, pp. 3608–3610, Apr. 2012. DOI: 10.1039/c2cc17561d; permission conveyed through Copyright Clearance Center, Inc.

Das *et al.* [112] used mannose-based dendrimer porphyrin conjugates (Figure 1.18), to bind the mannose-binding lectin concanavalin A (ConA). The dendrimers were constructed of either 12 or 36 mannose residues. This study was interesting as it demonstrated that more monosaccharide residues does not necessarily result in better lectin binding. Instead, the conjugate bearing fewer mannose residues on the dendrimer, had stronger binding to ConA. Highlighting the importance of saccharide presentation; accessibility by lectin CRD; and density, in lectin binding.
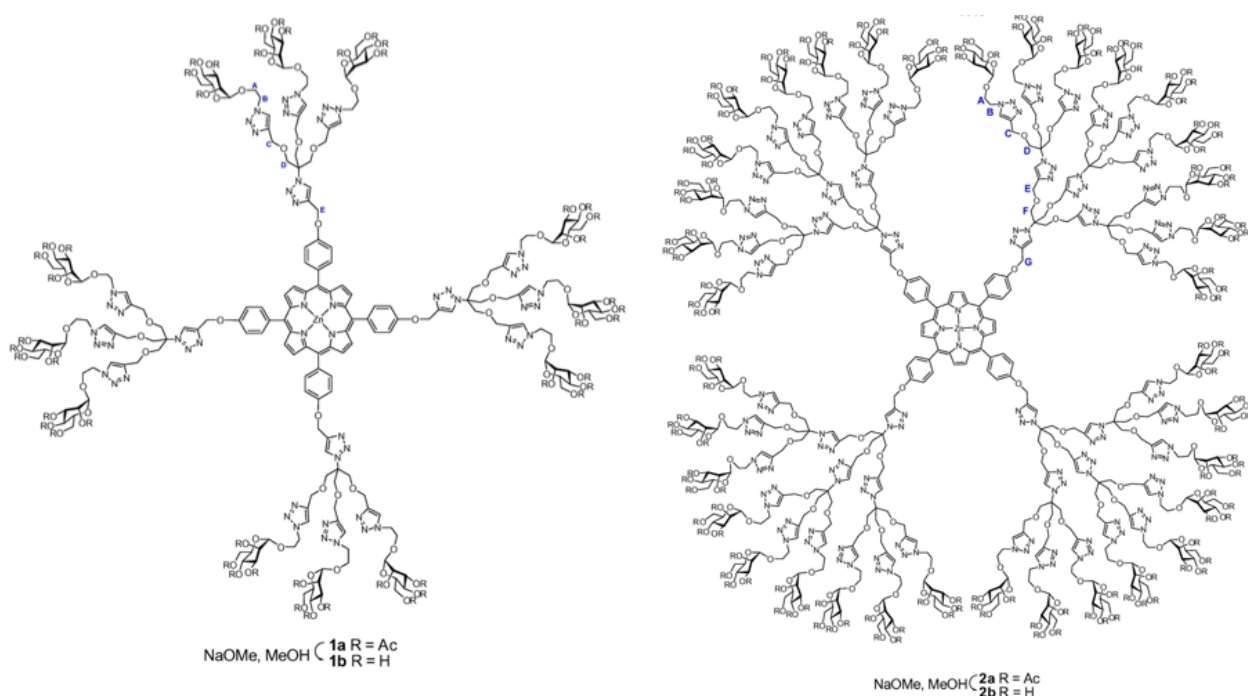
Figure 1.18: Structures of mannose-based dendrimer porphyrin conjugates used in Das *et al.*[112], bearing 12 (left) or 36 (right) mannose residues. Conjugates used in experiments were all deacetylated (1b or 2b). Reprinted from R. Das and B. Mukhopadhyay, "Use of 'click chemistry' for the synthesis of carbohydrate-porphyrin dendrimers and their multivalent approach toward lectin sensing," *Tetrahedron Letters*, vol. 57, no. 16, pp. 1775–1781, Apr. 2016. DOI: 10.1016/j.tetlet.2016.03.031, Copyright (2016), with permission from Elsevier.

Nanomaterials have also been used as a scaffold for glycans and PSs. As mentioned previously, nanomaterials can offer control over ligand density and presentation, which aids lectin binding. Despite the advantages offered by glycan-targeted and PS nanomaterial conjugates, studies are more limited than other glycan-PS conjugates. Rhee *et al.*[113] used virus-like particles that were

modified with metalloporphyrin and a sialic acid derivative (Figure 1.19) to target CD22 receptor on CHO cells. Improved cell death was observed at all concentrations when the sialic acid derivative was present. Selective uptake was also demonstrated, by comparing cell viability of CD22 negative and positive CHO cells. Interestingly, the authors note that they observed rapid decomposition when the virus-like particles were modified with an anionic porphyrin derivative, which may mean this approach is limited to cationic or neutral PSs for stable conjugate production.
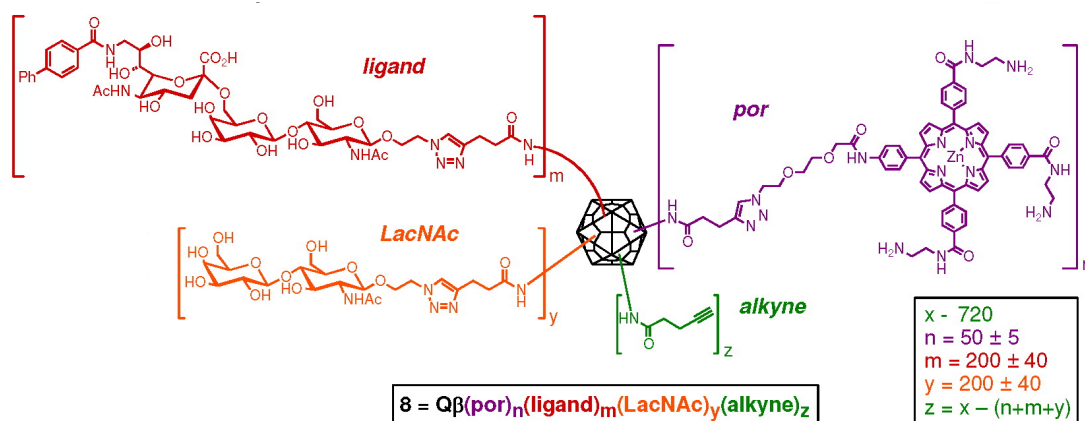
Figure 1.19: Structure of glycan/porphyrin modified virus-like particles used in J. K. Rhee, M. Baksh, C. Nycholat, *et al.*, "Glycan-targeted virus-like nanoparticles for photodynamic therapy," *Biomacromolecules*, vol. 13, no. 8, pp. 2333–2338, Aug. 2012. DOI: 10.1021/bm300578p. Control particles lacked the sialic acid derivative ligand (red). Reprinted (adapted) with permission from Rhee *et al.*[113]. Copyright (2012) American Chemical Society.

Brevet *et al.*[114] used silica nanoparticles modified with anionic porphyrin, with and without mannose (Figure 1.20), to target breast cancer *in vitro* (MDA-MB-231). With the mannose conjugated particles, 99% cell death of breast cancer cells was observed upon irradiation *in vitro*. Without mannose, 45% cell death was observed, demonstrating that when mannose was present there was improved phototoxicity. By introducing free mannose as an inhibitor, phototoxicity was inhibited. This suggested that the increased phototoxicity with the mannose conjugated particles, was due to a mannose-dependent interaction.
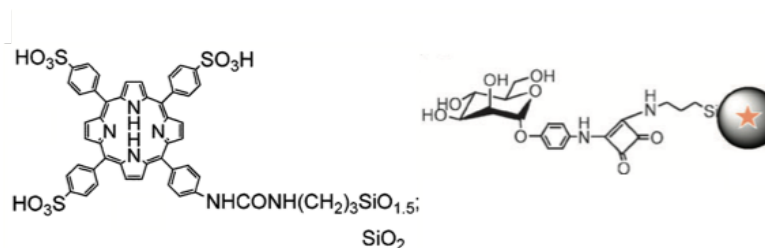
Figure 1.20: Structure of mannose/porphyrin modified silica particles used in Brevet *et al.*[114]. The porphyrin is encapsulated within the mesoporous silica nanoparticles (left) and then conjugated to mannose derivative (right). Control particles were unconjugated. Republished with permission of Royal Society of Chemistry, from D. Brevet, M. Gary-Bobo, L. Raehm, *et al.*, "Mannose-targeted mesoporous silica nanoparticles for photodynamic therapy," *Chemical Communications*, no. 12, pp. 1475–1477, 2009. DOI: 10.1039/b900427k; permission conveyed through Copyright Clearance Center, Inc.

More recently, Shao *et al.*[115] used iron oxide NPs, with the PS (hypericin) trapped in a polydopamine film on the surface of the particles, where lactose was then conjugated to the film (Lac-PHMs, Figure 1.21). The particles were used to target a liver cancer cell line that overexpress asialoglycoprotein receptors (ASGP-R). Control particles were produced following the same method, except an ethylene glycol derivative was used to modify the film instead of lactose (TEG-PHMs). Lac-PHMs showed targeted uptake by the liver cancer cell line that overexpresses ASGP-R (HepG2), and good cytotoxicity compared to free PS.
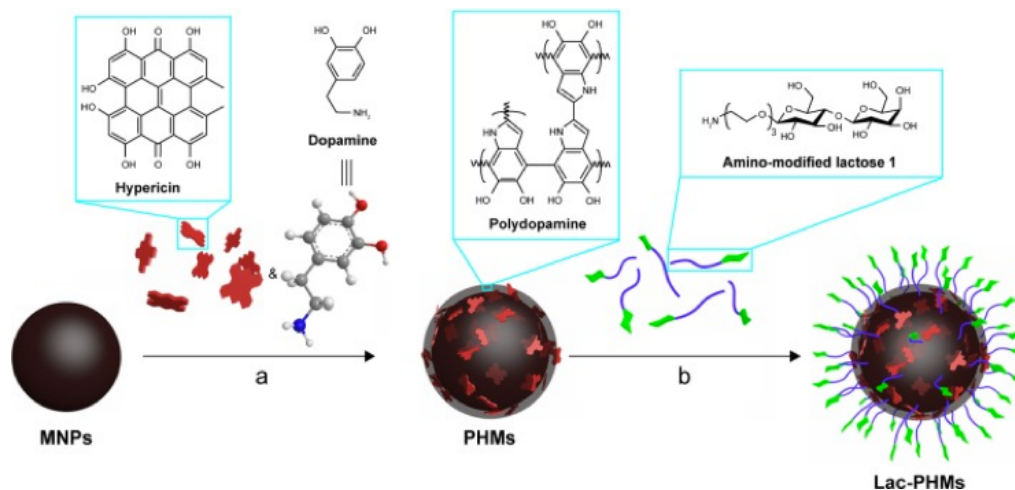
Figure 1.21: Illustration representing Lac-PHMs, synthesised by Shao *et al.*[115]. Republished with permission of Dove Medical Press Ltd. from C. Shao, K. Shang, H. Xu, *et al.*, "Facile fabrication of hypericin-entrapped glyconanoparticles for targeted photodynamic therapy.," *International journal of nanomedicine*, vol. 13, pp. 4319–4331, 2018. DOI: 10.2147/IJN.S161262 Copyright (2018); permission conveyed through Copyright Clearance Center, Inc.

Khan *et al.*[116] developed a polymeric NP using a porphyrin polymer derivative (poly-5,15-diphenyl(2,5'-dithienylen)-10,20-di(3,5-di-*O*-TEG-phenyl, PTTP), modified with acetylated β-glucose residues (PTTP-Glc-Ac, Figure 1.22). The PTTP-Glc-Ac was cytotoxic against *E. coli* and *Bacillus subtilis*, with 99% cell eradication. Although the authors used the glycan modifications for improvement of PS uptake across the bacterial membrane instead of lectin targeting, the method demonstrated an effective antibacterial approach using polymeric NPs against Gram-positive and Gram-negative bacteria.

Figure 1.22: Structure of PTTP-Glc-Ac, used in Khan *et al.*[116]. Republished with permission of Royal Society of Chemistry, from R. Khan, M. Ozkan, A. Khaligh, *et al.*, "Water-dispersible glycosylated poly (2,5'-thienylene)porphyrin-based nanoparticles for antibacterial photodynamic therapy," *Photochemical and Photobiological Sciences*, vol. 18, no. 5, pp. 1147–1155, 2019 copyright (2019); permission conveyed through Copyright Clearance Center, Inc.

Hu *et al.*[117] developed two dimensional glycoclusters, where mannose and PS (chlorin e6) were encapsulated in human serum albumin (HSA), which self-assembled onto two dimensional MnO_2 (2D glycocluster, Figure 1.23). The 2D glycoclusters were selectively taken up by mannose receptor overexpressed on the breast cancer cell line. The 2D glycocluster was cytotoxic against the breast cancer cell line *in vitro* after PDT treatment, and was used for imaging purposes *in vivo* for breast cancer in mice.
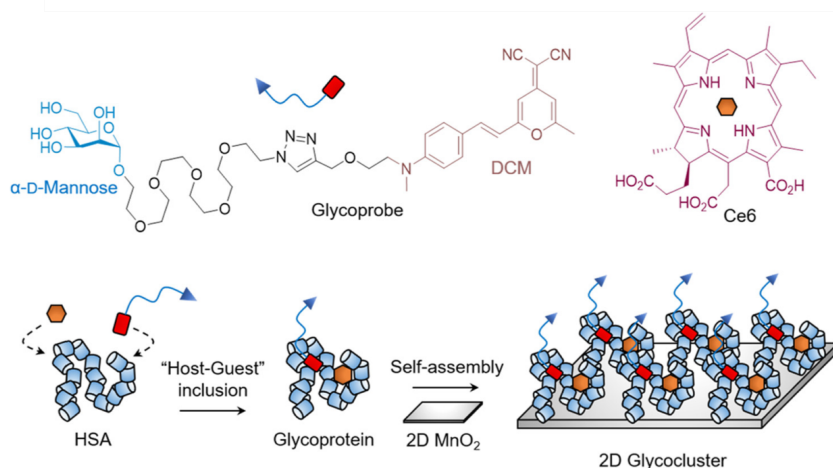
Figure 1.23: Structure and illustration of 2D glycocluster assembly, used in Hu *et al.*[117]. Reprinted (adapted) with permission from X. L. Hu, Q. Cai, J. Gao, *et al.*, "Self-Assembled 2D Glycoclusters for the Targeted Delivery of Theranostic Agents to Triple-Negative Breast Cancer Cells," *ACS Applied Materials and Interfaces*, 2019. ᴅᴏɪ: `10.1021/acsami.9b06016`. Copyright (2019) American Chemical Society.

1.4.4 Previous work by Russell group

The Russell group has previously developed targeted PDT of cancer cell lines, using the glycan-lectin interaction for targeting, and AuNPs as a scaffold. Using 4 nm AuNPs, the group has functionalised AuNPs with a zinc phthalocyanine derivative (Pc), and either lectin (jacalin) or glycan (lactose). To provide context of this PhD research, a more detailed review of these literary sources is provided below, as the studies in Chapter 5 follow on from the results shown in this section.

Lectin and Pc functionalised AuNPs

Obaid *et al.*[118] were the first to demonstrate use of targeted PDT through 4 nm AuNPs, using the plant lectin: jacalin. The lectin binds to Galβ1-3GalNAc residues (Thomsen-Friedenreich or 'T' antigen), that are expressed by 90% of primary human carcinomas; whereas in normal tissue, T antigens are usually hidden from the immune system, and not exposed on the cell surface[119]. Obaid *et al.* use Pc and a carboxylated PEG derivative to functionalise 4 nm

AuNPs (C11Pc-PEG-AuNPs). The C11Pc-PEG-AuNPs were conjugated with jacalin (jacalin-conjugated AuNPs, Figure 1.24) to form the test particles; or not conjugated to jacalin, to form the control particles (nonconjugated AuNPs). All images were obtained from Obaid *et al.*[118], unless stated otherwise.
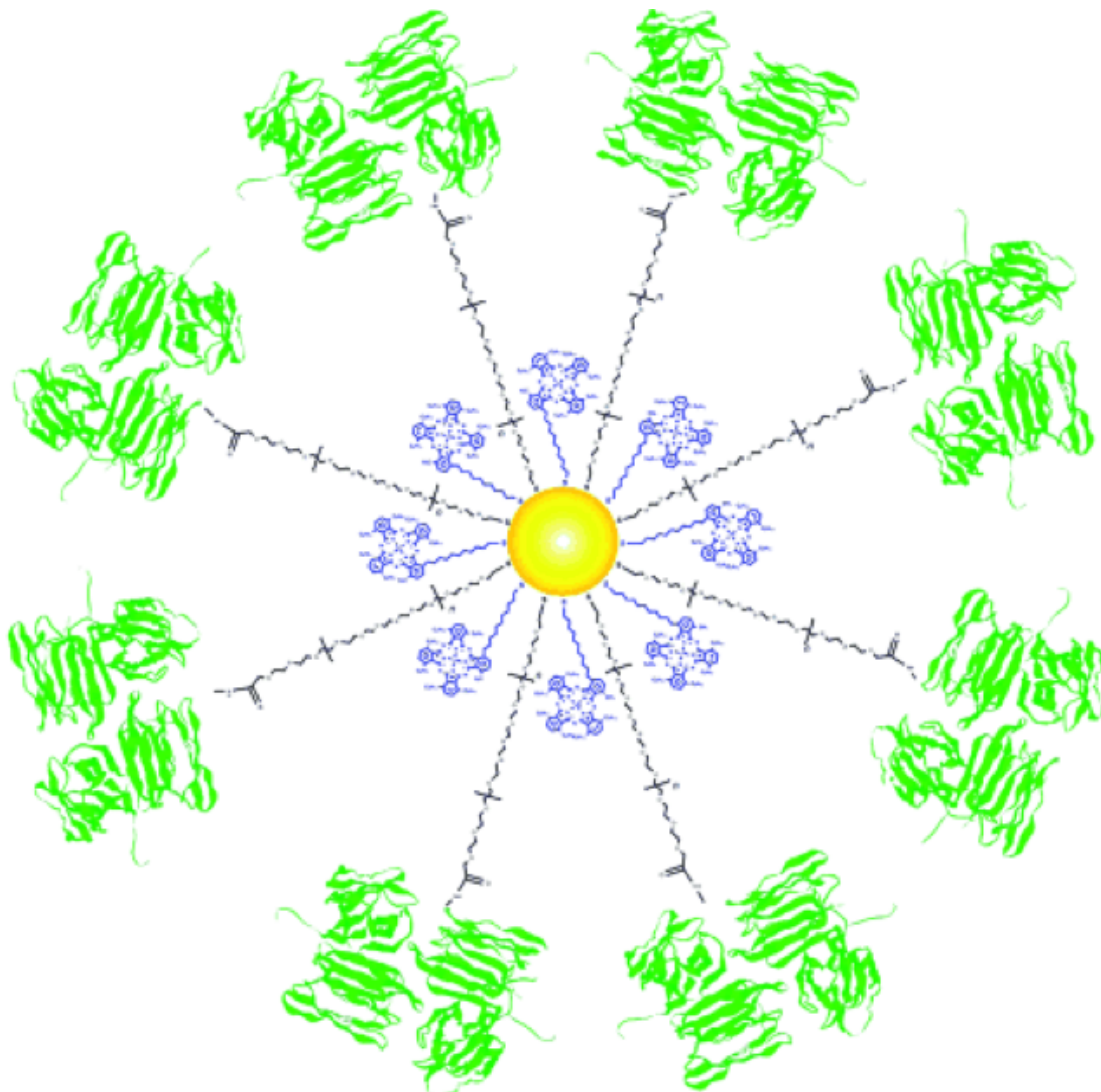
Figure 1.24: Jacalin-conjugated AuNPs, modified with jacalin (green) and phthalocyanine (blue). Republished with permission of John Wiley and Sons, from G. Obaid, I. Chambrier, M. J. Cook, *et al.*, "Targeting the oncofetal thomsen-friedenreich disaccharide using jacalin-PEG phthalocyanine gold nanoparticles for photodynamic cancer therapy," *Angewandte Chemie - International Edition*, vol. 51, no. 25, pp. 6158–6162, Jun. 2012. DOI: `10.1002/anie.201201468`; permission conveyed through Copyright Clearance Center, Inc. Copyright ©2012 WILEY-VCH Verlag GmbH & Co. KGaA, Weinheim.

The jacalin conjugated and nonconjugated AuNPs were then assessed for

their PDT cytotoxicity against a colon adenocarcinoma cell line (HT-29), see Figure 1.25. There was significant cytotoxicity observed upon irradiation when the jacalin was present (1.25b), suggesting T-antigen selective binding by the particles. However, to assess the selectivity, the cells were incubated with two jacalin-binding inhibitors: methyl-α-D-galactose (Me-α-gal); and asialofeutin, which is a protein glycosylated with T antigen. The PDT-induced cytotoxicity of the jacalin conjugated particles against HT-29 cells were tested in the presence of the inhibitors. The results from the inhibition studies are shown in Figure 1.25d.
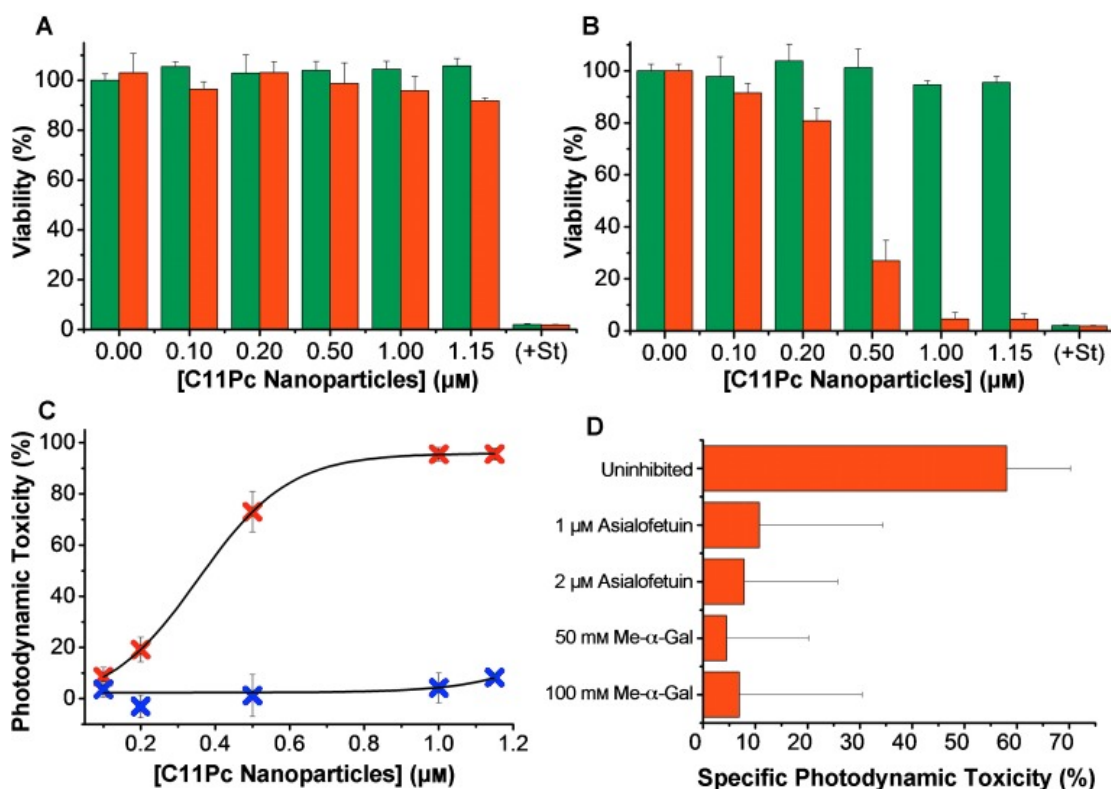
Figure 1.25: Cell viability assays of HT-29 cell line, after no irradiation (green) or irradiation (red), in the presence of: a) nonconjugated NPs and b) jacalin-conjugated NPs. St = staurosporine (positive control). d) Cell viability studies assessing cytotoxicity of Jacalin-conjugated AuNPs against HT-29 cells, in the presence of no inhibitor (uninhibited) or jacalin inhibitors (asialofeutin or Me-α-Gal). Republished with permission of John Wiley and Sons, from G. Obaid, I. Chambrier, M. J. Cook, *et al.*, "Targeting the oncofetal thomsen-friedenreich disaccharide using jacalin-PEG phthalocyanine gold nanoparticles for photodynamic cancer therapy," *Angewandte Chemie - International Edition*, vol. 51, no. 25, pp. 6158–6162, Jun. 2012. DOI: 10.1002/anie.201201468; permission conveyed through Copyright Clearance Center, Inc. Copyright ©2012 WILEY-VCH Verlag GmbH & Co. KGaA, Weinheim.

Figure 1.25d shows that the PDT cytotoxicity was due to a jacalin selec-

tive binding interaction, as inhibitor presence significantly reduces cytotoxicity upon irradiation. By inhibiting jacalin binding to the cells, the PS will not be located to the cell surface and endocytosed.

Consequently, the results demonstrated selective, glycan-lectin targeted PDT of HT-29 colon cancer cells, highlighting the potential of using this system for targeted PDT. However, there are limitations to modifying the drug with lectin instead of glycan. Natural lectins, such as the plant-based jacalin, are large biomolecules. Consequently, these large molecules can be immunogenic and toxic[50]. It is also much more difficult to obtain purified material with lectin compared to glycans, as lectins are usually extracted from biological material. Furthermore, recombinant lectins are often low yielding and high cost to obtain pure material [49]. Consequently, using glycans in drug conjugates for targeting presents advantages over a lectin-drug conjugate approach. Glycans offer improved aqueous solubility, biocompatibility, and established synthesis to generate purified compounds.

More recently, the Russell group focused on glycan modified AuNPs, for targeted PDT. Enhancing aqueous-solubility is of particular importance in PDT, as PSs are often hydrophobic dyes with poor solubility.

Glycan and Pc functionalised AuNPs

Galectin-1, a β-galactose-binding lectin, has been documented as being over-expressed in breast cancer. Garcia Calavia *et al.*[120] generated 4 nm AuNPs functionalised with a Pc derivative (C3Pc) and a lactose derivative (lactose), to target two breast cancer cell lines: MDA-MB-231 and SK-BR-3. Control particles were functionalised with C3Pc and a carboxylated PEG derivative (sPEG) (see Figure 1.26). A non-cancer, breast epithelial cell line was used as a control (MCF-10A). Note that all images shown in the following section are from Garcia Calavia *et al.*[120], unless stated otherwise.
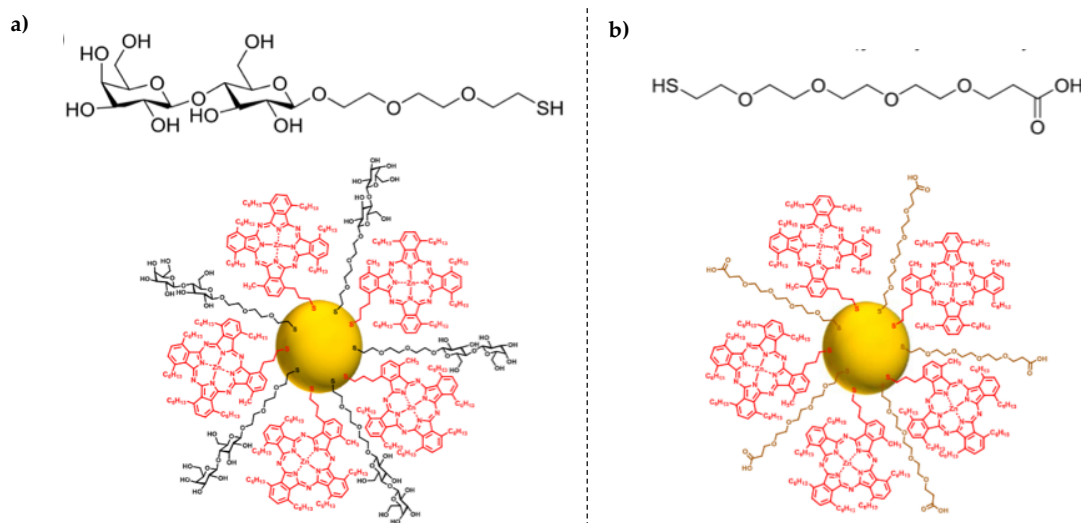
Figure 1.26: Particles used in PDT studies: a) lactose ligand (top) used in lactose-C3Pc-AuNPs (below); and b) sPEG ligand (top) used in sPEG-C3Pc-AuNPs (below). Reprinted from P. García Calavia, I. Chambrier, M. J. Cook, *et al.*, "Targeted photodynamic therapy of breast cancer cells using lactose-phthalocyanine functionalized gold nanoparticles," *Journal of Colloid and Interface Science*, vol. 512, pp. 249–259, Feb. 2018. DOI: 10.1016/J.JCIS.2017.10.030, Copyright (2018), with permission from Elsevier.

First, galectin-1 expression was assessed using an In-Cell ELISA kit. The expression was compared between the cancer cell lines: MDA-MB-231 and SK-BR-3, and expression was normalised to the number of cells, using a stain (Janus Green Whole-Cell Stain). The relative galectin-1 expression of each cell line can be seen in Figure 1.27.
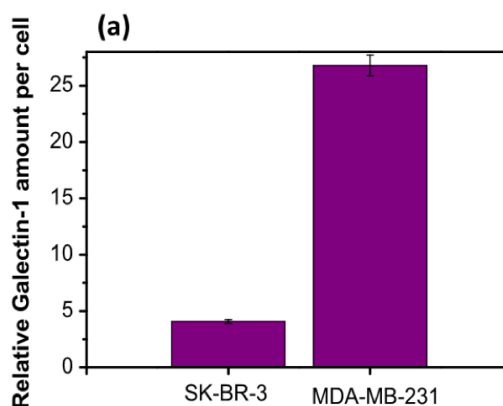
Figure 1.27: Detection of relative levels of galectin-1, compared between SK-BR-3 and MDA-MB-231. Reprinted from P. García Calavia, I. Chambrier, M. J. Cook, *et al.*, "Targeted photodynamic therapy of breast cancer cells using lactose-phthalocyanine functionalized gold nanoparticles," *Journal of Colloid and Interface Science*, vol. 512, pp. 249–259, Feb. 2018. DOI: 10.1016/J.JCIS.2017.10.030, Copyright (2018), with permission from Elsevier.

As can be seen from Figure 1.27, MDA-MB-231 showed the highest levels of galectin-1 expression. Therefore, the highest level of lactose-C3Pc-AuNP uptake, and consequently toxicity in PDT studies, was expected to be observed in the MDA-MB-231 cell line.

For the PDT studies, all the cell lines (MDA-MB-231, SK-BR-3 and MCF-10A) were first incubated with the lactose- or sPEG-C3Pc-AuNPs for 24 hours. Cell viability was assessed using CellTitre Blue® cell viability assay, and the results can be seen in Figure 1.28.
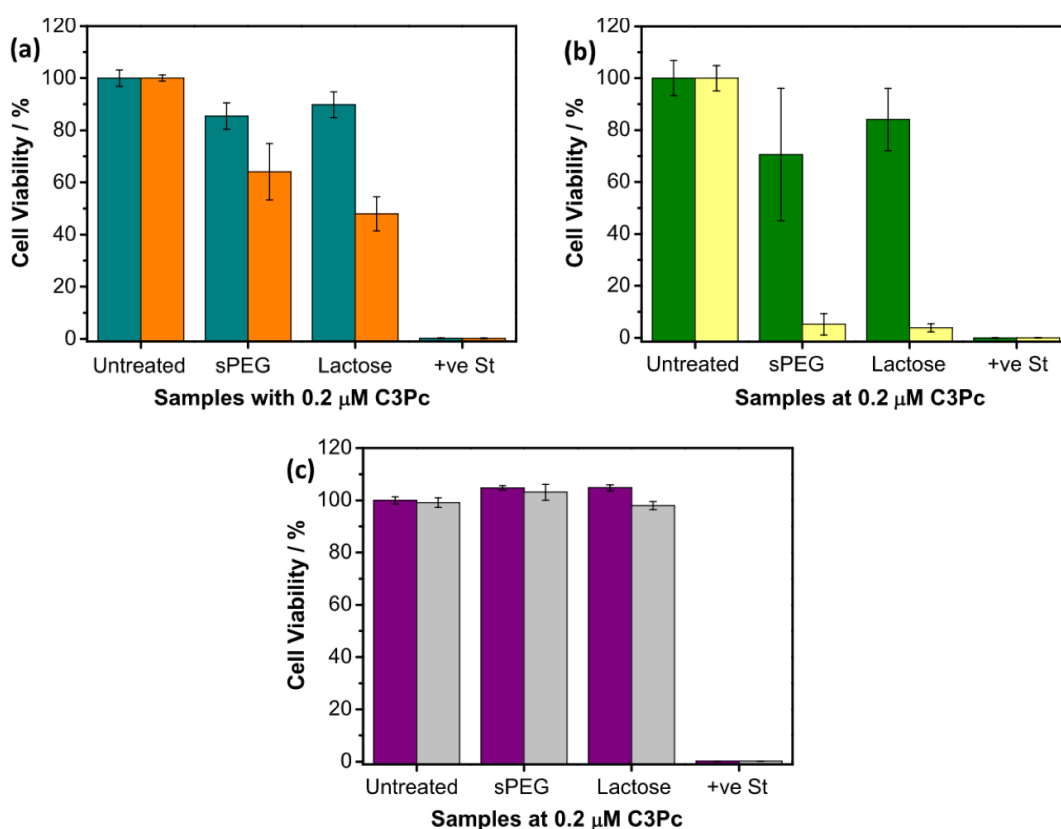
Figure 1.28: Cell viability after PDT treatment with no AuNPs (untreated), sPEG-C3Pc-AuNPs (sPEG) lactose-C3Pc-AuNPs (lactose), or 20 µM of cytotoxic staurosporine (+ve St), where particles were incubated for 24 hours. The particles were incubated with: a) MDA-MB-231; b) SK-BR-3; or c) MCF-10A (non-cancer) cell lines. Reprinted from P. García Calavia, I. Chambrier, M. J. Cook, *et al.*, "Targeted photodynamic therapy of breast cancer cells using lactose-phthalocyanine functionalized gold nanoparticles," *Journal of Colloid and Interface Science*, vol. 512, pp. 249–259, Feb. 2018. DOI: 10.1016/J.JCIS.2017.10.030, Copyright (2018), with permission from Elsevier.

From Figure 1.28, surprisingly the highest levels of cell death were observed with the SK-BR-3 cell line. In both cancer cell lines, both the sPEG- and lactose-

C3Pc-AuNPs showed cytotoxicity upon light irradiation. For the MCF-10A cell line, no cytotoxicity was observed upon AuNP treatment, suggesting the particles were not taken up by the cells. Consequently, the authors only focused on the cancer cell lines for all future studies.

As the SK-BR-3 cell line showed the most promising results after PDT treatment, the authors assessed whether selective uptake could be observed by reducing incubation time and testing different concentrations of C3Pc. Here, only the SK-BR-3 cell line was taken forward and incubation time was reduced to 3 hours (Figure 1.29).
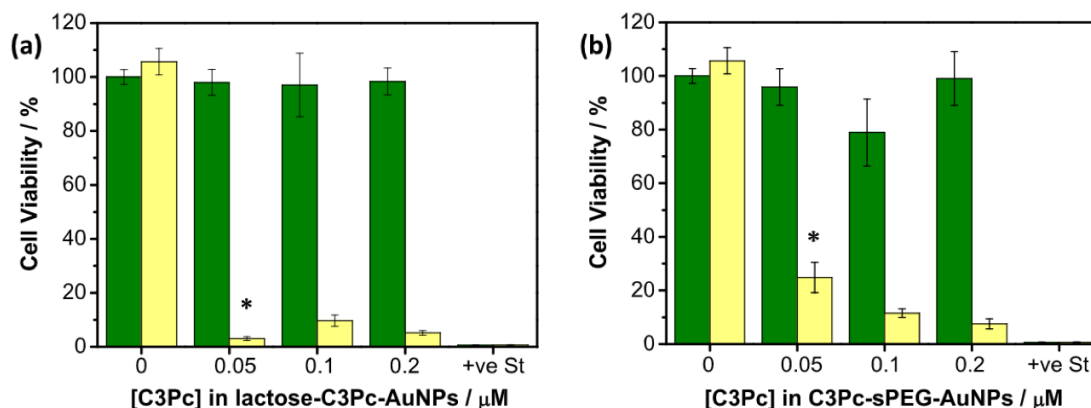
Figure 1.29: Cell viability of SK-BR-3 cell line after PDT treatment with: a) lactose-C3Pc-AuNPs; or b) sPEG-C3Pc-AuNPs. Positive control was 20 μM of cytotoxic staurosporine (+ve St). Particles were incubated for 3 hours. Reprinted from P. García Calavia, I. Chambrier, M. J. Cook, *et al.*, "Targeted photodynamic therapy of breast cancer cells using lactose-phthalocyanine functionalized gold nanoparticles," *Journal of Colloid and Interface Science*, vol. 512, pp. 249–259, Feb. 2018. DOI: 10.1016/J.JCIS.2017.10.030, Copyright (2018), with permission from Elsevier.

From Figure 1.29, a significant reduction in cell viability was observed in the presence of lactose-C3Pc-AuNPs, compared to sPEG-C3Pc-AuNPs, at 0.05 μM of C3Pc. The results suggested selective cell death of SK-BR-3 at 0.05 μM lactose-C3Pc-AuNPs.

The promising results from the 3 hour incubation of the lactose-C3Pc-AuNPs with the SK-BR-3 cell line, led the authors to further investigate the low cell death of the MDA-MB-231 cell line observed in Figure 1.28. The results were not as expected, as the cell line showed increased galectin-1 expression compared to SK-BR-3 (Figure 1.27), yet reduced cytotoxicity after PDT treatment with lactose-

C3Pc-AuNPs. Consequently, the authors designed a competitive inhibition approach. Using the ELISA, the lactose-C3Pc-AuNPs were incubated with MDA-MB-231 cells, before anti-galectin-1 antibody addition. The particles were incubated for either 3 or 24 hours. The aim was to see if the lactose based particles bound to galectin-1, and so the antibody binding would be blocked by the AuNPs, and thus there would be a reduction in galectin-1 detection. The relative galectin-1 expression, and consequently lactose binding, with and without the particles can be seen in Figure 1.30. Note that the following results were from Garcia Calavia 2016[121].
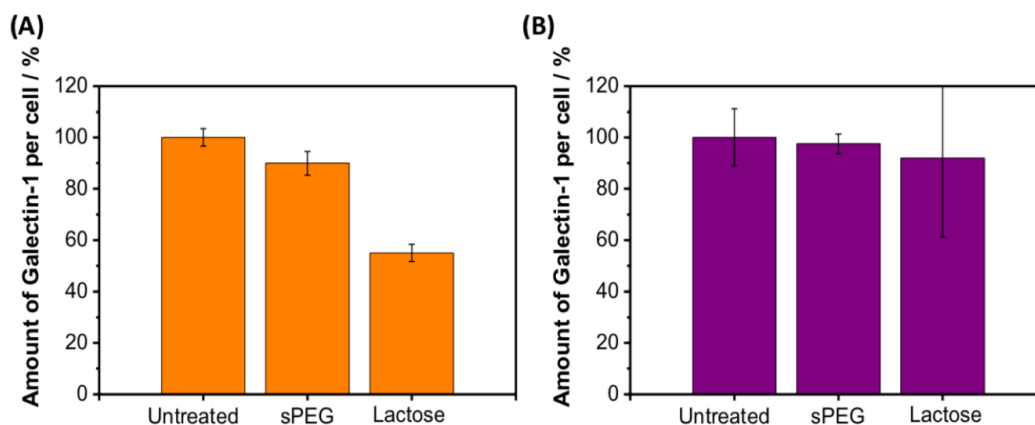
Figure 1.30: Assessing lactose binding by galectin-1 on MDA-MB-231 cell line, by competitive inhibition studies of InCell ELISA kit anti-galectin-1 antibody. AuNPs were incubated for: a) 3 hours; and b) 24 hours. Reprinted from P. Garcia Calavia, "Nanoparticles for the selective delivery of photosensitisers for photodynamic cancer therapy," PhD thesis, 2016, Copyright (2016), with permission from Paula Garcia Calavia.

Figure 1.30 demonstrated anti-galectin-1 antibody binding inhibition after 3 hours incubation of the lactose-C3Pc-AuNPs, as signal was reduced compared to no AuNPs, or in the presence of sPEG-C3Pc-AuNPs. As inhibition was observed after 3 hours in the presence of lactose-C3PC-AuNPs, the particles were taken forward for PDT treatment of MDA-MB-231 (Figure 1.31).
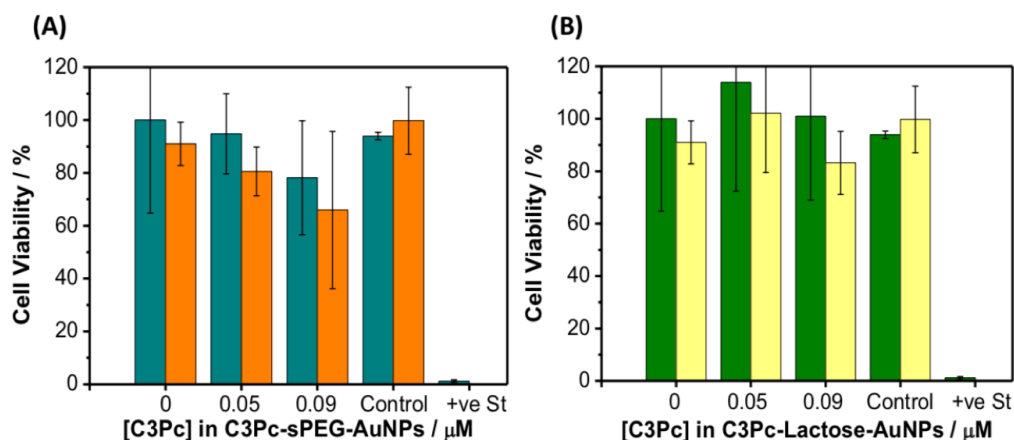
Figure 1.31: Cell viability of MDA-MB-231 cell line after PDT treatment with: a) lactose-C3Pc-AuNPs; or b) sPEG-C3Pc-AuNPs. Positive control was 20 μM of cytotoxic staurosporine (+ve St). Particles were incubated for 3 hours. Reprinted from P. Garcia Calavia, "Nanoparticles for the selective delivery of photosensitisers for photodynamic cancer therapy," PhD thesis, 2016, Copyright (2016), with permission from Paula Garcia Calavia.

There was no selective cell death observed for the MDA-MB-231 cell line as seen in Figure 1.30. However, the error was larger compared to the other PDT experiments.

In conclusion, these studies demonstrated selective cell death of the SK-BR-3 cell line with the lactose-C3Pc-AuNPs, after 3 hours incubation, but no selective cell death was observed for the MDA-MB-231 cell line after 3 hours. The improved cytotoxicity for the SK-BR-3 cell was unexpected as lower galectin-1 expression was detected, compared to the MDA-MB-231. The authors speculated that another lactose-binding protein, GLUT1, could be involved in the AuNP uptake. The results became further complexed with regard to the MDA-MB-231 cell line, as a galectin-1 inhibition assay showed selective binding to galectin-1 after 3 hours incubation of lactose-C3Pc-AuNPs; whereas, no cell death was observed with the same conditions in the PDT studies.

From the findings detailed above, this PhD research aims to provide a more complete picture of the glycan-lectin interactions, in hope of developing targeted eradication against both breast cancer cell lines. Here, different glycans will be assessed to determine an optimal glycan candidate. Furthermore, their uptake

41

by overexpressed breast cancer glycan-binding proteins, will be assessed using inhibition assays. All the previous studies by the Russell group have been performed using 4 nm AuNPs, whereas larger AuNPs have been shown to have better uptake by cancer cells. Therefore, by using larger AuNPs, and assessing glycan-lectin interactions on the cancer cell lines, improved uptake by both cancer cell lines is hoped to be achieved.

1.5   Literature review conclusions

Currently, clinical PDT is limited by poor PS accumulation in the target cell, and poor PS solubility. These lead to PS aggregation that reduces the photoactivity of the PS; and accumulation of PS in the skin, resulting in photosensitisation for weeks or months. Combining targeted elements with the PS may offer a way to improve the applications of clinical PDT, and improve patient outcomes.

One method of targeting is through direct lectin binding, by modifying PSs with glycans. From the literature, glycans have successfully been used to selectively target lectins, on both cancer and bacterial cells. The ubiquitous, selective nature of glycan-lectin interactions along with their overexpression on cancer cells, and their presence on pathogens, make lectin-targeted delivery a viable option for targeted PDT. From the literature, glycan modified PSs have been selectively taken up by both cancer and bacterial cells.

However, multivalent interactions are key for strong and selective glycan-lectin binding. From the literature, it has been demonstrated that nanoparticles can improve drug uptake and efficacy, as nanoparticles can provide solubility and have high drug-loading capacity due to their high area to volume ratio. Lacking a targeting element, PS-nanoparticle conjugates have shown better uptake by cancer cells, compared to the PS alone, which in part is due to the EPR effect. The nanoparticles also provide solubility, which improves the photoactivity of the PS.

More recently, efforts have been focused on nanoparticles modified with both

glycans and PS, to achieve targeted PDT. Using different materials, selective cell death has been observed in *in vitro* and *in vivo*, although studies are more limited. With regards to AuNPs, only one study has used AuNPs for direct lectin targeting PDT (Section 1.4.4)[120] . The findings were promising, showing selective cell death of a breast cancer cell line. However, the authors aimed to target an overexpressed galectin breast cancer cell line, but saw cytotoxicity with the particles against a cell line with lower expression levels of galectin. The study did not assess further for glycan-lectin interactions of the breast cancer cells but suggested other glycan-binding proteins may be involved. The system could be improved by probing the glycan-lectin interactions on the breast cancer cells to gain more insight into a glycan candidate, that provides selective cell eradication of both breast cancer cell lines.

1.6   Scientific aims

The aims of this PhD research were to explore the use of 16 nm AuNPs for direct lectin targeting of PS, towards two different drug targets: 1) the documented drug-resistant bacterial species: *Pseudomonas aeruginosa*; and 2) two aggressive breast cancer cell lines (MDA-MB-231 and SK-BR-3). Different approaches for effective PDT cell death will be explored, dependent on the cellular target. With cell-surface directed PS localisation for bacterial cells; and endocytosed PS for cancer cells.

References

[1] S. B. Zaman, A. Hussain, R. Nye, V. Mehta, K. Taib Mamun, and N. Hossain, "A Review on Antibiotic Resistance: Alarm Bells are Ringing," 2017. DOI: `10.7759/cureus.1403`.

[2] V. Schirrmacher, "From chemotherapy to biological therapy: A review of novel concepts to reduce the side effects of systemic cancer treatment (Review)," *International Journal of Oncology*, vol. 54, no. 2, pp. 407–419, 2019. DOI: `10.3892/ijo.2018.4661`.

[3] M. Barlow, *What antimicrobial resistance has taught us about horizontal gene transfer.* 2009. DOI: `10.1007/978-1-60327-853-9_23`.

[4] N. Mishra and J. Jaiswal, "Targeted Drug Delivery: A Review," Tech. Rep., 2016.

[5] J. M. Tarbell and L. M. Cancel, "The glycocalyx and its significance in human medicine," *Journal of Internal Medicine*, vol. 280, no. 1, pp. 97–113, 2016. DOI: `10.1111/joim.12465`.

[6] A. J. Alla, F. B. D' Andrea, J. K. Bhattarai, J. A. Cooper, Y. H. Tan, A. V. Demchenko, and K. J. Stine, "Selective capture of glycoproteins using lectin-modified nanoporous gold monolith.," *Journal of chromatography A*, vol. 1423, pp. 19–30, 2015. DOI: `10.1016/j.chroma.2015.10.060`.

[7] C. R. Bertozzi and D. Rabuka, "Structural basis of glycan diversity.," in *Essentials of glycobiology*, A. Varki, R. Cummings, J. Esko, H. Freeze, P.

Stanley, C. Bertozzi, G. Hart, and M. Etzler, Eds., 2nd, New York: Cold Spring Harbor Laboratory Press, 2009, ch. 2.

[8] M. E. Taylor, K. Drickamer, R. L. Schnaar, M. E. Etzler, and A. Varki, "Discovery and Classification of Glycan-Binding Proteins," 2017. DOI: 10.1101/glycobiology.3e.028.

[9] A. Naeem, M. Saleemuddin, and R. H. Khan, "Glycoprotein targeting and other applications of lectins in biotechnology.," *Current protein & peptide science*, vol. 8, no. 3, pp. 261–71, 2007.

[10] R. J. Pieters, "Maximising multivalency effects in protein-carbohydrate interactions.," en, *Organic & Biomolecular Chemistry*, vol. 7, no. 10, pp. 2013–25, 2009. DOI: 10.1039/b901828j.

[11] J. J. Lundquist and E. J. Toone, "The Cluster Glycoside Effect," *Chemical Reviews*, vol. 102, no. 2, pp. 555–578, 2002. DOI: 10.1021/cr000418f.

[12] J. Berg, J. Tymoczko, and L. Stryer, "Lectins are specific carbohydrate-binding proteins.," en, in *Biochemistry*, 5th, New York: W H Freeman, 2002, ch. 11.

[13] O. Otman, P. Boullanger, E. Drockenmuller, and T. Hamaide, "New amphiphilic glycopolymers by click functionalization of random copolymers – application to the colloidal stabilisation of polymer nanoparticles and their interaction with concanavalin A lectin.," en, *Beilstein journal of organic chemistry*, vol. 6, no. 1, p. 58, 2010. DOI: 10.3762/bjoc.6.58.

[14] S. Richards, L. Otten, and M. Gibson, "Glycosylated gold nanoparticle libraries for label-free multiplexed lectin biosensing.," *Journal of Materials Chemistry B*, 2015. DOI: 10.1039/C5TB01994J.

[15] W. Van Breedam, S. Pöhlmann, H. W. Favoreel, R. J. de Groot, and H. J. Nauwynck, *Bitter-sweet symphony: Glycan-lectin interactions in virus biology*, 2014. DOI: 10.1111/1574-6976.12052.

[16] Q. R. Johnson, R. J. Lindsay, L. Petridis, and T. Shen, *Investigation of carbohydrate recognition via computer simulation*, 2015. DOI: `10.3390/molecules20057700`.

[17] M. del Carmen Fernandez-Alonso, D. Diaz, M. Alvaro Berbis, F. Marcelo, J. Canada, and J. Jimenez-Barbero, "Protein-Carbohydrate Interactions Studied by NMR: From Molecular Recognition to Drug Design," *Current Protein and Peptide Science*, vol. 13, no. 8, pp. 816–830, 2013. DOI: `10.2174/138920312804871175`.

[18] W. I. Weis and K. Drickamer, "Structural basis of lectin-carbohydrate recognition.," *Annual review of biochemistry*, vol. 65, pp. 441–73, 1996. DOI: `10.1146/annurev.bi.65.070196.002301`.

[19] C. Berne, C. K. Ellison, A. Ducret, and Y. V. Brun, *Bacterial adhesion at the single-cell level*, 2018. DOI: `10.1038/s41579-018-0057-5`.

[20] F. S. Ielasi, M. Alioscha-Perez, D. Donohue, S. Claes, H. Sahli, D. Schols, and R. G. Willaert, "Lectin-glycan interaction network-based identification of host receptors of microbial pathogenic adhesins," *mBio*, vol. 7, no. 4, 2016. DOI: `10.1128/mBio.00584-16`.

[21] J. Pizarro-Cerdá and P. Cossart, *Bacterial adhesion and entry into host cells*, 2006. DOI: `10.1016/j.cell.2006.02.012`.

[22] J. Wu, H. Xu, W. Tang, R. Kopelman, M. Philbert, and C. Xi, "Eradication of bacteria in suspension and biofilms using methylene blue-loaded dynamic nanoplatforms.," *Antimicrobial agents and chemotherapy*, vol. 53, pp. 3042–8, 2009.

[23] N. Høiby, T. Bjarnsholt, M. Givskov, S. Molin, and O. Ciofu, "Antibiotic resistance of bacterial biofilms," *International Journal of Antimicrobial Agents*, vol. 35, no. 4, pp. 322–332, 2010. DOI: `10.1016/J.IJANTIMICAG.2009.12.011`.

[24] U. Römling and C. Balsalobre, "Biofilm infections, their resilience to therapy and innovative treatment strategies," *Journal of Internal Medicine*, vol. 272, no. 6, pp. 541–561, 2012. DOI: `10.1111/joim.12004`.

[25] C. W. Hall and T. F. Mah, "Molecular mechanisms of biofilm-based antibiotic resistance and tolerance in pathogenic bacteria," *FEMS Microbiology Reviews*, 2017. DOI: `10.1093/femsre/fux010`.

[26] J. N. Anderl, M. J. Franklin, and P. S. Stewart, "Role of antibiotic penetration limitation in Klebsiella pneumoniae biofilm resistance to ampicillin and ciprofloxacin," *Antimicrobial Agents and Chemotherapy*, 2000. DOI: `10.1128/AAC.44.7.1818-1824.2000`.

[27] H. Wu, C. Moser, H. Wang, N. Høiby, and Z. Song, "Strategies for combating bacterial biofilm infections." *International journal of oral science*, vol. 7, pp. 1–7, 2015. DOI: `10.1038/ijos.2014.65`.

[28] V. Aloush, S. Navon-Venezia, Y. Seigman-Igra, S. Cabili, and Y. Carmeli, "Multidrug-resistant Pseudomonas aeruginosa: risk factors and clinical impact." *Antimicrobial agents and chemotherapy*, vol. 50, no. 1, pp. 43–8, 2006. DOI: `10.1128/AAC.50.1.43-48.2006`.

[29] N. Mesaros, P. Nordmann, P. Plésiat, M. Roussel-Delvallez, J. Van Eldere, Y. Glupczynski, Y. Van Laethem, F. Jacobs, P. Lebecque, A. Malfroot, P. Tulkens, and F. Van Bambeke, "Pseudomonas aeruginosa: resistance and therapeutic options at the turn of the new millennium," *Clinical Microbiology and Infection*, vol. 13, no. 6, pp. 560–578, 2007. DOI: `10.1111/J.1469-0691.2007.01681.X`.

[30] R. Sommer, S. Wagner, A. Varrot, C. M. Nycholat, A. Khaledi, S. Aussler, J. C. Paulson, A. Imberty, and A. Titz, "The virulence factor LecB varies in clinical isolates: consequences for ligand binding and drug discovery," DOI: `10.1039/c6sc00696e`.

[31]   H. W. Kavunja, P. G. Voss, J. L. Wang, and X. Huang, *Identification of lectins from metastatic cancer cells through magnetic glyconanoparticles*, 2015. DOI: 10.1002/ijch.201400156.

[32]   F. T. Liu and G. A. Rabinovich, *Galectins as modulators of tumour progression*, 2005. DOI: 10.1038/nrc1527.

[33]   T. Krause and G. A. Turner, *Are selectins involved in metastasis?* 1999. DOI: 10.1023/A:1006626500852.

[34]   A. J. Cagnoni, J. M. Pérez Sáez, G. A. Rabinovich, and K. V. Mariño, "Turning-off signaling by siglecs, selectins, and galectins: Chemical inhibition of glycan-dependent interactions in cancer," *Frontiers in Oncology*, vol. 6, no. MAY, 2016. DOI: 10.3389/fonc.2016.00109.

[35]   L. Astorgues-Xerri, M. E. Riveiro, A. Tijeras-Raballand, M. Serova, C. Neuzillet, S. Albert, E. Raymond, and S. Faivre, *Unraveling galectin-1 as a novel therapeutic target for cancer*, 2014. DOI: 10.1016/j.ctrv.2013.07.007.

[36]   K. Wdowiak, T. Francuz, E. Gallego-Colon, N. Ruiz-Agamez, M. Kubeczko, I. Grochoła, and J. Wojnar, "Galectin Targeted Therapy in Oncology: Current Knowledge and Perspectives." *International journal of molecular sciences*, vol. 19, no. 1, 2018. DOI: 10.3390/ijms19010210.

[37]   J. M. Cousin and M. J. Cloninger, *The role of galectin-1 in cancer progression, and synthetic multivalent systems for the study of Galectin-1*, 2016. DOI: 10.3390/ijms17091566.

[38]   B. S. Bochner and N. Zimmermann, *Role of siglecs and related glycan-binding proteins in immune responses and immunoregulation*, 2015. DOI: 10.1016/j.jaci.2014.11.031.

[39]   J. Daly, M. Carlsten, and M. O'Dwyer, *Sugar free: Novel immunotherapeutic approaches targeting siglecs and sialic acids to enhance natural killer cell cytotoxicity against cancer*, 2019.

[40]   Y. Yu, B. R. Blokhuis, M. A. Diks, A. Keshavarzian, J. Garssen, and F. A. Re-
degeld, "Functional inhibitory siglec-6 is upregulated in human colorec-
tal cancer-associated mast cells," *Frontiers in Immunology*, vol. 9, no. SEP,
2018. DOI: 10.3389/fimmu.2018.02138.

[41]   X. Tu, T. LaVallee, and R. Lechleider, "CD22 as a target for cancer ther-
apy.," *Journal of experimental therapeutics & oncology*, vol. 9, no. 3, pp. 241–
8, 2011.

[42]   D. Ding, Y. Yao, S. Zhang, C. Su, and Y. Zhang, *C-type lectins facilitate
tumor metastasis (Review)*, 2017. DOI: 10.3892/ol.2016.5431.

[43]   L. Borsig, *Selectins in cancer immunity*, 2018. DOI: 10.1093/glycob/
cwx105.

[44]   H. Laubli and L. Borsig, "Selectins as Mediators of Lung Metastasis,"
Cancer Microenvironment, vol. 3, no. 1, pp. 97–105, 2010. DOI: 10.1007/
s12307-010-0043-6.

[45]   D.-R. Liu, Q.-L. Guan, M.-T. Gao, L. Jiang, and H.-X. Kang, "Mannose
receptor as a potential biomarker for gastric cancer: a pilot study.," *The
International journal of biological markers*, vol. 32, no. 3, e278–e283, 2017.
DOI: 10.5301/jbm.5000244.

[46]   J. Fang, T. Tao, Y. Zhang, and H. Lu, "A barcode mode based on gly-
cosylation sites of membrane type mannose receptor as a new potential
diagnostic marker for breast cancer.," *Talanta*, vol. 191, pp. 21–26, 2019.
DOI: 10.1016/j.talanta.2018.08.022.

[47]   I. van Die and R. D. Cummings, *The mannose receptor in regulation of
helminth-mediated host immunity*, 2017.

[48]   A. Aykac, M. C. Martos-Maldonado, J. M. Casas-Solvas, I. Quesada-
Soriano, F. García-Maroto, L. García-Fuentes, and A. Vargas-Berenguel,
"Beta-cyclodextrin-bearing gold glyconanoparticles for the development

of site specific drug delivery systems," *Langmuir*, vol. 30, no. 1, pp. 234–242, 2014. DOI: `10.1021/la403454p`.

[49] S. K. Lam and T. B. Ng, *Lectins: Production and practical applications*, 2011. DOI: `10.1007/s00253-010-2892-9`.

[50] C. M. Lehr and F. Gabor, "Lectins and glycoconjugates in drug delivery and targeting," *Advanced Drug Delivery Reviews*, vol. 56, no. 4, pp. 419–420, 2004. DOI: `10.1016/j.addr.2003.10.013`.

[51] B. Timko, K. Whitehead, W. Gao, D. Kohane, O. Farokhzad, D. Anderson, and R. Langer, "Advances in drug delivery.," *Annual review of materials research*, vol. 41, no. 1, pp. 1–20, 2011. DOI: `10.1146/annurev-matsci-062910-100359`.

[52] K. Jain, "Drug delivery systems – an overview.," in *Drug delivery systems*, vol. 437, Humana Press, 2008, ch. 1, pp. 1–50.

[53] R. Kojima, D. Aubel, and M. Fussenegger, "Novel theranostic agents for next-generation personalized medicine: small molecules, nanoparticles, and engineered mammalian cells.," *Current opinion in chemical biology*, vol. 28, pp. 29–38, 2015. DOI: `10.1016/j.cbpa.2015.05.021`.

[54] G. Chen, I. Roy, C. Yang, and P. N. Prasad, *Nanochemistry and Nanomedicine for Nanoparticle-based Diagnostics and Therapy*, 2016. DOI: `10.1021/acs.chemrev.5b00148`.

[55] G. N. Sharma, R. Dave, J. Sanadya, P. Sharma, and K. K. Sharma, "Various types and management of breast cancer: an overview.," *Journal of advanced pharmaceutical technology & research*, vol. 1, no. 2, pp. 109–26, 2010.

[56] V. Amendola, R. Pilot, M. Frasconi, O. M. Maragò, and M. A. Iatì, *Surface plasmon resonance in gold nanoparticles: A review*, 2017. DOI: `10.1088/1361-648X/aa60f3`.

[57] D. Hone, A. Haines, and D. Russell, "Rapid, quantitative colorimetric detection of a lectin using mannose-stabilized gold nanoparticles.," *Langmuir*, vol. 19, pp. 7141–7144, 2003. DOI: `10.1021/la034358v`.

[58] C. L. Schofield, B. Mukhopadhyay, S. M. Hardy, M. B. McDonnell, R. A. Field, and D. A. Russell, "Colorimetric detection of Ricinus communis Agglutinin 120 using optimally presented carbohydrate-stabilised gold nanoparticles," *The Analyst*, vol. 133, no. 5, p. 626, 2008. DOI: `10.1039/b715250g`.

[59] S.-J. Richards, E. Fullam, G. S. Besra, and M. I. Gibson, "Discrimination between bacterial phenotypes using glyco-nanoparticles and the impact of polymer coating on detection readouts," *J. Mater. Chem. B*, vol. 2, no. 11, pp. 1490–1498, 2014. DOI: `10.1039/C3TB21821J`.

[60] M. J. Marín, A. Rashid, M. Rejzek, S. Fairhurst, S. Wharton, S. Martin, J. McCauley, T. Wileman, R. Field, and D. Russell, "Glyconanoparticles for the plasmonic detection and discrimination between human and avian influenza virus.," *Organic & Biomolecular Chemistry*, vol. 11, pp. 7101–7107, 2013. DOI: `10.1039/c3ob41703d`.

[61] D. Kumar, I. Mutreja, K. Chitcholtan, and P. Sykes, "Cytotoxicity and cellular uptake of different sized gold nanoparticles in ovarian cancer cells," *Nanotechnology*, vol. 28, no. 47, 2017. DOI: `10.1088/1361-6528/aa935e`.

[62] Y. Du, L. Xia, A. Jo, R. M. Davis, P. Bissel, M. F. Ehrich, and D. G. I. Kingston, "Synthesis and Evaluation of Doxorubicin-Loaded Gold Nanoparticles for Tumor-Targeted Drug Delivery.," *Bioconjugate chemistry*, vol. 29, no. 2, pp. 420–430, 2018. DOI: `10.1021/acs.bioconjchem.7b00756`.

[63] J. N. BeMiller, "Gellans, Curdlan, Dextrans, Levans, and Pullulan," in *Carbohydrate Chemistry for Food Scientists*, Elsevier, 2019, pp. 271–278. DOI: `10.1016/b978-0-12-812069-9.00012-1`.

[64] H. Jang, S. R. Ryoo, K. Kostarelos, S. W. Han, and D. H. Min, "The effective nuclear delivery of doxorubicin from dextran-coated gold nanoparticles larger than nuclear pores," *Biomaterials*, vol. 34, no. 13, pp. 3503–3510, 2013. DOI: `10.1016/j.biomaterials.2013.01.076`.

[65] S. Islam, M. A. Bhuiyan, and M. N. Islam, *Chitin and Chitosan: Structure, Properties and Applications in Biomedical Engineering*, 2017. DOI: `10.1007/s10924-016-0865-5`.

[66] H. Mu, Q. Liu, H. Niu, Y. Sun, and J. Duan, "Gold nanoparticles make chitosan-streptomycin conjugates effective towards Gram-negative bacterial biofilm," *RSC Advances*, vol. 6, no. 11, pp. 8714–8721, 2016. DOI: `10.1039/c5ra22803d`.

[67] Y. Yuan, F. Liu, L. Xue, H. Wang, J. Pan, Y. Cui, H. Chen, and L. Yuan, "Recyclable Escherichia coli-Specific-Killing AuNP-Polymer (ESKAP) Nanocomposites," *ACS Applied Materials and Interfaces*, vol. 8, no. 18, pp. 11 309–11 317, 2016. DOI: `10.1021/acsami.6b02074`.

[68] J. Conde, F. Tian, Y. Hernandez, C. Bao, P. V. Baptista, D. Cui, T. Stoeger, and J. M. De La Fuente, "RNAi-based glyconanoparticles trigger apoptotic pathways for in vitro and in vivo enhanced cancer-cell killing," *Nanoscale*, vol. 7, no. 19, pp. 9083–9091, 2015. DOI: `10.1039/c4nr05742b`.

[69] F. Chiodo, M. Marradi, J. Calvo, E. Yuste, and S. Penadés, "Glycosystems in nanotechnology: Gold glyconanoparticles as carrier for anti-HIV prodrugs," *Beilstein Journal of Organic Chemistry*, vol. 10, pp. 1339–1346, 2014. DOI: `10.3762/bjoc.10.136`.

[70] D. Chatterjee, L. Fong, and Y. Zhang, "Nanoparticles in photodynamic therapy: An emerging paradigm.," *Advanced drug delivery reviews*, vol. 60, no. 15, pp. 1627–1637, 2008.

[71] S. Hatz, J. Lambert, and P. Ogilby, "Measuring the lifetime of singlet oxygen in a single cell: addressing the issue of cell viability.," en, *Photo-*

chemical & photobiological sciences, vol. 6, no. 10, pp. 1106–16, 2007. DOI: `10.1039/b707313e`.

[72] S. Hatz, L. Poulsen, and P. R. Ogilby, "Time-resolved singlet oxygen phosphorescence measurements from photosensitized experiments in single cells: effects of oxygen diffusion and oxygen concentration.," *Photochemistry and photobiology*, vol. 84, no. 5, pp. 1284–90, DOI: `10.1111/j.1751-1097.2008.00359.x`.

[73] R. Craig, C. McCoy, S. Gorman, and D. Jones, "Photosensitisers - the progression from photodynamic therapy to anti-infective surfaces.," *Expert opinion on drug delivery*, vol. 12, pp. 85–101, 2015.

[74] T. Dai, B. B. Fuchs, J. J. Coleman, R. A. Prates, C. Astrakas, T. G. St. Denis, M. S. Ribeiro, E. Mylonakis, M. R. Hamblin, and G. P. Tegos, "Concepts and Principles of Photodynamic Therapy as an Alternative Antifungal Discovery Platform," *Frontiers in Microbiology*, vol. 3, p. 120, 2012. DOI: `10.3389/fmicb.2012.00120`.

[75] Y. Konan, R. Gurny, and E. Allémann, "State of the art in the delivery of photosensitizers for photodynamic therapy.," *Journal of photochemistry and photobiology B: biology*, vol. 66, no. 2, pp. 89–106, 2002.

[76] M. Kuroki, K. Hachimine, H. Abe, H. Shibaguchi, M. Kuroki, S.-I. Maekawa, J. Yanagisawa, T. Kinugasa, T. Tanaka, and Y. Yamashita, "Sonodynamic therapy of cancer using novel sonosensitizers.," *Anticancer research*, vol. 27, no. 6A, pp. 3673–7, 2007.

[77] A. E. O'Connor, W. M. Gallagher, and A. T. Byrne, "Porphyrin and nonporphyrin photosensitizers in oncology: Preclinical and clinical advances in photodynamic therapy," *Photochemistry and Photobiology*, vol. 85, no. 5, pp. 1053–1074, 2009. DOI: `10.1111/j.1751-1097.2009.00585.x`.

[78] H. Pye, I. Stamati, G. Yahioglu, M. Butt, and M. Deonarain, "Antibody-Directed Phototherapy (ADP)," *Antibodies*, vol. 2, no. 4, pp. 270–305, 2013. DOI: 10.3390/antib2020270.

[79] A. J. Bullous, C. M. Alonso, and R. W. Boyle, *Photosensitiser-antibody conjugates for photodynamic therapy*, 2011. DOI: 10.1039/c0pp00266f.

[80] M. Embleton, S. Nair, B. Cookson, and M. Wilson, "Antibody-directed photodynamic therapy of methicillin resistant Staphylococcus aureus.," *Microbial drug resistance*, vol. 10, pp. 92–97, 2004. DOI: 10.1089/1076629041310000.

[81] H.-H. Han, C.-Z. Wang, Y. Zang, J. Li, T. D. James, and X.-P. He, "Supramolecular core-glycoshell polythiophene nanodots for targeted imaging and photodynamic therapy †," *Chem. Commun*, vol. 53, p. 9793, 2017. DOI: 10.1039/c7cc04525e.

[82] H. Sun, X. Zhu, P. Y. Lu, R. R. Rosato, W. Tan, and Y. Zu, *Oligonucleotide aptamers: New tools for targeted cancer therapy*, 2014. DOI: 10.1038/mtna.2014.32.

[83] G. Tegos, T. Demidova, D. Arcila-Lopez, H. Lee, T. Wharton, H. Gali, and M. Hamblin, "Cationic fullerenes are effective and selective antimicrobial photosensitizers.," *Chemistry & Biology*, vol. 12, pp. 1127–1135, 2005. DOI: 10.1016/j.chembiol.2005.08.014.

[84] M. Embleton, S. Nair, W. Heywood, D. Menon, B. Cookson, and M. Wilson, "Development of a novel targeting system for lethal photosensitization of antibiotic-resistant strains of Staphylococcus aureus.," *Antimicrobial agents and chemotherapy*, vol. 49, no. 9, pp. 3690–6, 2005. DOI: 10.1128/AAC.49.9.3690–3696.2005.

[85] A. Stallivieri, F. Baros, G. Jetpisbayeva, B. Myrzakhmetov, and C. Frochot, "The Interest of Folic Acid in Targeted Photodynamic Therapy," *Current Medicinal Chemistry*, vol. 22, no. 27, pp. 3185–3207, 2015. DOI: 10.2174/0929867322666150729113912.

[86]   C. A. Kruger and H. Abrahamse, *Utilisation of targeted nanoparticle photo-sensitiser drug delivery systems for the enhancement of photodynamic therapy*, 2018. DOI: `10.3390/molecules23102628`.

[87]   R. Fekrazad, A. Nejat, and K. A. Kalhori, "Antimicrobial Photodynamic Therapy With Nanoparticles Versus Conventional Photosensitizer in Oral Diseases," in *Nanostructures for Antimicrobial Therapy*, Elsevier, 2017, pp. 237–259, ISBN: 9780323461528. DOI: `10.1016/B978-0-323-46152-8.00010-X`.

[88]   G. B. Kharkwal, S. K. Sharma, Y.-Y. Huang, T. Dai, and M. R. Hamblin, "Photodynamic therapy for infections: clinical applications.," *Lasers in surgery and medicine*, vol. 43, no. 7, pp. 755–67, 2011. DOI: `10.1002/lsm.21080`.

[89]   B. M. Amos-Tautua, S. P. Songca, and O. S. Oluwafemi, *Application of porphyrins in antibacterial photodynamic therapy*, 2019. DOI: `10.3390/molecules24132456`.

[90]   M. Hamblin and T. Hasan, "Photodynamic therapy: a new antimicrobial approach to infectious disease?" *Photochemical & photobiological sciences*, vol. 3, pp. 436–450, 2004. DOI: `10.1039/b311900a`.

[91]   M. Wainwright, D. Phoenix, S. Laycock, D. Wareing, and P. Wright, "Photobactericidal activity of phenothiazinium dyes against methicillin-resistant strains of Staphylococcus aureus.," *FEMS microbiology letters*, vol. 160, no. 2, pp. 177–181, 1998. DOI: `10.1111/j.1574-6968.1998.tb12908.x`.

[92]   N. Kömerik, M. Wilson, and S. Poole, "The effect of photodynamic action on two virulence factors of gram-negative bacteria.," *Photochemistry and photobiology*, vol. 72, no. 5, pp. 676–680, 2007. DOI: `10.1562/0031-8655(2000)0720676TEOPAO2.0.CO2`.

[93] A. Tavares, C. Carvalho, M. Faustino, M. Neves, J. Tomé, A. Tomé, J. Cavaleiro, A. Cunha, N. Gomes, E. Alves, and A. Almeida, "Antimicrobial photodynamic therapy: study of bacterial recovery viability and potential development of resistance after treatment.," *Marine drugs*, vol. 8, pp. 91–105, 2010. DOI: `10.3390/md8010091`.

[94] F. Cieplik, D. Deng, W. Crielaard, W. Buchalla, E. Hellwig, A. Al-Ahmad, and T. Maisch, "Critical Reviews in Microbiology Antimicrobial photodynamic therapy-what we know and what we don't," 2018. DOI: `10.1080/1040841X.2018.1467876`.

[95] M. Kuimova, G. Yahioglu, and P. Ogilby, "Singlet oxygen in a cell: spatially dependent lifetimes and quenching rate constants.," *Journal of the American Chemical Society*, vol. 131, pp. 332–340, 2009. DOI: `10.1021/ja807484b`.

[96] S. K. Golombek, J.-N. May, B. Theek, L. Appold, N. Drude, F. Kiessling, and T. Lammers, "Tumor targeting via EPR: Strategies to enhance patient responses.," *Advanced drug delivery reviews*, vol. 130, pp. 17–38, 2018. DOI: `10.1016/j.addr.2018.07.007`.

[97] V. Torchilin, *Tumor delivery of macromolecular drugs based on the EPR effect*, 2011. DOI: `10.1016/j.addr.2010.03.011`.

[98] D. Van Straten, V. Mashayekhi, H. S. De Bruijn, S. Oliveira, D. J. Robinson, and M. Hamblin, "cancers Oncologic Photodynamic Therapy: Basic Principles, Current Clinical Status and Future Directions," 2017. DOI: `10.3390/cancers9020019`.

[99] C. Feng, D. Zhu, L. Chen, Y. Lu, J. Liu, N. Y. Kim, S. Liang, X. Zhang, Y. Lin, Y. Ma, and C. Dong, "Targeted Delivery of Chlorin e6 via Redox Sensitive Diselenide-Containing Micelles for Improved Photodynamic Therapy in Cluster of Differentiation 44-Overexpressing Breast Cancer," *Frontiers in Pharmacology*, vol. 10, p. 369, 2019. DOI: `10.3389/fphar.2019.00369`.

[100] G. Zheng, A. Graham, M. Shibata, J. R. Missert, A. R. Oseroff, T. J. Dougherty, and R. K. Pandey, "Synthesis of β-galactose-conjugated chlorins derived by enyne metathesis as galectin-specific photosensitizers for photodynamic therapy," *Journal of Organic Chemistry*, vol. 66, no. 26, pp. 8709–8716, 2001. DOI: `10.1021/jo0105080`.

[101] A. R. Soares, M. G. Neves, A. C. Tome, M. C. Iglesias-de La Cruz, A. Zamarrón, E. Carrasco, S. González, J. A. Cavaleiro, T. Torres, D. M. Guldi, and A. Juarranz, "Glycophthalocyanines as photosensitizers for triggering mitotic catastrophe and apoptosis in cancer cells," *Chemical Research in Toxicology*, vol. 25, no. 4, pp. 940–951, 2012. DOI: `10.1021/tx300035a`.

[102] S. Vedachalam, B. H. Choi, K. K. Pasunooti, K. M. Ching, K. Lee, H. S. Yoon, and X. W. Liu, "Glycosylated porphyrin derivatives and their photodynamic activity in cancer cells," *MedChemComm*, vol. 2, no. 5, pp. 371–377, 2011. DOI: `10.1039/c0md00175a`.

[103] J. P. Tomé, M. G. Neves, A. C. Tomé, J. A. Cavaleiro, A. F. Mendonça, I. N. Pegado, R. Duarte, and M. L. Valdeira, "Synthesis of glycoporphyrin derivatives and their antiviral activity against herpes simplex virus types 1 and 2," *Bioorganic and Medicinal Chemistry*, vol. 13, no. 12, pp. 3878–3888, 2005. DOI: `10.1016/j.bmc.2005.04.015`.

[104] M. Tanaka, H. Kataoka, M. Mabuchi, S. Sakuma, S. Takahashi, R. Tujii, H. Akashi, H. Ohi, S. Yano, A. Morita, and T. Joh, "Anticancer effects of novel photodynamic therapy with glycoconjugated chlorin for gastric and colon cancer.," *Anticancer research*, vol. 31, no. 3, pp. 763–9, 2011.

[105] C. F. Choi, J. D. Huang, P. C. Lo, W. P. Fong, and D. K. Ng, "Glycosylated zinc(II) phthalocyanines as efficient photosensitisers for photodynamic therapy. Synthesis, photophysical properties and in vitro photodynamic activity," *Organic and Biomolecular Chemistry*, vol. 6, no. 12, pp. 2173–2183, 2008. DOI: `10.1039/b802212g`.

[106] M. Lupu, P. Maillard, J. Mispelter, F. Poyer, and C. D. Thomas, *A glyco-porphyrin story: From chemistry to PDT treatment of cancer mouse models*, 2018. DOI: `10.1039/c8pp00123e`.

[107] C. Moylan, E. M. Scanlan, and M. O. Senge, "Chemical Synthesis and Medicinal Applications of Glycoporphyrins.," *Current medicinal chemistry*, vol. 22, no. 19, pp. 2238–348, 2015. DOI: `10.2174/0929867322666150429113104`.

[108] S. Singh, A. Aggarwal, N. V. K. Bhupathiraju, G. Arianna, K. Tiwari, and C. M. Drain, *Glycosylated Porphyrins, Phthalocyanines, and Other Porphyrinoids for Diagnostics and Therapeutics*, 2015. DOI: `10.1021/acs.chemrev.5b00244`.

[109] Z. Lu, X. Zhang, Y. Zhao, Y. Xue, T. Zhai, Z. Wu, and C. Li, "BODIPY-based macromolecular photosensitizer with cation-enhanced antibacterial activity," *Polymer Chemistry*, vol. 6, no. 2, pp. 302–310, 2015. DOI: `10.1039/C4PY00715H`.

[110] S. Silva, P. M. Pereira, P. Silva, F. A. Almeida Paz, M. A. Faustino, J. A. Cavaleiro, and J. P. Tomé, "Porphyrin and phthalocyanine glycodendritic conjugates: Synthesis, photophysical and photochemical properties," *Chemical Communications*, vol. 48, no. 30, pp. 3608–3610, 2012. DOI: `10.1039/c2cc17561d`.

[111] P. M. Pereira, S. Silva, J. A. Cavaleiro, C. A. Ribeiro, J. P. Tomé, and R. Fernandes, "Galactodendritic phthalocyanine targets carbohydrate-binding proteins enhancing photodynamic therapy," *PLoS ONE*, vol. 9, no. 4, 2014. DOI: `10.1371/journal.pone.0095529`.

[112] R. Das and B. Mukhopadhyay, "Use of 'click chemistry' for the synthesis of carbohydrate-porphyrin dendrimers and their multivalent approach toward lectin sensing," *Tetrahedron Letters*, vol. 57, no. 16, pp. 1775–1781, 2016. DOI: `10.1016/j.tetlet.2016.03.031`.

[113]   J. K. Rhee, M. Baksh, C. Nycholat, J. C. Paulson, H. Kitagishi, and M. G. Finn, "Glycan-targeted virus-like nanoparticles for photodynamic therapy," *Biomacromolecules*, vol. 13, no. 8, pp. 2333–2338, 2012. DOI: `10.1021/bm300578p`.

[114]   D. Brevet, M. Gary-Bobo, L. Raehm, S. Richeter, O. Hocine, K. Amro, B. Loock, P. Couleaud, C. Frochot, A. Morère, P. Maillard, M. Garcia, and J. O. Durand, "Mannose-targeted mesoporous silica nanoparticles for photodynamic therapy," *Chemical Communications*, no. 12, pp. 1475–1477, 2009. DOI: `10.1039/b900427k`.

[115]   C. Shao, K. Shang, H. Xu, Y. Zhang, Z. Pei, and Y. Pei, "Facile fabrication of hypericin-entrapped glyconanoparticles for targeted photodynamic therapy.," *International journal of nanomedicine*, vol. 13, pp. 4319–4331, 2018. DOI: `10.2147/IJN.S161262`.

[116]   R. Khan, M. Ozkan, A. Khaligh, and D. Tuncel, "Water-dispersible glycosylated poly (2,5'-thienylene)porphyrin-based nanoparticles for antibacterial photodynamic therapy," *Photochemical and Photobiological Sciences*, vol. 18, no. 5, pp. 1147–1155, 2019.

[117]   X. L. Hu, Q. Cai, J. Gao, R. A. Field, G. R. Chen, N. Jia, Y. Zang, J. Li, and X. P. He, "Self-Assembled 2D Glycoclusters for the Targeted Delivery of Theranostic Agents to Triple-Negative Breast Cancer Cells," *ACS Applied Materials and Interfaces*, 2019. DOI: `10.1021/acsami.9b06016`.

[118]   G. Obaid, I. Chambrier, M. J. Cook, and D. A. Russell, "Targeting the oncofetal thomsen-friedenreich disaccharide using jacalin-PEG phthalocyanine gold nanoparticles for photodynamic cancer therapy," *Angewandte Chemie - International Edition*, vol. 51, no. 25, pp. 6158–6162, 2012. DOI: `10.1002/anie.201201468`.

[119]   G. F. Springer, *T and Tn, general carcinoma autoantigens*, 1984. DOI: `10.1126/science.6729450`.

[120] P. García Calavia, I. Chambrier, M. J. Cook, A. H. Haines, R. A. Field, and D. A. Russell, "Targeted photodynamic therapy of breast cancer cells using lactose-phthalocyanine functionalized gold nanoparticles," *Journal of Colloid and Interface Science*, vol. 512, pp. 249–259, 2018. DOI: `10.1016/J.JCIS.2017.10.030`.

[121] P. Garcia Calavia, "Nanoparticles for the selective delivery of photosensitisers for photodynamic cancer therapy," PhD thesis, 2016.

Chapter 2

Materials and Methods

The following Chapter outlines the materials and methods used in the experiments carried out in this research.

2.1 Materials and instruments

2.1.1 Reagents

All reagents were of analytical grade and purchased from Sigma Aldrich, Merck, Fischer Scientific or Thermo Fischer Scientific, unless stated otherwise.

2.1.2 Cells

Bacterial strains

In this PhD research, the *Escherichia coli* strain: ORN 178, and the *Pseudomonas aeruginosa* strain: PAO1, were used. *Escherichia coli* ORN 178 was kindly provided by Professor Paul Orndorff (North Carolina State University, North Carolina, US); and *Pseudomonas aeruginosa* PAO1 was kindly provided by Dr Jacob Malone (John Innes Centre, Norwich, UK).

Human cell lines

Two breast adenocarcinoma cell lines (SK-BR-3 and MDA-MB-231), and a mammary epithelial cell line (MCF-10A) were used in these studies. The SK-BR-3 cell line was kindly provided by Professor Dylan Edwards (University of East Anglia, UK), which was obtained from LGC Standards. MDA-MB-231 and MCF-10A were purchased from ATCC (LGC Standards).

2.1.3 Instrumental techniques

A summary of the equipment used throughout this PhD research is shown in Table 2.1.

Table 2.1: List of equipment used throughout the PhD research.

Equipment	Manufacturer
UV-Vis spectrophotometer	Varian Cary$^®$ 50 UV-Vis Spectrophotometer
Plate reader	BMG Labtech CLARIOstar$^®$ High-Performance Microplate Reader
Fluorimeter	Hitachi F-4500 fluorescence spectrometer
TEM	FEI Tecnai$^®$ F20 S/TEM
DLS	Wyatt Technologies DynaPro Titan Dynamic Light Scattering System with a temperature-controlled MicroSampler
Centrifuge	Eppendorf 5810R Centrifuge
Chemiluminescent imaging	ImageQuant LAS 500 CCD camera
ESI-MS	Advion Expression Compact Mass Spectrometer
MALDI-TOF MS	Bruker Daltonics autoflex speed ToF/ToF mass spectrometer
NMR	Bruker Avange III HD 400 MHz
Confocal microscope	Carl Zeiss LSM 510 META confocal laser scanning microscope

The following provides detail on the instrumental techniques used in this PhD research.

Mass spectrometry

Two mass spectrometry methods were used. Firstly, ESI-MS (electrospray ionisation mass spectrometry) was used during ligand synthesis. Through direct injection, 10 μl of ~0.1 mg ml^{-1} was injected. The masses were recorded in positive mode and analysed using Advion Mass Express software.

Secondly, MALDI-TOF MS (matrix-assisted laser desorption ionisation time of flight mass spectrometry) analysis was used. Concentrated samples (~150 nM AuNPs) were prepared by performing a 1: 1 dilution of sample in DHB matrix, and then 2 μl of the mixture was spotted onto a MTP AnchorChip 384 target plate. The spot was left to dry at room temperature before analysis. The MALDI-TOF MS equipment used a nitrogen laser, and analysis was performed in a linear 50 shot mode, with 32x gain and 70% laser intensity.

Nuclear Magnetic Resonance Spectroscopy

Nuclear Magnetic Resonance (NMR) equipment used a broadband BBFO probe at 400 MHz (^{1}H) and 100 MHz (^{13}C) at 298 K. For the analysis, the chemical shifts (δ) are in parts per million (ppm). Compounds were assigned using proton, carbon, HSQC edited two-dimensional correlation spectroscopy and COSY. Assignment was performed using Mestrenova software (Mestrelab Research, S.L.).

UV-Vis spectrometry

UV-Vis measurements were obtained using a UV-Vis spectrophotometer or plate reader. For the UV-Vis spectrophotometer measurements, samples (1 ml) were added to a Quartz cuvette and measured using Cary WinUV software, with a 1 cm path length. For plate reader measurements, samples (50 μl) were loaded into 384-well microtitre plates (4titude), and measurements recorded using Omega series and MARS Data Analysis software (BMG Labtech).

Fluorimetery

Fluorescence measurements were obtained using a fluorimeter or a plate reader. For the fluorimeter measurements, samples (1 ml) were added to a Quartz cuvette and with a 1 cm path length, measurements were recorded using FluorEssence™ (Horiba) software. For the plate reader measurements, samples (120 μl) were loaded into Nunc Nunclon™ Surface 96-well microtitre plates, and measurements were recorded using Omega series and MARS Data Analysis software (BMG Labtech).

Transmission electron microscopy

For transmission electron microscopy (TEM) imaging, 400 mesh copper palladium grids with carbon-coated pyroxylin support film were used. To the grids, 10 μl of sample was adsorbed, followed by addition of 2% uranyl acetate (10 μl) for negative staining. The grids were placed into the TEM, operating at 200 kV, and imaged using an AMT XR60B digital camera (Deben).

Dynamic light scattering

Dynamic light scattering (DLS) is a technique used to measure the size of nanoparticles suspended in a liquid. These particles undergo random thermal motion, called Brownian motion, which is a result of the surrounding solvent molecules bombarding the nanoparticles[1]. The bombardment causes the nanoparticles to move, with smaller particles diffusing through the liquid quicker than larger particles[2]. Light is scattered in all directions upon striking the moving nanoparticles. However, the intensity of the scattered light fluctuates, as the particles are constantly moving due to Brownian motion[3]. Smaller particles diffuse quicker through the solution, and so exhibit more rapid rates of fluctuations in light scattering intensities compared to larger particles[2].

Consequently, DLS relies on a laser that irradiates a sample of nanoparticles. The size can then be determined by measuring the rate of fluctuation in light scattering intensities. The velocity (diffusion constant, see Equation 2.1) of the nanoparticles moving through the solution is obtained from the rate of fluctuations in light scattering intensities. The size of the particles can be determined using the Stokes-Einstein equation:

$$D = \frac{k_B T}{6 \pi \eta R_h} \tag{2.1}$$

Where D is the diffusion constant; K_B is the Boltzmann constant; T is the temperature; η is the viscosity; and R_h is the hydrodynamic radius[3]. DLS provides the nanoparticle size as hydrodynamic radius, as the size is calculated based on a hypothetical sphere that diffuses through the liquid at the same rate as the particle measured[4].

For Dynamic light scattering (DLS) size measurements, the sample (12 µl, in MQ water) was added to a 12 µl Quartz microcuvette. The sample was equilibrated for two minutes, and the mean average size was collected from three runs, with 10 measurements per run. The measurements were obtained using DYNAMICS software (Wyatt).

Confocal microscopy and image analysis

A plan-apochromat 63x/1.4 Oil DIC objective was used to obtain the images, and the data was processed using ImageJ/Fiji software. For quantification of fluorescence, each image was despeckled, followed by setting the minimum threshold to 23, with the 'Triangle' threshold method. The threshold was determined using the condition which provided the highest grey value, *i.e.*, the strongest interaction. The threshold was determined at the point where all background signal was removed and only fluorescence due to the dye interaction with the cell, was measured. The threshold was then applied throughout all images for analysis. Fluorescent binding to the cells was represented and

quantified by the integrated intensity, which was determined as follows. The integrated intensity of one image (I) was derived from the following equation:

$$I = \frac{(\text{Mean Grey Value } \times \text{Area})}{n} \tag{2.2}$$

Where the mean grey value is the average intensity of all pixels measured. The area is the total area of the selection within the image where the grey values were recorded, and n is the number of cells within that image.

The mean integrated intensity is consequently:

$$\text{Mean I} = \frac{(\sum \text{I})}{n} \tag{2.3}$$

Where $\sum$I is the sum of all integrated intensity for all images within one condition, and n is the number of images analysed within that condition.

2.2 Buffers and media composition

The composition of the buffers and media supplements used in this research is summarised in Table 2.2. The pH of each buffer was corrected with 1 M NaOH or 1 M HCl. All buffers and media that were used for cell culture were autoclaved at 121ºC for 10 minutes, and sterilised using a 0.22 μm syringe filter (Millex GP).

Table 2.2: List of buffers and their composition.

Buffer/Media	Composition
TB	10 mM Tris buffer
TBS	TB with 10 mM NaCl, 0.3625 mM $CaCl_2$, pH 7.8
TBT	TB with 0.05 % Tween 20, pH 7.8
PB	10 mM Phosphate buffer
PBS	10 mM PB with 150 mM NaCl, pH 7.4
MES	10 mM MES buffer, pH 5.5
MEST	10 mM MES with 0.05 % Tween 20, pH 5.5
Loading buffer	Laemmli sample buffer with 0.025% β-mercaptoethanol
Transfer buffer	25 mM TB, 192 mM glycine in 1 L of 20 % aqueous methanol, pH 8.6
LB media	10 g tryptone, 5 g of yeast extract and 10 g of NaCl in 1 L of de-ionised water
Imaging medium	NaCl (120 mM), KCl (5 mM), $CaCl_2$ (2 mM), $MgCl_2$ (1 mM), monosodium phosphate (1 mM), sodium bicarbonate (1 mM), HEPES (25 mM), D-glucose (11 mM) and BSA (1 mg ml^{-1}) in 50 ml of PB, pH 7.4
DMEM(-)	DMEM with 1% penicillin/streptomycin solution and phenol red
DMEM(+)	DMEM with 1% penicillin/streptomycin solution, phenol red and 10% FBS
Freezing medium	DMEM(+) or MEGM, with 10 % DMSO
MEGM	MEBM™ Basal Medium with MEGM™ Bullet Kit (BPE (2 ml), hydrocortisone (0.5 ml), hEGF (0.5 ml) and insulin (0.5 ml))

2.3 Preparation and characterisation of glycan ligands and functionalised gold nanoparticles

2.3.1 Glycan ligand synthesis

Through CuAAC, a series of glycan ligands were prepared. The azido and alkyne reagents (Figure 2.1) used in the synthesis were prepared by other members of the group (Simone Dedola, Simona Chessa and Jordan Hindes), with the exception of alkyne **(2)**, which was sourced commercially (Sigma).

a)
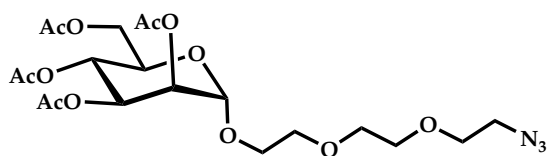
azide (1)

b)
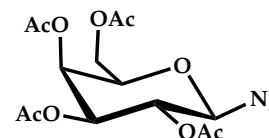
azide (2)

c)
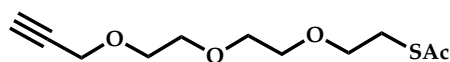
alkyne (1)

d)
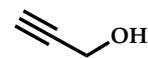
alkyne (2)

Figure 2.1: Structure of azide and alkyne reagents for glycan synthesis: a) azide (1), Ac-mannose-PEG$_3$-N$_3$; b) azide (2), Ac-galactose-N$_3$; c) alkyne (1), PEG$_3$-SAc; and d) alkyne (2), propargyl alcohol.

(1) S-10-(1-(8-(2,3,4,6-Tetra-O-acetyl-α-D-mannopyranosyloxy)-3,6-dioxaoctyl)-
-1H-[1,2,3]-triazol-4-yl)-3,6,9-trioxadecyl ethanethioate (Ac-mannose-PEG$_6$-SAc)
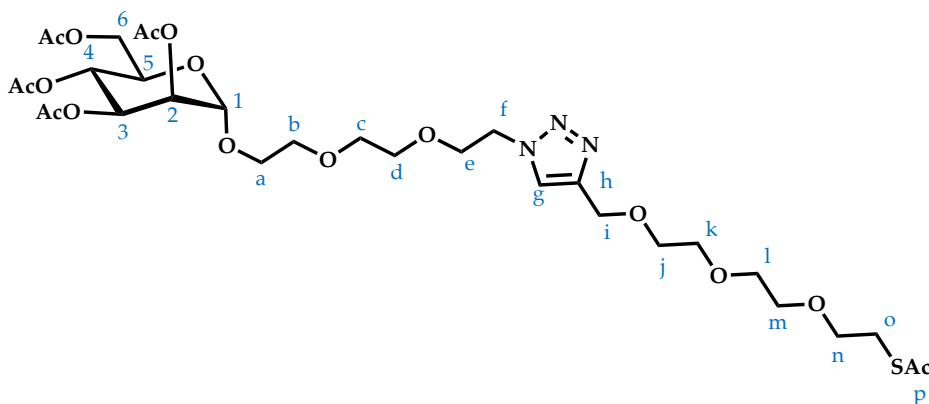
Figure 2.2: Structure of Ac-mannose-PEG$_6$-SAc, with annotations for NMR assignment.

Azide (1) was previously synthesised by the group following the method out-
lined in Otman *et al.*[5] and alkyne (1) was synthesised following Goswami *et
al.*[6]. Azide (1) (23 mg, 45.5 μmol) and alkyne (1) (12.3 mg, 50.1 μmol, 1.1 eqv.)
were each dissolved in 500 μl of DMF and mixed together. In MQ H$_2$O, 1 M
solutions of CuSO$_4$, NaAsc and THPTA were prepared. A premixed solution
of CuSO$_4$ (9.1 μmol, 0.2 eqv) and THPTA (22.8 μmol, 0.5 eqv) was prepared
and then added to the reaction mixture, followed by NaAsc (18.2 μmol, 0.4
eqv). The reaction was heated to 50ºC and stirred for 16 h. The reaction was
monitored by TLC (100% EtOAc) and ESI-MS (Advion, positive mode). The
DMF was evaporated under vacuum and the reaction mixture was dissolved in
DCM : H$_2$O (9.5:0.5) for organic/aqueous phase separation. The organic phase
(DCM) was extracted, dried over MgSO$_4$, filtered, and then the solvent was
evaporated under vacuum. The product was purified by silica gel chromatog-
raphy (DCM-MeOH 1:0 -> 0:1) to give **(1)** as an oil (22 mg, 64%); R$_f$ 0.24 (100%
EtOAc); [α]$_D$ +19.3 (*c* 1.0, 20ºC, CH$_3$OH); δ$_H$ (600 MHz, CD$_3$OD) 7.92 (s , 1H,
H-g), 5.11-5.17 (m, 3H, H-2, H-3, H-4), 4.78 (d, 1H, $J_{1,2}$ 1.7Hz, H-1), 4.53 (s, 2H,
H-i), 4.49 (m, 2H, H-f), 4.12 (dd , 1H, $J_{6,6'}$ 12.1 Hz, $J_{5,6}$ 4.8 Hz, H-6), 4.01 (m, 2H,

H-5 and H-6'), 3.81 (m, 2H, H-e), 3.72 (m, 1H, H-a), 3.49-3.58 (m, 15H, H-a', H-b, H-c, H-d, H-j, H-k, H-l, H-m), 3.46 (t, 2H, $J_{n,o}$ = 6.5 Hz, H-n), 2.95 (t , 3H, $J_{n,o}$ = 6.5 Hz, H-o), 2.20 (s, 3H, H-p) and 2.02, 1.95, 1.92, 1.84 (s, 12H, CH$_3$CO); δ_C (600 MHz, CD$_3$OD) 195.65 (C-p), 170.97, 170.20, 170.14, 170.10 (CH$_3$CO), 144.48 (C-g), 124.46 (C-h), 97.56 (C-1), 70.22, 70.18, 70.14, 70.09 69.33 (C-b, C-c, C-d, C-j, C-k, C-l, C-m, C-n), 69.43-69.33 (C-3 and C-4), 69.03 (C-e), 68.42 (C-5), 67.05 (C-a), 65.91 (C-2), 63.67(C-i), 62.20 (C-6), 50.07 (C-f), 29.05 (C-p), 28.23 (C-o) and 19.29, 19.26, 19.25, 19.18 (CH$_3$CO); HR ESI-MS found m/z 752.2899 [M$^+$H]$^+$ calculated for C$_{31}$H$_{49}$N$_3$O$_{16}$S.H 752.2979.

(2) 10-(1-(8-(α-D-Mannopyranosyloxy)-3,6-dioxaoctyl)-1H-[1,2,3]-triazol-4-yl)-3,6,9-trioxadecylthiol (ac-mannose-PEG$_6$-SH)
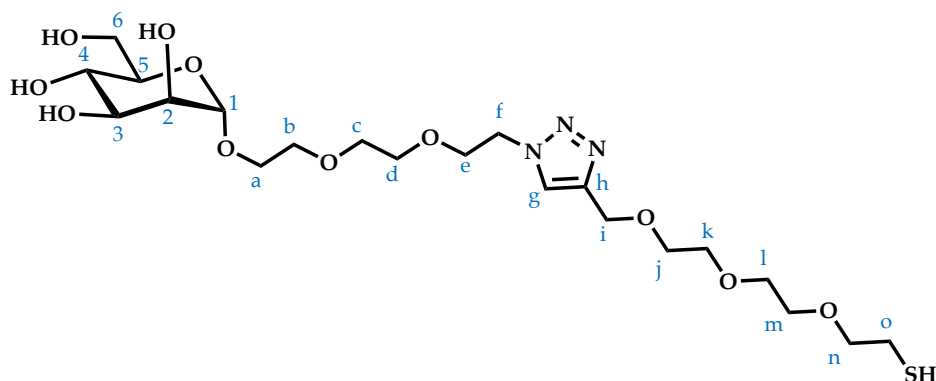
Figure 2.3: Structure of mannose-PEG$_6$-SH, with annotations for NMR assignment.

Compound **(1)** (17.2 mg, 22.89 µmol) was dissolved in anhydrous methanol (4.5 ml). Under nitrogen, sodium methoxide (0.023 M, 5 eqv.) was added and stirred at room temperature for one hour, until only deacetylated compound **(2)** could be detected. The reaction was monitored by ESI-MS (positive mode) and NMR. Amberlite 120 H$^+$ resin was added to neutralise the reaction mixture, and then filtered. The solvent was removed under vacuum. The product was purified by GPC, using a Toyopearl TSK-HW40S column (1.6 x 90 cm, 0.5 ml/min, H$_2$O), and collected between 176-196 min. The purified product **(2)** was an oil (10.8

mg, 87%); $[\alpha]_D$ + 7.7 (c 1.0, 20°C, H_2O); δ_H (600 MHz, D_2O); 7.93 (d, 1H, H-g), 4.70 (d, 1H, H-1), 4.56 – 4.52 (m, 2H, CH_2), 4.49-4.46 (m, 2H, CH_2), 3.82 (m, 2H, CH_2), 3.78 (dd, 1H, H-2), 3.74 – 3.68 (m, 1H, H-6), 3.68 – 3.61 (m, 3H, H-3, CH_2), 3.61 – 3.49 (m, 12H, H-6′, H-3, 5(CH_2)), 3.49 – 3.43 (m, 8H, H-4, H-5, 3(CH_2)), 2.76 (t, 1H), 2.54 (t, 1H); δ_C (600 MHz, D_2O) 143.6 (C-h), 125.3 (C-g), 99.9 (C-1), 72.7 (C-5), 70.4 (C-3), 69.9 (C-2), 69.7-68.3 (11(CH_2)) 66.7(C-4), 66.3(CH_2), 62.9(CH_2), 60.8(C-6), 49.9(CH_2), 43.3(CH_2), 37.1(CH_2); HR ESI-MS found m/z 542.2380 $[M^+H]^+$ calculated for $C_{21}H_{39}N_3O_{11}S.H$ 542.2378.

**(3) S-10-(1-(2,3,4,6-Tetra-O-acetyl-β-D-galactopyranosyl)-1H-1,2,3-triazol-4-yl)-
-3,6,9-trioxadecyl ethanethioate (Ac-galactose-PEG$_3$-SAc)**
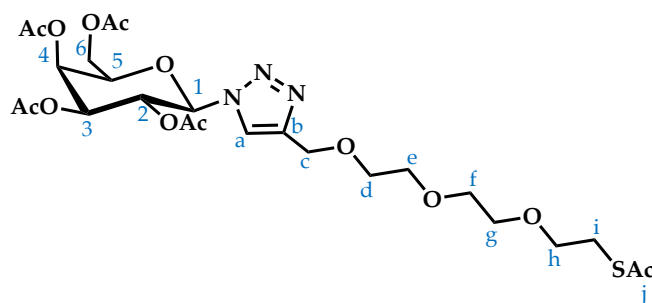
Figure 2.4: Structure of Ac-galactose-PEG$_3$-SAc, with annotations for NMR assignment.

Azide (2) was synthesised by another member of the group following the method outlined in Dedola *et al.*[7]. Azide (2) (33 mg, 88.5 µmol) and alkyne (1) (28 mg, 113.8 µmol, 1.1 eqv.) were each dissolved in 500 µl of DMF and mixed together. In MQ H_2O, 1 M solutions of $CuSO_4$, NaAsc and THPTA were prepared. A premixed solution of $CuSO_4$ (17.7 µmol, 17.7 µl, 0.2 eqv) and THPTA (44.2 µmol, 44.2 µl, 0.5 eqv) was prepared and then added to the reaction mixture, followed by NaAsc (35.4 µmol, 35.4 µl, 0.4 eqv). The reaction was heated to 50°C and stirred for 16 h. The reaction was monitored by TLC and Advion ESI-MS (positive mode). The DMF was evaporated under vacuum and reaction mixture dissolved in DCM: H_2O (9.5: 0.5) for organic/aqueous

phase extraction. The organic phase (DCM) was collected, dried over MgSO$_4$, filtered and then solvent evaporated under vacuum. The product was purified by silica gel chromatography (Hex-EtOAc 9.5: 0.5 -> 2.5: 7.5) to give **(3)** as an oil (45.6 mg, 85%); R$_f$ 0.44 (100% EtOAc); $[\alpha]_D$ -2.5 (*c* 1.0, 20°C, CHCl$_3$); δ_H (400 MHz, CDCl$_3$); 7.85 (s, 1H, H-a), 5.85 (d, 1H, H-1), 5.60 – 5.50 (m, 2H, H-3, H-4), 5.25 (dd, 1H, H-2), 4.64 (s, 2H, CH$_2$), 4.28 – 4.06 (m, 3H, H-5, H-6, H-6′), 3.68 – 3.55 (m, 10H, 5(CH$_2$)), 3.08 (m, 2H, CH$_2$), 2.32 (s, 3H), 2.22 (s, 3H), 2.16 (s, 3H), 2.06 – 1.97 (m, 7H), 1.88 (s, 3H), 1.31 – 1.20 (m, 2H), 2.26 (s, 3H, CH$_3$), 2.16 (s, 3H, CH$_3$), 1.98 (s, 3H, CH$_3$), 1.94 (s, 3H, CH$_3$), 1.82 (s, 3H, CH$_3$); δ_C (600 MHz, CDCl$_3$) 171.1, 170.3, 169.9, 169.8 and 169.0 (**C**OCH$_3$), 145.9 (C-b), 121.3 (C-a), 86.4 (C-1), 74.1 (C-5), 70.8 (C-2), 70.51, 70.49, 70.3 and 69.8 (CH$_2$), 67.9 (C-3), 66.8 (C-4) 64.5 (CH$_2$), 61.3 (C-6), 60.3 (CH$_2$), 30.5 (CO**C**H$_3$), 28.7 (CH$_2$), 21.0, 20.6, 20.5 and 20.2 (CO**C**H$_3$); HR ESI-MS found m/z 641.7872 [M$^+$Na]$^+$ calculated for C$_{25}$H$_{37}$N$_3$O$_{13}$S.Na 642.1939.

(4) 10-(1-(β-D-Galactopyranosyl)-1H-1,2,3-triazol-4-yl)-3,6,9-trioxadecylthiol (gal-PEG$_3$-SH)
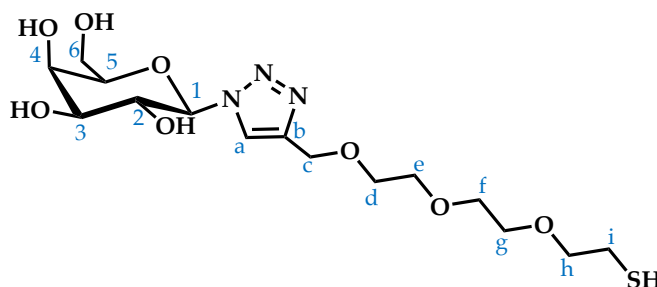
Figure 2.5: Structure of galactose-PEG$_3$-SH, , with annotations for NMR assignment.

Compound **(3)** (21.2 mg, 20.0 μmol) was dissolved in anhydrous methanol (4.5 ml). Under nitrogen, sodium methoxide (0.02 M, 5 eqv.) was added and stirred at room temperature for one hour, until only deacetylated compound **(4)** could be detected. The reaction was monitored by ESI MS and NMR. Amberlite 120 H$^+$ resin was added to neutralise the reaction mixture, and then filtered.

The solvent was removed under vacuum. The product was purified by GPC, using a Toyopearl TSK-HW40S column (60 cm, 0.5 ml/min, H_2O), and collected between 220-240 min. The purified product was a fine powder (11.4 mg, 81%); $[\alpha]_D$ +15.2 (c 1.0, 20°C, H_2O); δ_H (400 MHz, D_2O) 8.20 (s, 1H, H-a), 5.60 (d, 1H, $J_{1,2}$ = 9.51 Hz, H-1), 4.63 (s, 2H, H-c), 4.12 (t, 1H, $J_{1,2}$= 9.51, $J_{2,3}$ = 9.51, H-2) 3.98 (d, 1H,$J_{3,4}$ = 3.34, H-4), 3.91 (m, 1H, H-5), 3.78 (dd, 1H, $J_{2,3}$ = 9.51, $J_{3,4}$ = 3.34, H-3), 3.71-3.52 (m, 12H, H-6, CH_2) 2.60 (t, 2H, H-i); δ_C (400 MHz, D_2O) 144.13 (C-b), 124.09 (C-a), 87.96 (C-1), 78.23 (C-5), 72.85 (C-3), 72.10 (C-h), 69.62 (C-2), 69.47, 69.42, 69.10, 68.95 (C-d/C-e/C-f/C-g), 68.47 (C-4), 62.92 (C-c), 60.75 (C-6), 22.98 (C-i); HR ESI-MS found m/z 817.2931 $[M^+H]^+$ calculated for $C_{30}H_{52}N_6O_{16}S_2.H$ (disulphide product) 817.2954.

(5) (1-(2,3,4,6-tetra-O-acetyl-(β-ᴅ-galactopyranosyl))-1H-1,2,3-triazol-4-yl)methanol
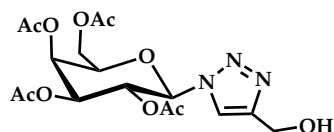
Figure 2.6: Structure of acetylated galactose-based lectin inhibitor structure.

Compound **(5)** and **(6)** have been synthesised previously, with full characterisation detailed[8]. Briefly, following the same conditions outlined for compound **(1)** and **(3)** synthesis, azide (2) (311 mg, 833μmol) was mixed with alkyne (2) (1.1 eqv, 51.4 mg, 917 μmol), $CuSO_4$ (0.2 eqv), NaAsc (0.4 eqv) and THPTA (0.5 eqv). The reaction was heated to 50°C and stirred for 16 h. The DMF was evaporated under vacuum and the organic layer was extracted and then dried over $MgSO_4$. The reaction mixture was purified by silica chromatography to give **(5)** (280 mg, 78%).

74

(6) (1-(β-ᴅ-Galactopyranosyl)-1H-1,2,3-triazol-4-yl)methanol (inhibitor)
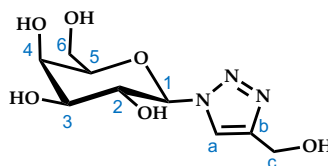
Figure 2.7: Structure of galactose-based lectin inhibitor, with annotations for NMR assignment.

As with compounds **(2)** and **(4)**, compound **(5)** (24 mg) was deacetylated by sodium methoxide, and purified by GPC to provide compound **(6)** (11.2 mg, 77%). As compounds **(5)** and **(6)** have been synthesised and fully characterised elsewhere, confirmatory characterisation was performed. The purified product **(6)** was a fine powder; δ_H (400 MHz, D_2O); 8.11 (s, 1H, H-b), 5.58 (d, $J_{1,2}$ = 9.2Hz, H-1), 4.64 (s, 2H, H-c), 4.11 (t, $J_{1,2}$ = 9.2Hz, H-2), 3.97 (dd, 1H, $J_{3,4}$ = 3.3 Hz, $J_{4,5}$ = 1.1 Hz, H-4), 3.89 (dd, 1H, $J_{4,5}$ = 1.1 Hz, H-5), 3.76 (dd, 1H, $J_{3,4}$ = 3.3 Hz, H-3), 3.66 (d, 2H, H-6). ESI-MS found m/z 284.1 $[M^+Na]^+$ calculated for $C_9H_{15}N_3O_6$.Na 284.1. These data are in accord with published values.

2.3.2 Synthesis of 16 nm AuNPs

Synthesis of 16 nm citrate stabilised AuNPs (citrate-AuNPs) were prepared following the method developed by Turkevich *et al.*[9]. To 100 ml of water, 12.5 mg of gold(III) chloride trihydrate was added and heated to 60ºC whilst stirring. In a separate flask, 50 mg of sodium citrate tribasic dihydrate was added to 50 ml of water and stirred whilst heating to 60ºC. The heated sodium citrate solution was added to the gold chloride solution, whilst rapidly stirring and heated up to 85ºC. The solution was then left to stir for 2.5 h. The solution was then removed from the heat and cooled to room temperature. The solution was passed through a filter (0.22 μm, GP Millex), ready for characterisation. The extinction spectrum was measured using a plate reader (350-800 nm), and the data was processed in R. Particle size was obtained using TEM and DLS.

2.3.3 Functionalisation of AuNPs

For all AuNP suspensions, the concentration is calculated by the extinction maxima value (~520 nm).

Functionalisation of AuNPs with galactose-PEG$_3$-SH ligand

A 10 mM (4 mg ml^{-1}) galactose-PEG$_3$-SH (see Figure 2.8) solution was prepared in MQ water, and serial dilutions were performed to generate 5 mM and 1 mM galactose-PEH$_3$-SH solutions. To vials containing 9.8 ml of 3 nM citrate-AuNPs, 200 µl of either the 1, 5 or 10 mM stock solutions were added, to provide a total volume of 10 ml, and final galactose-PEG$_3$-SH concentrations of 20 µM, 100 µM and 200 µM, respectively. The solutions were stirred for 72 h at room temperature. To purify the suspensions and remove excess ligand, the suspensions were transferred to spin columns (10 kDa MW cut-off), and centrifuged at 4,000 g for 10 min. The concentrated galactose-PEG$_3$-SH functionalised AuNP suspensions (gal-AuNPs) were diluted in 10 ml of MQ water and centrifuged for a further 10 min at 4,000 g. The process was then repeated two more times. The purified gal-AuNPs were characterised using MALDI-TOF MS to detect galactose-PEG$_3$-SH, and UV-Vis extinction spectrum was recorded in a plate reader (350-800 nm).
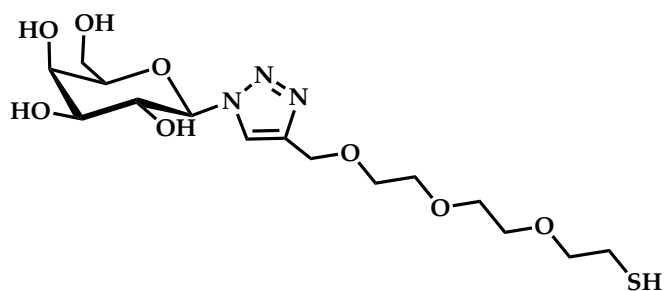
Figure 2.8: Galactose-PEG$_3$-SH ligand structure for AuNP functionalisation.

Functionalisation of AuNPs with PEG$_3$-SH ligand

A 10 mM PEG$_3$-SH (see Figure 2.9) solution was prepared in MQ water. To a vial containing 9.8 ml of 3 nM citrate-AuNPs, 200 μl of the 10 mM stock solutions were added, to provide a total volume of 10 ml, and final PEG$_3$-SH concentrations of 200 μM. The solution was stirred for 72 h at room temperature. To purify the suspensions and remove excess ligand, the suspensions were transferred to spin columns (10 kDa MW cut-off), and centrifuged at 4,000 g for 10 min. The concentrated PEG$_3$-SH functionalised AuNP suspension (PEG$_3$-AuNPs) were diluted in 10 ml of MQ water and centrifuged for a further 10 min at 4,000 g. The process was then repeated two more times. The purified gal-AuNPs were characterised using MALDI-TOF MS to detect PEG$_3$-SH, and UV-Vis extinction spectrum was recorded in a plate reader (350-800 nm).
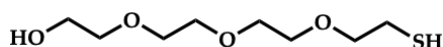
Figure 2.9: PEG$_3$-SH ligand structure for AuNP functionalisation.

Functionalisation of AuNPs with the cationic ligand: TMAC

The 'two-step phase transfer' method was adapted from Hassinen *et al.*[10], where the cationic ligand: *N,N,N*-trimethyl(11-mercaptoundecyl)ammonium chloride (TMAC) was used to modify the AuNPs. The structures of the ligands used for the two-step phase transfer can be seen in Figure 2.10.
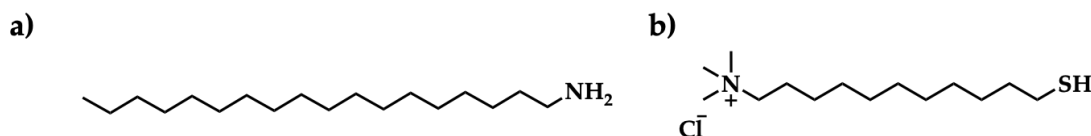
Figure 2.10: Ligand structures used for TMAC AuNP functionalisation: a) ODA and b) TMAC.

To a 50 ml falcon tube, 30 ml of 3 nM citrate-AuNPs were added. A 2 mM solution of ODA (3.23 mg) was prepared in toluene (6 ml), and added to the citrate-AuNP suspension. The tube was then shaken vigorously and the organic fraction containing the ODA functionalised AuNPs (ODA-AuNPs) were

transferred to a fresh tube. To remove the displaced citrate and excess ODA, the particles were washed by adding MilliQ water, shaking, and then discarding the aqueous layer. The method was repeated three times.

The washed ODA-AuNPs were transferred to a fresh tube and 3 ml of MilliQ water was added. A 4 mM stock solution of TMAC (1.12 mg) was prepared in ethanol (1 ml). To the ODA-AuNPs and water mixture, 150 µl of the TMAC solution was added and the tube was shaken vigorously. To the solution, 2 drops of 2 M HCl were added, followed by a further 150 µl of TMAC solution. The mixture was shaken vigorously and the aqueous layer was transferred to a fresh tube. As an emulsion formed, the solution was centrifuged at 4,000 g for 5 min. The residual organic layer was discarded. The aqueous layer was washed with 6 ml of toluene, by vortexing the mixture, centrifugation of the mixture at 4, 000 g for 5 min, discarding the organic layer and repeating seven times to ensure removal of ODA and excess TMAC. The TMAC-AuNPs were analysed by MALDI-TOF MS, and UV-Vis extinction spectrum was measured using the plate reader.

Functionalisation of AuNPs with mixed monolayer of chlorin e6 and glycan ligands

To functionalise the AuNPs with the PS: chlorin e6 (ce6), EDC coupling was used to conjugate a ce6-NH_2 derivative to carboxylic acid functionalised AuNPs, to generate the final ce6 conjugated ligand (ce6-PEG_4-SH). The ligands used for AuNP functionalisation, and final ligand structures, can be seen in Figure 2.11.
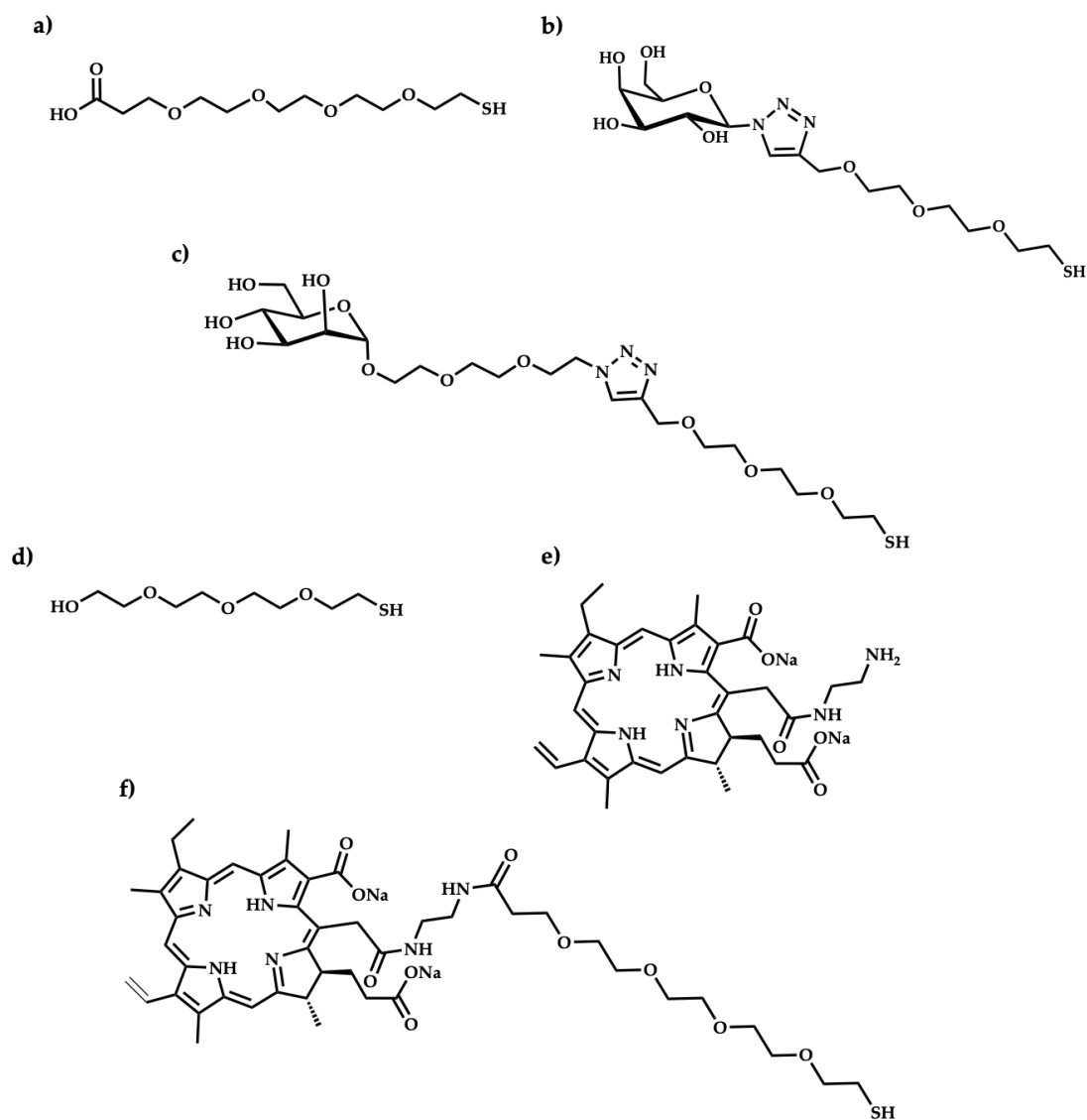
Figure 2.11: Ligand structures used for glycan-/ce6-AuNP functionalisation: a) COOH-PEG$_4$-SH; b) galactose-PEG$_3$-SH; c) mannose-PEG$_6$-SH; d) PEG$_3$-SH; e) ce6-NH$_2$; and f) ce6-PEG$_4$-SH.

Stock solutions of COOH-PEG$_4$-SH (2.8 mg ml^{-1}) and galactose-PEG$_3$-SH (4 mg ml^{-1}) were prepared in MQ water, to provide a final concentration of 10 mM. To a vial with 9.8 ml of 3 nM citrate-AuNPs, 50 µl of COOH-PEG$_4$-SH and 150 µl of galactose-PEG$_3$-SH stock solutions (10 mM) were added, to provide final concentrations of the COOH-PEG$_4$-SH and galactose-PEG$_3$-SH at 50 µM and 150 µM, respectively. The suspension was stirred for 72 h. To purify the suspension and remove excess ligand, the solution was transferred to

spin columns (10 kDa MW cut-off), and centrifuged at 4,000 g for 10 min. The concentrated galactose-PEG$_3$-SH and COOH-PEG$_4$-SH functionalised AuNP suspension (galactose-/COOH-AuNPs) was diluted in 10 ml of MQ water and centrifuged for a further 10 min at 4,000 g. The process was then repeated two more times.

NHS (3.5 mg ml^{-1}) and EDC (5.8 mg ml^{-1}) stock solutions were prepared in MQ water, to provide a final concentration of 30 mM. In a fresh vial, purified gal-/COOH-AuNPs were diluted in MES to provide a final volume of 9.9 ml. To the gal-/COOH-AuNPs, 50 μl of the 10 mM EDC and NHS stocks were added, to provide a final concentration of 150 μM. The reaction mixture was stirred for 2 h at room temperature. To purify the suspension and remove excess ligand, the suspension was transferred to spin columns (10 kDa MW cut-off), and centrifuged at 4,000 g for 10 min. The concentrated galactose-PEG$_3$-SH and NHS activated functionalised AuNP suspension (galactose-/NHS-AuNPs) was diluted in 10 ml of MQ water and centrifuged for a further 10 min at 4,000 g. The process was then repeated two more times.

A 73 mM stock solution of the ce6-NH$_2$ derivative (50 mg) was prepared in 1 ml of MeOH. In a fresh vial, purified gal-/NHS-AuNPs were diluted in PB to provide a final volume of 9.9795 ml. To the gal-/NHS-AuNPs, 20.5 μl of the ce6-NH$_2$ stock solution was added, to provide a final concentration of 150 μM. The reaction mixture was stirred for 16 h at room temperature, in the dark. To purify the suspension and remove excess ligand, the suspension was transferred to spin columns (10 kDa MW cut-off), and centrifuged at 4,000 g for 10 min. The concentrated galactose-PEG$_3$-SH and ce6-PEG$_4$-SH functionalised AuNP suspension (gal-/ce6-AuNPs) was diluted in 10 ml of MQ water and centrifuged for a further 10 min at 4,000 g. The process was then repeated six more times. The purified suspension was characterised using MALDI-TOF MS, and the extinction spectrum was recorded using the plate reader (350-800 nm).

The process was repeated with mannose-PEG$_6$-SH and PEG$_3$-SH, to provide man-/ce6-AuNPs and PEG$_3$-/ce6-AuNPs. The particles were also assessed for

singlet oxygen production, which is detailed in Section 2.5.3.

2.4 Targeted bacterial lectin binding using glyco- nanoparticles

2.4.1 Bacterial culture

All bacterial culture experiments was performed under sterile conditions. From -80°C glycerol stocks containing the bacterial strains (*E. coli* ORN178 or *P. aeruginosa* PAO1), a sterile pipette tip was used to 'scratch' the surface of frozen bacterial glycerol stock, and transfer material to 10 ml LB liquid media. The cultures were then used for experiments as detailed below, or ready to make fresh glycerol stocks by plating onto LB agar plates and selecting individual colonies.

2.4.2 Bacterial lectin expression assessed by Western blot analysis

From the overnight culture, 1: 1000 dilution was performed into fresh LB media (500 ml). The absorbance at 600 nm was immediately recorded. Absorbance at 600 nm was recorded every 2 h for the first 12 h, and then at regular intervals up to 78 h. The measurements were processed in R, to provide the bacterial growth curve.

At different time points throughout growth, 2 ml samples were taken from the bacterial cultures and centrifuged at 10, 000 g for 10 min. The supernatant was discarded and the pellet was resuspended in 100 ul of MQ water. To Eppendorf tubes, 10 µl of bacterial sample was added followed by 10 µl of loading buffer. The samples were heated at 95°C for 20 minutes. The samples were then vortexed thoroughly. The samples, including the protein ladder and LecA (100 ng) standard, were added to the wells of RunBlue precast 4-

20 % gel (Expedeon) and ran by gel electrophoresis (16 V, one hour) in 1 x RunBlue running buffer (Expedeon). The gel was transferred onto nitrocellulose membrane (32 V, 4°C, one hour) in transfer buffer. The membrane was then coated with Ponceau stain for 10 minutes, and washed with MQ water until enough background stain had been removed to see clear protein bands. The stained membrane was then imaged.

The stain was then washed with PBST for 10 minutes, three times. The membrane was then covered with PBST + 1 % BSA, overnight at 4°C. From the stock solution of anti-LecA antibody (CusaBio Technology LLC), 20 µl was transferred into 10 ml of PBST (1: 500 dilution). The membrane was washed for 5 min with PBST, three times. The anti-LecA antibody solution (1:500) was added to the washed membrane, and shaken at 37°C for one hour. The membrane was washed with PBST for five minutes, three times. To the membrane, 10 ml of goat anti-rabbit HRP-secondary antibody solution (1:2000 dilution in PBST) was added to the membrane and shaken at 37°C for one hour. The membrane was washed with PBST for five minutes, three times. The membrane was imaged by applying Pierce^{TM} ECL Western Blotting Substrate, following the manual. Chemiluminescent image was obtained using automatic exposure.

2.4.3   Colorimetric binding studies

The UV-Vis based plate assays were adapted from Marin *et al.*[11], and the filter based plate assay was developed in collaboration with scientists at Iceni Diagnostics. All AuNP concentrations were obtained from the extinction value at the extinction maxima (~520 nm), using the Beer-Lambert Law.

UV-Vis absorption using 384-well plate format to monitor lectin binding by gal-AuNPs

To the wells of a 384-well plate, 100 µl of TBT was added for 1 hour at room temperature, to block the wells. Gal-AuNPs were resuspended in TB to 2.5 nM,

determined by UV-Vis spectrometry. The TBT from the wells was removed, and gal-AuNPs were added to the wells (50 μl), and the extinction measured using a plate reader. A 36.3 μM stock solution of LecA (1.85 mg ml⁻¹) was prepared in TBS, and subsequently diluted in TBS to provide the desired concentrations. A concentrated stock solution of 7.25 μM of ConA (0.75 mg ml⁻¹) was prepared in TBS. Concentrated lectin solutions (8 μl) were added to the AuNP suspensions. Note that the solution was diluted 1 in 7.25 when added to the well (8 μl of lectin solution with 50 μl of AuNP suspension) but the concentrations listed in Chapter 4 represent the final concentration inside the well. Consequently for a 1 μM lectin solution inside the well, 8 μl of a concentrated 7.25 μM lectin solution must be added. The same method was applied throughout the binding studies. The extinction was measured every 10 min for 1 hour, and the results were analysed using R.

Filter plate assay using 384-well plate format to monitor lectin binding by gal-AuNPs

To the wells of a 384-well plate, 100 μl of TBT was added for 1 hour at room temperature, to block the wells. Gal-AuNPs were resuspended in TB to 2.5 nM. The TBT from the wells was removed, and gal-AuNPs were added to the wells (50 μl). Concentrated solutions of lectin (LecA or ConA) were prepared in TBS. To the AuNP suspensions, 8 μl of concentrated lectin solutions were added for 1 hour. To a 384-well filter plate, 100 μl of TBT was added and filtered under vacuum. The AuNP-lectin solutions were then added to the washed filter plate wells, and filtered under vacuum. The wells were washed once with TBT, and imaged using a phone camera.

Filter plate assay using 384-well plate format to monitor bacterial binding by functionalised AuNPs

For *E. coli* binding studies, overnight bacterial cultures were grown to stationary phase (4 h) in LB at 37ºC, whilst shaking at 200 rpm. For *P. aeruginosa* binding studies, cultures were grown for 16 h in LB at 37ºC, whilst shaking at 200 rpm. The bacterial cultures were centrifuged at 4,000 g for 10 min and supernatant removed. The cultures were resuspended in TB and centrifuged at $4,000 \, g$ for 10 min, and repeated a further two times. A serial dilution of bacterial culture was performed in TBS, to provide different cell densities. Functionalised AuNPs were diluted in TB (2.5 nM). To Eppendorf tubes, 50 µl of AuNP suspension was added, followed by 8 ul of bacterial solution, and left for 1 hour at room temperature. To a 384-well filter plate, 100 µl TBT was added to the wells of the plate and filtered through the wells by applying vacuum. To the washed wells, the AuNP-bacterial solution was added and filtered through the wells by applying vacuum. The wells were washed once with TBT. The plate was imaged using a phone camera.

2.5 Developing targeted photodynamic therapy of breast cancer cells

2.5.1 Human cell line culture

All cell culture was performed under sterile conditions. There were three cell lines used in these studies, two breast cancer cell lines: MDA-MB-231 and SK-BR-3, and one non-cancer cell line: MCF-10A. The cancer cell lines were cultured in DMEM(+), and the MCF-10A cell line was cultured in MEGM. All reagents were heated to 37ºC before addition to the cells.

Starting new cell cultures

Vials of the three cell lines were removed from storage in liquid nitrogen. The cells were thawed at room temperature. To the thawed cells, 1 ml of media was added, and using a pipette, the cells were gently mixed to ensure dispersion in to the media. The cells were then transferred to 75 cm^2 Nunc Easy flasks, and a further 10 ml of media was added to make a total volume of 12 ml. All the flasks were then incubated at 37°C, 5% CO_2 atmosphere. After 24 h, the media was removed and replenished with 12 ml of fresh media to remove any residual DMSO from the freezing medium.

Subculturing

The cells were subcultured every five days. The cell culture media was discarded and washed with 5 ml of PBS. Next, 5 ml of 0.25% trypsin EDTA was added to the flasks and incubated at 37°C for 5 min. The flasks were tapped, to dislodge the cells. To quench the trypsin, 5 ml of DMEM(+) was added to the flasks containing the cancer cell lines. For the MCF-10A cell line, 5 ml of soybean trypsin inhibitor solution (1 mg ml^{-1}, in PBS) was added to quench the trypsin. The solutions were added to a 15 ml falcon tube and centrifuged at 800 rcf for 5 min (MDA-MB-231, SK-BR-3), or 130 rcf for 7 min (MCF-10A). The cultures were resuspended in 10 ml of media. The cultures were then diluted 1: 4 in media and transferred into fresh culture flasks, and incubated at 37°C at 5% CO_2.

Making new cell stocks for long-term storage

To make new frozen stocks of each cell line, the same method was applied as described above in Section 2.5.1. However, after centrifugation of the cells, the cells were resuspended in freezing medium and aliquoted in to 1.8 ml Nunc cryotubes. A cryogen freezing container was prepared by filling with isopropanol, before the tubes were added to the container. The container was

placed at -80°C overnight, before being transferred to liquid nitrogen for long-term storage.

Cell counting

To count the cells, a Neubauer haemocytometer was cleaned with ethanol, and coverslip held in place with attached clips. To the haemocytometer, 10 μl of cell culture was added, and placed under a microscope, where gridlines can be seen. There were four sets of 4 x 4 squares, where the number of cells within these areas were counted. The number was then averaged, and multiplied by 10^4, to provide a concentration of cells per ml. The cell cultures were diluted in media to provide the desired cell concentration.

2.5.2   Confocal microscopy studies

Biotinylated-polyacrylamide-glycan binding to cell lines

The biotinylated-polyacrylamide-glycan (PAA-glycan) probes used were PAA-gal, PAA-glc, PAA-lac, PAA-man, and PAA without glycan as a control. Cells were cultured as described in Section 2.5.1. However, after centrifugation the cells were resuspended in either DMEM(-) (cancer cell lines) or MEGM (MCF-10A). The cells were counted and diluted to a working concentration of 1×10^4 cells ml^{-1}. To Nunc 6-well multidishes, an 18 mm diameter glass coverslip was placed in each well. To each well, 2 ml of cell culture was added, and incubated for 24 h at 37°C at 5% CO_2. The culture media was discarded, and washed with 3 ml of PBS, twice. A 40 μg ml^{-1} of each PAA-glycan was prepared in either DMEM(-) (MDA-MB-231 or SK-BR-3) or MEGM (MCF-10A), and 1 ml per well was added. The cells were incubated for 1 hour at 37°C 5% CO_2. The media was then discarded and washed twice with 3 ml of PBS. Then, Alexa Fluor 488 labelled streptavidin (AF488-st, 10 μg ml^{-1}) was added to each well for 30 min, at 37°C 5% CO_2. The wells were then washed twice with 3 ml of PBS. Finally, 1 ml of 0.83 μg ml^{-1} of BioTracker Orange dye was added to the cells and incubated

for 30 min at 37°C, 5% CO_2. The wells were then washed with PBS, three times, and resuspended in 1 ml of DMEM(+) or MEGM.

For confocal microscopy imaging, the coverslips were held in place with a Ludin chamber. The cover slip was washed three times with imaging medium (1 ml), and 1 ml of imaging medium was added to the cover slip for imaging. A heating stage was used to hold the Ludin chamber in the confocal microscope, and heated to 37°C. The AF488-st was excited with 488 nm argon-ion laser (emission collected from 505-530 nm), and the Biotracker Orange dye was excited with 514 nm argon-ion laser (emission wavelengths 550 nm<). Differential interference contrast (DIC) images were collected alongside the fluorescence imaging. Controls were PAA (no glycan), just cells (no dyes), and cells with just AF488-st (no PAA-glycan), to assess non-selective binding and any autofluorescence by the cells.

Glycan-/ce6-AuNP binding to cell lines

Following the same preparation as Section 2.5.2, the cells were seeded onto cover slips in Nunc 6-well multidishes as 1 x 10^4 cells ml^{-1}. After washing with PBS, glycan-/ce6-AuNPs (gal-, man- or PEG$_3$-) were added to the wells at a ce6 solution concentration of 50 nM, in DMEM(-) or MEGM. The cells were incubated for 3 h at 37°C at 5% CO^2. The cells were washed three times with PBS, and 0.83 µg ml^{-1} (in DMEM(+) or MEGM) of BioTracker Orange dye was added to each well, and incubated for 30 min at 37°C at 5% CO_2. The cells were washed with 3 ml of PBS, three times, and resuspended in DMEM(+) or MEGM. The cells were imaged following the same method outlined in Section 2.5.2.

Inhibiting gal-/ce6-AuNP interaction with cancer cell lines

Inhibitors of SGLT (Canagliflozin), galectins (33DFTG) and GLUT (WZB117) receptors were used in these studies, at a concentration of 50 µM, and prepared in

DMEM(-) or MEGM. Gal-/ce6-AuNPs were used at ce6 solution concentration of 50 nM, prepared in DMEM(-) or MEGM. Canagliflozin and WZB117 were purchased from Sigma, and 33DFTG was purchased from Generon Ltd.

The cells were seeded as described in Section 2.5.2. For these studies, only the cancer cell lines were used. The cells were washed with PBS, three times. To each well 1 ml of inhibitor solution was added, and incubated for 1 hour at 37ºC at 5% CO_2. The cells were washed with 3 ml of PBS, three times. Then following the same method as Section 2.5.2, the galactose-/ce6-AuNPs were added and imaged using confocal microscopy.

2.5.3 Singlet oxygen studies

The singlet oxygen studies followed the method outlined in Garcia-Calavia[12].

To a quartz cuvette, 1 ml of either gal-/ce6-AuNPs, man-/ce6-AuNPs, PEG_3-/ce6-AuNPs or gal-AuNPs were added. The particles were diluted to provide ce6 concentration at 300 nM. The fluorescence was measured using a fluorimeter, with excitation wavelength at 360 nm and emission wavelengths between 380-600 nm. A stock solution of ABMA was prepared in methanol (0.512 mM). To the AuNP solution, 2 ul of ABMA was added to provide a final concentration of 1 μM. The fluorescence was measured immediately. The solution was then irradiated with a 633 nm He/Ne LASER. The fluorescence was measured every 5 min for 30 min. The fluorescence at 433 nm was plotted against time to assess singlet oxygen production, in R. The experiment was repeated but without irradiation.

2.5.4 Photodynamic therapy studies

The photodynamic therapy studies are adapted from the method outlined in Garcia-Calavia[12].

All the cell lines were cultured as detailed in Section 2.5.2. The cells were seeded in to two, white-bottom Nunc Nunclon™ Surface 96-well microplates at

a concentration of 1×10^4 cells ml^{-1}, with 100 μl culture per well. The two plates were incubated at 37°C at 5% CO_2 for 24 h. The wells were then washed three times with 200 μl PBS. Different concentrations of gal-/ce6-AuNP suspensions were prepared in DMEM(-) or MEGM, and added to the cells (50 μl). The plates were incubated for 3 h at 37°C at 5% CO_2. The media was then discarded and washed three times with 200 μl PBS. DMEM(+) or MEGM was then added to the wells (100 μl).

Both plates were kept at room temperature, with one of the plates taken forward for irradiation whilst the other was kept in the dark (non-irradiated). For irradiation, a 633 nm 10 mW HeNe laser, that had a biconvex diverging lens, was held 50 cm above the plate, and each well was irradiated for 6 mins. This provided a total light dose of 10.5 J cm^{-2}, and an irradiance of 29 mW cm^{-2}.

After irradiation, both plates were placed back into the incubator for 48 h. To measure cell viability, the CellTitre Blue Cell Viability assay kit was used. To each well 20 μl of reagent was added, to both the irradiated and non-irradiated plate. The plates were shaken at 200 rpm for 10 s, before being incubated for 4 h at 37°C at 5% CO_2. The plates were then shaken for 10 s at 200 rpm, and then fluorescence was measured using a plate reader, with excitation at 561 nm and emission at 594 nm.

References

[1] A. Rudin and P. Choi, *The Elements of Polymer Science and Engineering*, 3rd ed. 2013, ch. 6, ISBN: 9780123821782. DOI: 10.1016/C2009-1-64286-6.

[2] P. M. Carvalho, M. R. Felício, N. C. Santos, S. Gonçalves, and M. M. Domingues, *Application of light scattering techniques to nanoparticle characterization and development*, 2018. DOI: 10.3389/fchem.2018.00237.

[3] J. Stetefeld, S. A. McKenna, and T. R. Patel, *Dynamic light scattering: a practical guide and applications in biomedical sciences*, 2016. DOI: 10.1007/s12551-016-0218-6.

[4] J. K. Armstrong, R. B. Wenby, H. J. Meiselman, and T. C. Fisher, "The hydrodynamic radii of macromolecules and their effect on red blood cell aggregation," *Biophysical Journal*, 2004. DOI: 10.1529/biophysj.104.047746.

[5] O. Otman, P. Boullanger, D. Lafont, and T. Hamaide, "New amphiphilic glycopolymers based on a polycaprolactone-maleic anhydride copolymer backbone: characterization by 15 N NMR and application to colloidal stabilization of nanoparticles.," *Macromolecular chemistry and physics*, vol. 209, pp. 2410–2422, 2008. DOI: 10.1002/macp.200800300.

[6] L. N. Goswami, Z. H. Houston, S. J. Sarma, S. S. Jalisatgi, and M. F. Hawthorne, "Efficient synthesis of diverse heterobifunctionalized clickable oligo(ethylene glycol) linkers: Potential applications in bioconju-

gation and targeted drug delivery," *Organic and Biomolecular Chemistry*, vol. 11, no. 7, pp. 1116–1126, 2013. DOI: `10.1039/c2ob26968f`.

[7] S. Dedola, "'Click chemistry' to synthesise potential glycosidase inhibitors," PhD thesis, 2009.

[8] I. Carvalho, P. Andrade, V. L. Campo, P. M. M. Guedes, R. Sesti-Costa, J. S. Silva, S. Schenkman, S. Dedola, L. Hill, M. Rejzek, S. A. Nepogodiev, and R. A. Field, "'Click chemistry' synthesis of a library of 1,2,3-triazole-substituted galactose derivatives and their evaluation against Trypanosoma cruzi and its cell surface trans-sialidase," *Bioorganic & Medicinal Chemistry*, vol. 18, pp. 2412–2427, 2010. DOI: `10.1016/j.bmc.2010.02.053`.

[9] J. Turkevich, P. C. Stevenson, and J. Hillier, "A study of the nucleation and growth processes in the synthesis of colloidal gold," *Discussions of the Faraday Society*, vol. 11, no. 0, p. 55, 1951. DOI: `10.1039/df9511100055`.

[10] J. Hassinen, V. Liljeström, M. A. Kostiainen, and R. H. A. Ras, "Rapid Cationization of Gold Nanoparticles by Two-Step Phase Transfer," *Angewandte Chemie International Edition*, vol. 54, no. 27, pp. 7990–7993, 2015. DOI: `10.1002/anie.201503655`.

[11] M. J. Marín, A. Rashid, M. Rejzek, S. Fairhurst, S. Wharton, S. Martin, J. McCauley, T. Wileman, R. Field, and D. Russell, "Glyconanoparticles for the plasmonic detection and discrimination between human and avian influenza virus.," *Organic & Biomolecular Chemistry*, vol. 11, pp. 7101–7107, 2013. DOI: `10.1039/c3ob41703d`.

[12] P. G. Calavia, "Nanoparticles for the selective delivery of photosensitisers for photodynamic cancer therapy," Tech. Rep., 2016.

Chapter 3

Preparation and characterisation of glycan ligands and functionalised gold nanoparticles

The following chapter illustrates the synthesis and characterisation for the materials used throughout this PhD research, which relies on glycoAuNPs for cell targeting and PDT-induced cell killing. For AuNP functionalisation, ligands were either synthesised by copper catalysed 'click chemistry' and loaded onto the AuNP surface through ligand displacement; or by direct conjugation to the AuNP surface, through EDC coupling.

3.1 Introduction

3.1.1 AuNPs

The experiments carried out in this thesis rely on ligand-functionalised 16 nm AuNPs. The AuNP surface can be modified with multiple types of ligand, making them a good candidate from a targeted drug delivery standpoint, as both targeting and eradication elements can be combined onto the surface[1]. AuNPs also have unique optical and electrical properties, compared to the bulk

material[2]. Their properties are affected by size and shape of the particles, which means ligand modified AuNPs can be used to detect binding interactions[3][4][5], and is a property exploited throughout this PhD research.

Optical properties of AuNPs

The optical properties of AuNPs is owed to the phenomenon of 'surface plasmon resonance' (SPR). As described in Huang *et al.*[6], upon interaction with an oscillating electric field of incident light, the free electrons of the AuNP can collectively oscillate. The surface oscillation of the free electrons creates a separation of charge (see Figure 3.1) between the negatively charged electrons and the positively charged lattice, resulting in a dipole oscillation in the direction of the electromagnetic field.
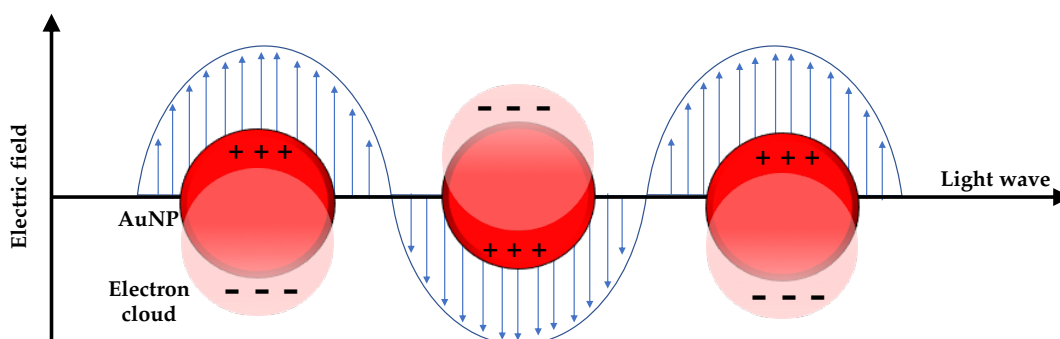
Figure 3.1: Surface plasmon resonance of AuNPs.

The SPR band is the wavelength at which maximum oscillation is obtained, creating a strong absorption of light [6]. The electron density on the surface dictates the SPR band, and so any factors that affect this electron density affect the SPR band. As a result, there is a red-shift in SPR band as AuNP size increases. Other factors that affect the SPR band are the particle shape, pH, surface chemistry, and how close the AuNPs come in proximity to one another[7]. Consequently, the SPR band can be used to characterise AuNP size and surface functionalisation, and to monitor AuNP interactions.

Functionalisation of AuNPs

The AuNPs used in this PhD research were synthesised by reducing hydrogen tetrachloroaurate with sodium citrate, a method developed by Turkevich *et al.*[8]. The product is AuNPs stabilised with citrate (citrate-AuNPs) through electrostatic interaction. The citrate-AuNPs have low stability in ionic solutions, and irreversibly aggregate. Aggregation with increasing ionic strength is largely explained by the Derjaguin-Landau-Verwey-Overbeak theory (DLVO)[9][10], where particle interaction is determined by the sum of attractive van der Waals interactions, and opposing repulsive electrostatic double layer (EDL) forces[11]. With increasing ionic strength of a solution, the EDL is compressed and neutralised, and so particles aggregate through attractive van der Waals interactions[1]. Consequently, when using ligand functionalised AuNPs in a biological setting, a ligand should be selected that aids stability.

Ligand design for surface functionalisation of AuNPs

The surface of AuNPs may be functionalised through covalent and ionic bonding, or physical adsorbtion (Figure 3.2)[12]. Consequently, a wide range of molecules can be used to functionalise the AuNPs, including antibodies, peptides, DNA, glycans, proteins, charged molecules, amine and thiol derivatives[13][14].
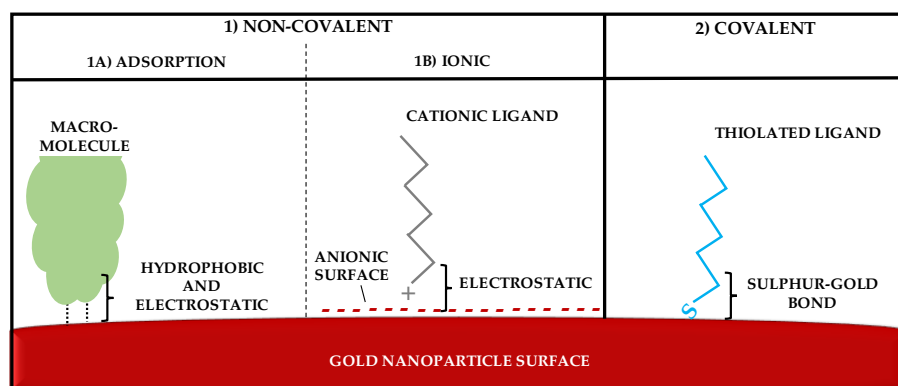
Figure 3.2: Illustration of non-covalent (1A and 1B) and covalent (2) surface interactions with AuNPs.

During AuNP synthesis, the particles are stabilised with a ligand, such as negatively charged citrate ions. Citrate-gold interactions are weak (~2 kcal mol^{-1}), and so the stabilising citrate ligands can then be displaced by other ligands, that form stronger interactions with the gold surface[15]. Thiolated ligands are often selected for modifying AuNPs (Figure 3.3), as they form strong bonds (40-50 kcal mol^{-1}) with the gold surface (sulfur-gold bond)[16]. Displacement with thiolated ligands creates much more stable particles, that can withstand harsher conditions[17].

1) Citrate-AuNPs

2) Glycan-AuNPs

Thiolated glycan ligand

AuNP surface
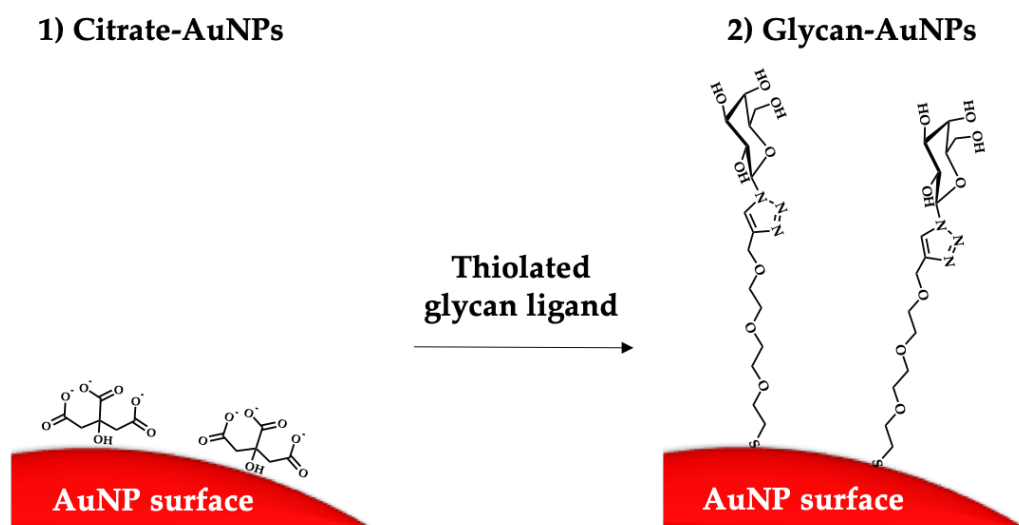
AuNP surface

Figure 3.3: Functionalisation of AuNPs with thiolated glycan ligand. Citrate-AuNPs (1) are mixed with thiolated glycan ligand, which displaces the citrate on the AuNP surface to form strong sulfur-gold bonds (2).

Further steric stability can be provided by introducing poly(ethylene glycol) (PEG) components to the ligand[18]. PEG presence on the AuNP surface has been demonstrated to improve bioavailability, as it forms a hydrated barrier that sterically inhibits opsonisation and clearance from the blood [19]. Consequently, in this PhD research, the ligands that were synthesised for AuNP functionalisation were tethered by a short PEGylated thiol, providing anti-fouling properties by reducing protein adsorption onto the AuNP surface[1].

Characterisation of AuNPs

In this PhD research, 16 nm AuNPs were used as a scaffold for glycan and PS ligands. The size of AuNPs can be determined using dynamic light scattering (DLS) and transmission electron microscopy (TEM)[20]. DLS relies on light scattering by AuNPs in solution, and so determines the hydrodynamic size; whereas TEM uses dried AuNP samples for analysis. This can often result in small differences in recorded AuNP size, with DLS recording a slightly elevated number[21].

As mentioned in Section 3.1.1, 16 nm AuNPs have unique optical and electrical properties, where the AuNPs undergo colorimetric changes based on their size, surface chemistry and interactions. These colorimetric changes can be monitored by UV-Vis spectrometry, which allows UV-Vis to be a useful tool in characterising AuNPs. When functionalising AuNPs with thiolated ligand, small changes in the SPR band are observed, with a red-shift of a few nanometres. The sulphur-gold bond reduces the density of free electrons on the particle surface, which alters the plasma frequency and results in a red-shift in the SPR band[22]. With AuNP binding interactions, the changes observed in the SPR band can vary between analytes. Common effects include red-shifts; broadening and distortion of the extinction spectrum; and reduction in extinction at the extinction maximum, from particle precipitation[23][24][25].

3.1.2   Ligand conjugation methods

Two methods used for ligand synthesis were explored, namely Cu(I)-catalysed Huisgen azide-alkyne 1,3-dipolar cycloaddition (CuAAC)[26], and EDC coupling[27].

CuAAC 'click chemistry'

The CuAAC reaction is a type of click chemistry[28], which is defined as reactions that are high yielding; stereoselective; wide scope; modular; and by-

products that can be removed by non-chromatographic methods. The reaction and purification must also be simple, where the reagents are readily available; performed in water, or solvent that is easy to remove; and non-chromatographic purification method; with stable products[28]. The CuAAC reaction generates 1,2,3-triazoles, as can be seen in Figure 3.4.
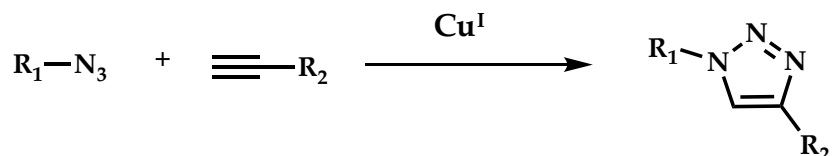
Figure 3.4: CuAAC reaction generating 1,2,3-triazoles.

The versatility of the reaction, along with its ability to be performed in water, has resulted in its wide-spread use in glycoconjugation, including oligosaccharides, macrocycles, glycoclusters and glycopeptides[29]. The relative ease of generating the azido and alkyne starting reagents, also caters for this versatility. For these studies, the CuAAC reaction was used to conjugate azido-based glycans to an alkyne-based PEGylated thiol for AuNP functionalisation, and to generate a galactose-based lectin inhibitor.

CuAAC has been employed to directly functionalise glycans onto the surface of AuNPs, where alkyne modified AuNPs were 'clicked' to azido sialic acid[30] or GlcNAc[31] derivatives. However, the drawbacks of this methodology was that the particles can aggregate and precipitate out of solution due to the copper sulphate and sodium ascorbate salts, with low conversion[31]. It can also be more difficult to characterise the ligands synthesised on the particle surface, compared to in solution. Preparation in solution may also improve reproducibility, as pure ligand can be characterised and weighed out, so the same amount of ligand can be added for AuNP modification each time. Consequently, the CuAAC reaction was performed in solution to generate glycan ligands, and then purified before addition to AuNPs for citrate displacement, an approach that has been documented[24][32][33].

EDC conjugation

N-(3-Dimethylaminopropyl)-*N'*-ethylcarbodiimide (EDC) is a 'zero-length cross-linker', where the conjugation of two compounds does not add any additional atoms from the crosslinker [34]. EDC is used to conjugate primary amines to carboxylated reagents, forming an amide bond (see Figure 3.5). The conjugation reaction is water soluble and does not produce hazardous by-products. It is traditionally the most commonly used bioconjugation technique. *N*-hydroxysuccinimide (NHS) is often employed to improve the efficiency of the coupling reaction. EDC conjugates NHS to the carboxylic acid, forming a more stable NHS ester intermediate compared to the o-acylisourea intermediate[35].

Figure 3.5: EDC conjugation generating an amide bond: 1) Less efficient EDC conjugation as o-acylisourea intermediate is less stable and can undergo hydrolysis; 2) more efficient EDC conjugation, through addition of NHS that generates a more stable NHS ester intermediate.

Direct ligand conjugation to the AuNPs can be achieved by functionalising AuNPs with an amino or carboxylate ligand, then coupling of a secondary ligand to the modified particles, with the aid of EDC and NHS, as seen in Figure 3.6.

Figure 3.6: Direct conjugation of AuNPs through EDC conjugation. The AuNPs were functionalised with glycan and carboxylated ligands (1) through displacement of citrate ligands. EDC and NHS were added to the glycan-/COOH-AuNPs to generate NHS-activated particles: glycan-/NHS-AuNPs (2). Finally, the ce6-NH$_2$ derivative is added to the particles to generate glycan-/ce6-AuNPs (3).

This approach of directly conjugating ligands to the AuNP surface through EDC coupling, has been used for attaching antibodies[27], peptides[36], lectins[37], fluorophores[38], enzymes[39] and aptamers[40]. Direct EDC conjugation was used in these studies to conjugate an amine based PS (ce6) to carboxyl functionalised AuNPs, which has been demonstrated elsewhere using gold nanomaterials[41][42][43].

3.2 Scientific aims

The aim of this chapter was to synthesise thiolated glycan ligands and glycan-based lectin inhibitor through CuAAC. Then prepare a series of functionalised AuNPs for bacterial and cancer cell targeting, and photodynamic therapy applications.

3.3 Results and discussion

3.3.1 Glycan ligand synthesis

Through CuAAC, a series of glycan ligands were prepared. The azido and alkyne reagents (Figure 3.7) used in the synthesis were prepared by other group members (Simone Dedola, Simona Chessa and Jordan Hindes), with the exception of alkyne **(2)**, which was sourced commercially (Sigma).

a)   b)

azide (1)   **azide (2)**

c)   d)
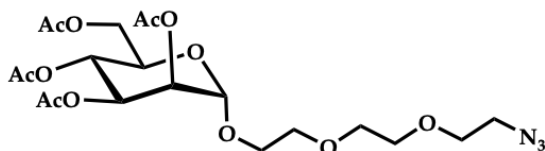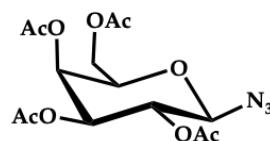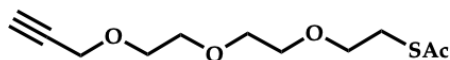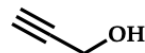
alkyne (1)   **alkyne (2)**

Figure 3.7: Structure of azide and alkyne reagents for glycan synthesis: a) azide (1), Ac-mannose-PEG$_3$-N$_3$; b) azide (2), Ac-galactose-N$_3$; c) alkyne (1), PEG$_3$-SAc; and d) alkyne (2), propargyl alcohol.

Synthesis of the glycan ligands were performed under standard CuAAC conditions, and deprotected by sodium methoxide[26][44]. Full experimental method is detailed in Chapter 2, and the final structures of the acetylated and deacetylated glycan products can be seen in Table 3.1.

Experimental detail of glycan synthesis can be found in Chapter 2.3.1, along with full characterisation of each novel compound. As the compounds **5** and **6** are known and full characterisation is documented elsewhere[44], confirmation of compound **6** synthesis was determined by NMR spectroscopy and high resolution electrospray ionisation mass spectrometry (HR ESI-MS).
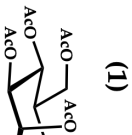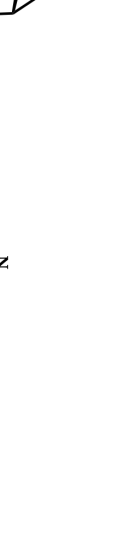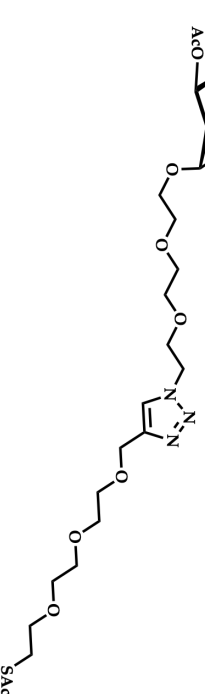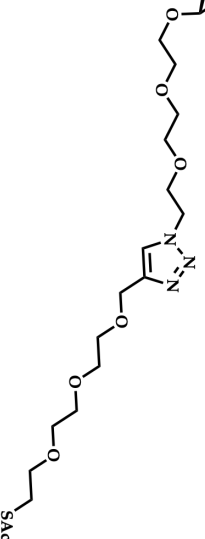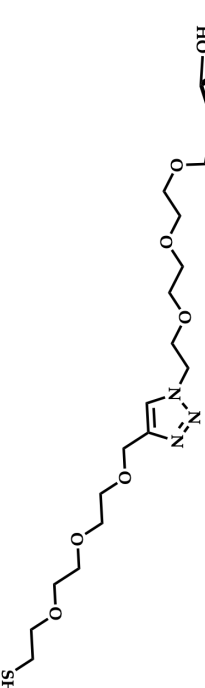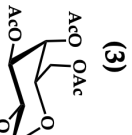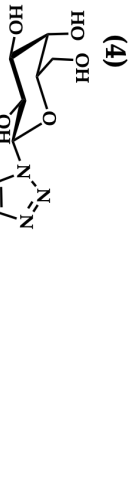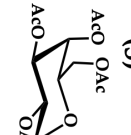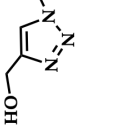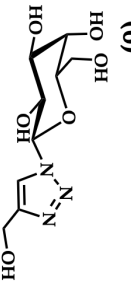
Glycan ligand synthesis by CuAAC was selected as a synthetic strategy, as it provided simple reagent preparation (installation of azido and alkyne functional groups). As summarised in in Table 3.1, the click reaction also provided relatively good yields (64-85%), and was a simple synthetic methodology, with straightforward purification.

For the galactose binding lectins targeted in this PhD research, hydrophobic structures at the anomeric position of the galactose derivatives are required to achieve high binding affinity, through CH-π interactions by aromatic amino acids in the CRD (discussed further in Chapter 4)[45]. Consequently, CuAAC provides further advantages when synthesising the galactose derivatives, as the click chemistry reaction generated hydrophobic 1,2,3-triazole derivatives at the anomeric position, as seen with products **4** and **6** (Table 3.1).

3.3.2 Synthesis of 16 nm citrate capped AuNPs

The 16 nm AuNPs were prepared following the method outlined in Chapter 2.3.2. The method resulted in citrate capped AuNPs (citrate-AuNPs). To characterise the citrate-AuNPs, UV-Vis, DLS and TEM were used. The UV-Vis extinction spectrum can be seen in Figure 3.8.

Table 3.1: Summary of glycan ligands synthesised by CuAAC in this PhD research.

Azide	Alkyl	Acetylated product	Yield / %	Deacetylated product
(1)	(1)	(1)	64	(2)
(2)	(1)	(3)	85	(4)
(2)	(2)	(5)	78	(6)

Figure 3.8: UV-Vis extinction spectrum (350-800 nm) of citrate-AuNPs.

The 16 nm AuNPs have a characteristic SPR band at ~520 nm, which can be seen from the spectrum in Figure 3.8, with the extinction maximum represented by the vertical black line. Note that extinction is used for AuNPs, as the spectrum is the combined effect of light absorption and scattering, by the particles[46].

Next, the size of the particles was assessed. Common techniques used to determine the size of AuNPs are dynamic light scattering (DLS) and transmission electron microscopy (TEM)[20]. Figure 3.9 shows the DLS and TEM data for the citrate-AuNPs.

a)

Mean size = 17 nm

b)

Mean size = 16.4 nm

100 nm
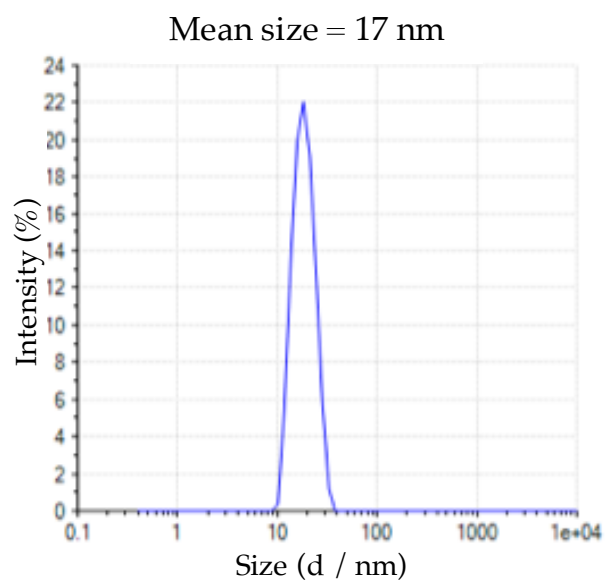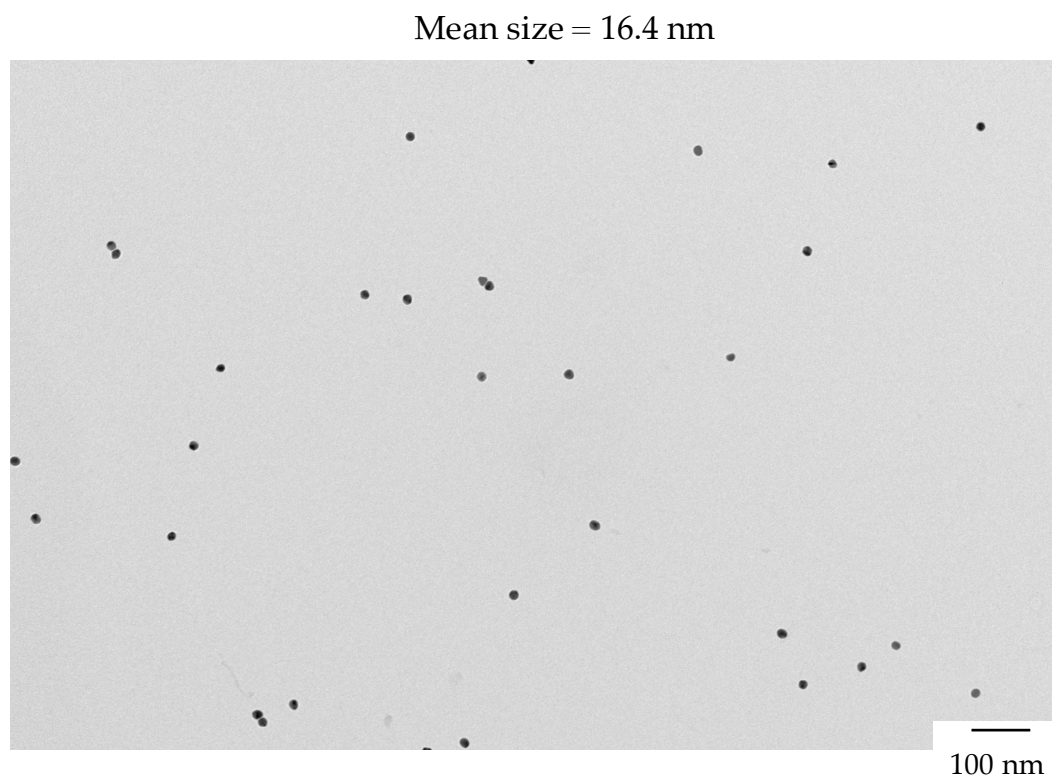
Figure 3.9: Size characterisation of citrate capped AuNPs by: a) DLS and b) TEM.

From Figure 3.9, the DLS provides an average size of 17 nm, with the TEM data showing a slightly lower average of 16.4 nm. It is common for there to be small differences between the recorded DLS and TEM size average, as DLS provides an average of the hydrodynamic diameter, so the particles are in solution; whereas TEM provides the size in dried form [47].

3.3.3   Ligand functionalised AuNPs

Once the citrate-AuNPs were characterised, they were subjected to functionalisation with different thiolated ligands for binding studies.

Galactose-PEG$_3$-AuNPs (gal-AuNPs)

The AuNPs were stabilised by citrate that associates with the surface through electrostatic interactions. As mentioned previously, thiolated compounds can displace the citrate on the surface, forming much stronger interactions with the gold surface. Consequently, all ligands used in the PhD studies had a thiol terminus for nanoparticle functionalisation. For all ligand functionalisation studies, the method is detailed in Chapter 2.3.3.

The galactose ligand (compound **4**), was used to functionalise the AuNPs (gal-AuNPs), and were used in Chapters 4 and 5 for lectin binding. To characterise the functionalised AuNPs, UV-Vis extinction and MALDI-TOF were used. The chemical interaction from ligand exchange, lowers the surface conductivity. Changes to the nanoparticle surface affects their interaction with light, which in turn, alters the SPR band[22]. With ligand functionalised AuNPs, small red-shifts of ~1-5 nm can be observed for smaller ligands, and so the extinction spectrum serves as a useful tool for characterising modified AuNPs.

The UV-Vis extinction spectra comparing citrate-AuNPs and gal-AuNPs can be seen in Figure 3.10. As can be seen from Figure 3.10, by comparing the extinction maxima of the citrate-AuNPs (black vertical line) and the gal-AuNPs (blue, dotted vertical line), the gal-AuNPs displayed a 2 nm red-shift, suggesting

successful functionalisation of the AuNPs with the galactose ligand.
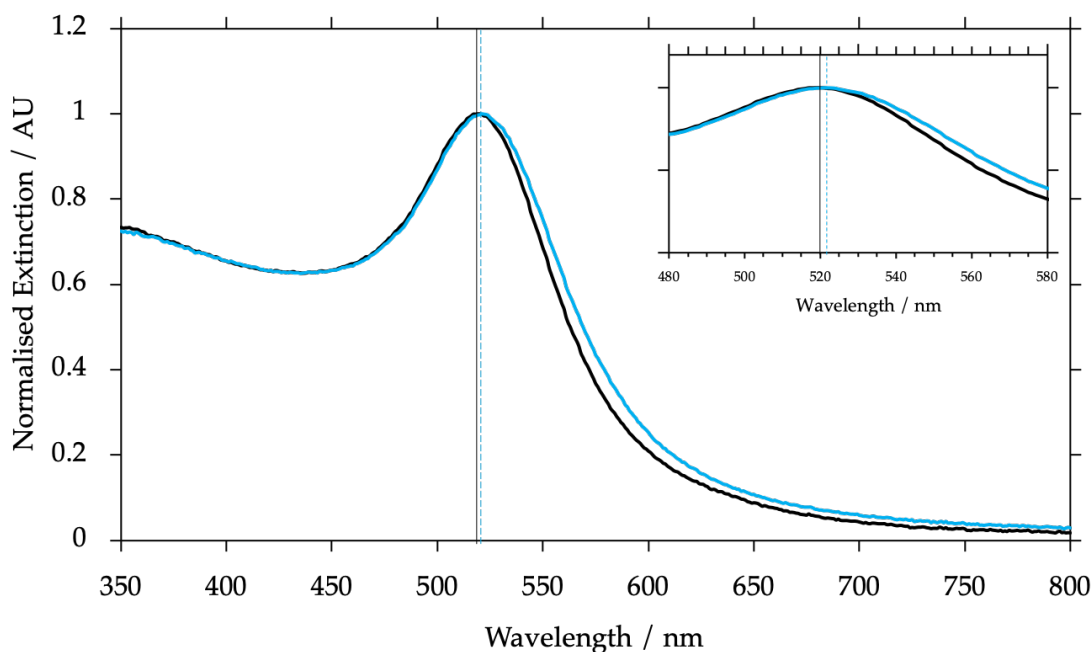
Figure 3.10: Extinction spectra of citrate-AuNPs (black line) and gal-AuNPs (blue line). Extinction maxima of the spectra are highlighted by vertical lines for citrate-AuNPs (black, solid line) and gal-AuNPs (blue, dotted line). Inset represent zoomed in region around extinction maxima.

Next, the presence of the ligand was confirmed using MALDI-TOF analysis (Figure 3.11). The ionisation of the ligand often results in both the thiol and disulfide compounds being detected. There is a lot of 'background' from the DHB matrix observed below 400 MW. Being able to detect the disulfide can often help characterisation if the thiolated ligand is difficult to distinguish from the DHB matrix. The mass of [galactose-PEG$_3$-SH$^+$Na]$^+$ (thiol) is 432, and the mass of [galactose-PEG$_3$-S-S-PEG$_3$-galactose$^+$Na]$^+$ (disulfide) is 839. As can be seen form Figure 3.11d, the galactose-PEG$_3$-SH ligand was detected in the purified gal-AuNP suspension.
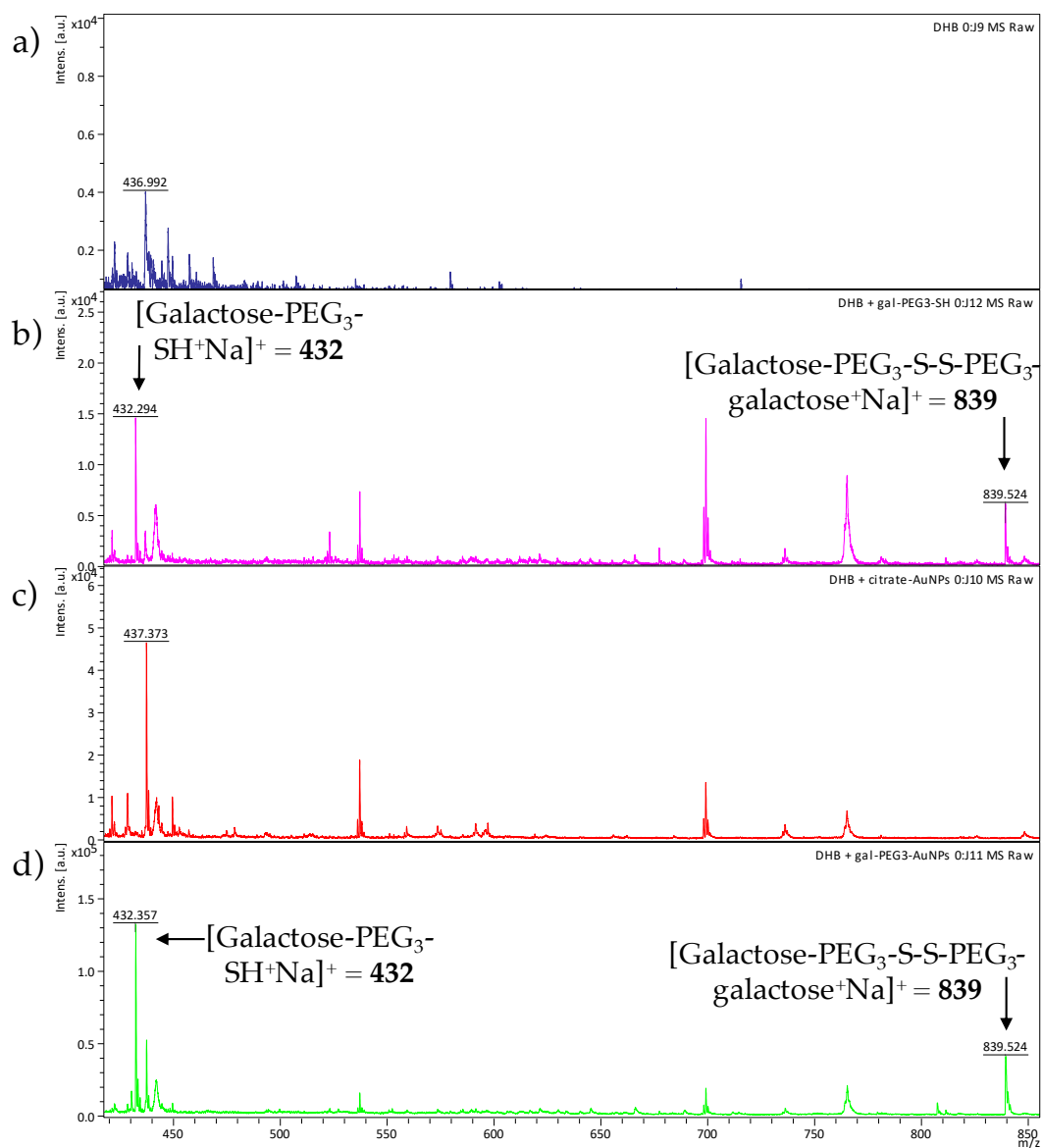
Figure 3.11: MALDI-TOF analysis of gal-AuNPs. a) DHB matrix; b) DHB matrix with gal-PEG$_3$-SH; c) DHB matrix with citrate-AuNPs; and d) DHB matrix with gal-AuNPs.

Hence, gal-AuNPs were shown to be successfully functionalised with the UV-Vis extinction spectrum showing a red-shift of the SPR peak of the gal-AuNPs compared to the citrate-AuNPs; and with the detection of the ligand by MALDI-TOF.

TMAC-AuNPs

For non-selective, electrostatic binding interactions to bacteria, positively charged AuNPs were synthesised. The positively charged AuNPs interact with negatively charged groups on the bacterial cell surface, such as phospholipids, lipopolysaccharides and teichoic acids [48]. For these studies, the commercially available ligand: TMAC (*N,N,N*-trimethyl-(11-mercaptoundecyl)ammonium chloride), was used. Introducing a positively charged ligand to the negatively charged citrate-AuNPs proved problematic at first, as the citrate-AuNPs aggregated upon addition of the TMAC ligand. Different approaches were taken, such as addition in different solutions (water, Tris buffer), addition with PEGylated ligand, and dropwise addition, but the citrate-AuNPs aggregated each time. Successful addition was found by employing the technique developed by Hassinen *et al.*[49], where a two-step phase transfer method was used (see Figure 3.12).
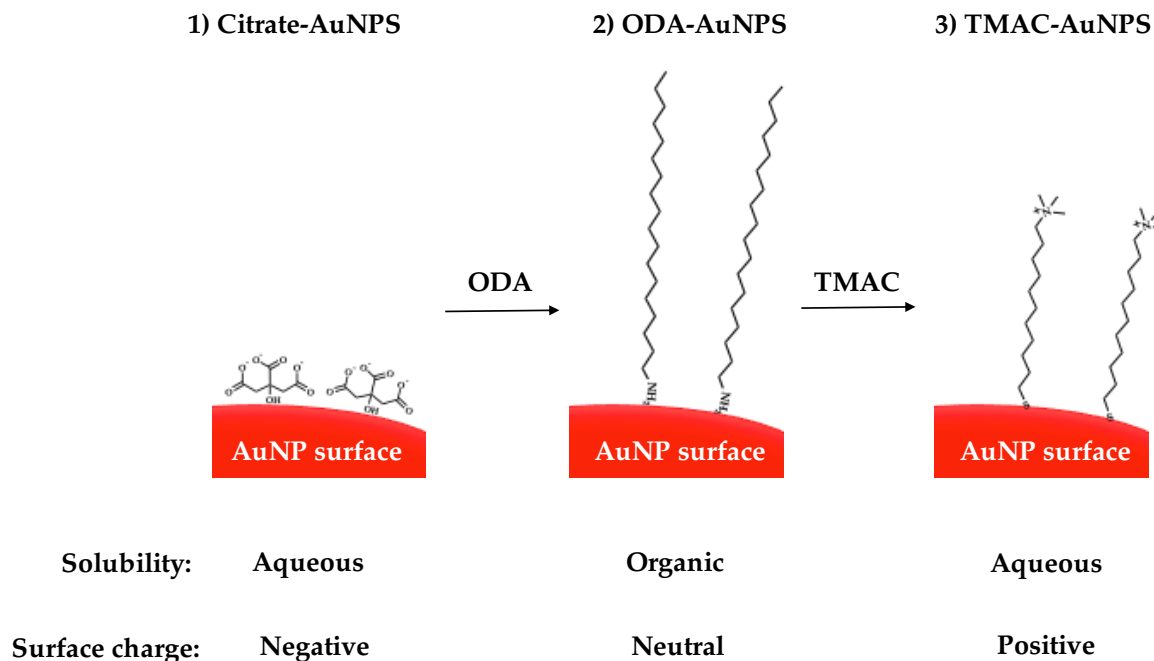
Figure 3.12: Two-step phase transfer method developed by Hassinen *et al.*[49]. ODA = octadecylamine; TMAC = *N,N,N*-trimethyl-(11-mercaptoundecyl)ammonium chloride.

As seen in Figure 3.12, in the two-step phase transfer method, a neutral charged ligand (octadecylamine, ODA) was used to displace the citrate on the citrate-AuNPs. The ODA-AuNPs were soluble in toluene, and so addition of toluene followed by shaking, resulted in ODA-AuNP transfer into the organic phase; any citrate-AuNPs remained in the aqueous phase and were discarded. The organic layer was transferred into a new tube, where water and cationic ligand were added. After shaking, the cationic-AuNPs were transferred into the aqueous phase. Acid addition (HCl) promoted protonation of the amine, and disassociation of any residual ODA from the AuNP surface. As well as relying on ligand solubility, the ligands also interacted with the AuNP surface to varying degrees. The electrostatic citrate interaction (2 kcal mol^{-1}) is weaker than the the amine-gold interaction (4 kcal mol^{-1})[50], which in turn, is weaker than the thiol-gold bond (40-50 kcal mol^{-1})[16].

In this PhD research, TMAC was used as the cationic ligand, and ODA was used as the transfer reagent. The purified, TMAC-AuNP extinction spectrum can be seen in Figure 3.13.
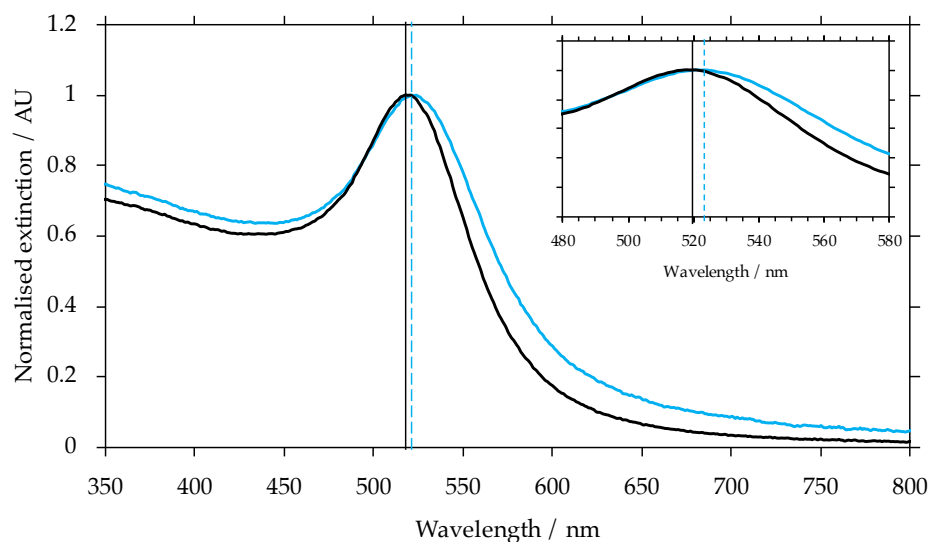
Figure 3.13: Normalised UV-Vis extinction spectra (350-800 nm) comparing citrate-AuNPs and TMAC functionalised AuNPs (TMAC-AuNPs). Extinction maxima of the spectra are highlighted by vertical lines for citrate-AuNPs (black, solid line) and TMAC-AuNPs (blue, dotted line). Inset represent zoomed in region around extinction maxima.

As can be seen from Figure 3.13, there was a red-shift of 4 nm in the extinction maximum of the AuNPs functionalised with TMAC, compared to the citrate-AuNPs. The red-shift demonstrated that the AuNPs were functionalised by citrate displacement with the thiolated TMAC ligand.

The TMAC-AuNPs were also assessed by MALDI-TOF analysis to determine the presence of TMAC (Figure 3.14). Figure 3.14c showed that the citrate was displaced by the ODA, as ODA was detected in the MALDI-TOF with the ODA-AuNPs suspension ($[ODA^+H]^+$ = 270, Figure 3.14e). The ODA-AuNPs were then subjected to ligand displacement by the thiolated TMAC ligand. TMAC loses chloride in the MALDI-TOF, and consequently the mass detected was 246 (Figure 3.14d). TMAC was detected in the TMAC-AuNP suspension, as seen in Figure 3.14f, with detection of the TMAC mass at 246. There was no ODA detected in the spectrum of the TMAC-AuNPs, suggesting the ODA was successfully displaced by the TMAC ligand.
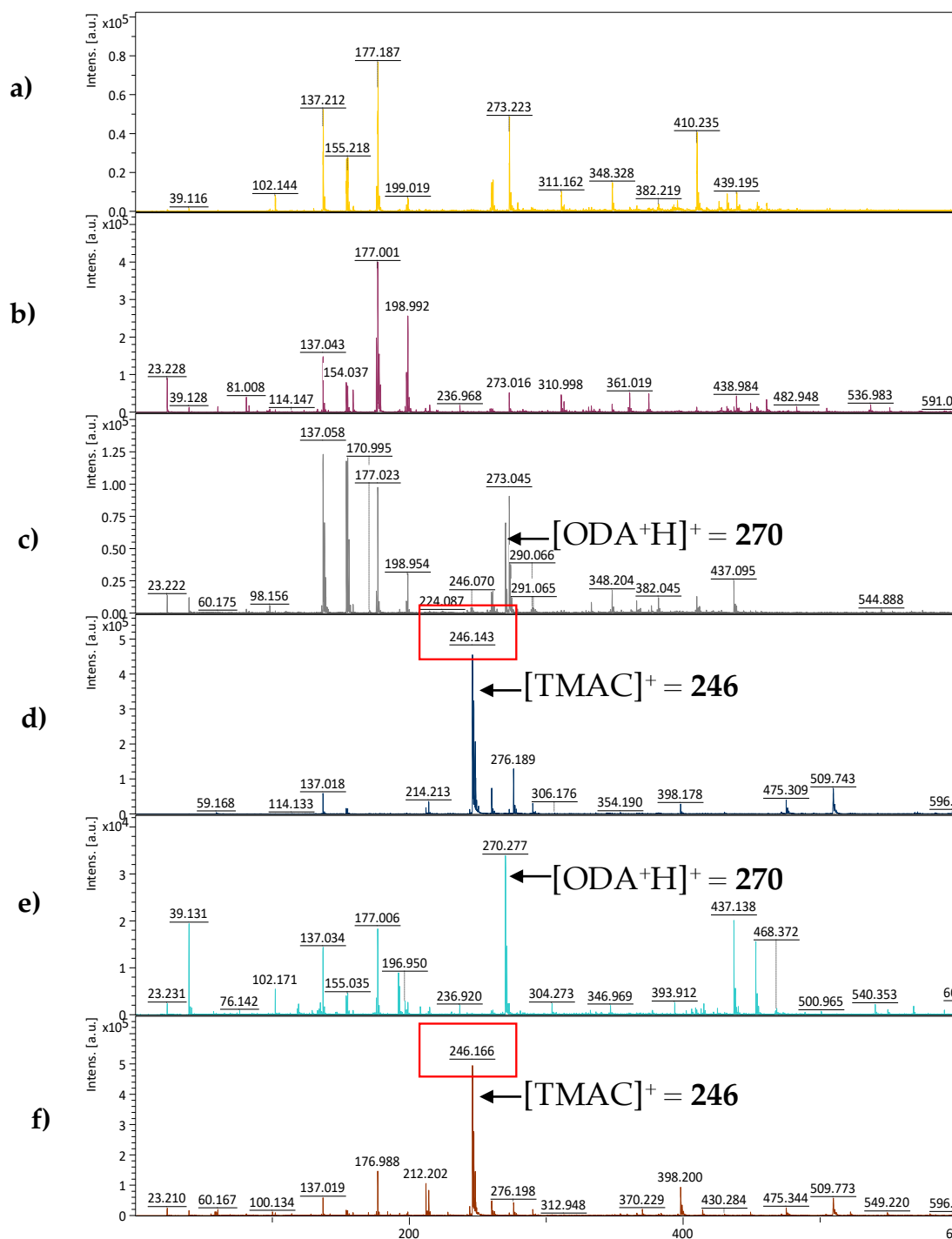
Figure 3.14: MALDI-TOF analysis of two-phase synthesis of TMAC-AuNPs, with a) DHB matrix; b) DHB matrix with AuNPs; c) DHB matrix with ODA-AuNPs; d) DHB matrix with TMAC; e) DHB matrix with ODA; and f) DHB matrix with TMAC-AuNPs.

The combined UV-Vis extinction spectrum of the TMAC-AuNPs, and the

111

MALDI-TOF data demonstrated successful functionalisation of the AuNPs with TMAC. The two-step phase transfer method consistently provided stable TMAC-AuNPs.

PEG$_3$-AuNPs

For the cationic TMAC-AuNP binding studies to *E. coli*, neutral charged AuNPs were prepared as control particles. For this, PEG$_3$-SH was used as the control ligand to functionalise the AuNPs (PEG$_3$-AuNPs), see Figure 3.15 for ligand structure.
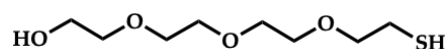
Figure 3.15: PEG$_3$-SH ligand structure for AuNP functionalisation.

After purification, the PEG$_3$-AuNPs were characterised by UV-Vis spectroscopy, which can be seen in Figure 3.16. From Figure 3.16, there was a red-shift of 3 nm for the extinction maxima of the PEG$_3$-AuNPs (blue line) compared to the citrate-AuNPs (black line), suggesting successful functionalisation of the AuNPs with PEG$_3$-SH.
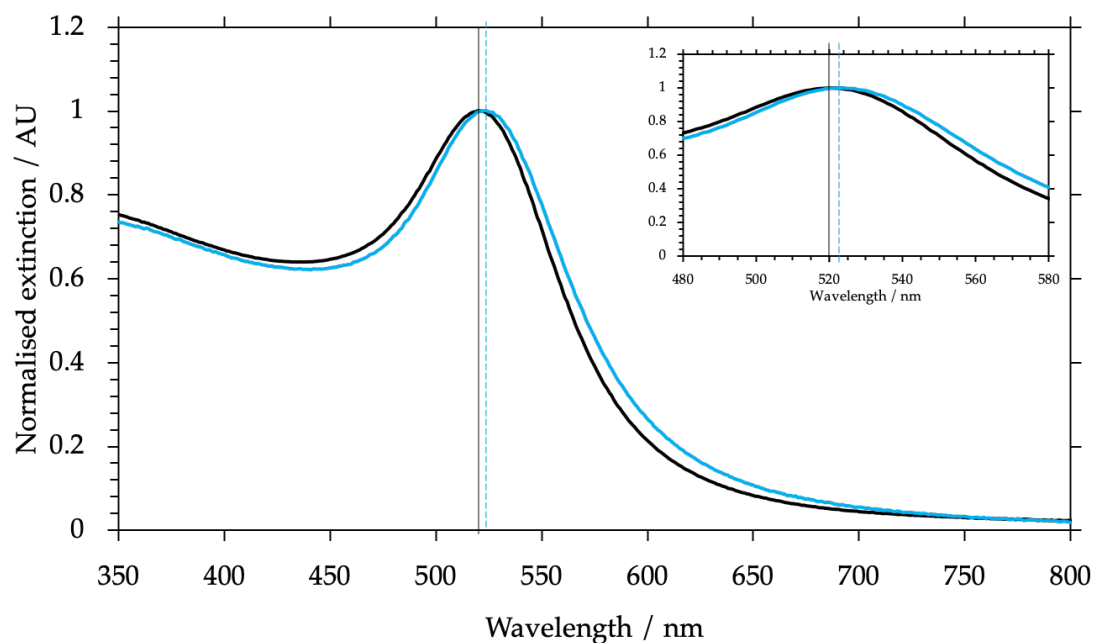
Figure 3.16: Normalised UV-Vis extinction spectra (350-800 nm) comparing citrate-AuNPs and PEG$_3$-AuNPs. Extinction maxima of the spectra are highlighted by vertical lines for citrate-AuNPs (black, solid line) and PEG$_3$-AuNPs (blue, dotted line). Inset represent zoomed in region around extinction maxima.

The PEG$_3$-AuNPs were then analysed by MALDI-TOF to assess ligand presence in the PEG$_3$-AuNP suspension. The results of the MALDI-TOF analysis can be seen in Figure 3.17, with [PEG$_3$-SH$^+$Na]$^+$ (233) detected in the PEG$_3$-AuNP suspension (3.17c).
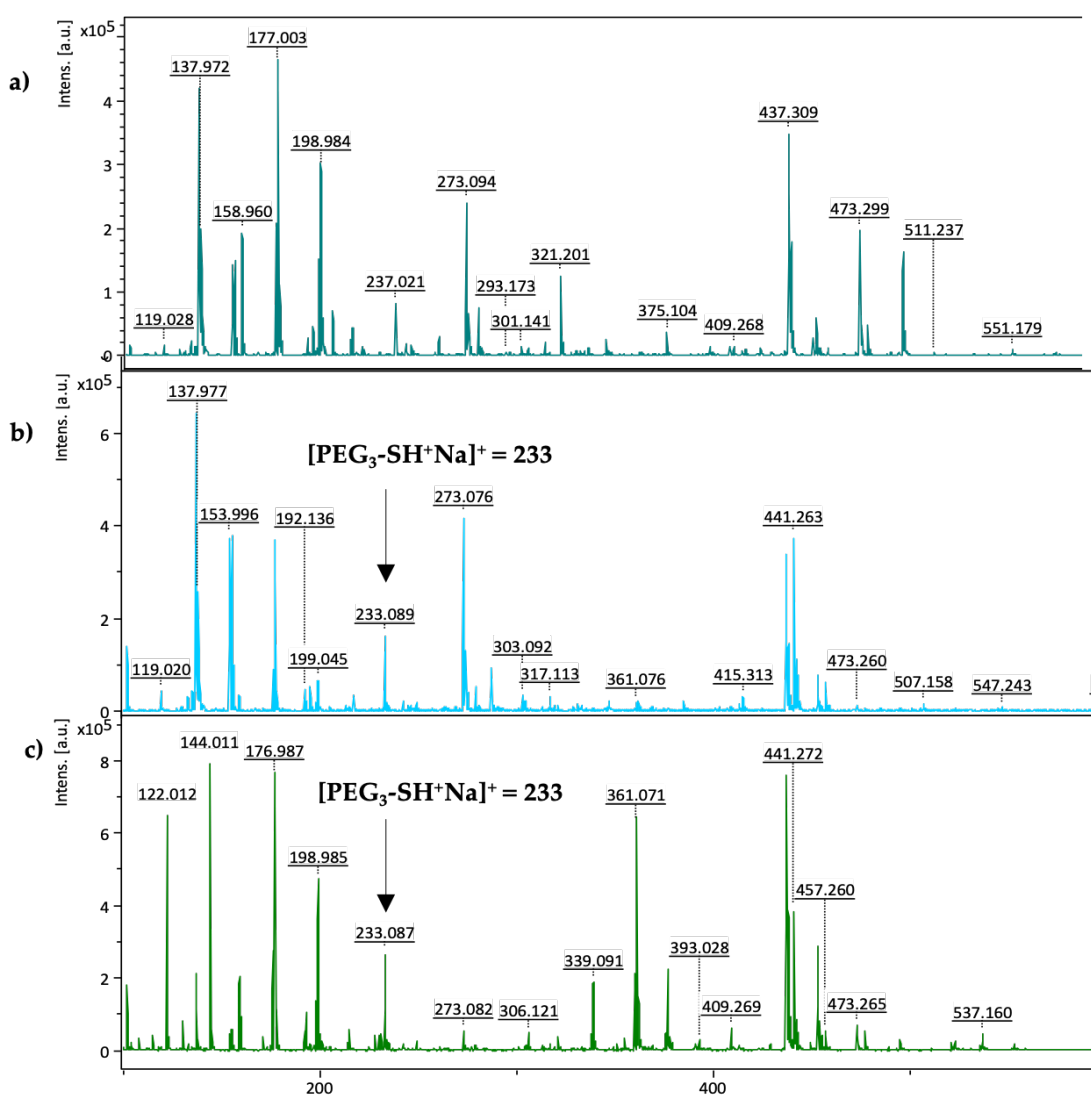
Figure 3.17: MALDI-TOF analysis of PEG$_3$-AuNPs. a) DHB matrix with AuNPs; b) DHB matrix with PEG$_3$-SH; and c) DHB matrix with PEG$_3$-AuNPs

Consequently, the red-shift in the UV-Vis extinction maxima of the PEG$_3$-AuNPs, and the detection of the PEG$_3$-SH ligand in the PEG$_3$-AuNP suspension by MALDI-TOF, suggested successful functionalisation of the AuNPs.

Glycan-/chlorin e6-PEG$_4$-AuNPs, 3: 1 (glycan-/ce6-AuNPs)

For the next set of AuNP functionalisation studies, heterogeneous surface functionalisation was needed, as both drug (PS) and targeting element (glycan) were

required on the AuNP surface for targeted photodynamic therapy studies. EDC coupling was used to conjugate the PS: chlorin e6 (ce6), to the particle surface, to generate glycan and ce6 functionalised AuNPs (glycan-/ce6-AuNPs). The ligands that were used in these studies are shown in Figure 5.12.
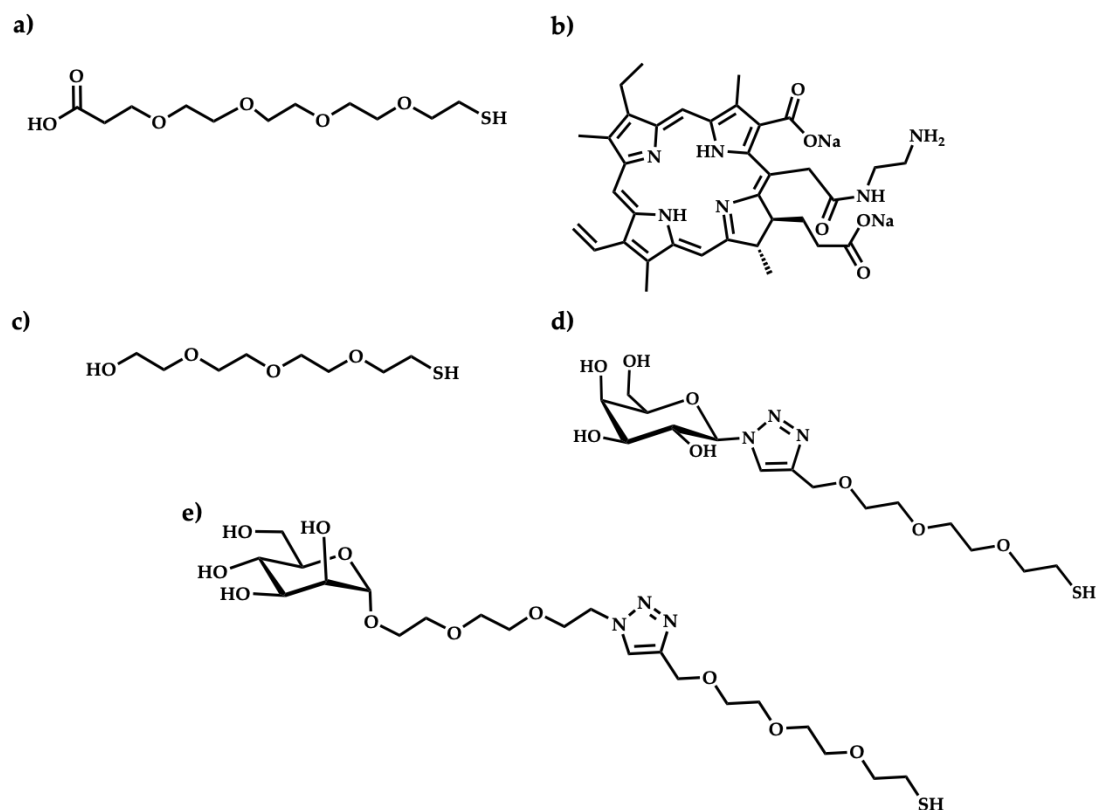
Figure 3.18: Ligands used in glycan-/ce6-AuNP functionalisation. a) COOH-PEG$_4$-SH; b) chlorin e6 amine derivative (ce6-NH$_2$); c) PEG$_3$-SH; d) galactose-PEG$_3$-SH; and e) mannose-PEG$_6$-SH.

To generate the glycan-/ce6-AuNPs, a mixture of glycan ligand and carboxyl PEGylated thiol (COOH-PEG$_4$-SH) (see Figure 5.12a) were added to the citrate-AuNPs, at a ratio of 3:1 for glycan:COOH-PEG$_4$-SH. The purified particles were then activated using EDC and NHS. An amine derivative of the ce6 (Figure 5.12b) was then added to the activated particles, which generated the glycan-/ce6-AuNPs, and summarised in Figure 3.19 (reproduced from Section 3.1.2).

1) Glycan-/COOH-AuNPS   **2) Glycan-/NHS-AuNPS**   **3) Glycan-/ce6-AuNPS**
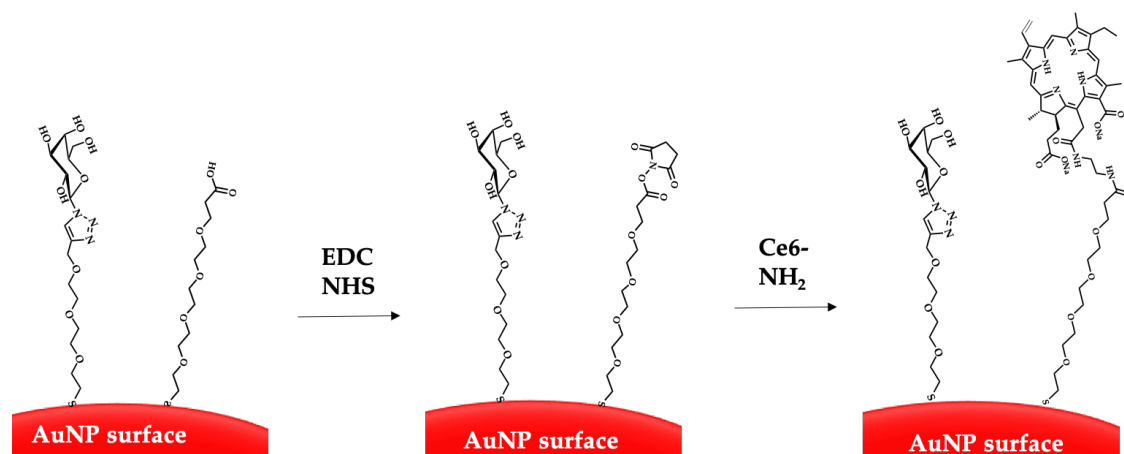
Figure 3.19: Direct conjugation of AuNPs through EDC conjugation (same as 3.6). The AuNPs were functionalised with glycan and carboxylated ligands (1) through displacement of citrate ligands. EDC and NHS were added to the glycan-/ce6-AuNPs to generate NHS-activated particles: glycan-/NHS-AuNPs (2). Finally, the ce6-NH$_2$ derivative is added to the particles to generate glycan-/ce6-AuNPs (3).

The structure of the ce6 derivative, after EDC conjugation, is shown in Figure 3.20.
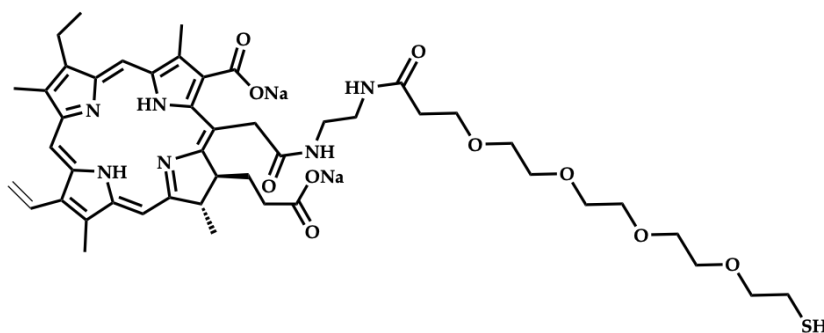
Figure 3.20: Structure of EDC conjugated ce6 derivative

Compounds **2** (mannose-PEG$_6$-SH) and **4** (galactose-PEG$_3$-SH) were the glycans used in these set of AuNP functionalisation studies. As a control for future studies, PEG$_3$-SH was also used (see Figure 5.12). The extinction spectra of the glycan-/ce6-AuNPs can be seen in Figure 3.21.
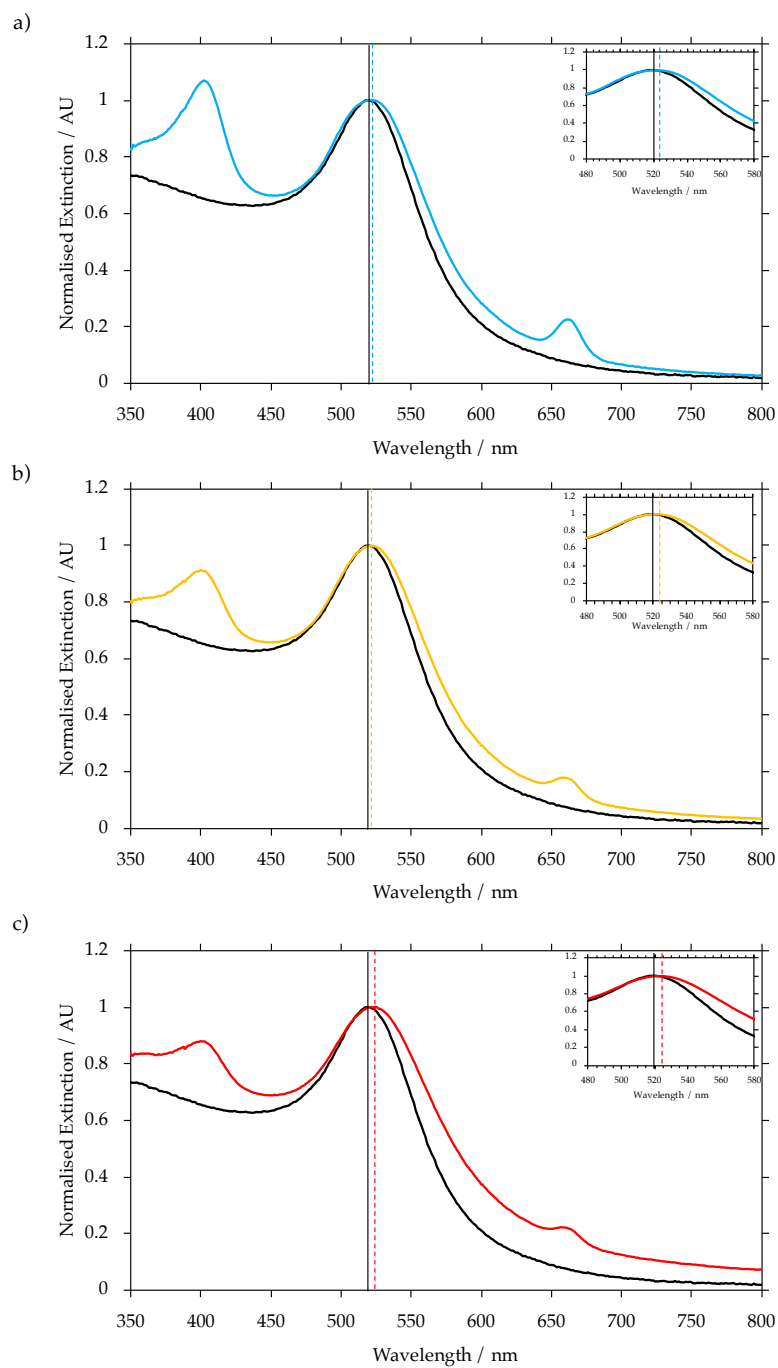
Figure 3.21: Extinction spectra of citrate-AuNPs (black line) and glycan-/ce6-AuNPs. a) galactose-/ce6-AuNPs (blue line); b) mannose-PEG$_6$-/ce6-AuNPs (yellow line); and c) PEG$_3$-/ce6-AuNPs (red line). Vertical black line represents extinction maximum for citrate-AuNPs, dotted lines represent extinction maxima for the modified glycans. Insets represent zoomed in region around extinction maxima.

From Figure 3.21, ce6 presence was determined by the characteristic absorp-

tion peaks at ~400 nm and ~654 nm[51]. The red-shift in extinction maxima for all glycan-/ce6-AuNPs was observed, suggesting successful functionalisation. The solutions were also assessed by MALDI-TOF (Figure 3.22).
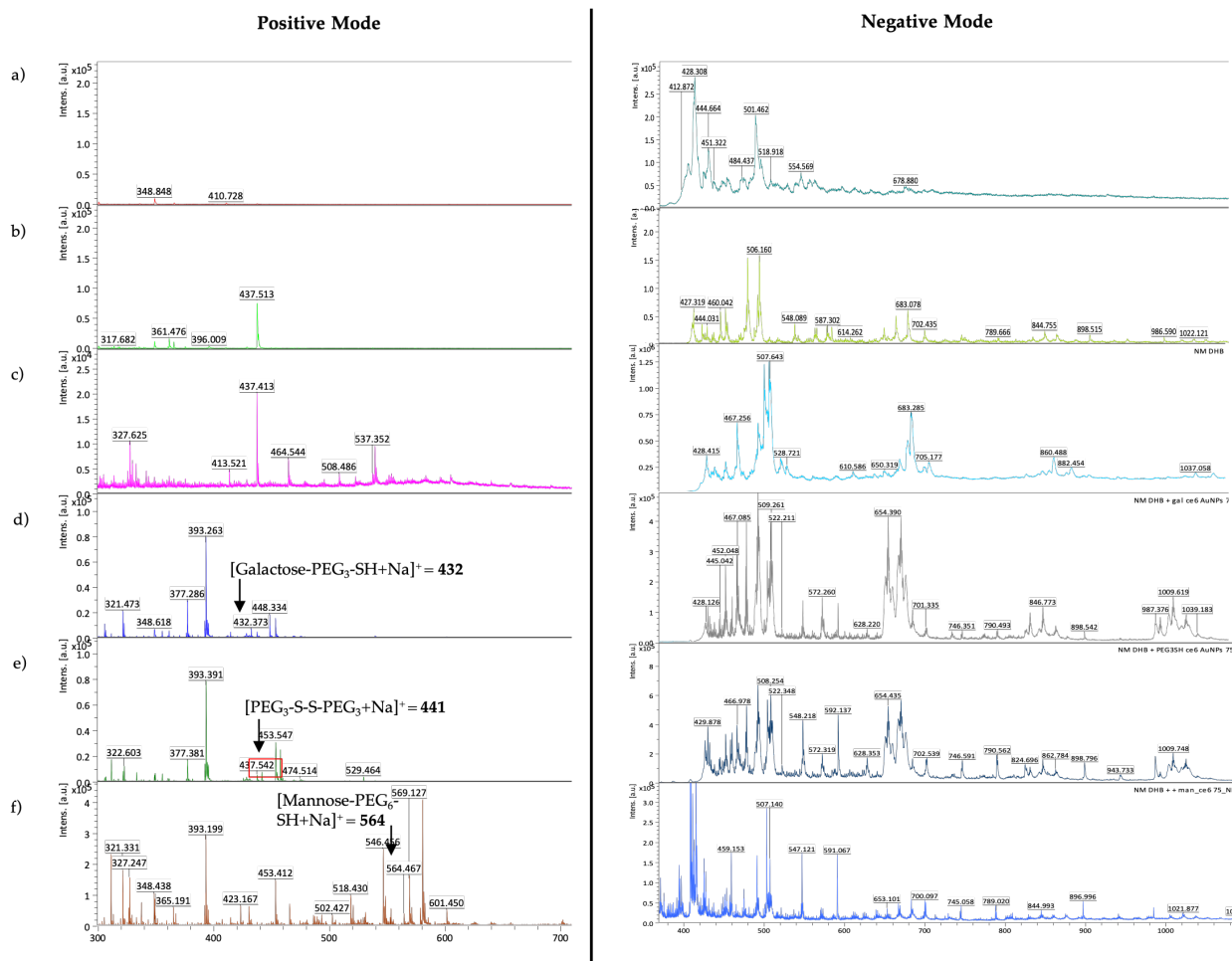
Figure 3.22: Positive (left) and negative (right) mode MALDI-TOF analysis of glycan-/ce6-AuNPs, with a) DHB matrix; b) DHB matrix with AuNPs; c) DHB matrix with ce6; d) DHB matrix with gal-/ce6-AuNPs; e) DHB matrix with PEG$_3$-/ce6-AuNPs; and f) DHB matrix with man-/ce6-AuNPs.

As can be seen from Figure 3.22, the glycan (galactose-PEG$_3$-SH and mannose-PEG$_6$-SH) and PEG$_3$-SH ligands were detected in the MALDI-TOF in positive mode, from the spectra in Figure 3.22d, e and f (highlighted with black arrows). However, the ce6-PEG$_4$-SH was not detected in positive or negative mode (Figure 3.22d, e and f). Neither the ce6-NH$_2$ ([ce6-NH$_2$$^+$H]$^+$ = 683; [ce6-NH$_2$$^+$Na]$^+$ = 705; [ce6-NH$_2$$^-$H]$^-$ = 681) nor the ce6-PEG$_4$-SH ([ce6-PEG$_4$-SH$^+$H]$^+$ = 947;

118

[ce6-PEG$_4$-SH$^+$Na]$^+$ = 969; [ce6-PEG$_4$-SH$^-$H]$^-$ = 945) masses were detectable in the MALDI-TOF. Although there were broad signals around 683, this signal was also detected in the citrate-AuNPs (Figure 3.22b, neg mode), which makes distinguishing the ce6 signals difficult. Consequently, it was not possible to use the MALDI-TOF to confirm ce6 conjugation. However, presence of ce6 was detected by the characteristic signals in the UV-Vis spectra (Figure 3.21), and coupled with the MALDI-TOF data, the glycan and PEG ligands were detected in the functionalised suspensions. Chapter 5 offers further investigation through singlet oxygen studies and cellular binding studies, for presence of ce6 and glycan on the AuNP surface.

3.4 Conclusions

In conclusion, two novel glycan ligands were synthesised through CuAAC: galactose-PEG$_3$-SH and mannose-PEG$_6$-SH. The glycans were 'clicked' to a alkyne PEGylated thiol derivative, to allow for strong interaction to the AuNP surface through the sulfur-gold bond. The PEGylated tether provides advantages such as steric stability and resistance to non-specific protein binding. In biological applications, presence of PEG has also shown increased circulation time, as there is reduced opsonisation, through the reduction in non-specific protein binding. As well as ligands for AuNP functionalisation, CuAAC was also used to synthesise a galactose-based lectin inhibitor, for future lectin binding studies.

Next, 16 nm citrate stabilised AuNPs were synthesised and characterised. The UV-Vis extinction spectrum of AuNPs is dependent on size, shape, surface interactions and the surrounding environment. A small red-shift in the SPR band was observed when thiolated ligands were used to functionalise the AuNPs. The galactose-PEG$_3$-SH was used to functionalise the AuNPs for lectin binding studies in Chapter 4. The introduction of the positively charged ligand 'TMAC', proved difficult to ligand exchange with the citrate on the citrate-

AuNPs, without causing aggregation of the particles. A method developed by Hassinen *et al.*[49], where a neutral transfer ligand was used to exchange the citrate on the surface, before the cationic ligand was introduced, overcame the aggregation issues. The TMAC-AuNPs were consistently generated through this method.

For the PDT studies (Chapter 5), a series of glycan and ce6 functionalised AuNPs were generated. For this, a commercially available amine derivative of the ce6 was used. Heterogeneous functionalisation of the AuNP surface of glycan and carboxyl ligands was obtained, and then the ce6 was introduced to the purified particles through EDC coupling. Both the characteristic peaks from the ce6 and AuNPs could be seen in the UV-Vis spectrum, demonstrating successful conjugation of the ce6 to the AuNP surface.

References

[1] L. Guerrini, R. Alvarez-Puebla, N. Pazos-Perez, L. Guerrini, R. A. Alvarez-Puebla, and N. Pazos-Perez, "Surface Modifications of Nanoparticles for Stability in Biological Fluids," *Materials*, vol. 11, no. 7, p. 1154, 2018. DOI: `10.3390/ma11071154`.

[2] V. Amendola, R. Pilot, M. Frasconi, O. M. Maragò, and M. A. Iatì, *Surface plasmon resonance in gold nanoparticles: A review*, 2017. DOI: `10.1088/1361-648X/aa60f3`.

[3] Y.-C. Yeh, B. Creran, V. M. Rotello, W. Doering, G. Davis, B. Shojaei, M. J. Natan, S. S. Gambhir, M. D. Wang, S. Nie, S. Roux, O. Tillement, Y.-T. Chang, R. W. Murray, and D. Mukbopadhyay, "Gold nanoparticles: preparation, properties, and applications in bionanotechnology," *Nanoscale*, vol. 4, no. 6, pp. 1871–1880, 2012. DOI: `10.1039/C1NR11188D`.

[4] M. Sabela, S. Balme, M. Bechelany, J. M. Janot, and K. Bisetty, *A Review of Gold and Silver Nanoparticle-Based Colorimetric Sensing Assays*, 2017. DOI: `10.1002/adem.201700270`.

[5] C. C. Chang, C. P. Chen, T. H. Wu, C. H. Yang, C. W. Lin, and C. Y. Chen, *Gold nanoparticle-based colorimetric strategies for chemical and biological sensing applications*, 2019. DOI: `10.3390/nano9060861`.

[6] X. Huang and M. A. El-Sayed, "Gold nanoparticles: Optical properties and implementations in cancer diagnosis and photothermal therapy,"

Journal of Advanced Research, vol. 1, no. 1, pp. 13–28, 2010. DOI: `10.1016/j.jare.2010.02.002`.

[7]   S. Peng, J. M. McMahon, G. C. Schatz, S. K. Gray, and Y. Sun, "Reversing the size-dependence of surface plasmon resonances," *Proceedings of the National Academy of Sciences of the United States of America*, vol. 107, no. 33, pp. 14 530–14 534, 2010. DOI: `10.1073/pnas.1007524107`.

[8]   J. Turkevich, P. C. Stevenson, and J. Hillier, "A study of the nucleation and growth processes in the synthesis of colloidal gold," *Discussions of the Faraday Society*, vol. 11, no. 0, p. 55, 1951. DOI: `10.1039/df9511100055`.

[9]   B. Derjaguin and L. Landau, "Theory of the stability of strongly charged lyophobic sols and of the adhesion of strongly charged particles in solutions of electrolytes," *Progress in Surface Science*, vol. 43, no. 1-4, pp. 30–59, 1993. DOI: `10.1016/0079-6816(93)90013-L`.

[10] E. J. Verwey and J. T. G. Overbeek, *Theory of the stability of lyophobic colloids*, 1955. DOI: `10.1016/0095-8522(55)90030-1`.

[11] E. M. Hotze, T. Phenrat, and G. V. Lowry, "Nanoparticle Aggregation: Challenges to Understanding Transport and Reactivity in the Environment," 2010. DOI: `10.2134/jeq2009.0462`.

[12] D. Lombardo, M. A. Kiselev, and M. T. Caccamo, "Smart Nanoparticles for Drug Delivery Application: Development of Versatile Nanocarrier Platforms in Biotechnology and Nanomedicine," *Journal of Nanomaterials*, vol. 2019, 2019. DOI: `10.1155/2019/3702518`.

[13] R. K. DeLong, C. M. Reynolds, Y. Malcolm, A. Schaeffer, T. Severs, and A. Wanekaya, "Functionalized gold nanoparticles for the binding, stabilization, and delivery of therapeutic DNA, RNA, and other biological macromolecules," *Nanotechnology, Science and Applications*, vol. 3, no. 1, pp. 53–63, 2010. DOI: `10.2147/NSA.S8984`.

[14] P. García Calavia, G. Bruce, L. Pérez-García, and D. A. Russell, *Photosensitiser-gold nanoparticle conjugates for photodynamic therapy of cancer*, 2018. DOI: `10.1039/c8pp00271a`.

[15] F. Chen, X. Li, J. Hihath, Z. Huang, and N. Tao, "Effect of anchoring groups on single-molecule conductance: Comparative study of thiol-, amine-, and carboxylic-acid-terminated molecules," *Journal of the American Chemical Society*, vol. 128, no. 49, pp. 15 874–15 881, 2006. DOI: `10.1021/ja065864k`.

[16] E. Pensa, E. Cortés, G. Corthey, P. Carro, C. Vericat, M. H. Fonticelli, G. Benítez, A. A. Rubert, and R. C. Salvarezza, "The Chemistry of the Sulfur–Gold Interface: In Search of a Unified Model," *Accounts of Chemical Research*, vol. 45, no. 8, pp. 1183–1192, 2012. DOI: `10.1021/ar200260p`.

[17] F. Y. Kong, J. W. Zhang, R. F. Li, Z. X. Wang, W. J. Wang, and W. Wang, "Unique roles of gold nanoparticles in drug delivery, targeting and imaging applications," *Molecules*, vol. 22, no. 9, 2017. DOI: `10.3390/molecules22091445`.

[18] J. S. Kang and T. A. Taton, "Oligothiol graft-copolymer coatings stabilize gold nanoparticles against harsh experimental conditions.," *Langmuir : the ACS journal of surfaces and colloids*, vol. 28, no. 49, pp. 16 751–60, 2012. DOI: `10.1021/la301249a`.

[19] Ș. Nițică, A. I. Moldovan, V. Toma, C. S. Moldovan, I. Berindan-Neagoe, G. Știufiuc, C. M. Lucaciu, and R. Știufiuc, "PEGylated Gold Nanoparticles with Interesting Plasmonic Properties Synthesized Using an Original, Rapid, and Easy-to-Implement Procedure," *Journal of Nanomaterials*, vol. 2018, pp. 1–7, 2018. DOI: `10.1155/2018/5954028`.

[20] S. Mourdikoudis, R. M. Pallares, and N. T. Thanh, *Characterization techniques for nanoparticles: Comparison and complementarity upon studying nanoparticle properties*, 2018. DOI: `10.1039/c8nr02278j`.

[21] T. G. Souza, V. S. Ciminelli, and N. D. Mohallem, "A comparison of TEM and DLS methods to characterize size distribution of ceramic nanoparticles," in *Journal of Physics: Conference Series*, 2016. DOI: 10.1088/1742-6596/733/1/012039.

[22] P. Zijlstra, P. M. Paulo, K. Yu, Q. H. Xu, and M. Orrit, "Chemical interface damping in single gold nanorods and its near elimination by tip-specific functionalization," *Angewandte Chemie - International Edition*, vol. 51, no. 33, pp. 8352–8355, 2012. DOI: 10.1002/anie.201202318.

[23] D. Alba-Molina, M. T. Martín-Romero, L. Camacho, and J. J. Giner-Casares, "Ion-mediated aggregation of gold nanoparticles for light-induced heating," *Applied Sciences (Switzerland)*, vol. 7, no. 9, 2017. DOI: 10.3390/app7090916.

[24] E. Marin, M. Briceño, and C. Caballero-George, "Critical evaluation of biodegradable polymers used in nanodrugs.," *International journal of nanomedicine*, vol. 8, pp. 3071–3090, 2013. DOI: 10.2147/IJN.S47186.

[25] D. Hone, A. Haines, and D. Russell, "Rapid, quantitative colorimetric detection of a lectin using mannose-stabilized gold nanoparticles.," *Langmuir*, vol. 19, pp. 7141–7144, 2003. DOI: 10.1021/la034358v.

[26] S. Dedola, D. L. Hughes, S. A. Nepogodiev, M. Rejzek, and R. A. Field, "Synthesis of α- and β-d-glucopyranosyl triazoles by CuAAC 'click chemistry': reactant tolerance, reaction rate, product structure and glucosidase inhibitory properties," *Carbohydrate Research*, vol. 345, no. 9, pp. 1123–1134, 2010. DOI: 10.1016/j.carres.2010.03.041.

[27] T. Stuchinskaya, M. Moreno, M. J. Cook, D. R. Edwards, and D. A. Russell, "Targeted photodynamic therapy of breast cancer cells using antibody–phthalocyanine–gold nanoparticle conjugates," *Photochemical & Photobiological Sciences*, vol. 10, no. 5, p. 822, 2011. DOI: 10.1039/c1pp05014a.

[28] H. C. Kolb, M. G. Finn, and K. B. Sharpless, "Click Chemistry: Diverse Chemical Function from a Few Good Reactions," *Angewandte Chemie International Edition*, vol. 40, no. 11, pp. 2004–2021, 2001. DOI: `10.1002/1521-3773(20010601)40:11<2004::AID-ANIE2004>3.0.CO;2-5`.

[29] G. Pergolizzi, S. Dedola, and R. A. Field, "Contemporary glycoconjugation chemistry," *Carbohydrate Chemistry*, vol. 42, pp. 1–46, 2017. DOI: `10.1039/9781782626657-00001`.

[30] M. Chikae, T. Fukuda, K. Kerman, K. Idegami, Y. Miura, and E. Tamiya, "Amyloid-β detection with saccharide immobilized gold nanoparticle on carbon electrode," *Bioelectrochemistry*, vol. 74, no. 1, pp. 118–123, 2008. DOI: `10.1016/j.bioelechem.2008.06.005`.

[31] V. Poonthiyil, T. K. Lindhorst, V. B. Golovko, and A. J. Fairbanks, "Recent applications of click chemistry for the functionalization of gold nanoparticles and their conversion to glyco-gold nanoparticles.," *Beilstein journal of organic chemistry*, vol. 14, pp. 11–24, 2018. DOI: `10.3762/bjoc.14.2`.

[32] I. Papp, C. Sieben, K. Ludwig, M. Roskamp, C. Böttcher, S. Schlecht, A. Herrmann, and R. Haag, "Inhibition of influenza virus infection by multivalent sialic-acid- functionalized gold nanoparticles," *Small*, vol. 6, no. 24, pp. 2900–2906, 2010. DOI: `10.1002/smll.201001349`.

[33] M. C. Martos-Maldonado, M. B. Thygesen, K. J. Jensen, and A. Vargas-Berenguel, "Gold-ferrocene glyco-nanoparticles for high-sensitivity electrochemical detection of carbohydrate-lectin interactions," *European Journal of Organic Chemistry*, no. 14, pp. 2793–2801, 2013. DOI: `10.1002/ejoc.201300205`.

[34] Y. J. Hwang, J. Granelli, and J. Lyubovitsky, "Effects of zero-length and non-zero-length cross-linking reagents on the optical spectral properties and structures of collagen hydrogels," *ACS Applied Materials and Interfaces*, vol. 4, no. 1, pp. 261–267, 2012. DOI: `10.1021/am2013147`.

[35] O. Craciunescu and L. Moldov, "Designing Bio-Inspired Composite Materials for Medical Applications," in *Nanocomposites and Polymers with Analytical Methods*, InTech, 2011. DOI: `10.5772/17363`.

[36] D. Bartczak and A. G. Kanaras, "Preparation of peptide-functionalized gold nanoparticles using one pot EDC/Sulfo-NHS coupling," *Langmuir*, vol. 27, no. 16, pp. 10 119–10 123, 2011. DOI: `10.1021/la2022177`.

[37] G. Obaid, I. Chambrier, M. J. Cook, and D. A. Russell, "Targeting the oncofetal thomsen-friedenreich disaccharide using jacalin-PEG phthalocyanine gold nanoparticles for photodynamic cancer therapy," *Angewandte Chemie - International Edition*, vol. 51, no. 25, pp. 6158–6162, 2012. DOI: `10.1002/anie.201201468`.

[38] M. Alloisio, M. Rusu, S. Ottonello, M. Ottonelli, S. Thea, and D. Comoretto, "Synthesis of fluorescent core-shell metal nanohybrids: A versatile approach," *Materials*, vol. 9, no. 12, 2016. DOI: `10.3390/ma9120997`.

[39] S. Shikha, K. G. Thakur, and M. S. Bhattacharyya, "Facile fabrication of lipase to amine functionalized gold nanoparticles to enhance stability and activity," *RSC Advances*, vol. 7, no. 68, pp. 42 845–42 855, 2017. DOI: `10.1039/c7ra06075k`.

[40] C. Arib, S. Milano, A. Gerbino, and J. Spadavecchia, "Aptamer Grafting onto (on) and into (in) Pegylated Gold Nanoparticles: Physicochemical Characterization and In vitro Cytotoxicity Investigation in Renal Cells," *Journal of Nanomedicine & Nanotechnology*, vol. 09, no. 06, 2018. DOI: `10.4172/2157-7439.1000520`.

[41] S. Wang, P. Huang, L. Nie, R. Xing, D. Liu, Z. Wang, J. Lin, S. Chen, G. Niu, G. Lu, and X. Chen, "Single continuous wave laser induced photodynamic/plasmonic photothermal therapy using photosensitizer-functionalized gold nanostars," *Advanced Materials*, vol. 25, no. 22, pp. 3055–3061, 2013. DOI: `10.1002/adma.201204623`.

[42] L. Vieira, M. Castilho, I. Ferreira, J. Ferreira-Strixino, K. Hewitt, and L. Raniero, "Synthesis and characterization of gold nanostructured Chorin e6 for Photodynamic Therapy," *Photodiagnosis and Photodynamic Therapy*, vol. 18, pp. 6–11, 2017. DOI: `10.1016/J.PDPDT.2016.12.012`.

[43] J. Gil-Tomás, L. Dekker, N. Narband, I. P. Parkin, S. P. Nair, C. Street, and M. Wilson, "Lethal photosensitisation of bacteria using a tin chlorin e6-glutathione-gold nanoparticle conjugate," *Journal of Materials Chemistry*, vol. 21, no. 12, pp. 4189–4196, 2011. DOI: `10.1039/c0jm03555f`.

[44] I. Carvalho, P. Andrade, V. L. Campo, P. M. M. Guedes, R. Sesti-Costa, J. S. Silva, S. Schenkman, S. Dedola, L. Hill, M. Rejzek, S. A. Nepogodiev, and R. A. Field, "'Click chemistry' synthesis of a library of 1,2,3-triazole-substituted galactose derivatives and their evaluation against Trypanosoma cruzi and its cell surface trans-sialidase," *Bioorganic & Medicinal Chemistry*, vol. 18, pp. 2412–2427, 2010. DOI: `10.1016/j.bmc.2010.02.053`.

[45] R. U. Kadam, M. Bergmann, D. Garg, G. Gabrieli, A. Stocker, T. Darbre, and J.-L. Reymond, "Structure-Based Optimization of the Terminal Tripeptide in Glycopeptide Dendrimer Inhibitors of <i>Pseudomonas aeruginosa</i> Biofilms Targeting LecA," *Chemistry - A European Journal*, vol. 19, no. 50, pp. 17 054–17 063, 2013. DOI: `10.1002/chem.201302587`.

[46] A. R. Shafiqa, A. Abdul Aziz, and B. Mehrdel, "Nanoparticle Optical Properties: Size Dependence of a Single Gold Spherical Nanoparticle," in *Journal of Physics: Conference Series*, vol. 1083, Institute of Physics Publishing, 2018. DOI: `10.1088/1742-6596/1083/1/012040`.

[47] H. Fissan, S. Ristig, H. Kaminski, C. Asbach, and M. Epple, "Comparison of different characterization methods for nanoparticle dispersions before and after aerosolization," *Analytical Methods*, vol. 6, no. 18, p. 7324, 2014. DOI: `10.1039/C4AY01203H`.

[48]   M. S. Verma, J. L. Rogowski, L. Jones, and F. X. Gu, "Colorimetric biosensing of pathogens using gold nanoparticles," *Biotechnology Advances*, 2015. DOI: `10.1016/j.biotechadv.2015.03.003`.

[49]   J. Hassinen, V. Liljeström, M. A. Kostiainen, and R. H. A. Ras, "Rapid Cationization of Gold Nanoparticles by Two-Step Phase Transfer," *Angewandte Chemie International Edition*, vol. 54, no. 27, pp. 7990–7993, 2015. DOI: `10.1002/anie.201503655`.

[50]   R. C. Hoft, M. J. Ford, A. M. McDonagh, and M. B. Cortie, "Adsorption of Amine Compounds on the Au(111) Surface:FIXME A Density Functional Study," *The Journal of Physical Chemistry C*, vol. 111, no. 37, pp. 13 886–13 891, 2007. DOI: `10.1021/jp072494t`.

[51]   J. D. Spikes and J. C. Bommer, "Photosensitizing properties of mono-l-aspartyl chlorin e6 (NPe6): A candidate sensitizer for the photodynamic therapy of tumors," *Journal of Photochemistry and Photobiology B: Biology*, vol. 17, no. 2, pp. 135–143, 1993. DOI: `10.1016/1011-1344(93)80006-U`.

Chapter 4

Targeted bacterial lectin binding using glyconanoparticles

The rise of antibiotic drug-resistance is making bacterial infections increasingly difficult to tackle, rendering many conventional antibacterial drugs ineffective. Consequently, alternative and selective antibiotic treatments are urgently needed. By developing selective antibacterial drugs, patient outcomes are improved by reducing side effects, and improving drug efficacy through reducing antibiotic exposure to non-target bacteria. Herein, an alternative antibacterial strategy was explored in the form of targeted photodynamic therapy, where glycan modified 16 nm AuNPs are used to target lectin that is located on the cell surface of the target pathogen: *Pseudomonas aeruginosa*.

4.1 Introduction

The following section outlines why *Pseudomonas aeruginosa* (*P. aeruginosa*) was selected as the target pathogen for this work, as well as how it was targeted.

4.1.1 *P. aeruginosa* as a target pathogen

P. aeruginosa are highly adaptable, Gram-negative bacteria, associated with multi-drug resistance and hardy infections. In part, their adaptability is due to their large genome, which allows the bacteria to colonise diverse environments and hold an arsenal of virulence factors[1]. Classified as a human opportunistic pathogen, *P. aeruginosa* can reside in the gut microbiota of healthy individuals, and occasionally cause mild infections. However, *P. aeruginosa* pose the biggest threat to those with compromised immunity, causing severe and life-threatening infections. *P. aeruginosa* are one of the leading causes of hospital-acquired infections [2]. As well as colonising diverse environments on the human body (skin, lungs, ears, eyes, gut, urinary tract, blood)[3], their adaptable nutrient intake allows the bacteria to survive in a wide range of environments outside the body too, such as in soil, water systems[4] and on plastic surfaces[5]. This causes further complications in a clinical setting, as *P. aeruginosa* can flourish on medical surfaces, such as implanted devices.

P. aeruginosa drug resistance and pathogenecity

Conventional antimicrobial drugs that are used to treat *P. aeruginosa* infections belong to the fluoroquinolone, aminoglycoside, β-lactam and polymyxin families[6]. However, *Pseudomonal* infections are becoming increasingly difficult to eradicate. *P. aeruginosa* are naturally resistant to many different antibiotics, and can quickly develop resistance due to their high adaptability and low membrane permeability[1]. There are already documented cases of *P. aeruginosa* resistance to last resort antimicrobial drugs, such as colistin[7]. A surveillance report by the European Centre for Disease Prevention and Control (ECDC), analysed *P. aeruginosa* resistance levels to multiple antimicrobial groups in invasive clinical isolates. Although resistance levels varied by country, 5.5% of all isolates were completely resistant to all antimicrobials tested[6]. Furthermore, the World Health Organisation (WHO) developed a 'global priority pathogens

list' and recognised *P. aeruginosa* as 'critical', the highest priority[8]. The list was designed to direct global research efforts and funding towards pathogens that most critically need new drugs to treat drug-resistant infections. Further highlighting the urgency in developing alternative strategies to tackle *P. aeruginosa* infections.

On top of their increasing drug resistance, *P. aeruginosa* readily form biofilms. Biofilms are an adhered, complex community of microorganisms, surrounded by an extracellular polymeric substance (EPS)[9]. The EPS allows microorganisms to secrete and share enzymes, DNA, proteins and virulence factors[10], that offer further protection by lowering drug susceptibility and increasing pathogenicity. *P. aeruginosa* biofilms are a particular concern in chronic wounds (burns, deep cuts, post-surgical wounds); implanted devices (catheters, ventilation equipment); and in the lungs of individuals with the genetic disorder Cystic Fibrosis (CF). It is estimated that 80% of all CF sufferers will contract a *P. aeruginosa* infection by the age of 18[11]; an infection linked with high mortality[12]. With this in mind, alternative treatments must be able to effectively eradicate both the planktonic and biofilm states of *P. aeruginosa*.

4.1.2   Identifying an alternative *P. aeruginosa* drug target

As mentioned previously, *P. aeruginosa* are equipped with a plethora of virulence factors. Virulence factors are molecules and components produced by a pathogen that offer protection against host defences; they promote colonisation, invasiveness and pathogenicity[13]. These virulence factors may be host invasive (proteases, toxins); drug resistive (β-lactamases, increased efflux pump expression); protective (flagella, alginate); competitive (siderophores); or adhesive (lectins, fimbrial adhesins)[14]. A diagram summarising *P. aeruginosa* virulence factors is shown in Figure 4.1. Of particular interest in this project, is the cell surface-associated lectin: LecA.
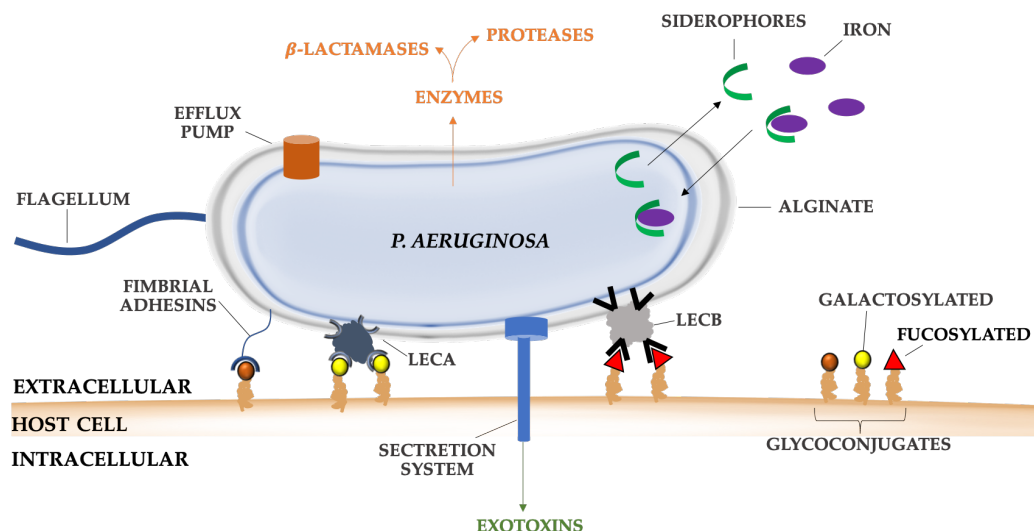
Figure 4.1: A summary of *P. aeruginosa* virulence factors, adapted from Chatterjee *et al.*[14].

LecA as a *P. aeruginosa* drug target

LecA is a small protein that can be found associated with the outer membrane. Its expression is regulated by quorum sensing, which is where expression is regulated by growth phase, growth environment and cell density. Expression of LecA is associated with later growth stages, from late-log and into stationary phase [15]. The full role of LecA is still to be unravelled but so far, LecA has been shown to be an adhesion factor, used for attachment to human cells[16]; exert cytotoxic effects on lung epithelial cells [17]; alter intestinal epithelial barrier permeability[18]; and contribute to biofilm formation[19]. Consequently, LecA is of therapeutic interest as it is present in both planktonic and biofilm *P. aeruginosa* cultures.

4.1.3   LecA glycan binding and ligand design

LecA is homotetrameric protein with a molecular weight of 51 kDa, and the structure can be seen in Figure 4.2. LecA exhibits narrow selectivity for the monosaccharide D-galactose, and to *N*-acetyl-D-galactosamine but at a much lower affinity [20]. The predominant natural ligand of LecA is αGal1-4βGal1-

4βGlc-ceramide (globotriaosylceramide), but it can also bind to a range of natural glycoconjugates with terminal α-galactose based disaccharides, such as αGal1-3Gal, αGal1-4Gal and αGal1-6Glc[21].

a)

b)
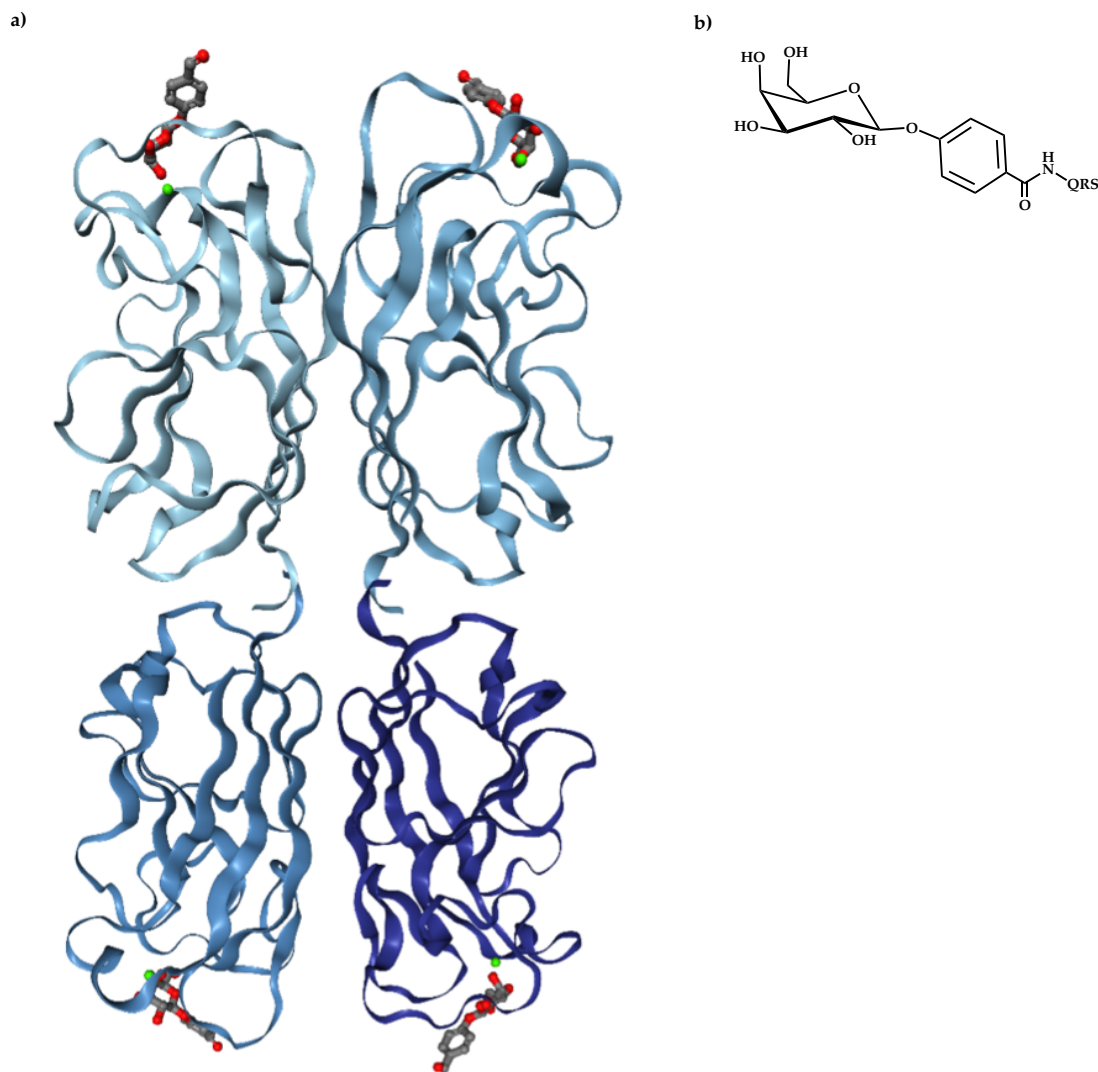
Figure 4.2: LecA tetramer crystal structure, in the presence of calcium ions (green spheres) and bound to (b) a tripeptide (QRS = glutamine, arginine, serine) phenyl β-D-galactopyranoside (grey and red sticks). PDB ID 4LKD, from Kadam *et al.*[22].

Introducing a hydrophobic group at the anomeric position improves affinity, with greatest affinity observed with β-D-galactose and aromatic substitutes at the anomeric position[23]. The anomeric hydroxyl is exposed to the sol-

vent and so is available for substitution. Kadam *et al.*[22] demonstrated that an aromatic group improves affinity through CH-π interactions (hydrophobic stacking) formed with His50 of LecA, with a K_d of 14.1 µM (Figure 4.3). Thus, affinity is improved compared to D-galactose, which has a K_d of ~88µM [23]
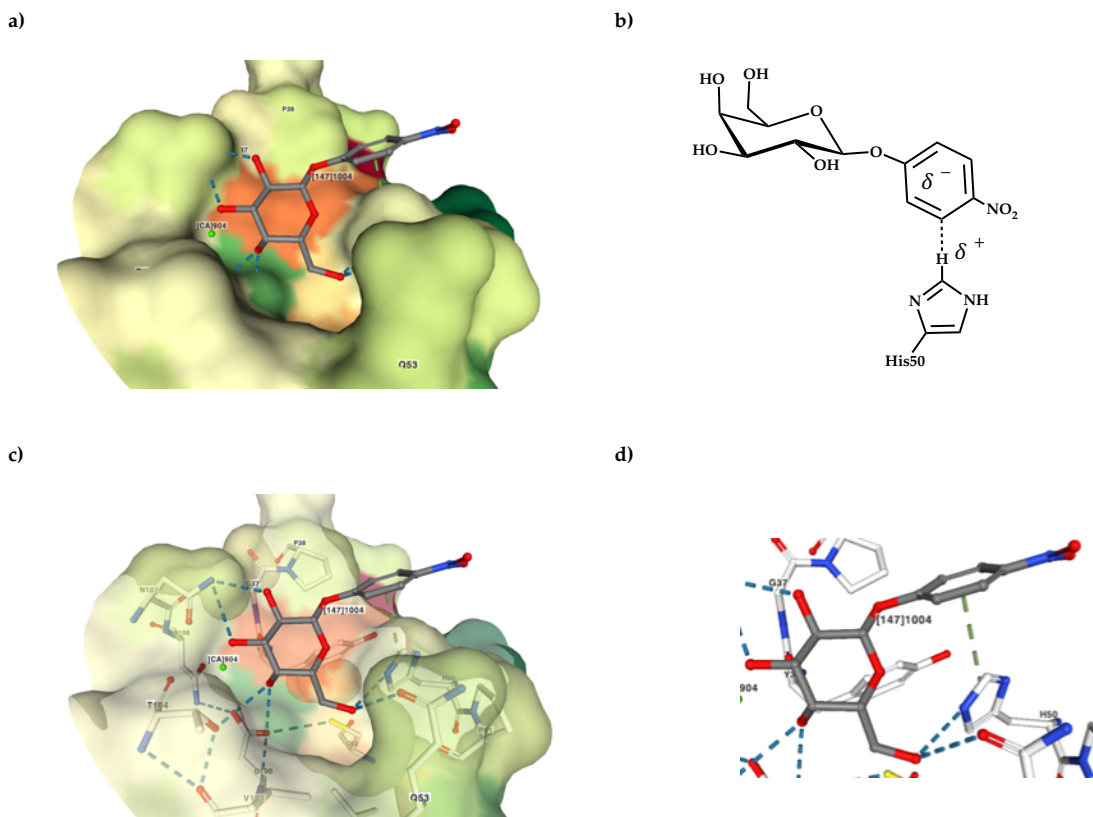
Figure 4.3: (a) LecA CRD bound to β-D-galactoside derivative (b) and calcium ion (green spheres). (c) and (d) show key LecA CRD amino acids for galactose binding, with hydrogen bonds (blue dotted lines) and π interactions (green dotted lines). (b) demonstrates the CH-π interaction of His50 in the LecA CRD with the hydrophobic, phenyl derivative of the galactoside. PDB ID: 3ZYF from Kadam *et al.* and [22].

As well as hydrophobic groups, multivalency is key to achieve the highest binding affinity to LecA [24]. A variety of different scaffolds have been used to hold multivalent galactose-based residues, such as dendrimers[25][22][26], polymer particles[27], calixarenes[28], fullerenes[29], glycoclusters[30][31][32][33], peptides[34] and AuNPs[24], all of which display binding affinities in the low nanomolar range (K_d<200 nM), whereas monovalent structures have µM K_d values.

Of relevance to this research are AuNPs. AuNPs offer advantages over the smaller multivalent constructs as they are: relatively easy to modify, and can be modified with different ligands; and they aim to replicate the natural, cell-surface glycan presentation of the glycocalyx, allowing for high valency[24]. With regards to LecA binding, AuNPs have only been used by Reynolds *et al.*[24] for LecA binding. The group used 2 nm AuNPs as a scaffold for a β-galactose ligand (Figure 4.4) at different densities, mixed with mannose or glucose, as spacer ligands.
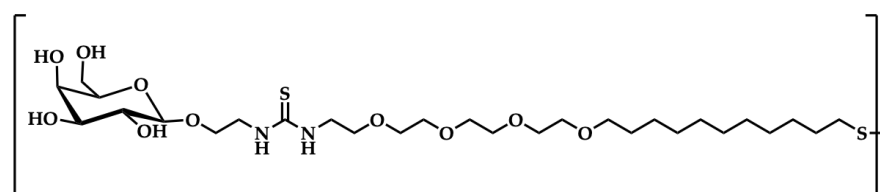
Figure 4.4: β-galactose ligand used in Reynolds *et al.*[24].

The AuNPs modified with 100% galactose, provided the greatest affinity (K_d of 50 nM). Interestingly, this high affinity LecA binding was achieved without incorporating an aromatic group at the anomeric position, highlighting the potential AuNPs can offer as scaffolds to achieve high-affinity and multivalent structures for LecA binding.

For this PhD research, both the hydrophobic group at the anomeric position, and multivalent presentation were combined to target LecA. A β-galactose ligand (Figure 4.5) was used with a hydrophobic, triazole ring at the anomeric position. Larger, 16 nm AuNPs were used as a scaffold for the galactose ligand. The larger particles provide a larger surface area meaning higher density of ligands per particle.
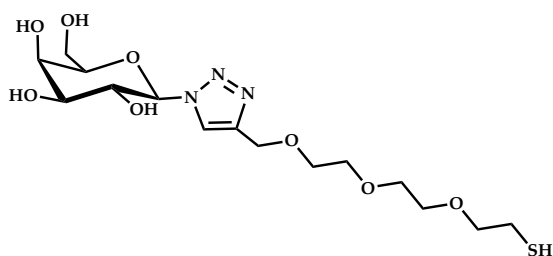
Figure 4.5: Structure of β-galactose ligand (galactose-PEG$_3$-SH) used to functionalise AuNPs.

4.1.4 Monitoring cell-surface glycan-lectin interactions using AuNPs

For effective antibacterial PDT, the PS should be localised to the bacterial cell surface. For this PhD research, galactose-modified AuNPs (gal-AuNPs) were used to target the *P. aeruginosa* cell surface associated lectin: LecA. The unique optical properties of AuNPs offer a method of assessing and optimising the galactose-LecA interaction, before introducing the PS.

Monitoring glycan-lectin binding by UV-Vis absorption

As detailed in Chapter 1.3.2, the AuNP optical properties are due to the surface plasmon resonance (SPR), resulting in a strong absorption of light[35]. For a monodisperse solution of 16 nm AuNPs, this wavelength is ~520 nm. Glycan functionalised AuNPs (glycoAuNPs) can bind to their respective multimeric lectins, and form aggregates due to crosslinking of multimeric lectins and multivalent glycoAuNPs (see Figure 4.6).

GlycoAuNPs

Aggregated glycoAuNPs
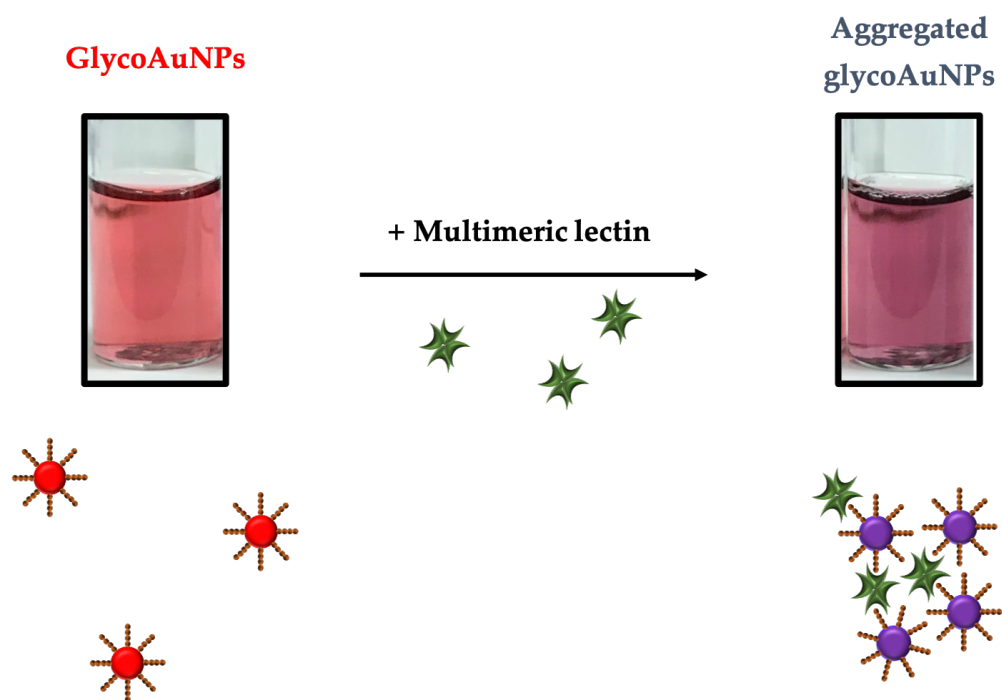
+ **Multimeric lectin**

Figure 4.6: Image demonstrating aggregates formed between glycoAuNPs in the presence of multimeric lectin, leading to a colour change from red to purple/blue.

The electron density on the surface dictates the SPR band. As AuNP size increases, there is a red shift in SPR wavelength that creates a colour change. The colour change can also be observed when AuNPs come into close proximity with one another and 'aggregate'. This principle has been demonstrated by the Field and Russell groups to monitor lectin[36][37], toxin[38] and viral[39] binding, and will be exploited throughout this chapter. By using UV-Vis spectroscopy, the complete AuNP spectrum can be monitored to assess changes that may indicate binding. As bacterial cells interfere with the extinction spectra in the UV-Vis plate assay format, an alternative method was required to monitor bacterial binding.

Monitoring glycan-lectin binding by filtration

A new filtration-based technique was developed at Iceni Diagnostics to assess bacteria-glycoAuNP binding, still based on colour observations. A 384-well

plate, with a 0.45 μm filter at the bottom of each well was used. The premixed solution of glycoAuNPs and either lectin or bacterial sample were added to the wells. A vacuum was applied below the well surface to draw the solution through the filter (see Figure 4.7).
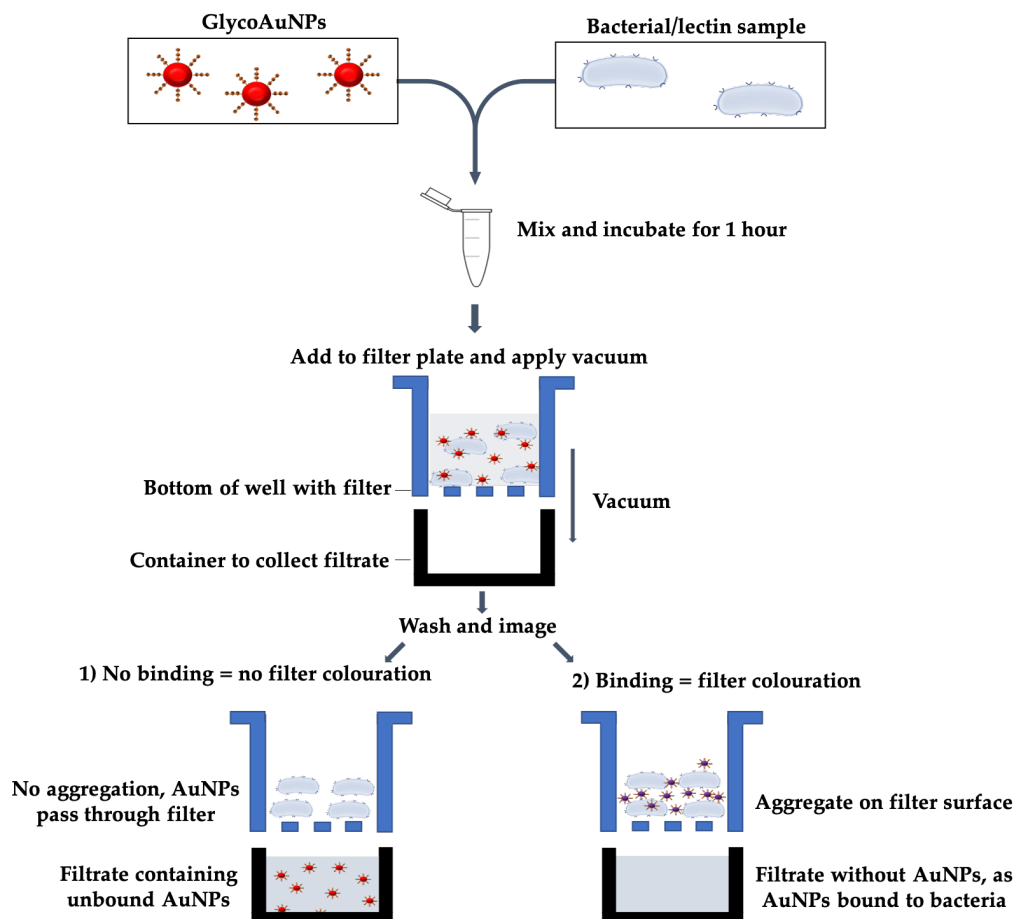
Figure 4.7: Image demonstrating filter plate assay method.1) No binding between bacteria and glycoAuNPs, which results in the particles passing through the filter, and no colouration of the filter. Bacteria are too large to pass through the filter and so remain on the filter surface. 2) Aggregates form between glycoAuNPs and multimeric lectin or bacterial culture that are too large to pass through the filter, leading to a red/purple/blue colouration on the filter surface.

For the lectin studies, the aggregates formed between the lectin and glycoAuNP were too large to pass through the filter. The same was true of bacterial cell aggregates, and so when the vacuum was applied, the cells remain on the surface of the filter along with any cell bound glycoAuNPs. In both cases, aggregates were trapped on the surface of the filter, leaving a red/purple/blue colouration on the filter, depending on the sample.

138

4.2   Scientific aims

The aim of this work was to develop targeted eradication of *P. aeruginosa*, through photodynamic therapy (PDT), using galactose and PS modified AuNPs. Targeting was set out to be achieved through galactose binding of the *P. aeruginosa* cell surface lectin: LecA. Firstly, galactose modified AuNPs (gal-AuNPs) will be used to demonstrate and optimise binding to LecA, initially to the soluble lectin, and then to the *P. aeruginosa*. Then the PS will be introduced to the AuNP surface, for *P. aeruginosa* eradication through PDT.

4.3   Results and discussion

4.3.1   Bacterial binding by 16 nm AuNPs

The first step was to demonstrate that 16 nm AuNPs can be used to detect intact bacterial cells in the filter plate assay format. The filter plate technique provides many advantages for detecting bacterial samples, in that the technique is relatively straightforward and easy-to-use, without the need for sample extraction; and provides visual results within an hour, simplifying data analysis. For the following studies, *Escherichia coli* (*E. coli*) was used as a convenient model microorganism, and AuNPs were functionalised with the cationic ligand 'TMAC' (TMAC-AuNPs). Control AuNPs were functionalised with an uncharged ethylene glycol based ligand (PEG$_3$-SH). Detail of TMAC-AuNP and PEG$_3$-AuNP preparation and characterisation are shown in Chapters 2 and 3 respectively, with both ligand structures shown in Figure 4.8.

a)   b)
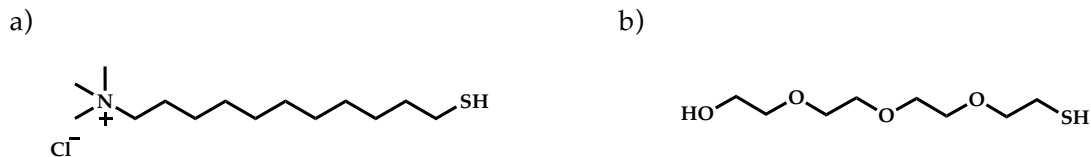
Figure 4.8: Structures of cationic TMAC ligand (a) and uncharged PEG$_3$ ligand (b).

The positively charged AuNPs form electrostatic interactions with negatively charged groups on the bacterial surface, such as phospholipids, lipopolysaccharides and teichoic acids [40]. TMAC-based AuNPs have been shown to bind to *Staphylococcus aureus*, using 11 nm TMAC-AuNPs[41]. By altering ratios of TMAC and a negatively charged ligand (11-mercaptodeconoic acid, MUA) (Figure 4.9) on the AuNP surface, discrimination between Gram-negative (*E. coli* and *Acinetobacter baumannii*) and Gram-positive bacteria (*Staphylococcus aureus* and *Enterococcus faecium*) was possible; where, higher TMAC densities bound and eradicated Gram-negative bacteria[42]. Interestingly, this study also demonstrated higher cytotoxicity with larger AuNPs (2.5 vs 5.3 vs 9.5 nm).
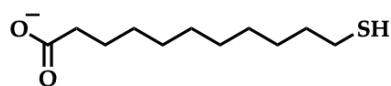
Figure 4.9: Structure of negatively charged ligand: MUA, used in Pillai *et al.*[42].

Glycan-lectin interactions provide greater selectivity but require much more consideration to obtain binding, such as the timing of lectin expression; accessibility of the lectin; as well as density, presentation and structure of the glycan ligand. Therefore, TMAC-AuNPs were selected as they can achieve wide-spread binding across the whole of the bacterial surface, and the interaction is much simpler in comparison to glycan-lectin binding.

The results from the filter plate assay can be seen in Figure 4.10. Binding was observed between the TMAC-AuNPs and both cell densities tested. The *E. coli* cells were too large to pass through the filter, and became trapped on the filter surface. Any AuNPs bound to the *E. coli* were trapped too, providing a red colouration of the filter. The binding was due to the charge interaction between the cationic-AuNPs and negatively charged groups on the bacterial surface, as no binding was observed with the uncharged PEG_3-AuNPs.
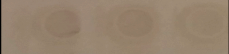
		Cationic-AuNPs			PEG$_3$-AuNPs		
OD *of E. coli* **/ AU**	0.8	●	●	●	○	○	○
	0.4	●	●	●	○	○	○
	0	○	○	○	○	○	○

Figure 4.10: Image of the filter plate assay results, assessing binding of TMAC-AuNPs to *E. coli* strain ORN178. Cell density decreases from top to bottom, OD = 0.8 (~3x10^8 cells/ml), 0.4 (~0.7x10^8 cells/ml) and 0. Uncharged PEG$_3$-AuNPs are used as a negative control. Note that this image shown above is multiple images of the same plate and experiment, combined. Wells are masked/hidden when taking a picture of the whole plate.

Once the ability of the filter plate to detect bacterial binding by 16 nm AuNPs was confirmed, selective binding by glycan-AuNPs to the target pathogen: *P. aeruginosa*, was developed.

4.3.2 LecA lectin expression by *P. aeruginosa*

The *P. aeruginosa* strain used for the following studies was PAO1, because it is the most commonly used strain, referred to as the 'reference strain' for studying *P. aeruginosa*[43]. Although wildtype PAO1 expresses LecA, expression was first confirmed to ensure the strain was behaving as expected for the consecutive binding studies. Samples were taken at different time points through growth, and expression was probed using Western blot analysis. The growth curve for PAO1 can be seen in Figure 4.11a, and shows the corresponding lag (0-4 hours), log (4-24 hours) and stationary (>24 hours) phases.

The composite chemiluminescence and white light image from the Western blot used to detect LecA expression, can be seen in Figure 4.11b. From Figure 4.11, LecA expression was detected after 10 hours (lane 7). The monomeric form of LecA was the predominant band detected (~12.75 kDa), which was expected under the protein denaturing SDS-PAGE conditions; although under physiological conditions, the protein is tetrameric.

a)

b)

1 = Ladder   4 = 6 hours   7 = 10 hours   10 = 24 hours   13 = 36 hours   16 = 78 hours

2 = 2 hours   5 = 8 hours   8 = 11 hours   11 = 28 hours   14 = 48 hours   17 = LecA

3 = 4 hours   6 = 9 hours   9 = 12 hours   12 = 32 hours   15 = 56 hours
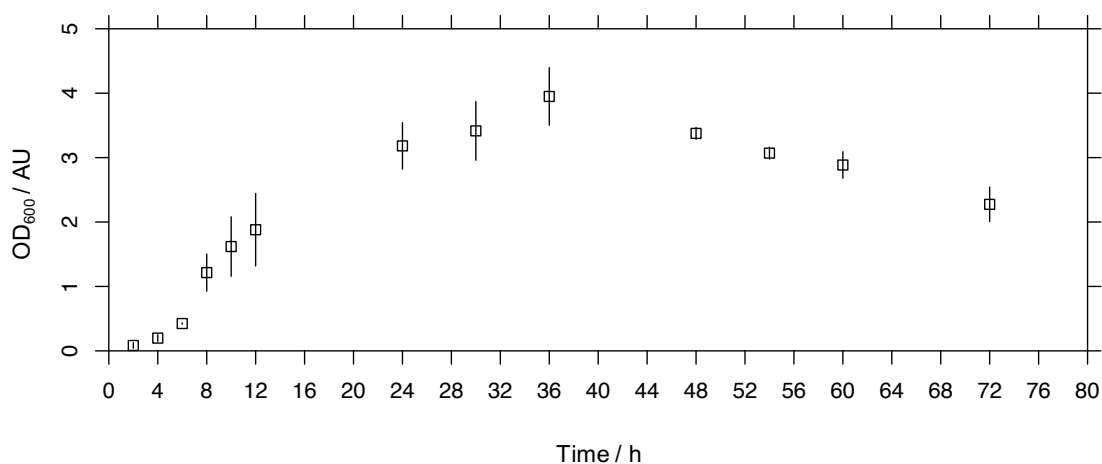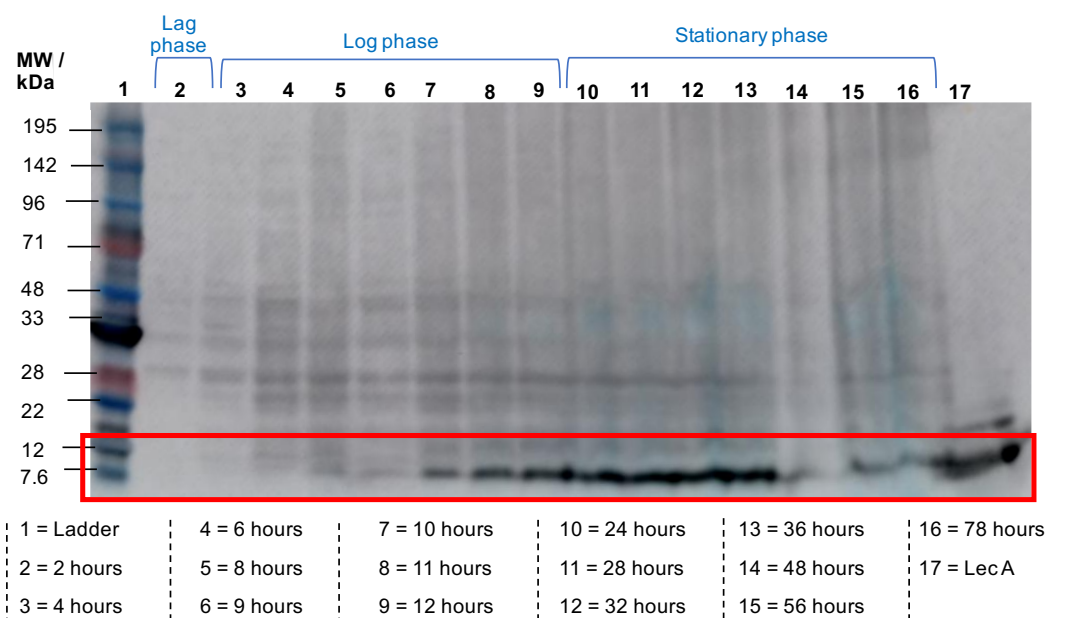
Figure 4.11: (a) The growth curve of *P. aeruginosa* (PAO1), error bars = +/- SD, n=5. (b) Composite image from overlay of chemiluminescence and white light imaging, from Western blot analysis of LecA expression at different time points during growth. The red box highlights where LecA runs on the blot.

By comparing Figure 4.11a and Figure 4.11b, expression of LecA was in the later stages of the log phase, and into the stationary phase. As mentioned previously, LecA expression is regulated through quorum sensing, and so expression is associated with later growth stages[15]. For the LecA expression

142

experiments, the cell densities were not normalised *i.e.,* there was no loading control. Therefore, it was possible that LecA was expressed at lower time points but not detected due to lower cell densities loaded, as observed by the lower optical density at lower time points in Figure 4.11a. However, the aim of the experiment was to detect presence of LecA expression and not to quantify protein expression at different time points. Therefore, as LecA expression was detected after 10 hours, all future studies with PAO1 will be performed after 10 hours to ensure lectin expression.

4.3.3   Gal-AuNPs binding optimisation to LecA

Once the LecA expression by *P. aeruginosa* was confirmed, gal-AuNPs (galactose-PEG_3-SH functionalised AuNPs) were prepared as outlined in Chapter 2.3.3 (characterisation shown in Chapter 3.3.3). Before introducing the complex environment of bacteria, the binding of the gal-AuNPs with pure LecA protein was assessed. For the binding studies, commercially available LecA (Sigma) was used in the UV-Vis and filter plate assay formats.

Concentration of galactose-PEG_3-SH for AuNP functionalisation

The first step was to determine the galactose-PEG_3-SH ligand concentration needed to functionalise the AuNPs, to observe binding to LecA. Here, a range of concentrations were used to functionalise the AuNPs (20, 100 and 200 μM). Binding between gal-AuNPs and LecA (0-1000 nM) was assessed, in the presence and absence of $CaCl_2$ (Figure 4.12). General trends can be drawn from the full UV-Vis extinction spectra in Figure 4.12. For example, higher LecA concentrations show decreased extinction around the AuNP extinction maxima (~520 nm), and increased extinction at longer wavelengths (~575 nm >). However, to aid quantitative analysis and interpretation of the data, a single wavelength was selected.
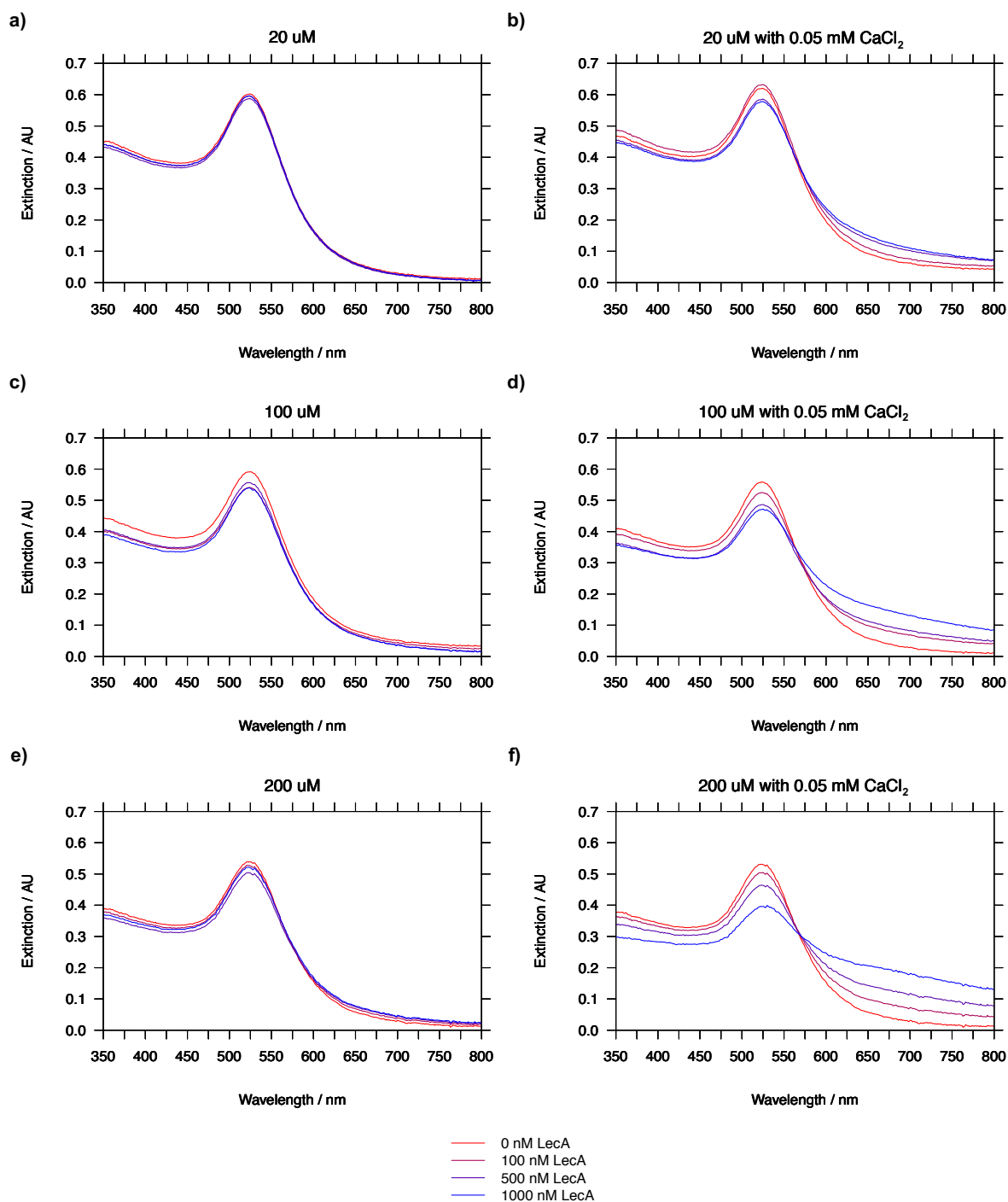
Figure 4.12: Full UV-Vis extinction spectra (350-800 nm) for binding optimisation studies of LecA by gal-AuNPs. Shown for illustrative purposes to demonstrate the changes in the full spectra, in the presence of lectin, and consequently particle aggregation. Different concentrations of gal-PEG$_3$-SH were used for functionalisation of AuNPs, at 20 (a and b), 100 (c and d) and 200 (e and f) μM. Binding of LecA (0-1000 nM, red to blue lines) was assessed in the absence (a, c, and e) and presence (b, d and f) of 0.05 mM CaCl$_2$. N=3.

144

The wavelength that provides the best sensitivity for lectin detection, will be the one that has the biggest difference in extinction values between gal-AuNPs with and without LecA. To determine this, the extinction spectrum for gal-AuNPs was subtracted from the extinction spectrum of gal-AuNPs with LecA (1000 nM). The data used in this analysis were the gal-AuNPs functionalised with 200 μM of galactose-PEG$_3$-SH, with CaCl$_2$, as this was where the biggest response to LecA was observed. The processed data is shown in Figure 4.13.
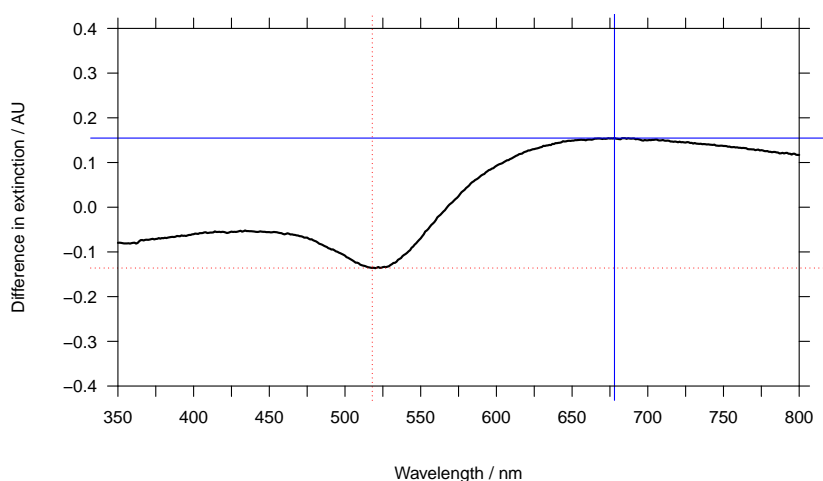
Figure 4.13: Mean difference in extinction spectra (350-800 nm, black line) of 200 μM gal-AuNPs, in the presence and absence of 1000 nM LecA, in the presence of CaCl$_2$. Greatest extinction differences observed at 518 nm (red, dashed line) and 678 nm (blue, solid line). Data extracted from Figure 4.12f, n=3.

A positive value means that there is an increase in extinction at that specific wavelength, when LecA is present; and so a negative value represents a decrease in extinction when LecA is present. The wavelengths that gave the greatest differences were observed at 518 nm (-0.136 AU, red line) and 678 nm (0.155 AU, blue line), which reflects the spectra in Figure 4.12. Therefore, for all future data, only the extinction value at 678 nm will be represented. This wavelength was chosen as it gave the greatest difference between gal-AuNPs, with and without LecA.

The extinction value at 678 nm (Ex$_{678}$) for each condition are shown in Figure 4.14, with the corresponding filter plate assay results shown in Figure

4.15. Please note that throughout this chapter, the negative control (1000 nM ConA) data will be represented by a bar chart as only one concentration was tested. In Figure 4.14, ConA was subjected to the same buffer conditions as LecA, as well as being tested with the different gal-AuNPs, and so the colour of the bars are the corresponding controls for each condition for LecA binding.
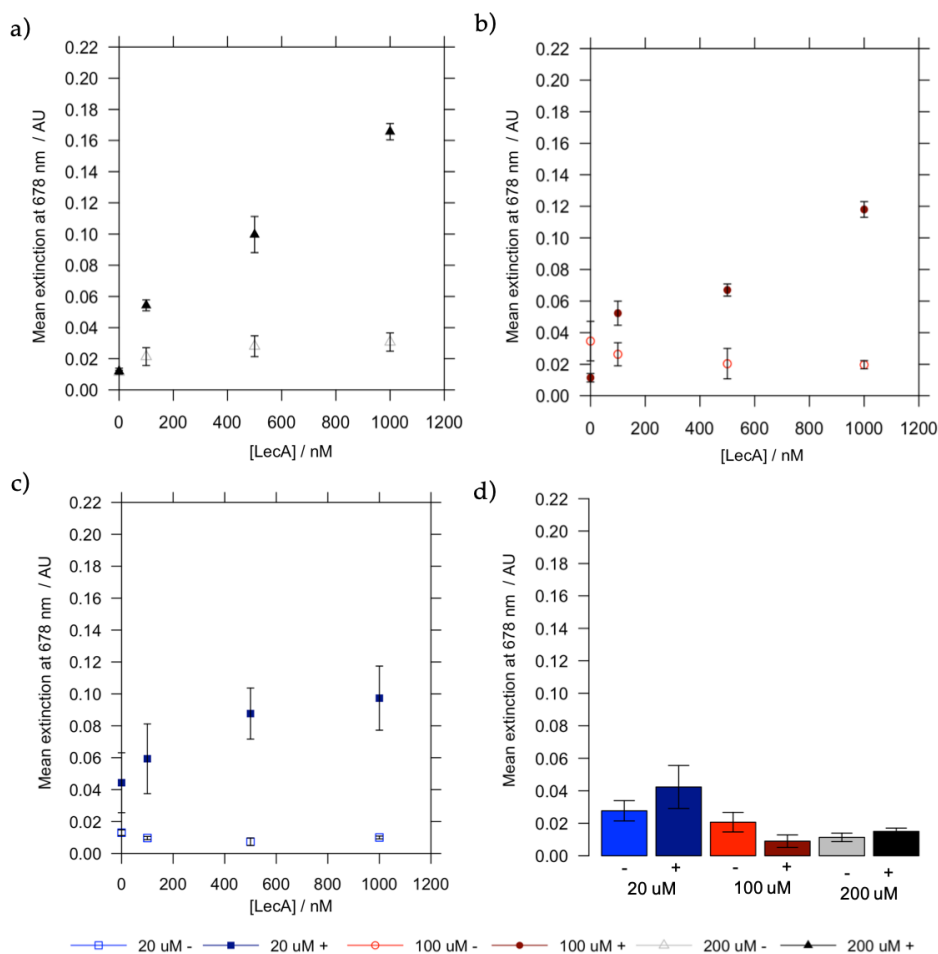
Figure 4.14: Binding optimisation studies of LecA by gal-AuNPs. AuNPs were functionalised with different concentrations of galactose-PEG$_3$-SH, including: a) 200 μM (triangles); b) 100 μM (circles); and c) 20 μM (squares). Binding of LecA (0-1000 nM) was assessed in the absence (-, light colour shapes) and presence (+, dark colour shapes) of CaCl$_2$. d) ConA is used as a negative control, tested with each set of particles, with (+) and without (-) CaCl$_2$. For each condition, the mean extinction at 678 nm was measured. Error bars = +/- SD, n = 3.

There are three conclusions that can be drawn from the results in Figures 4.14 and 4.15. Firstly, the higher concentration of galactose-PEG$_3$-SH (200 μM) used to functionalise the AuNPs provides greater colloidal stability, in the presence of CaCl$_2$. This can be seen by comparing the extinction values of the particle

146

solutions with just buffer (0 nM LecA) in Figure 4.14. For gal-AuNPs function-
alised with 200 μM ligand (Figure 4.14a), there was no significant difference
in Ex_{678} in the presence (black, filled triangle) and absence (grey triangle) of
$CaCl_2$, at 0 nM LecA. However, for the AuNP solution that was functionalised
with 20 μM galactose-PEG_3-SH (Figure 4.14c), there was less stability when
$CaCl_2$ was present in the buffer, as seen by an increase in Ex_{678} when $CaCl_2$ was
present in Figure 4.14c (dark blue squares) for 0 nM LecA (just buffer). It was
important to assess the particle stability in the buffer that was used for lectin
binding studies, as changes in the spectrum must reflect binding interactions
between the gal-AuNPs and lectin, and not from salt effects.

Secondly, the AuNPs modified with 200 μM galactose-PEG_3-SH (Figure
4.14a) showed significantly higher Ex_{678} with 1000 nM LecA, compared to 20
μM (Figure 4.14b) and 100 μM (Figure 4.14c). The 200 μM gal-AuNPs also
were more sensitive than the other gal-AuNP solutions, as seen by significantly
different Ex_{678} between each LecA concentration tested (Figure 4.14a). The
increased Ex_{678} values suggested a greater extent of aggregation of the gal-
AuNPs, and was reflected in the filter plate results (Figure 4.15), by greater
colouration of the filter with 200 μM.

		20 uM $CaCl_2$ present		100 uM $CaCl_2$ present		200 uM $CaCl_2$ present	
		-	+	-	+	-	+
[LecA]/nM	0						
	100						
	500						
	1000						
[ConA]/nM	1000						

Figure 4.15: Filter plate assay results of gal-AuNPs with increasing concentrations of LecA (0-1000 nM, top to bottom), in the presence (+) and absence (-) of $CaCl_2$. The galactose-PEG_3-SH ligand concentration for AuNP functionalisation increases from left to right (20, 100, 200 μM). ConA is used as a negative control. Please note that this is a collection of images combined together. Wells are hidden when one image is taken from above, and so the same plate is taken from multiple angles and then the different images are combined for easier comparison.

Finally, calcium ions are critical for the galactose-LecA interaction. LecA

is a C-type lectin, where metal ions are necessary for carbohydrate binding, and so the loss of binding without $CaCl_2$ was not surprising. Furthermore, the crystal structure of galactose and LecA[44] in the presence of calcium ions has been solved[20], demonstrating ion coordination was required for optimal binding interactions. Without $CaCl_2$, low to no observable binding to LecA was observed for all gal-AuNPs in both colorimetric and filter plate assays.

Temperature for binding studies

As *P. aeruginosa* is a human opportunistic pathogen, and LecA is a virulence factor[14], binding was assessed at body temperature (37°C) as well as room temperature (25°C), to see if binding could be improved. The previous binding experiments were all performed at 25°C. The Ex_{678} are shown in Figure 4.16, and corresponding filter plate assay results are shown in Figure 4.17. There was significantly increased aggregation at 25°C at LecA concentrations from 64 nM and above.
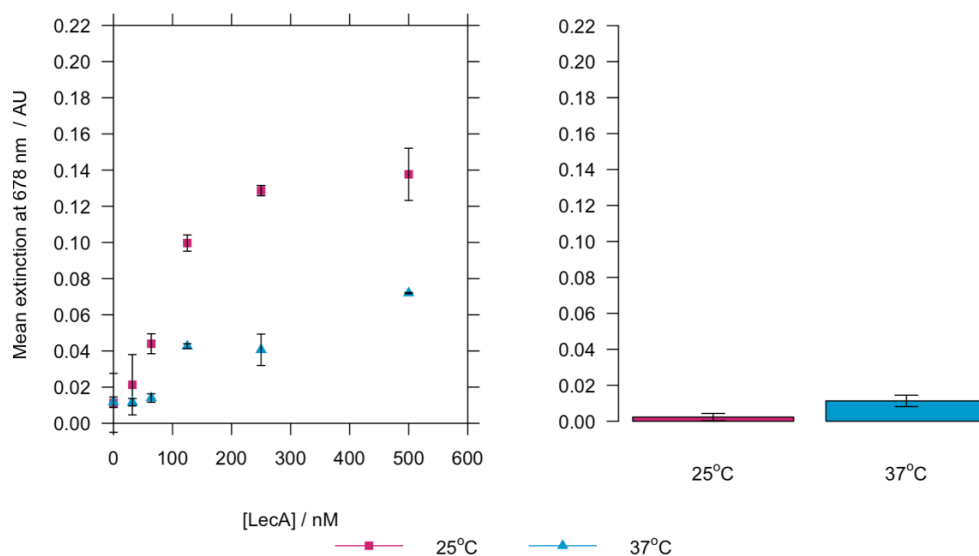
Figure 4.16: Mean Ex_{678} for UV-Vis plate assay assessing temperature for LecA and gal-AuNP interaction at 25°C (pink) and 37°C (blue). Negative control is ConA (1000 nM). Error bars = SD, n = 3.

The improved binding was confirmed by the filter plate assay results shown

148

in Figure 4.17, where a clear difference in filter colouration can be seen between the two temperatures. At 25ºC, binding was observed from 64 nM of LecA; whereas at 37ºC, binding was only detectable from 125 nM of LecA. In the filter plate assay (Figure 4.17), by eye, the filter colouration appeared much more intense at 25ºC, by comparing the two concentrations of LecA (250 and 500 nM) that showed binding at both temperatures.
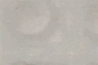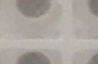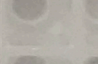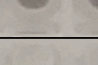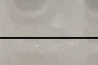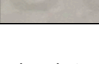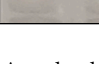
| | | Temperature | |
		25ºC	37ºC
	0		
	32		
[LecA] / nM	64		
	125		
	250		
	500		
[ConA] / nM	1000		

Figure 4.17: Image of filter plate assay results comparing interaction of LecA and gal-AuNPs at 25ºC (left) and 37ºC (right). Increasing LecA concentrations from 0-500 nM (top to bottom). Negative control is ConA (1000 nM).

The effect of improved binding at lower temperatures has been seen through hemagglutination assays. Gilbo-Garber *et al.*[45] assessed the hemagglutinating activity of LecA at temperatures from 4ºC to 50 ºC, and found activity decreased as temperature increased. The authors speculate that the lower binding temperature may be due to *P. aeruginosa* preference to colonise damaged, cooler tissue.

4.3.4   Selectivity of gal-AuNPs and LecA interaction

To assess that the aggregation observed between the gal-AuNPs and LecA in the previous Sections (4.3.2 and 4.3.3) was due to the galactose residues present

on the AuNP surface selectively binding to the LecA CRD, competitive inhibition experiments were performed. For this, a galactose-derivative inhibitor (inhibitor) was used (Figure 4.18), with its preparation outlined in Chapter 2.3.1. For all inhibition studies, the inhibitor was used at a final concentration of 1 mM.
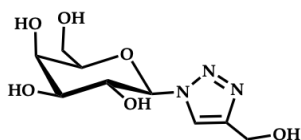
Figure 4.18: Structure of galactose-derivative inhibitor (inhibitor) used for LecA binding inhibition studies.

Figure 4.19 shows the Ex_{678} for gal-AuNP binding in the presence (blue) and absence (pink) of inhibitor. Without the inhibitor, results were as expected, showing an increase in Ex_{678} with increasing LecA concentrations, along with background Ex_{678} values for ConA.
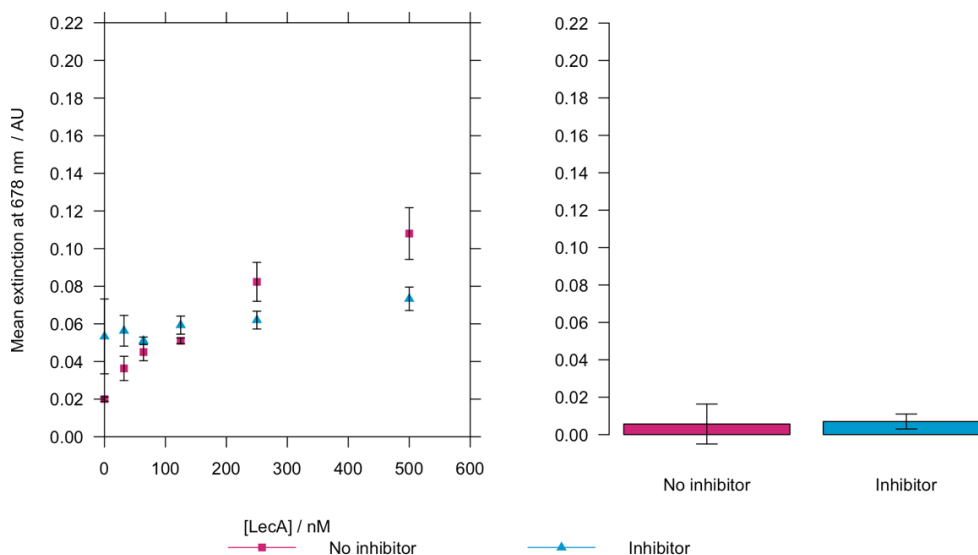
Figure 4.19: Mean Ex_{678} for UV-Vis plate assay assessing selectivity of LecA and gal-AuNP interaction in the absence (pink) and presence (blue) of 1 mM inhibitor. Negative control is ConA (1000 nM). Error bars = SD, n = 3.

By comparing the Ex_{678} in the presence and absence of LecA, there was a notable reduction at Ex_{678} with 250 and 500 nM LecA when the inhibitor was present. However, when gal-AuNPs were in the presence of the inhibitor, there

150

was an overall increased Ex_{678}. When the inhibitor was present, there was no significant increase at Ex_{678} as LecA concentration increased but the background level (0 nM LecA) was higher than expected. There was no significant difference between the ConA Ex_{678} values, with and without the inhibitor. The ConA appeared to be adding some stability to the solution, reducing gal-AuNP and inhibitor interaction.

From looking at the filter plate assay results in Figure 4.20, there was clear inhibition of LecA binding by the gal-AuNPs, in the presence of inhibitor. No detectable colouration of the filter was observed for any LecA concentration when inhibitor was present. The increase in Ex_{678} observed when inhibitor was present in Figure 4.19, was not reflected in the filter plate assay results. These set of experiments may demonstrate a limitation of the UV-Vis plate assay for monitoring glycan-lectin interactions.

Figure 4.20: Filter plate assay results of gal-AuNPs with increasing concentrations of LecA (0-500 nM, top to bottom), in the presence (+) and absence (-) of inhibitor. Negative control is ConA (1000 nM).

Overall, these experiments demonstrated that the aggregation observed between the gal-AuNPs and LecA was a specific interaction, as the LecA inhibitor was shown to disrupt this interaction.

4.3.5 Binding of gal-AuNPs to *P. aeruginosa*

The gal-AuNPs were assessed for binding to *P. aeruginosa* in just the filter plate assay. The UV-Vis assay was not used as the bacterial absorption largely masked the AuNP extinction spectra. As discussed in Section 4.3.2, LecA expression was detected in the later log phase and into the stationary phase of *P. aeruginosa* growth. Therefore, bacteria were cultured for 16 hours for the following experiments. To assess selectivity of the interaction, inhibitor was used.

The filter plate assay results of the bacterial binding by gal-AuNPs can be seen in Figure 4.21. Binding was observed between the gal-AuNPs and *P. aeruginosa* cultures at an optical density (OD) of 0.4, seen by the colouration of the filter. Negative controls (0 nM LecA, 1000 nM ConA) and positive control (1000 nM LecA) behaved as expected. In the presence of the inhibitor, colouration was lost at OD 0.4, suggesting the gal-AuNP interaction with *P. aeruginosa* was through a selective galactose binding event. Interestingly, the appearance of the bound gal-AuNPs on the filter was different when bound to bacteria or just lectin. The bacterial binding was more 'speckled' in appearance, which was also seen in Figure 4.10 between the cationic-AuNPs and *E. coli*.
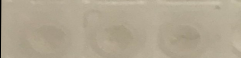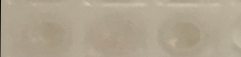
Figure 4.21: Filter plate assay results of gal-AuNPs with increasing *P. aeruginosa* cell densities (OD 0.1-0.8), in the presence (+) and absence (-) of inhibitor. Positive control is LecA (1000 nM) and negative controls are buffer (no lectin or bacteria) and ConA (1000 nM).

At this point, the aim was to assess the sensitivity of the gal-AuNP binding interaction with PAO1. Unfortunately, the results could not be repeated. Many repeats of the same conditions, along with different cell densities, gal-AuNP concentrations and $CaCl_2$ concentrations were tested but no binding was observed.

In 2018, Donnier-Marechal *et al.*[30] also demonstrated similar findings. The group developed galactose glycoclusters that exhibited high affinity to LecA (K_d = ~80 nM) but could not confirm binding to *P. aeruginosa* PAO1 through adhesion assays, using these glycoclusters. The authors suggested that improvements could be made by increasing valency. The LecA used to optimise these conditions was soluble LecA. Possibly, when LecA is attached to the outer membrane, the presentation for glycan binding may differ. Bacteria present a complex environment for binding. Bacteria, and especially *P. aeruginosa* , undergo differential gene expression depending on growth state, cell density and environmental factors[46][47][48]. LecA was shown to be expressed with this *P. aeruginosa* strain over biological repeats but other factors may affect accessibility of the lectin. Variability in the phenotype could arise from small changes to the environment, or through mutations, resulting in large effects on binding[49].

4.4   Conclusions

This chapter demonstrates the use of 16 nm galactose-AuNPs for the selective detection of the *P. aeruginosa* lectin LecA, using a UV-Vis based plate assay and a novel filter based assay. The filter plate assay provides a method of detecting bacterial binding with 16 nm AuNPs, in a high throughput design by using 384-well plates. UV-Vis plate based methods are difficult to monitor bacterial binding interactions, as the change in UV-Vis spectra relies on the glycoAuNPs being in close enough contact with each other to alter the way they interact with light. Bacterial cells such as *E. coli* and *P. aeruginosa* are 0.5-2 μm in length. To the best of our knowledge, no study has quantitatively determined the density

of the *P. aeruginosa* cell-surface lectins. Consequently, the cell-surface density is unknown, and so the inter-lectin spacing may mean that the glycoAuNPs are too distant from one another to observe characteristic changes in the extinction spectra. The absorption spectra of bacteria also masks large portions of the gal-AuNPs, and so it is difficult to determine extinction spectra changes from bacterial presence, and changes due to binding.

The ability of the filter plate assay to detect bacterial binding by 16 nm AuNPs was first assessed using TMAC-AuNPs and *E. coli*. Non-specific and widespread binding is achieved by using positively charged ligands (TMAC). The TMAC-AuNPs bound to negatively charged groups on the bacterial cell surface. The binding was shown by a red colouration on the filter surface, which suggested even a wide-spread coverage of the particles on the cell surface did not elicit a blue change in colour. As mentioned above, this is likely due to the spacing of the particles on the surface of bacteria. Interestingly, the binding gave a more 'speckled' presentation on the filter, as oppose to a film-like appearance across the surface with LecA aggregates.

LecA expression was then examined at different time points through *P. aeruginosa* growth. LecA was expressed in the later stages of log phase and stationary phase of growth (10 hours >). As bacteria can provide complex environments, the binding of gal-AuNPs to the target LecA was assessed separately. Confirmation of the importance of $CaCl_2$ for galactose-LecA binding was shown, with no binding detected when $CaCl_2$ was absent. Higher concentrations of galactose ligand for AuNP functionalisation showed more aggregation with LecA, than those with lower concentrations of galactose ligand. This suggested more galactose was on the surface of the AuNPs, and this higher density gave stronger binding. Multivalency is key to achieving strong LecA interactions.

Effects on binding were assessed at 25°C and 37°C. Greater binding was observed with the lower temperature of 25°C, which is consistent with reports in the literature of hemagglutination by LecA is better at lower temperatures. The binding observed between the gal-AuNPs and LecA was shown to be a

154

selective interaction by using a galactose-derivative LecA inhibitor (inhibitor). By introducing 1 mM of inhibitor, the filter plate assay demonstrated loss of binding by lack of filter colouration. The inhibitory studies also highlight limitations of the UV-Vis plate assay, as there was increased background (0 nM LecA) Ex_{678} values of the gal-AuNPs when inhibitor was present. Although, no detectable increase in Ex_{678} was observed with increasing LecA concentrations when inhibitor was present. Even with the higher Ex_{678} value, there was still a notable inhibition in the Ex_{678} at higher LecA concentrations (>250 nM).

The gal-AuNPs were then shown to bind *P. aeruginosa* at an OD of 0.4. The interaction was shown to be galactose-specific as inhibitor presence inhibited the binding. This was shown by a loss of red colouration on the filter when inhibitor was present. The inhibitor also demonstrates that the gal-AuNPs can still pass through the filter at those densities of bacteria, and so the colouration of the filter is due to bound gal-AuNPs, not that the particles are stuck from bacteria blocking the filter. The experiment was repeated many times but the results could not be reproduced. Elsewhere, similar results have been attained with galactose glycoconjugates, where strong LecA binding was achieved but could not demonstrate bacterial binding[30].

In conclusion, the results from this chapter have demonstrated that 16 nm AuNPs can be used to detect bacterial binding using a novel, filtration-based plate assay. Furthermore, gal-AuNPs were shown to selectively bind LecA at 64 nM. The gal-AuNPs selectively bound *P. aeruginosa* cultures of OD 0.4 but were not reproducible. Unfortunately, due to time constraints, exploring the reasons behind the loss of binding was not possible. If there was more time, some of the experiments that would have been carried out would have been cultures from different growth points, lower temperatures for binding experiments, and different densities of galactose on the surface.

References

[1] N. Mesaros, P. Nordmann, P. Plésiat, M. Roussel-Delvallez, J. Van Eldere, Y. Glupczynski, Y. Van Laethem, F. Jacobs, P. Lebecque, A. Malfroot, P. Tulkens, and F. Van Bambeke, "Pseudomonas aeruginosa: resistance and therapeutic options at the turn of the new millennium," *Clinical Microbiology and Infection*, vol. 13, no. 6, pp. 560–578, 2007. DOI: `10.1111/J.1469-0691.2007.01681.X`.

[2] V. Aloush, S. Navon-Venezia, Y. Seigman-Igra, S. Cabili, and Y. Carmeli, "Multidrug-resistant Pseudomonas aeruginosa: risk factors and clinical impact.," *Antimicrobial agents and chemotherapy*, vol. 50, no. 1, pp. 43–8, 2006. DOI: `10.1128/AAC.50.1.43-48.2006`.

[3] D. Golemi-Kotra, "Pseudomonas Infections," *xPharm: The Comprehensive Pharmacology Reference*, pp. 1–8, 2008. DOI: `10.1016/B978-008055232-3.63828-0`.

[4] A. J. Spiers, A. Buckling, and P. B. Rainey, "The causes of Pseudomonas diversity," Tech. Rep., 2000, pp. 2345–2350.

[5] A. Siryaporn, S. L. Kuchma, G. A. O'toole, and Z. Gitai, "Surface attachment induces Pseudomonas aeruginosa virulence," vol. 111, no. 47, pp. 16 860–16 865, 2014. DOI: `10.1073/pnas.1415712111`.

[6] ECDC, "Antimicrobial resistance surveillance in Europe," Tech. Rep., 2017.

[7] H. R. Goli, M. R. Nahaei, M. Ahangarzadeh Rezaee, A. Hasani, H. Samadi Kafil, and M. Aghazadeh, "Emergence of colistin resistant Pseudomonas aeruginosa at Tabriz hospitals, Iran.," *Iranian journal of microbiology*, vol. 8, no. 1, pp. 62–9, 2016.

[8] E. Tacconelli, E. Carrara, A. Savoldi, S. Harbarth, M. Mendelson, D. L. Monnet, C. Pulcini, G. Kahlmeter, J. Kluytmans, Y. Carmeli, M. Ouellette, K. Outterson, J. Patel, M. Cavaleri, E. M. Cox, C. R. Houchens, M. L. Grayson, P. Hansen, N. Singh, U. Theuretzbacher, N. Magrini, A. O. WHO Pathogens Priority List Working Group, S. S. Al-Abri, N. A. Jalil, N. Benzonana, S. Bhattacharya, A. J. Brink, F. R. Burkert, O. Cars, G. Cornaglia, O. J. Dyar, A. W. Friedrich, A. C. Gales, S. Gandra, C. G. Giske, D. A. Goff, H. Goossens, T. Gottlieb, M. G. Blanco, W. Hryniewicz, D. Kattula, T. Jinks, S. S. Kanj, L. Kerr, M.-P. Kieny, Y. S. Kim, R. S. Kozlov, J. Labarca, R. Laxminarayan, K. Leder, L. Leibovici, G. Levy-Hara, J. Littman, S. Malhotra-Kumar, V. Manchanda, L. Moja, B. Ndoye, A. Pan, D. L. Paterson, M. Paul, H. Qiu, P. Ramon-Pardo, J. Rodríguez-Baño, M. Sanguinetti, S. Sengupta, M. Sharland, M. Si-Mehand, L. L. Silver, W. Song, M. Steinbakk, J. Thomsen, G. E. Thwaites, J. W. van der Meer, N. V. Kinh, S. Vega, M. V. Villegas, A. Wechsler-Fördös, H. F. L. Wertheim, E. Wesangula, N. Woodford, F. O. Yilmaz, and A. Zorzet, "Discovery, research, and development of new antibiotics: the WHO priority list of antibiotic-resistant bacteria and tuberculosis.," *The Lancet. Infectious diseases*, vol. 18, no. 3, pp. 318–327, 2018. DOI: `10.1016/S1473-3099(17)30753-3`.

[9] J. Wu, H. Xu, W. Tang, R. Kopelman, M. Philbert, and C. Xi, "Eradication of bacteria in suspension and biofilms using methylene blue-loaded dynamic nanoplatforms.," *Antimicrobial agents and chemotherapy*, vol. 53, pp. 3042–8, 2009.

[10]   N. Høiby, T. Bjarnsholt, M. Givskov, S. Molin, and O. Ciofu, "Antibi-
        otic resistance of bacterial biofilms," *International Journal of Antimicrobial
        Agents*, vol. 35, no. 4, pp. 322–332, 2010. DOI: `10.1016/J.IJANTIMICAG.
        2009.12.011`.

[11]   S. Rajan and L. Saiman, "Pulmonary infections in patients with cystic
        fibrosis.," *Seminars in respiratory infections*, vol. 17, no. 1, pp. 47–56, 2002.

[12]   J. S. Elborn, D. J. Shale, and J. R. Britton, "Cystic fibrosis: current sur-
        vival and population estimates to the year 2000.," *Thorax*, vol. 46, no. 12,
        pp. 881–5, 1991. DOI: `10.1136/thx.46.12.881`.

[13]   J. W. Peterson, *Bacterial Pathogenesis*. University of Texas Medical Branch
        at Galveston, 1996, ISBN: 0963117211.

[14]   M. Chatterjee, C. Anju, L. Biswas, V. Anil Kumar, C. Gopi Mohan, and
        R. Biswas, "Antibiotic resistance in Pseudomonas aeruginosa and alter-
        native therapeutic options," *International Journal of Medical Microbiology*,
        vol. 306, no. 1, pp. 48–58, 2016. DOI: `10.1016/J.IJMM.2015.11.004`.

[15]   S. P. Diggle, K. Winzer, S. R. Chhabra, K. E. Worrall, M. Cámara, and
        P. Williams, "The Pseudomonas aeruginosa quinolone signal molecule
        overcomes the cell density-dependency of the quorum sensing hierarchy,
        regulates rhl-dependent genes at the onset of stationary phase and can
        be produced in the absence of LasR," *Molecular Microbiology*, vol. 50,
        no. 1, pp. 29–43, 2003. DOI: `10.1046/j.1365-2958.2003.03672.x`.

[16]   C. Chemani, A. Imberty, S. De Bentzmann, M. Pierre, M. Wimmerová,
        B. P. Guery, and K. Faure, "Role of LecA and LecB Lectins in Pseu-
        domonas aeruginosa-Induced Lung Injury and Effect of Carbohydrate
        Ligands," *INFECTION AND IMMUNITY*, vol. 77, no. 5, pp. 2065–2075,
        2009. DOI: `10.1128/IAI.01204-08`.

[17]   O. Bajolet-Laudinat, S. Girod-de Bentzmann, J. M. Tournier, C. Madoulet,
        M. C. Plotkowski, C. Chippaux, and E. Puchelle, "Cytotoxicity of Pseu-

domonas aeruginosa internal lectin PA-I to respiratory epithelial cells in primary culture.," *Infection and immunity*, vol. 62, no. 10, pp. 4481–7, 1994.

[18] R. S. Laughlin, M. W. Musch, C. J. Hollbrook, F. M. Rocha, E. B. Chang, and J. C. Alverdy, "The key role of Pseudomonas aeruginosa PA-I lectin on experimental gut-derived sepsis.," *Annals of surgery*, vol. 232, no. 1, pp. 133–42, 2000. DOI: `10.1097/00000658-200007000-00019`.

[19] S. P. Diggle, R. E. Stacey, C. Dodd, M. Cámara, P. Williams, and K. Winzer, "The galactophilic lectin, LecA, contributes to biofilm development in Pseudomonas aeruginosa," *Environmental Microbiology*, vol. 8, no. 6, pp. 1095–1104, 2006. DOI: `10.1111/j.1462-2920.2006.001001.x`.

[20] G. Cioci, E. P. Mitchell, C. Gautier, M. Wimmerová, D. Sudakevitz, S. Pérez, N. Gilboa-Garber, and A. Imberty, "Structural basis of calcium and galactose recognition by the lectin PA-IL of <i>Pseudomonas aeruginosa</i>," *FEBS Letters*, vol. 555, no. 2, pp. 297–301, 2003. DOI: `10.1016/S0014-5793(03)01249-3`.

[21] J. Rodrigue, G. Ganne, B. Blanchard, C. Saucier, D. Giguère, T. C. Shiao, A. Varrot, A. Imberty, and R. Roy, "Aromatic thioglycoside inhibitors against the virulence factor LecA from Pseudomonas aeruginosa," *Organic & Biomolecular Chemistry*, vol. 11, no. 40, p. 6906, 2013. DOI: `10.1039/c3ob41422a`.

[22] R. U. Kadam, M. Bergmann, D. Garg, G. Gabrieli, A. Stocker, T. Darbre, and J.-L. Reymond, "Structure-Based Optimization of the Terminal Tripeptide in Glycopeptide Dendrimer Inhibitors of <i>Pseudomonas aeruginosa</i> Biofilms Targeting LecA," *Chemistry - A European Journal*, vol. 19, no. 50, pp. 17 054–17 063, 2013. DOI: `10.1002/chem.201302587`.

[23] R. U. Kadam, M. Bergmann, M. Hurley, D. Garg, M. Cacciarini, M. A. Swiderska, C. Nativi, M. Sattler, A. R. Smyth, P. Williams, M. Cámara,

A. Stocker, T. Darbre, and J.-L. Reymond, "A glycopeptide dendrimer inhibitor of the galactose-specific lectin LecA and of Pseudomonas aeruginosa biofilms.," *Angewandte Chemie (International ed. in English)*, vol. 50, no. 45, pp. 10631–5, 2011. DOI: `10.1002/anie.201104342`.

[24]   M. Reynolds, M. Marradi, A. Imberty, S. Penadés, and S. Pérez, "Multivalent Gold Glycoclusters: High Affinity Molecular Recognition by Bacterial Lectin PA-IL," *Chemistry - A European Journal*, vol. 18, no. 14, pp. 4264–4273, 2012. DOI: `10.1002/chem.201102034`.

[25]   M. Bergmann, G. Michaud, R. Visini, X. Jin, E. Gillon, A. Stocker, A. Imberty, T. Darbre, and J.-L. Reymond, "Organic & Biomolecular Chemistry Multivalency effects on Pseudomonas aeruginosa biofilm inhibition and dispersal by glycopeptide dendrimers targeting lectin LecA," *Organic & Biomolecular Chemistry*, vol. 14, 2015. DOI: `10.1039/c5ob01682g`.

[26]   R. Visini, X. Jin, M. Bergmann, G. Michaud, F. Pertici, O. Fu, A. Pukin, T. R. Branson, D. M. E. Thies-Weesie, J. Kemmink, E. Gillon, A. Imberty, A. Stocker, T. Darbre, R. J. Pieters, and J.-L. Reymond, "Structural Insight into Multivalent Galactoside Binding to <i>Pseudomonas aeruginosa</i> Lectin LecA," *ACS Chemical Biology*, vol. 10, no. 11, pp. 2455–2462, 2015. DOI: `10.1021/acschembio.5b00302`.

[27]   T. R. Flockton, L. Schnorbus, A. Araujo, J. Adams, M. Hammel, and L. J. Perez, "Inhibition of Pseudomonas aeruginosa Biofilm Formation with Surface Modified Polymeric Nanoparticles.," *Pathogens (Basel, Switzerland)*, vol. 8, no. 2, 2019. DOI: `10.3390/pathogens8020055`.

[28]   S. Cecioni, S. Faure, U. Darbost, I. Bonnamour, H. Parrot-Lopez, O. Roy, C. Taillefumier, M. Wimmerová, J. P. Praly, A. Imberty, and S. Vidal, "Selectivity among two lectins: Probing the effect of topology, multivalency and flexibility of "clicked" multivalent glycoclusters," *Chemistry - A European Journal*, vol. 17, no. 7, pp. 2146–2159, 2011. DOI: `10.1002/chem.201002635`.

[29] S. Cecioni, V. Oerthel, J. Iehl, M. Holler, D. Goyard, J. P. Praly, A. Imberty, J. F. Nierengarten, and S. Vidal, "Synthesis of dodecavalent fullerene-based glycoclusters and evaluation of their binding properties towards a bacterial lectin," *Chemistry - A European Journal*, vol. 17, no. 11, pp. 3252–3261, 2011. DOI: `10.1002/chem.201003258`.

[30] M. Donnier-Maréchal, S. Abdullayev, M. Bauduin, Y. Pascal, M.-Q. Fu, X.-P. He, E. Gillon, A. Imberty, E. Kipnis, R. Dessein, and S. Vidal, "Tetraphenylethylene-based glycoclusters with aggregation-induced emission (AIE) properties as high-affinity ligands of bacterial lectins," *Organic & Biomolecular Chemistry*, vol. 16, no. 45, pp. 8804–8809, 2018. DOI: `10.1039/C8OB02035C`.

[31] C. Ligeour, O. Vidal, L. Dupin, F. Casoni, E. Gillon, A. Meyer, S. Vidal, G. Vergoten, J. M. Lacroix, E. Souteyrand, A. Imberty, J. J. Vasseur, Y. Chevolot, and F. Morvan, "Mannose-centered aromatic galactoclusters inhibit the biofilm formation of Pseudomonas aeruginosa," *Organic and Biomolecular Chemistry*, vol. 13, no. 31, pp. 8433–8444, 2015. DOI: `10.1039/c5ob00948k`.

[32] F. Zuttion, C. Ligeour, O. Vidal, M. Wälte, F. Morvan, S. Vidal, J. J. Vasseur, Y. Chevolot, M. Phaner-Goutorbe, and H. Schillers, "The anti-adhesive effect of glycoclusters on: Pseudomonas aeruginosa bacteria adhesion to epithelial cells studied by AFM single cell force spectroscopy," *Nanoscale*, vol. 10, no. 26, pp. 12 771–12 778, 2018. DOI: `10.1039/c8nr03285h`.

[33] F. Pertici, N. J. De Mol, J. Kemmink, and R. J. Pieters, "Optimizing divalent inhibitors of pseudomonas aeruginosa lectin leca by using a rigid spacer," *Chemistry - A European Journal*, vol. 19, no. 50, pp. 16 923–16 927, 2013. DOI: `10.1002/chem.201303463`.

[34] S.-F. Huang, C.-H. Lin, Y.-T. Lai, C.-L. Tsai, T.-J. R. Cheng, and S.-K. Wang, "Development of Pseudomonas aeruginosa Lectin LecA Inhibitors us-

ing Bivalent Galactosides Supported on Polyproline Peptide Scaffolds,"
Chemistry - An Asian Journal, 2018. DOI: `10.1002/asia.201701724`.

[35] X. Huang and M. A. El-Sayed, "Gold nanoparticles: Optical properties
and implementations in cancer diagnosis and photothermal therapy,"
Journal of Advanced Research, vol. 1, no. 1, pp. 13–28, 2010. DOI: `10.1016/`
`j.jare.2010.02.002`.

[36] D. Hone, A. Haines, and D. Russell, "Rapid, quantitative colorimet-
ric detection of a lectin using mannose-stabilized gold nanoparticles.,"
Langmuir, vol. 19, pp. 7141–7144, 2003. DOI: `10.1021/la034358v`.

[37] C. L. Schofield, B. Mukhopadhyay, S. M. Hardy, M. B. McDonnell, R. A.
Field, and D. A. Russell, "Colorimetric detection of Ricinus communis
Agglutinin 120 using optimally presented carbohydrate-stabilised gold
nanoparticles," *The Analyst*, vol. 133, no. 5, p. 626, 2008. DOI: `10.1039/`
`b715250g`.

[38] C. L. Schofield, R. A. Field, and D. A. Russell, "Glyconanoparticles for
the colorimetric detection of cholera toxin," *Analytical Chemistry*, vol. 79,
no. 4, pp. 1356–1361, 2007. DOI: `10.1021/ac061462j`.

[39] M. J. Marín, A. Rashid, M. Rejzek, S. Fairhurst, S. Wharton, S. Martin, J.
McCauley, T. Wileman, R. Field, and D. Russell, "Glyconanoparticles for
the plasmonic detection and discrimination between human and avian
influenza virus.," *Organic & Biomolecular Chemistry*, vol. 11, pp. 7101–
7107, 2013. DOI: `10.1039/c3ob41703d`.

[40] M. S. Verma, J. L. Rogowski, L. Jones, and F. X. Gu, "Colorimetric biosens-
ing of pathogens using gold nanoparticles," *Biotechnology Advances*, 2015.
DOI: `10.1016/j.biotechadv.2015.03.003`.

[41] B. Fang, S. Gon, M. Park, K.-N. Kumar, V. M. Rotello, K. Nusslein, and
M. M. Santore, "Bacterial adhesion on hybrid cationic nanoparticle-
polymer brush surfaces: ionic strength tunes capture from monovalent

to multivalent binding.," *Colloids and surfaces. B, Biointerfaces*, vol. 87, no. 1, pp. 109–15, 2011. DOI: `10.1016/j.colsurfb.2011.05.010`.

[42] P. P. Pillai, B. Kowalczyk, K. Kandere-Grzybowska, M. Borkowska, and B. A. Grzybowski, "Engineering Gram Selectivity of Mixed-Charge Gold Nanoparticles by Tuning the Balance of Surface Charges," *Angewandte Chemie*, vol. 128, no. 30, pp. 8752–8756, 2016. DOI: `10.1002/ange.201602965`.

[43] J. Klockgether, A. Munder, J. Neugebauer, C. F. Davenport, F. Stanke, K. D. Larbig, S. Heeb, U. Schöck, T. M. Pohl, L. Wiehlmann, and B. Tümmler, "Genome diversity of Pseudomonas aeruginosa PAO1 laboratory strains," *Journal of Bacteriology*, vol. 192, no. 4, pp. 1113–1121, 2010. DOI: `10.1128/JB.01515-09`.

[44] K. Karaveg, Z.-J. Liu, W. Tempel, R. J. Doyle, J. P. Rose, and B.-C. Wang, "Crystallization and preliminary X-ray diffraction analysis of lectin-1 from <i>Pseudomonas aeruginosa</i>," *Acta Crystallographica Section D Biological Crystallography*, vol. 59, no. 7, pp. 1241–1242, 2003. DOI: `10.1107/S0907444903008710`.

[45] N. Gilboa-Garber and D. Sudakevitz, "The hemagglutinating activities of <i>Pseudomonas aeruginosa</i> lectins PA-IL and PA-IIL exhibit opposite temperature profiles due to different receptor types," *FEMS Immunology & Medical Microbiology*, vol. 25, no. 4, pp. 365–369, 1999. DOI: `10.1111/j.1574-695X.1999.tb01361.x`.

[46] Y. Choi, H.-Y. Park, S. J. Park, S.-J. Park, S.-K. Kim, C. Ha, S.-J. Im, and J.-H. Lee, "Growth phase-differential quorum sensing regulation of anthranilate metabolism in Pseudomonas aeruginosa.," *Molecules and cells*, vol. 32, no. 1, pp. 57–65, 2011. DOI: `10.1007/s10059-011-2322-6`.

[47] J. R. Wiens, A. I. Vasil, M. J. Schurr, and M. L. Vasil, "Iron-regulated expression of alginate production, mucoid phenotype, and biofilm for-

mation by Pseudomonas aeruginosa," *mBio*, vol. 5, no. 1, 2014. DOI: `10.1128/mBio.01010-13`.

[48] C. Harmer, K. Alnassafi, H. Hu, M. Elkins, P. Bye, B. Rose, S. Cordwell, J. A. Triccas, C. Harbour, and J. Manos, "Modulation of gene expression by Pseudomonas aeruginosa during chronic infection in the adult cystic fibrosis lung.," *Microbiology (Reading, England)*, vol. 159, no. Pt 11, pp. 2354–63, 2013. DOI: `10.1099/mic.0.066985-0`.

[49] A. E. LaBauve and M. J. Wargo, "Growth and Laboratory Maintenance of Pseudomonas aeruginosa," *Current protocols in microbiology*, vol. 0 6, Unit, 2012. DOI: `10.1002/9780471729259.mc06e01s25`.

Chapter 5

Developing targeted photodynamic therapy of breast cancer cells

The PhD research carried out in this chapter developed a targeted photodynamic therapy approach to selectively kill cultured breast cancer cells. The final system used 16 nm AuNPs functionalised with PS (ce6) and glycan (galactose) to localise the PS to the target cell surface (gal-/ce6-AuNPs). Two breast cancer cell lines (MDA-MB-231 and SK-BR-3) and one non-cancer breast cell line (MCF-10A) were used.

5.1   Introduction

Breast cancer is one of the leading types of cancer worldwide, accounting for over two million of all cancer diagnoses (11.6%) in 2018[1]. It is the most common cancer found in women, and although men are 100 times less likely to have breast cancer[2], poor prognosis is often observed due to slow diagnosis. Breast cancer is well known for its varied and heterogeneous disease presentation[3], making it difficult to easily classify the cancer. The most common types of breast cancer arise in the glandular tissue (adenocarcinomas)[4]. The glandular tissue is composed of: lobules, which are the milk-producing glands; and ducts,

which are responsible for milk delivery[5]. Breast carcinomas can be classified as invasive or in situ (non-invasive). Invasive means that the tumour has spread to other breast tissue, or to other areas in the body (metastasised). Common areas for metastasis are the lungs, brain, bone and liver[6].

5.1.1 Current treatments

Treatment of breast cancer depends on the type, and what stage the cancer is. The stage of cancer is dependent on a host of factors, including tumour size, phenotypic/genetic traits, and whether the cancer has metastasised. The presence of varying receptors on the cancer cell surface affect prognosis. The three main receptors are oestrogen receptor (ER), progesterone receptor (PR) and human epidermal growth factor receptor 2 (HER2)[7]. If receptor expression is higher than the corresponding healthy breast cells, the breast cancer will be determined receptor positive. In contrast, if levels are not above those of the healthy cells, the cancer is deemed receptor negative. Consequently a mixture of classifications can be made with ER-, PR-, and HER2- negative and positive combinations. Triple negative breast cancer (TNBC) is when the cancer is ER-, PR-, and HER2-negative. TNBC is associated with poor prognosis from being metastatic, aggressive and fewer treatment options available [8].

Common treatments for breast cancer include surgery, radiotherapy, chemotherapy, immunotherapy, hormone therapy and targeted therapy [9]. With ER-positive and/or PR-positive cancer, the hormones (oestrogen and progesterone) can promote proliferation of the cancer cells. Hormone therapy inhibits hormone signalling to the cancer cells, reducing cancer growth. For HER2-positive cancer, a range of targeted therapies have been developed and are in clinical use. For example, the monoclonal antibody Herceptin blocks growth signals through HER2, reducing tumour growth and invasiveness[10]. However, each breast cancer treatment has its limitations.

The lack of selectivity by conventional therapies results in nasty and well-

documented side effects, including sickness, susceptibility to infections, fatigue, loss of hair, blood clots, loss of appetite, sores and heart failure[11]. A major problem faced by both passive and targeted therapies that are currently available is the phenomenon of adaptive treatment tolerance (ATT), where anti-cancer drugs become less effective after repeat treatments. Possible explanations given for ATT are low uptake of the drug through the plasma membrane and increased efflux of the drug by the cancer cells activating drug-resistance mechanisms[12].

For the work herein, two breast cancer cell lines were used: MDA-MB-231, which is a TNBC line; and SK-BR-3, which is HER2-positive (ER- and PR-negative). The low, targeted treatment options available for TNBC, and the development of resistance by HER2-positive cancer cell lines to targeted therapies, coupled with their aggressive characteristics, highlights the importance of developing alternative therapies against these types of breast cancer. By exploring different methods of targeting, an approach to tackle multiple cancer subtypes may be possible. One such example may be their cell surface lectin repertoire.

5.1.2 Glycan-binding proteins as alternative drug targets

Cell-surface glycans are used by all cells to interact with their environment. By interacting with glycan binding proteins (lectins), these glycan-protein interactions allow cells to signal and communicate with one another; interact with the immune system; and attach to their surroundings[13]. For cancer, these glycan-protein interactions are key for avoiding immunosurveillance, and re-attachment to new tissue during metastasis[14]. Cancer cells are also associated with increased metabolism due to their unregulated, increased growth[15]. Therefore, glycan transporters are also increased. For breast cancer cells, there are key lectins and glycan-binding receptors that have been identified as being upregulated, which include galectins[16][17], glucose transporters (GLUTs)[18][19] and the mannose receptor[20][21].

167

Galectins

Galectins are lectins that bind β-D-galactosides[22]. In mammals, the galectin family is composed of 16 galectins, named galectin-1 to -16, with 12 of the family found in humans[23]. Galectins are subgrouped into prototype, tandem-repeat type or chimera type based on their CRD[24]. Prototype galectins have one CRD and encompass galectin-1, -2, -5, -7, -10, -11, -13 and -14, -15 and -16. Tandem-repeat type galectins are where two distinct CRDs are bridged by a linker, and include galectins: -4, -6, -8, -9 and -12 [23]. The final subgroup, the chimeric galectin-3, has one CRD with a repetitive amino acid sequence of proline, tyrosine and glycine at the N-terminus[25]. Some of the prototype galectins can form homodimers, such as galectin-1. Galectins can be found intracellular and extracellular, and can associate with the cell membrane[26]. They are found in various cell types, in both healthy and disease-state tissue. This diverse expression gives galectins many roles in the body, including immune modulation, cell migration and cell differentiation[27][28].

In cancer, galectins have been shown to play a role in apoptosis, cell growth, adhesion, metastasis, cellular repair, cell cycle regulation and suppression of T cell action[22]. Galectin-1 and -3 have received the most attention with regards to breast cancer, with extracellular and increased expression associated with progressed disease state[29]. Although galectin-3 has mixed roles documented in breast cancer, some studies, such as Ilmer *et al.* [30], show low expression of galectin-3 is associated with a poor prognosis. Zhang *et al.*[31] demonstrated that galectin-3 expression is high in TNBC, and that knockdown of galectin-3 increased sensitivity to apoptotic cell death induced by arsenic trioxide. The authors state that the TNBC cell line had increased galectin-3 expression, so possibly the variability in the literature arises from difference in presentation of galectin-3 between different breast cancer types and/or the stage of the cancer, as White *et al.*[32] demonstrated that galectin-3 is important for metastasis.

GLUTs

There are 13 members of the facilitative glucose transporter (GLUT) family in mammals, again numbered GLUT-1 through to GLUT-13. As the name suggests, GLUTs are responsible for glucose uptake but they also show selectivity for other hexoses, such as galactose and fructose, to varying degrees depending on the receptor[33]. Overexpression of GLUT-1 has been associated with aggressive breast cancers[19]. Other GLUTs that have been shown to be overexpressed in breast cancer are GLUT-2[34], GLUT-3[15] and GLUT-12[35]. Overexpression of GLUTs is associated with increased invasiveness and poor prognosis [33].

Mannose receptor

The mannose receptor is part of the mannose receptor family, and is a transmembrane receptor that can present up to ten C-type lectin-like domains. Mannose receptor is commonly expressed on macrophages, dendritic cells, and endothelial cells, and consequently has a role in immune modulation. Mannose receptor is associated with rapid internalisation, and is effective at molecule clearance, both self and non-self[36]. The mannose receptor has been demonstrated to be expressed in breast cancer but not healthy breast tissue, albeit to varying levels between different breast cancer types[3].

Consequently, in this PhD research, galactose, glucose, lactose and mannose were assessed for targeted binding of glycoconjugates to the cancer cell lines.

5.1.3 Nanoparticles for improved anti-cancer drug therapy

To sustain the high nutrient demand of fast-growing cells, cancer cells stimulate new blood vessel growth. However, the vasculature growth is erratic, creating large pores, and resulting in 'leaky' blood vessels that leads to a phenomenon known as the 'Enhanced Permeability Retention (EPR)' effect[37]. Drug molecules are able to 'leak' into the tumour mass through the pores, and as the cancer microenvironment often lacks a lymphatic system to clear the par-

ticles, this results in the accumulation of the drug in the tumour[38]. This forms the basis for passive targeting for many anti-cancer drugs. For passive targeting to be effective, the drug must avoid clearance by the reticuloendothelial system. Nanoparticles have been used in passive targeting, as they prolong circulation time in the blood, allowing for more effective accumulation in the tumour[39]. However, the effectiveness of passive targeting is limited. The extent of the EPR effect will vary between tumours, and the drug still needs to be effectively taken up by the cell and reach the target site of action.

Nanoparticles have the advantage of exhibiting high 'loading capacity' of a ligand/drug due to their high surface area to volume ratio, and can be modified with different ligands on their surface[40]. Consequently, both eradication and targeting elements can be coupled to the nanoparticles, to develop targeted delivery of the drug to the cancer cells (see Figure 5.1).
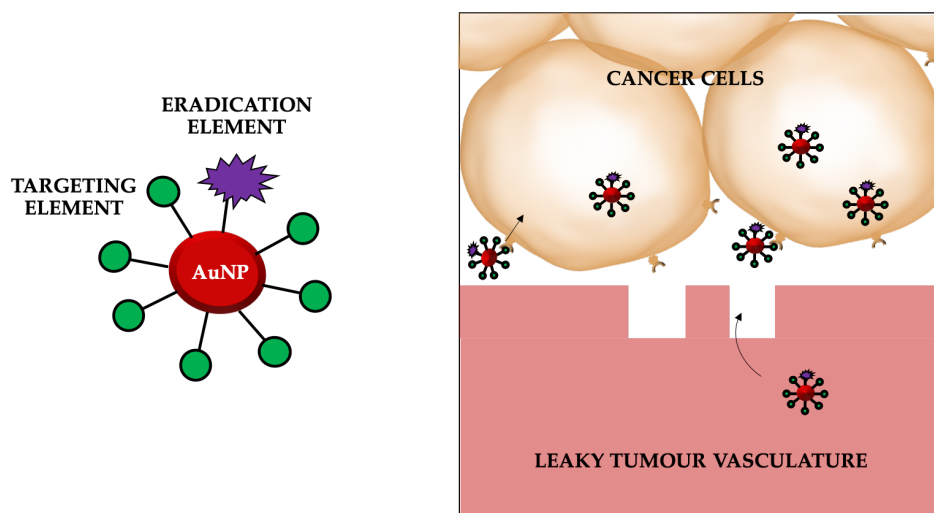
Figure 5.1: AuNPs modified with targeting and eradication elements (left) used for active targeting of cancer cells (right).

Nanoparticle based drug delivery can enhance safety and efficacy of the therapeutic [41], as they aim to carry the drug to the diseased area at a controlled rate [42]. This results in more drug reaching the target site, which lowers the amount of drug that needs to be administered. Lower doses of selective drugs

reduces the risk of non-target cell uptake, and consequently, reduces side effects.

One method of interest that has been employed for anti-cancer treatment through nanoparticles is photodynamic therapy (PDT). The drug used in PDT is a dye (PS), and so often hydrophobic. Coupling the dye to nanoparticles can improve the dispersibility and delivery. The nanoparticles can also offer multi-copy ligand presentation, and so, a targeting element can be introduced with the PS.

For the following studies, a chlorin e6 derivative (ce6, see Figure 5.2) was selected as the PS. Absorption of light by the PS would ideally be in the wavelength range where blood and tissue absorption is low, known as the 'therapeutic window' (600-800 nm)[43]. Ce6 absorbs at ~650 nm, which is key for therapeutic applications. Ce6 also exhibits good photostability, low dark toxicity, *i.e.*, does not generate ROS without light, and has high efficacy. However, ce6 has poor water solubility, and so can cause photosensitivity in therapeutic applications. Hydrophobic PSs can precipitate and non-specifically interact with healthy tissue, such as skin[44]. By conjugating ce6 to nanoparticles, solubility can be improved along with lower skin accumulation[45]. Consequently, by improving ce6 solubility and directing cellular uptake by the cancer cells, side effects can be reduced.
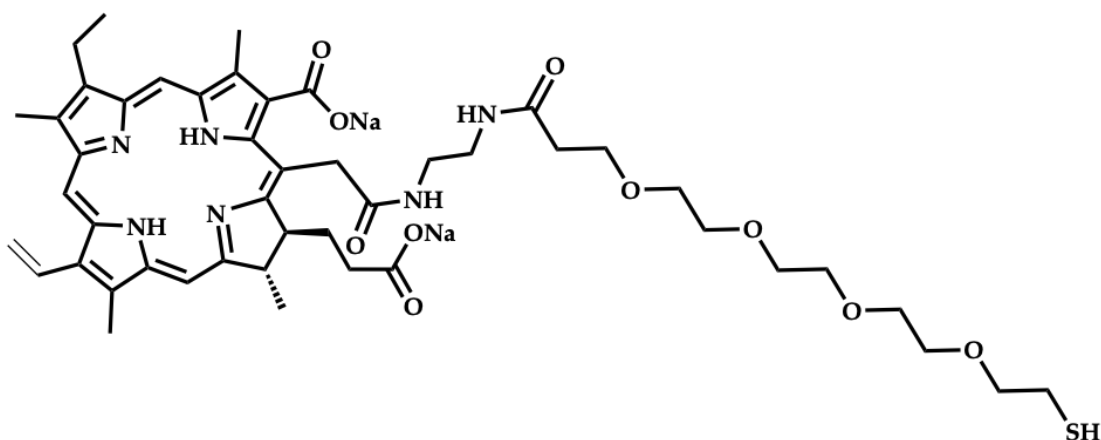
Figure 5.2: The structure of the chlorin e6 (ce6) derivative used for the PDT studies.

5.1.4 Targeted photodynamic therapy of breast cancer

To improve delivery of the PS into breast cancer cells, AuNPs have been used as a scaffold and coupled with different targeting ligands, including antibodies[46] and lactose [47]. In Garcia-Calavia *et al.*[47], 4 nm AuNPs were functionalised with lactose for targeting to galectins, coupled with a PS for cell killing. The study found increased expression of galectin-1 in MDA-MB-231 compared to SK-BR-3, but saw better cell death against SK-BR-3. With 3 hours treatment, cell death was only observed for SK-BR-3 cells. These results were not as expected, as the lactose was expected to selectively target overexpressed galectin-1 on the MDA-MB-231 cell line (findings are discussed in detail in Chapter 1.4.4).

Considering the results from Garcia-Calavia *et al.*[47], identifying a glycan candidate by comparing differential glycan binding may improve cell killing of both cell lines. Larger particles (17 nm) have also been demonstrated to have better uptake by cancer cells, than smaller particles (4 nm)[48]. By combining larger particles and identifying a candidate glycan through glycan binding studies, improvements to selective cell killing of the breast cancer lines were hoped to be made.

5.2 Scientific aims

The aim of the following experiments is to explore differential glycan binding by different breast cancer and healthy cell lines. Then using this information, a glycan candidate will be selected for delivering ce6 to the breast cancer cells for targeted cell uptake, and consequently, targeted cell killing by PDT.

5.3 Results and discussion

5.3.1 Comparing differences in cancer and non-cancer glycan interactions

The aim of the following studies was to determine differences in glycan binding between the cancer and non-cancer cell lines, to identify the best candidate for selective nanoparticle targeting.

Assessing glycan binding using glycan functionalised polyacrylamide polymer

The first step to design targeted binding was to compare the glycan binding profile of cancer and non-cancer cells, to determine difference in selectivity. For theses studies, commercially available polymer glycoconjugates (GlycoNZ) were used. The polymer was polyacrylamide (PAA) functionalised with glycan and biotin (PAA-glycan). The polymer was functionalised with galactose (PAA-gal), glucose (PAA-glc), lactose (PAA-lac) or mannose (PAA-man). As a negative control, PAA functionalised with biotin but no glycan was used (PAA). The binding was assessed by confocal microscopy, using a fluorescent Alexa Fluor 488 streptavidin conjugate (AF488-st) to detect PAA-glycan uptake by the cells (see Figure 5.3). To assess localisation of PAA-glycan, a dye that localises in acidic organelles was used (BioTracker$^{\text{TM}}$ 560 Orange Lysosome Dye). Full experimental details are described in Chapter 2.5.2.
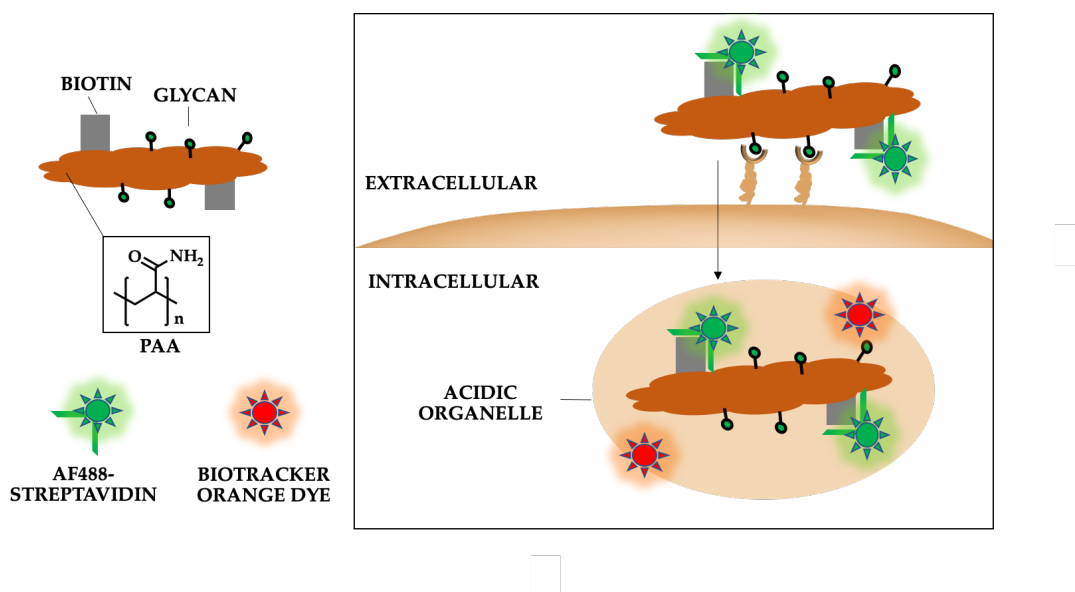
Figure 5.3: Illustration of confocal imaging studies assessing PAA-glycan interaction with cells.

In this work, two breast adenocarcinoma cell lines (MDA-MB-231 and SK-BR-3), along with a non-cancer breast epithelial cell line (MCF-10A) were used. The following will present the confocal images and quantification for each cell line and PAA-glycan interaction.

Cancer cell line: MDA-MB-231

Figure 5.4 shows a summary of images for MDA-MB-231 binding to the different PAA-glycans, and the quantified results are shown in Figure 5.6. From Figure 5.4, the localisation of the PAA-glycans was observed. Firstly, from the controls, there was no detectable non-specific binding between the PAA and the cells (Figure 5.4, cells + PAA + AF488-st), as no fluorescence was observed without glycan present on the PAA. The MDA-MB-231 cell line did not non-specifically bind or take-up the AF488-st, as seen by the lack of fluorescence when just cells and AF488-st were present (cells + AF488-st). Consequently, fluorescence from AF488-st was only detected when PAA-glycan was present (Figure 5.4), suggesting that the AF488-st was bound to biotin on the PAA-glycan.

Figure 5.4: Example of processed confocal images from PAA-glycan (galactose, glucose, lactose and mannose, top to bottom) binding to MDA-MB-231. Images are separated into no filter (differential interference contrast image, DIC), AF488-st (green filter), BioTracker Orange dye (orange filter) and composite, from left to right. AF488-st represents glycan binding, and BioTracker Orange dye represents acidic organelles.

With regards to PAA-glycan binding, all glycans appear to be localising in the acidic organelles within the MDA-MB-231 cell line, as seen from the overlap between the fluorescence from the green (AF488-st) and orange filters (BioTracker™ 560 Orange Lysosome Dye). To highlight this, Figure 5.5 shows enlarged images of MDA-MB-231 in the presence of PAA-glc, where it can be seen that the fluorescence from the green (Figure 5.5b) and orange filters (Figure 5.5c) overlap (Figure 5.5d), suggesting that the PAA-glc was localised in the acidic organelles, such as the lysosomes.
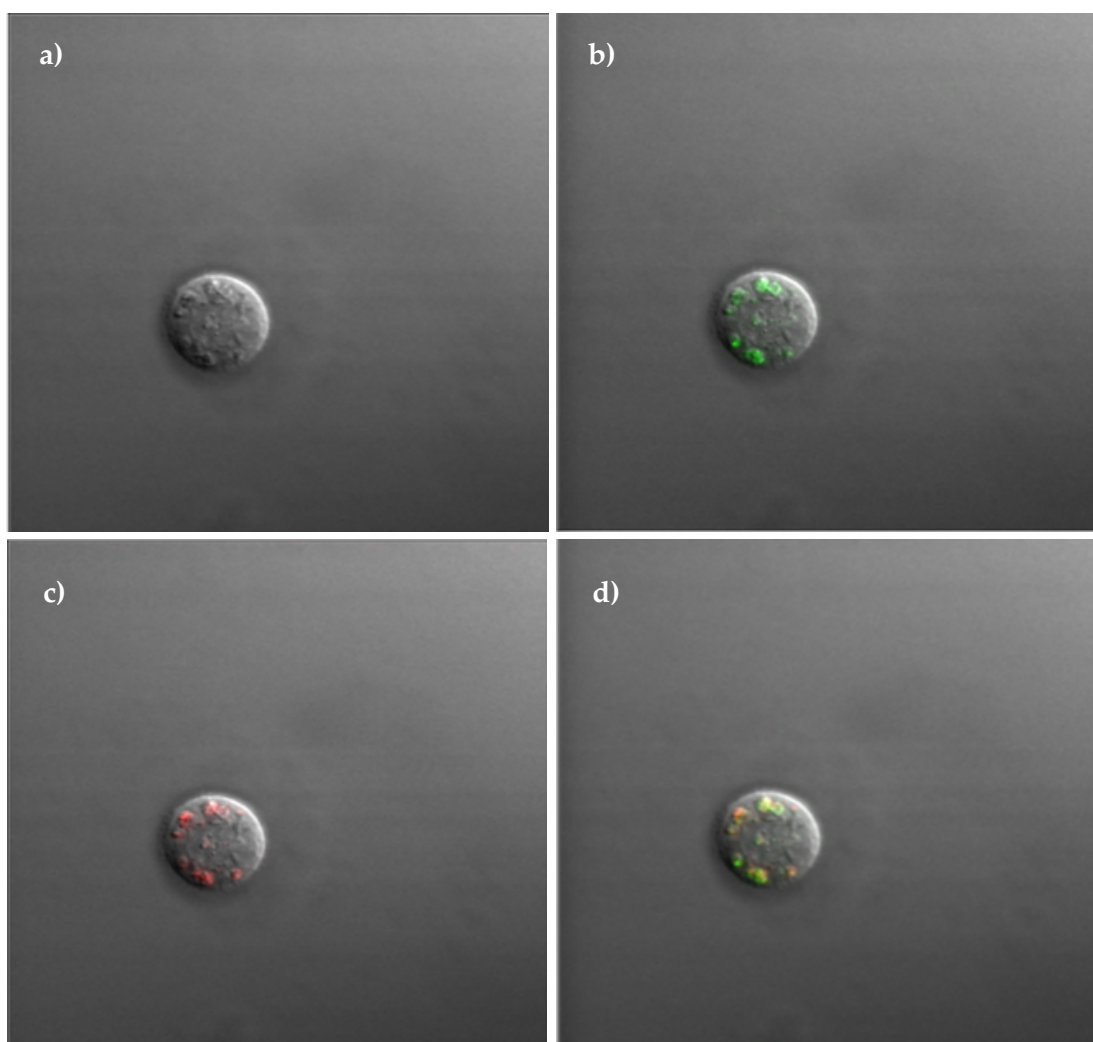
Figure 5.5: Enlarged images from Figure 5.4 of MDA-MB-231 in the presence in PAA-glc . Images are separated into: a) no filter (DIC); b) AF488-st (green filter) ; c) BioTracker Orange dye (orange filter); and d) composite image. AF488-st represents glycan binding, and BioTracker Orange dye represents acidic organelles.

From the confocal images in Figure 5.4, PAA-glc appeared to have the strongest fluorescence, where the PAA-man had lower levels of binding, however, to be able to quantify the observations from the confocal images, the mean integrated intensity of each condition was determined (Figure 5.6).

Cell line = MDA−MB−231

Figure 5.6: Quantitative analysis of confocal images from PAA-glycan binding to MDA-MB-231, showing the integrated intensity for each glycan (galactose, glucose, lactose and mannose, left to right) and controls. Error bars = +/- SEM, n=7 images. * = $p < 0.05$; ** = $p < 0.01$; *** = $p < 0.005$; ns = not significant.

From Figure 5.6, the strongest interaction was between PAA-glc and MDA-MB-231, as seen by PAA-glc showing the highest integrated intensity value of all of the glycans tested. There was also a statistically significant interaction between PAA-gal and PAA-lac for MDA-MB-231. However, no statistically significant interaction was detected with PAA-man and MDA-MB-231. From the confocal images (Figure 5.4) and from the the integrated intensity (Figure 5.6), there appears to be some level of binding between the PAA-man and MDA-MB-231 but did not demonstrate a consistent, statistically significant interaction,

177

which is emphasised by the weaker signal in the confocal images.

The low mannose interaction result was surprising as MDA-MB-231 has been documented to overexpress the mannose receptor[3]. Possibly the presentation of the mannose on the PAA was not optimal for mannose receptor binding.

Cancer cell line: SK-BR-3

Figure 5.7 shows a summary of the confocal images assessing PAA-glycan interactions with the cancer cell line: SK-BR-3. As with MDA-MB-231, the controls demonstrate that there was no detectable non-specific binding by the PAA with the SK-BR-3 cell line, as seen by the lack of fluorescence with the control PAA in Figure 5.7 (cells + PAA +AF488-st). Only fluorescence was detected with the green filter when PAA-glycan was present, demonstrating that the AF488-st was bound to the biotin on the PAA-glycan and did not non-specifically bind to the cells (cells + AF488-st, Figure 5.7). From Figure 5.7, PAA-gal and PAA-glc gave the strongest binding result, as the images had more fluorescent 'spots' in the green filter (AF488-st).

To assess the localisation of the PAA-gal and PAA-glc, enlarged images can be seen in Figure 5.8. PAA-gal appeared to be taken up by the SK-BR-3 cells and localised in the acidic organelles, such as the lysosomes. This can be seen from Figure 5.8b, which is the composite image of PAA-gal with SK-BR-3 cells. For PAA-glc (Figure 5.8c and d), the PAA-glycan predominantly appeared to be localised in the acidic organelles, as the fluorescence emitted from the AF488-st and BioTracker Orange dyes overlapped. However, PAA-glc was also present elsewhere in the cell, as can be seen in Figure 5.8d, where AF488-st (green spot) was not colocalised with the BioTracker Orange dye.
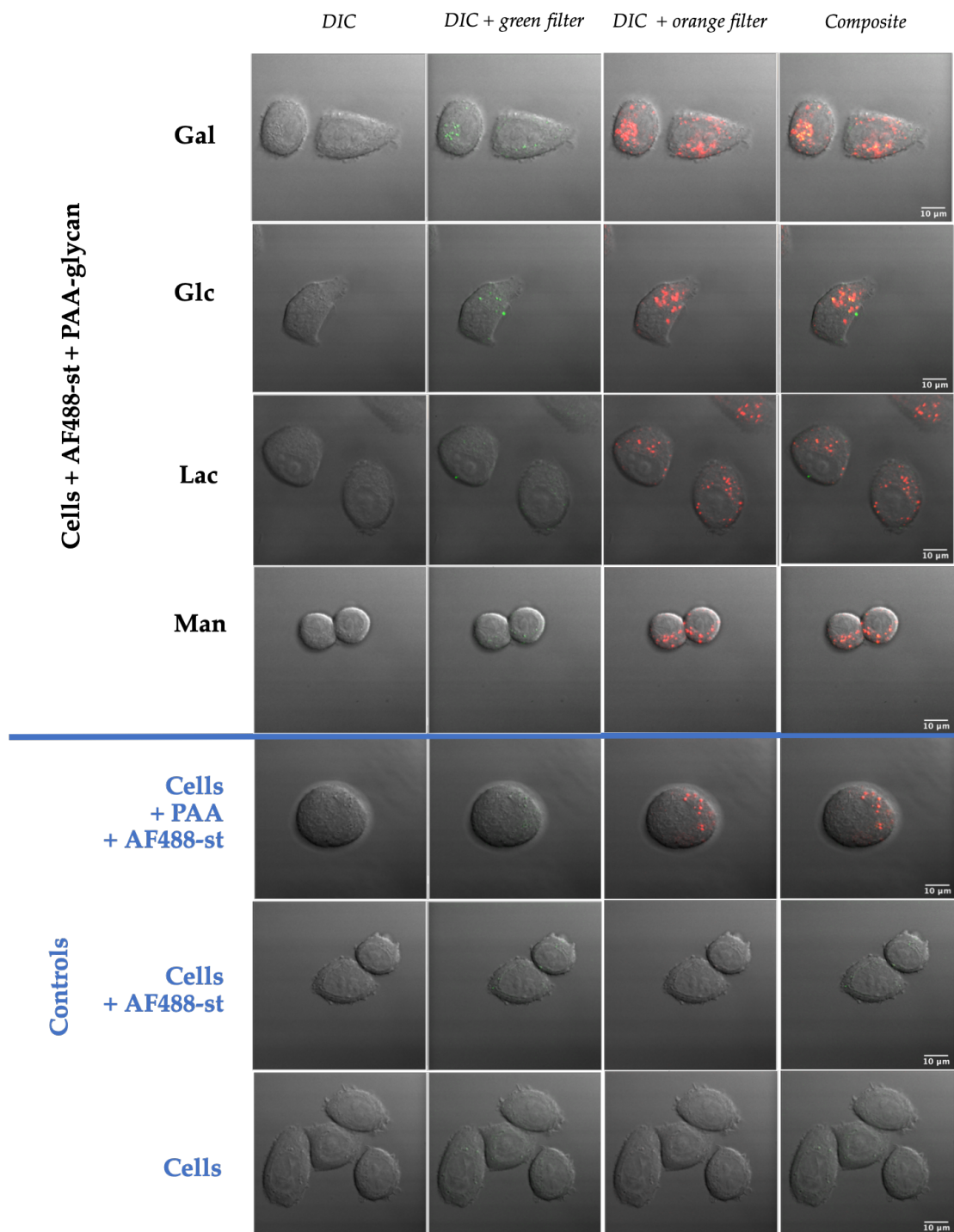
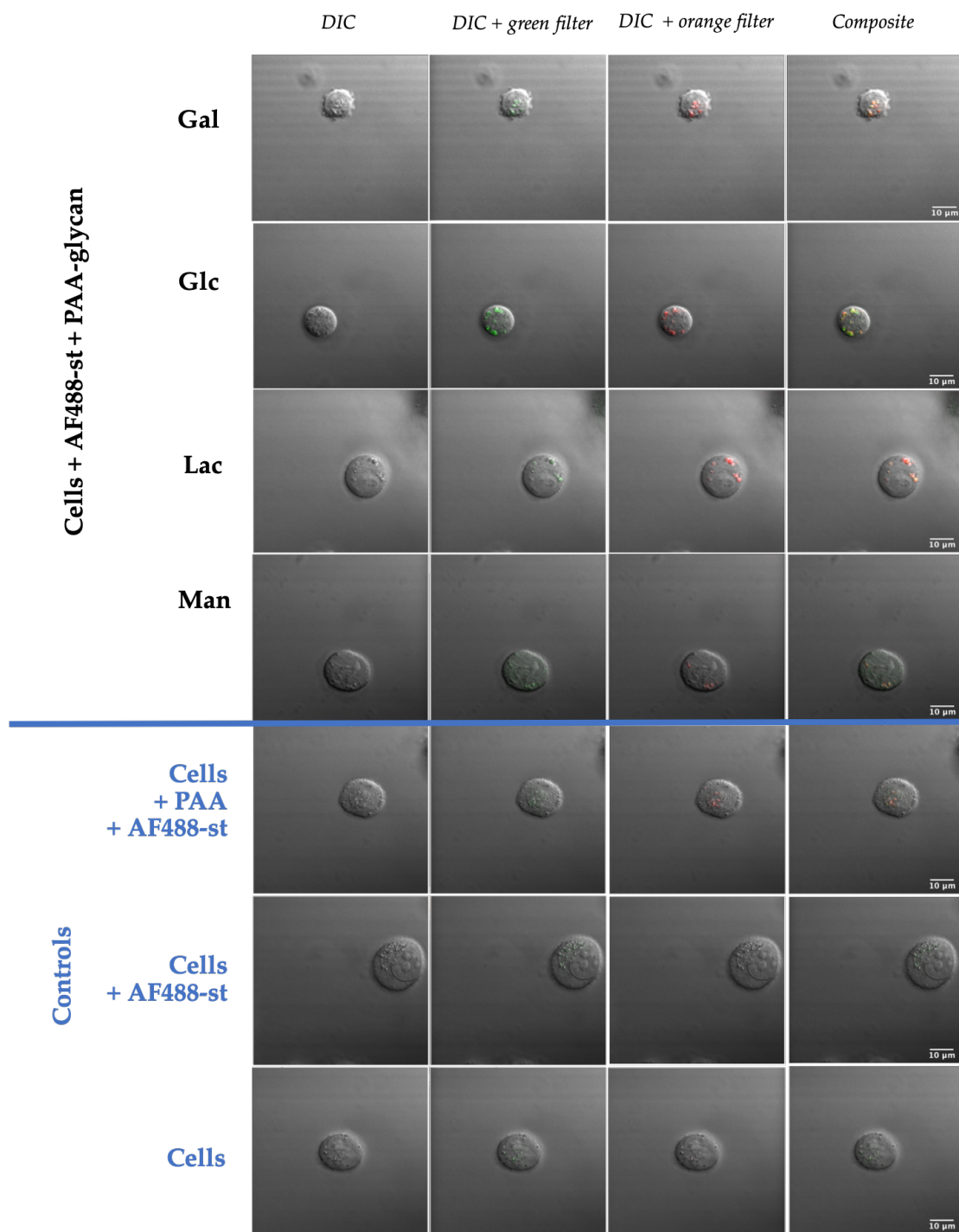**Figure 5.7:** Example of processed confocal images from PAA-glycan (galactose, glucose, lactose and mannose, top to bottom) binding to SK-BR-3. Images are separated into no filter (DIC image), AF488-st (green filter), BioTracker Orange dye (orange filter) and composite, from left to right. AF488-st represents glycan binding, and BioTracker Orange dye represents acidic organelles.

Further investigation would be needed to determine the full localisation of the PAA-glc across the cell, but possibly the uptake of the PAA-glc is slower than that of the PAA-gal, and consequently PAA-glc could still be localised on the cell surface. This could be explained by the PAA-gal and PAA-glc interacting with different cell surface receptors, which could effect rate of cellular uptake.
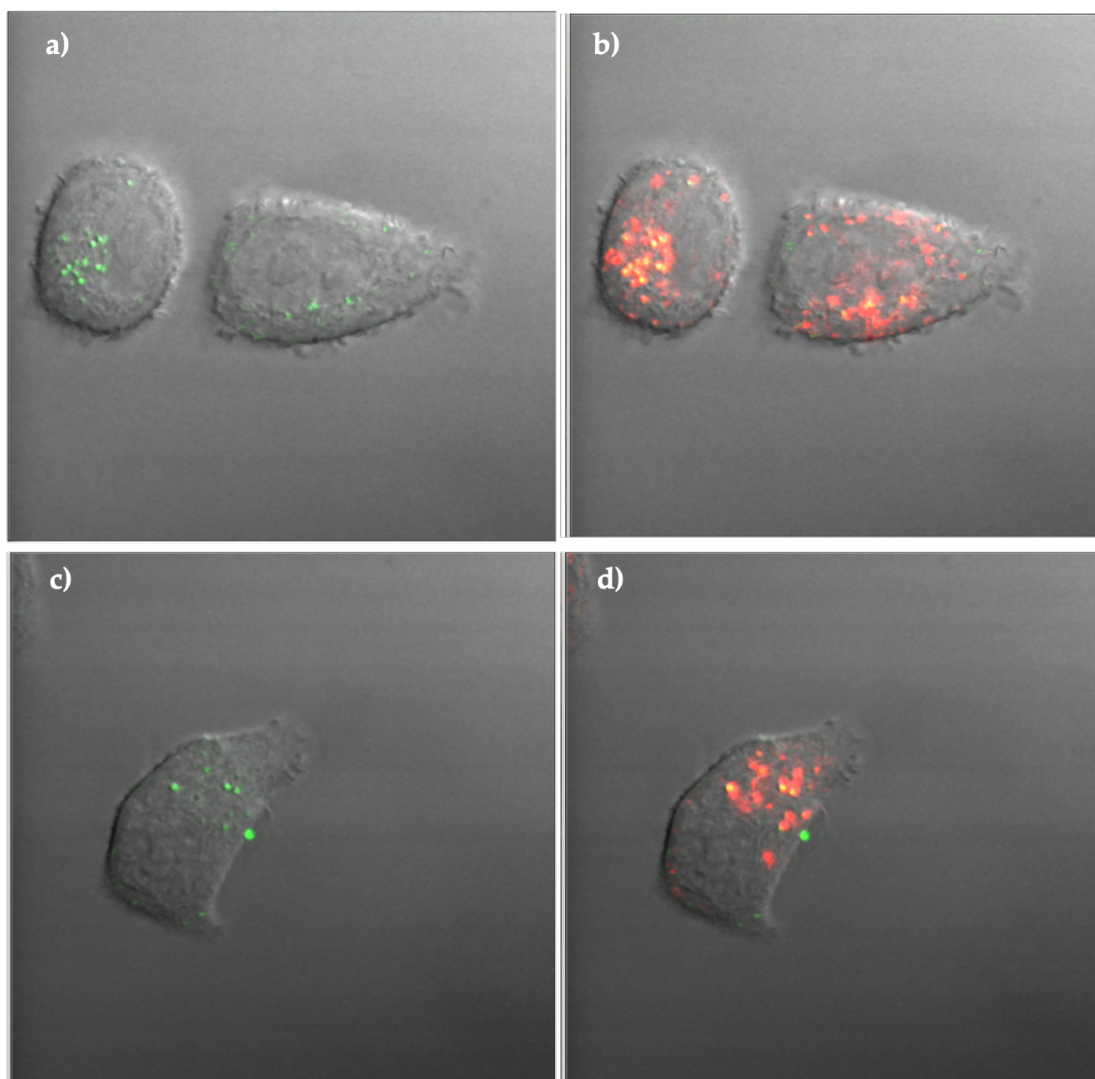
Figure 5.8: Enlarged images from Figure 5.7 of SK-BR-3 in the presence in PAA-gal (a) and b)) and PAA-glc (c) and d)). Images are separated into: AF488-st (green filter) (a) and c)) and composite image (b) and d)). AF488-st represents glycan binding, and BioTracker Orange dye represents acidic organelles.

The quantification of the confocal images can be seen in Figure 5.9. From Figure 5.9, PAA-gal clearly showed the greatest interaction with SK-BR-3, followed by PAA-glc, which is consistent with the confocal images in Figure 5.7. Both PAA-lac and PAA-man did not show a significant binding interaction with SK-BR-3, which reflected the corresponding images in Figure 5.7.
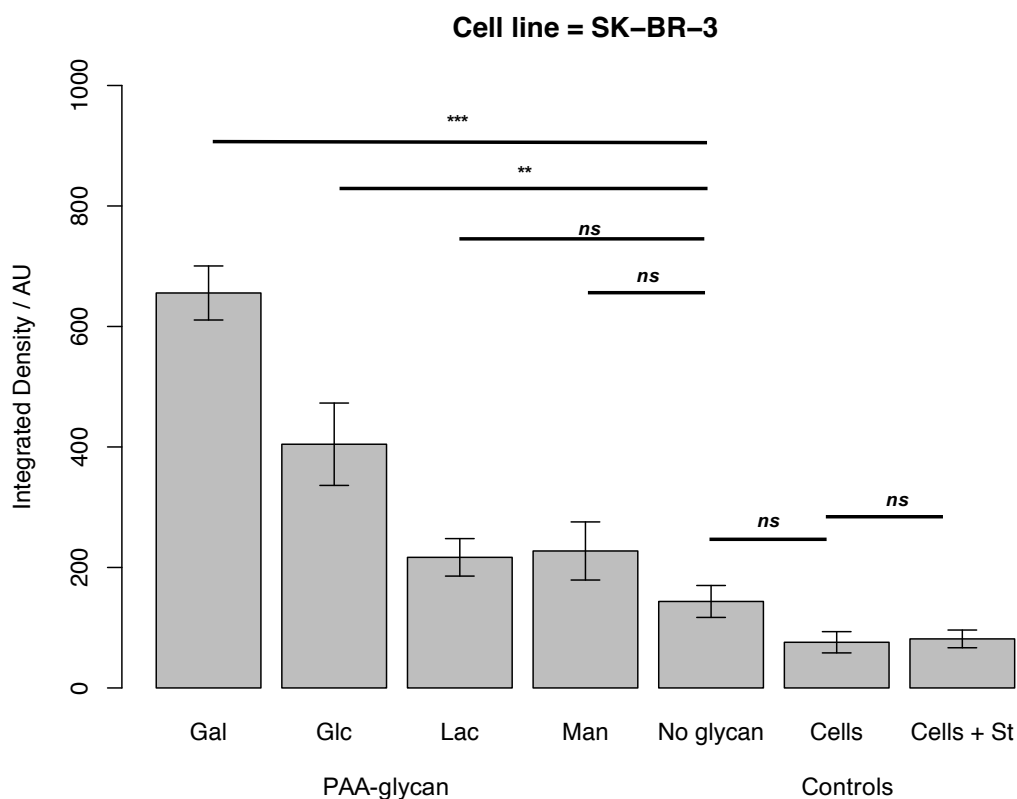
Figure 5.9: Quantitative analysis of confocal images from PAA-glycan binding to SK-BR-3, showing the integrated intensity for each glycan (galactose, glucose, lactose and mannose, left to right) and controls. Error bars = +/- SEM, n=7 images. * = $p < 0.05$; ** = $p < 0.01$; *** = $p < 0.005$; ns = not significant.

Consequently, the PAA-glycan binding studies with SK-BR-3 showed strongest interaction with PAA-gal, which was demonstrated to localise intracellularly, in the acidic organelles.

Non-cancer cell line: MCF-10A

A summary of the confocal images for each condition can be seen in Figure 5.10.
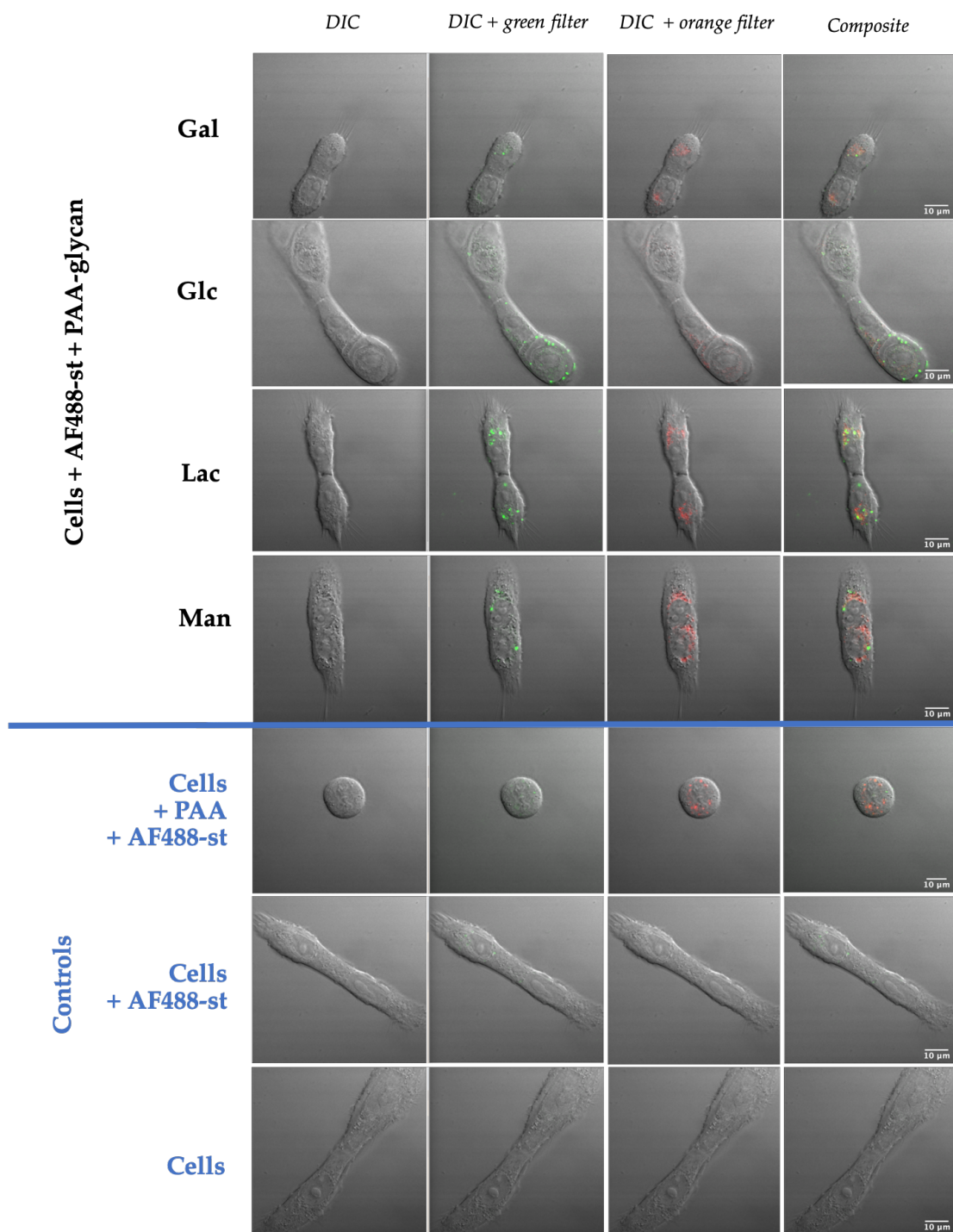
Figure 5.10: Example of processed confocal images from PAA-glycan (galactose, glucose, lactose and mannose, top to bottom) binding to MCF-10A. Images are separated into no filter (DIC image), AF488-st (green filter), BioTracker Orange dye (orange filter) and composite, from left to right. AF488-st represents glycan binding, and BioTracker Orange dye represents acidic organelles.

From Figure 5.10, MCF-10A interacts greatest with lactose, glucose and mannose. There appeared to be some interaction with galactose, but fewer fluorescent 'spots' in the images suggested a lower interaction with galactose.

The confocal images also provide information on the localisation of the PAA-glycans within the cell, from using a dye which localises in the acidic organelles (orange filter). PAA-lac was observed to localise in the acidic organelles, although there were areas in the images where the AF488-st and BioTracker Orange dye fluorescence did not overlap, suggesting PAA-lac was localised elsewhere in the cell. The PAA-man was predominantly not localised in the acidic organelles as low colocalisation between the AF488-st and BioTracker Orange. For PAA-glc, there appeared to be no localisation of the PAA-glycan within the acidic organelles. The difference in localisation between the PAA-glycans suggests different uptake methods, whether that be the receptor involved, or rate of uptake. The quantified results of the PAA-glycan interaction with MCF-10A can be seen in Figure 5.11.
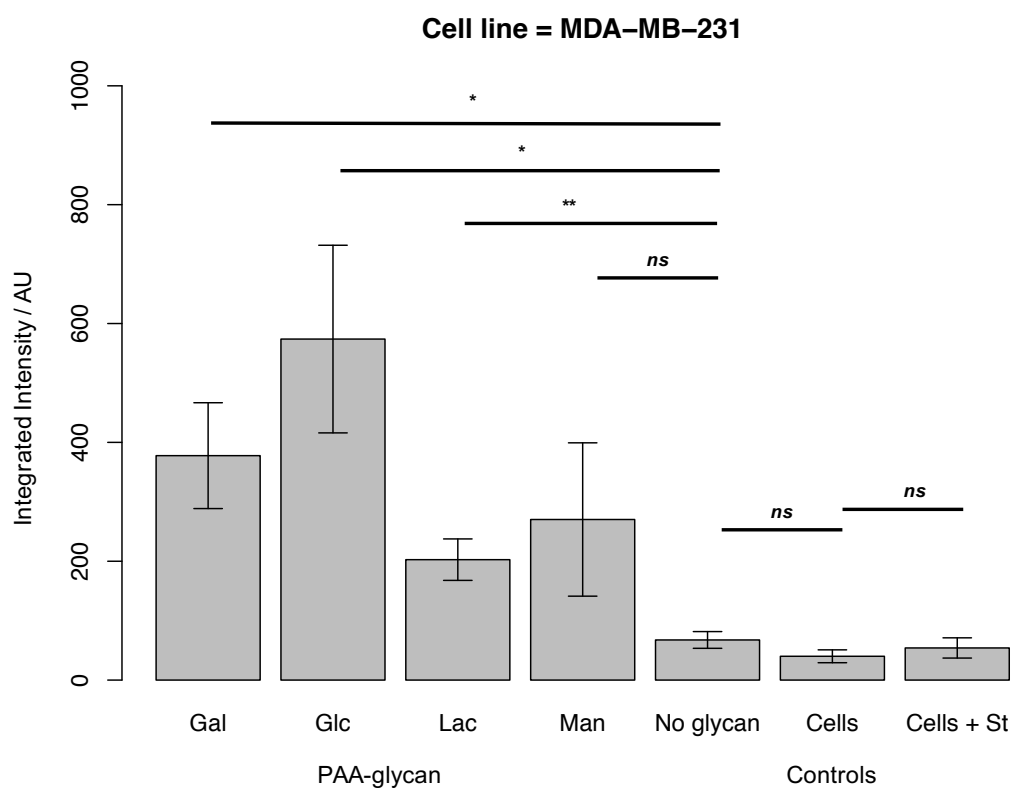

Figure 5.11: Quantitative analysis of confocal images from PAA-glycan binding to MCF-10A, showing the integrated intensity for each glycan (galactose, glucose, lactose and mannose, left to right) and controls. Error bars = +/- SEM, n=7 images. * = p < 0.05; ** = p < 0.01; *** = p < 0.005; ns = not significant.

The strongest interaction was observed between MCF-10A and PAA-lac, with PAA-glc and PAA-man also showing significant interactions with MCF-10A. The PAA-gal had larger variability, and although there was some fluorescence observed by the confocal images (Figure 5.10), there was not a consistent, statistically significant interaction.

A table summarising the binding by PAA-glycans and each cell line is shown in Table 5.1. Blue cell shading represents a statistically significant interaction observed between the PAA-glycan and the cell line; and black cell shading represents no statistically significant interaction between the PAA-glycan and the cell line. Dark blue cell shading represents the strongest interaction observed between each cell line and PAA-glycan.

Table 5.1: Summary of statistically significant interactions observed between PAA-glycan and each cell line.

PAA-glycan	Cell line		
	MDA-MB-231	SK-BR-3	MCF-10A
Gal	light blue	dark blue	black
Glc	dark blue	light blue	light blue
Lac	light blue	black	dark blue
Man	black	black	light blue

At first look, the low binding interaction of PAA-man and MDA-MB-231 was surprising as MDA-MB-231 has been documented to overexpress mannose receptor[21]. However, the presentation and density of mannose on the scaffold (PAA in this case) will effect cellular uptake. Possibly the presentation used for the PAA-glycan is poor for the MDA-MB-231 mannose receptor binding and uptake. Successful mannose based targeting approaches to MDA-MB-231 have used nanoparticles[49][50], and so assessing a different scaffold for these glycans may be important for assessing selectivity.

From comparing all the PAA-glycan results with each cell line (Table 5.1), galactose appears to give the best selectivity for the breast cancer cell lines, as no statistically significant interaction was detected with MCF-10A. Therefore,

galactose was taken forward for AuNP functionalisation to develop targeted PDT against the breast cancer cell lines. As mentioned previously, glycan presentation can effect cellular uptake, which is determined by the scaffold. Therefore, galactose based AuNP cellular uptake was also assessed, to ensure selectivity was still achieved for the breast cancer cell lines. The next step was to assess whether the AuNPs functionalised with glycans and PS that will be used for targeted PDT studies, reproduced a similar selectivity as the PAA-glycans.

5.3.2 Singlet oxygen production by glycan-/ce6-AuNPs

To assess the AuNP uptake by the cell lines, the AuNPs that will be used in the PDT studies were assessed. For the PDT studies, the AuNP surface must hold the PS for cell eradication through singlet oxygen production, and glycan for targeting to the cancer cell. The synthesis of PS and glycan functionalised AuNPs are detailed in Chapter 2.3.3. The PS used was a ce6 derivative, and the glycans used were galactose and mannose, with PEG_3 as a control. The structure of the ligands can be seen in Figure 5.12.
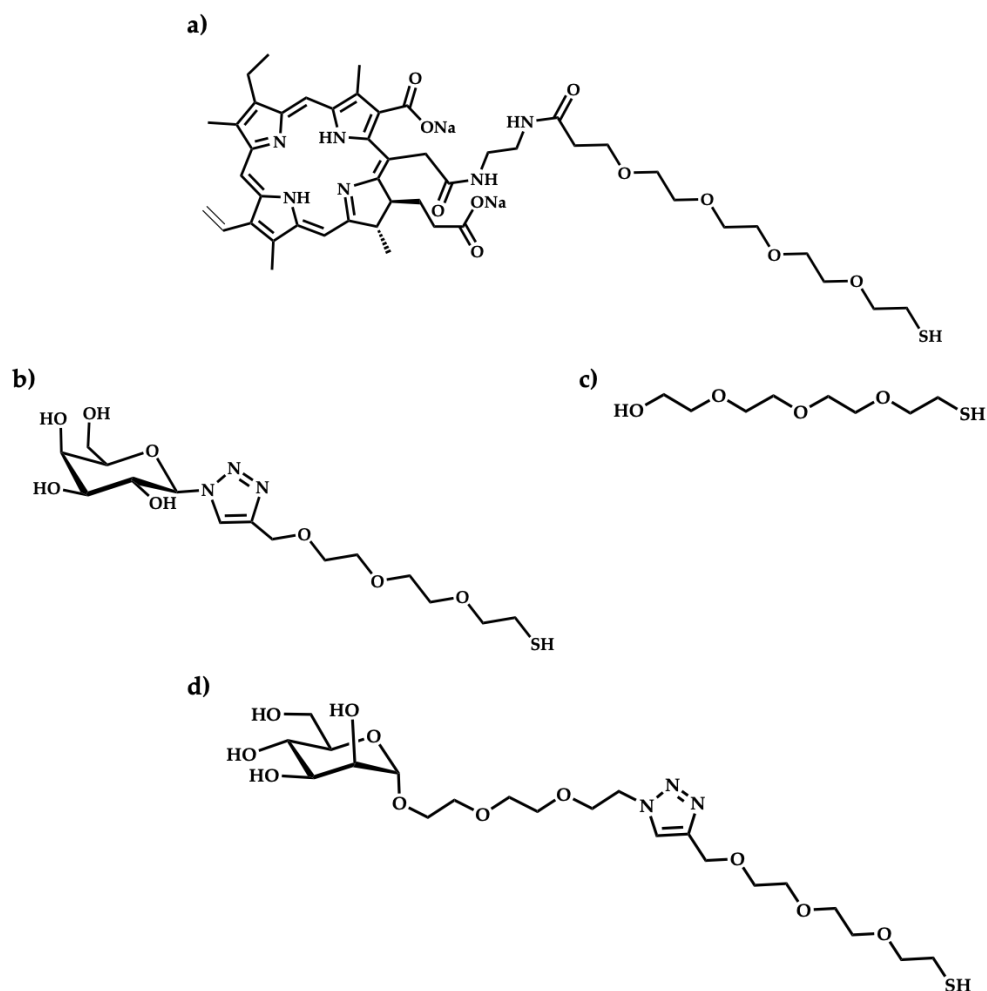
Figure 5.12: The structure of the ligands used to functionalise 16 nm AuNPs for the AuNP uptake and PDT studies: a) ce6-PEG$_4$-SH; b) galactose-PEG$_3$-SH; c) PEG$_3$-SH; and d) mannose-PEG$_6$-SH.

Before assessing cellular uptake of the glycan-/ce6-AuNPs (gal-/ce6-AuNPs, man-/ce6-AuNPs or PEG$_3$-/ce6-AuNPs), the ability of the ce6 to generate singlet oxygen was assessed. To assess singlet oxygen production a fluorescent probe was used , where the probe's fluorescence was quenched on generation of singlet oxygen. The probe used was 9,10-anthracenediyl-bis(methylene)dimalonic acid (ABMA). The ABMA and glycan/ce6-AuNP solutions were mixed, and upon irradiation with 633 nm He/Ne laser, the ce6 was excited, resulting in generation of singlet oxygen. The singlet oxygen then quenches the fluorescence of the ABMA [51], resulting in a reduction in fluorescence at 431 nm. Figure 5.13 shows the structure of ABMA and the corresponding quenched, 9,10-endoperoxide

product, upon singlet oxygen generation.
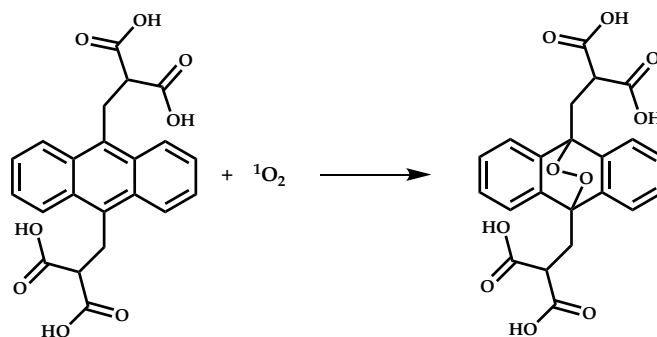
Figure 5.13: Fluorescent quenching of ABMA (left) by singlet oxygen, generating the non-fluorescent endoperoxide product (right).

The different glycan-/ce6-AuNP solutions with ABMA were irradiated, and the fluorescence measured every five minutes. To ensure the singlet oxygen generation was a result of irradiation with 633 nm laser, fluorescence of ABMA and glycan/ce6-AuNPs were measured without light. As a control, gal-AuNPs (no ce6) were used, so that any singlet oxygen generation was a result of the ce6 presence on the AuNPs. Figure 5.14 shows the normalised fluorescence emission intensity at 431 nm for each glycan-/ce6-AuNPs in the presence of ABMA, with (+) and without (-) irradiation.
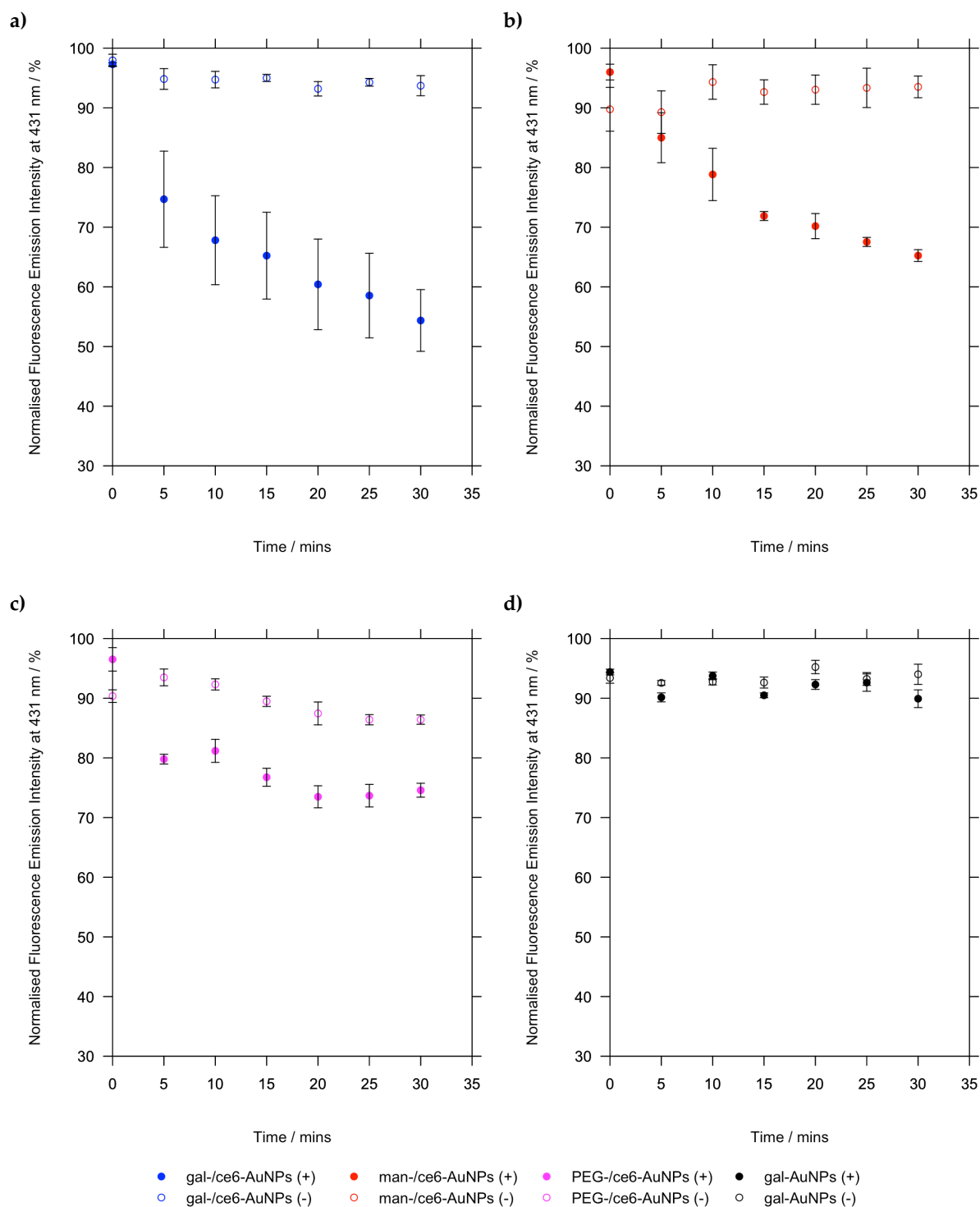
Figure 5.14: Processed fluorescence emission at 431 nm of ABMA, over 30 minutes in the presence of different glycan-/ce6-AuNPs to monitor singlet oxygen generation by ce6. a) gal-/ce6-AuNPs, with (blue, filled circles) and without irradiation (blue circles); b) man-/ce6-AuNPs, with (red, filled circles) and without irradiation (red circles); c) PEG₃-/ce6-AuNPs, with (magenta, filled circles) and without irradiation (magenta circles); and d) gal-AuNPs (control, no ce6) with (grey, filled circles) and without irradiation (grey circles). Error bars = SE, n=3.

188

As can be seen from Figure 5.14, all conditions where ce6 was present on the particles (Figure 5.14a, b and c) showed a reduction in fluorescence with irradiation, and so singlet oxygen was generated. The percentage change in fluorescence after 30 minutes for each set of glycan-/ce6-AuNPs and ABMA solutions, are shown in Table 5.2 (extracted from the data shown in Figure 5.14). A negative value represents a decrease in fluorescence, and so quenching of the ABMA fluorescence from singlet oxygen generation.

Table 5.2: Summary of the change in fluorescence at 431 nm for ABMA in the presence of glycan/ce6-AuNPs, with and without irradiation.

AuNPs	Change in fluorescence at 431 nm after 30 mins / %	
	Irradiated	Not irradiated
Gal-/ce6-	- 42.9	- 4.3
Man-/ce6-	- 30.8	+ 3.8
PEG$_3$-/ce6-	- 21.9	- 3.9
Gal-	- 4.5	+ 0.6

+ = increase in fluorescence; - = decrease in fluorescence

As mentioned previously, when singlet oxygen is generated, ABMA is converted to a non-fluorescent endoperoxide product (Figure 5.13). From Table 5.2, all ce6 containing particles showed singlet oxygen generation, demonstrating the ability of the ce6 to generate singlet oxygen is not inhibited by the conjugation to the AuNPs. Gal-/ce6-AuNPs demonstrated the greatest quenching of the ABMA fluorescence signal, suggesting that the gal-/ce6-AuNPs had the greatest ability to generate singlet oxygen. From looking at the control AuNPs (gal-AuNPs), there was a background reduction of ABMA fluorescence by 4.5% with irradiation, where all glycan-/ce6-AuNPs were below this background level without irradiation. Therefore, the glycan-/ce6-AuNPs were all shown to generate singlet oxygen, in a light-dependent manner.

5.3.3 Glycan binding by cancer and non-cancer breast cell lines using glycan-/ce6-AuNPs

Once the glycan-/ce6-AuNPs were shown to behave as expected (generate singlet oxygen), the particles were assessed for cellular uptake by the different cell lines. Galactose showed the best selectivity for cancer cells in the PAA-glycan studies, and so was assessed using AuNPs as a scaffold instead of the polymer (PAA). For the following studies, mannose was also chosen as overexpression of mannose receptor on MDA-MB-231 has been documented. Therefore, to assess whether the cell line was behaving differently, or whether it was the compound, man-/ce6-AuNPs uptake by the cell lines was also performed. As a control, PEG$_3$-/ce6-AuNPs were used to assess any non-selective uptake by the cell lines.

Cancer cell line: MDA-MB-231

As with the PAA-glycan studies, the cellular uptake of the AuNPs was monitored using confocal microscopy and then integrated intensity was measured to quantify the cellular uptake, and the dye in this case was the ce6. The localisation of the particles was also tested using the 'BioTracker^{TM} 560 Orange Lysosome Dye', which localises in acidic organelles. The confocal images of the glycan-/ce6-AuNP uptake can be seen in Figure 5.15. For gal-/ce6-AuNPs and PEG$_3$-/ce6-AuNPs, the localisation of the particles was mixed, with the particles predominantly localising in the acidic organelles but also demonstrating fluorescence elsewhere in the cell. As for the man-/ce6-AuNPs, strong interaction was shown in the acidic organelles, from the colocalisation with the BioTracker Orange dye. These differences in AuNP localisation suggest that different receptors were involved for AuNP uptake.

Figure 5.15: Example of processed confocal images from MDA-MB-231 binding by AuNPs: gal-/ce6, man-/ce6, PEG$_3$-/ce6- and no AuNPs, from top to bottom. Images are separated into no filter (DIC image), glycan-/ce6-AuNPs (red filter), BioTracker Orange dye (orange filter) and composite, from left to right. Red filter (ce6) represents glycan binding, and BioTracker Orange dye represents acidic organelles.

Figure 5.16 shows enlarged images from Figure 5.15, where the fluorescence shown is from the ce6 (red filter) on the particles. The control cells, which is cells without AuNPs (Figure 5.16d), demonstrated that there is not autofluorescence by the MDA-MB-231 cell line with the excitation and emission wavelengths used. Consequently, as can be seen from Figure 5.16, all glycan-/ce6-AuNPs interacted with the MDA-MB-231 cell line, as fluorescence was detected in all images with AuNPs (Figure 5.16a-c).
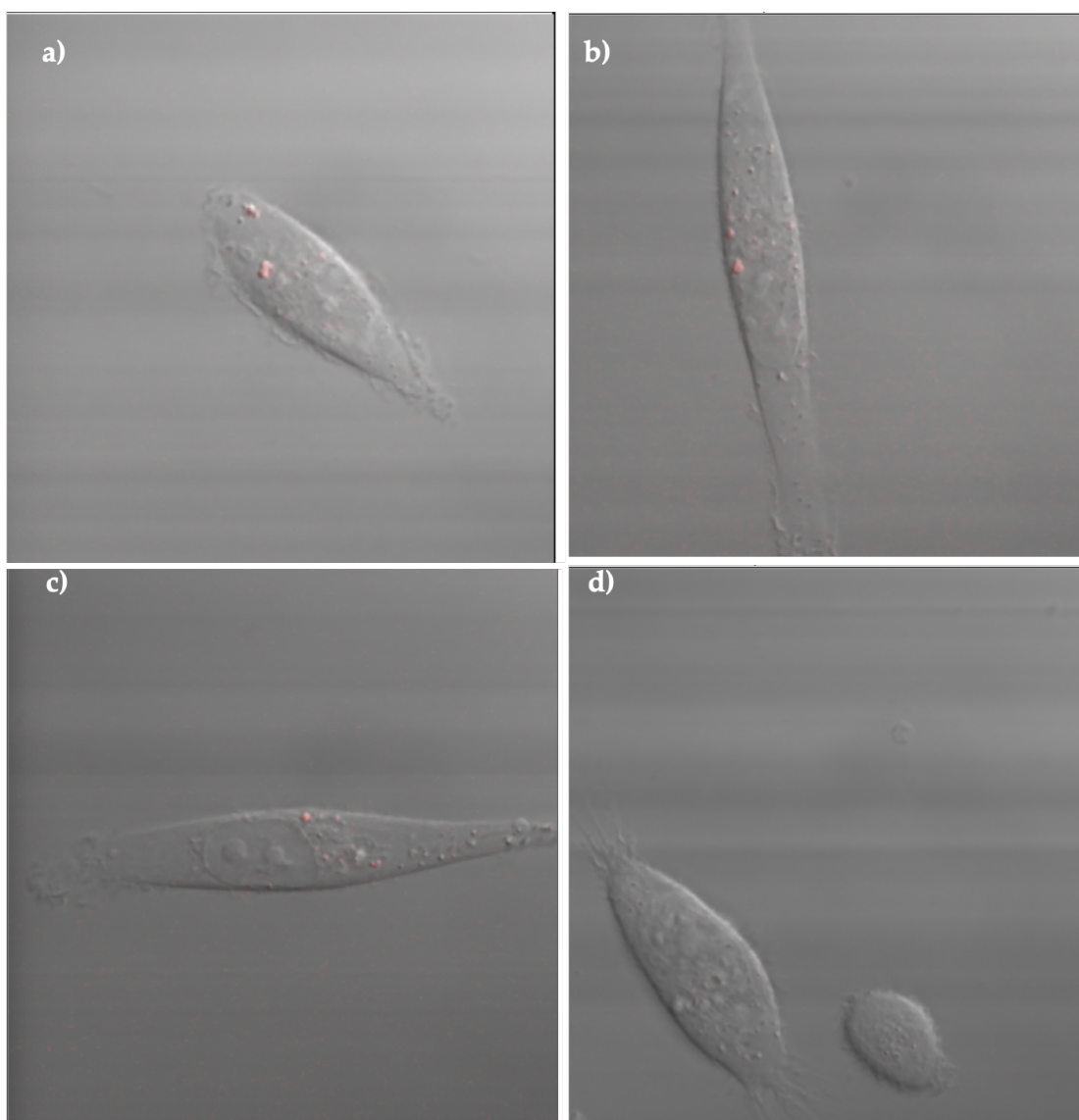
Figure 5.16: Enlarged confocal images from Figure 5.15, with MDA-MB-231 binding by AuNPs: a) gal-/ce6-AuNPs; b) man-/ce6-AuNPs; c) PEG$_3$-/ce6-AuNPs; and d) no AuNPs. Images are with red filter for chlorin e6 fluorescence.

To assess the AuNPs that provided the greatest interaction with MDA-MB-231, the integrated intensity was measured and shown in Figure 5.17.
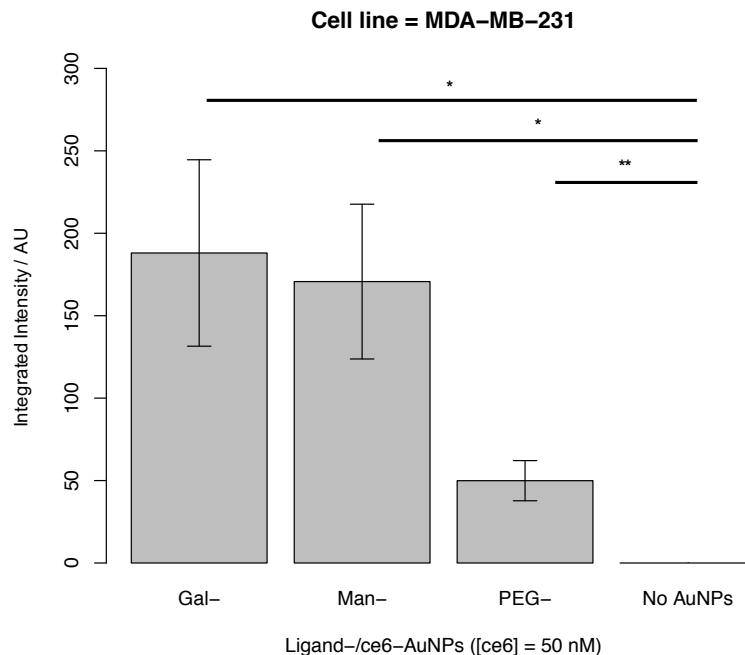
Figure 5.17: Quantitative analysis of confocal images from glycan-/ce6-AuNP binding to MDA-MB-231, showing the integrated intensity for the different AuNPs: gal-/ce6-, man-/ce6-, PEG$_3$-/ce6 and no AuNPs, left to right. Error bars = +/- SEM, n=7 images. * = p < 0.05; ** = p < 0.01; *** = p < 0.005; ns = not significant.

Figure 5.17 shows the greatest interaction with MDA-MB-231 was with gal-/ce6-AuNPs and man-/ce6-AuNPs. There was also a statistically significant interaction detected between the PEG$_3$-/ce6-AuNPs and MDA-MB-231, although to a lesser extent that the glycan-/ce6-AuNPs. The results from the AuNP uptake studies were more consistent with the literature than the PAA-glycan studies, as mannose based particles were shown to interact with the MDA-MB-231 cell line, demonstrating that the cell line is behaving as expected and the low binding of the PAA-man may have been due to the ligand presentation. However, consistent between the PAA-glycan and AuNP studies within this PhD research, the MDA-MB-231 cell line showed significant interaction with galactose.

Cancer cell line: SK-BR-3

Figure 5.18 shows the confocal images from the glycan-/ce6-AuNP uptake with breast cancer cell line: SK-BR-3. The gal-/ce6-AuNPs were the only particles tested that interacted with SK-BR-3, demonstrating a galactose selective uptake by the SK-BR-3 cells. The localisation of the gal-/ce6-AuNPs was predominantly not localised in acidic organelles, as seen with lack of colocalisation with BioTracker Orange dye. The quantified results can be seen in Figure 5.19.

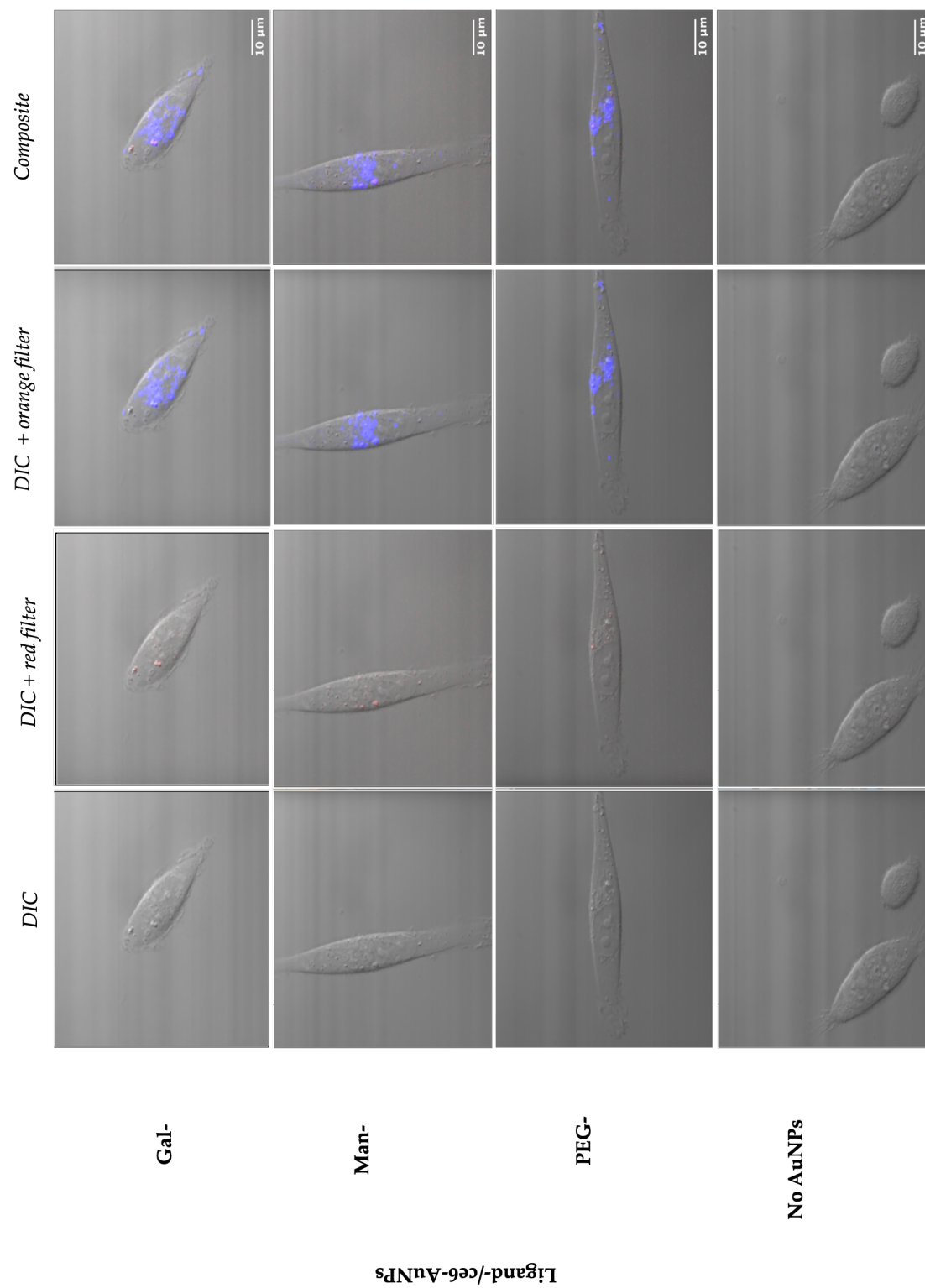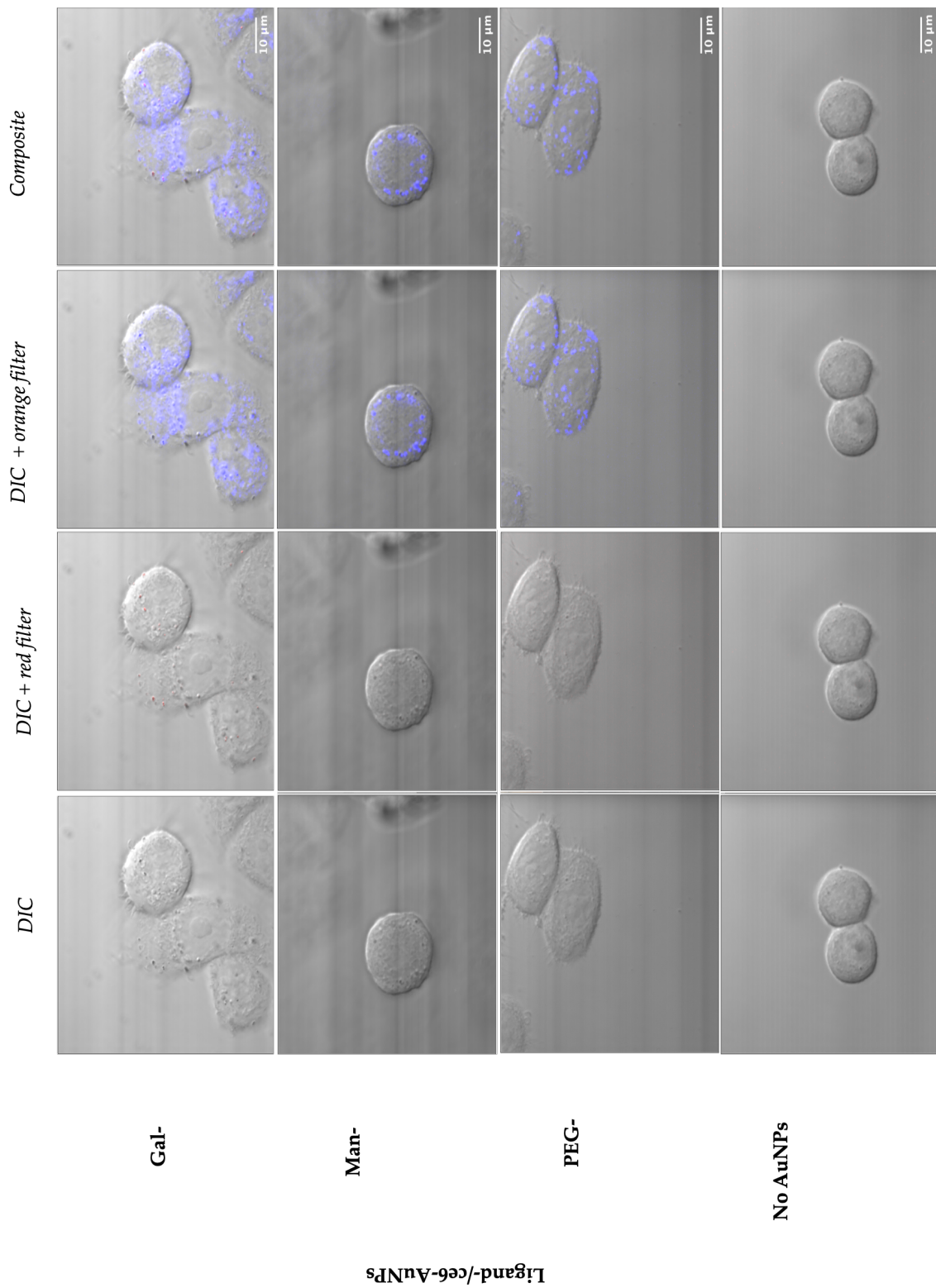**Figure 5.18:** Example of processed confocal images from SK-BR-3 binding by AuNPs: gal-/ce6-, man-/ce6-, PEG₃-/ce6- and no AuNPs, from top to bottom. Images are separated into no filter (DIC image), glycan-/ce6-/ce6-AuNPs (red filter), BioTracker Orange dye (orange filter), and composite, from left to right. Red filter (ce6) represents glycan binding, and BioTracker Orange dye represents acidic organelles.

As can be seen in Figure 5.19, gal-/ce6-AuNPs were the only particles to show a statistically significant interaction with SK-BR-3, reflecting the images in Figure 5.18. The results from the AuNP uptake by SK-BR-3 also matched the results from the PAA-glycan studies, as PAA-gal had the highest level of binding with SK-BR-3 (Figure 5.9).

Cell line = SK–BR–3
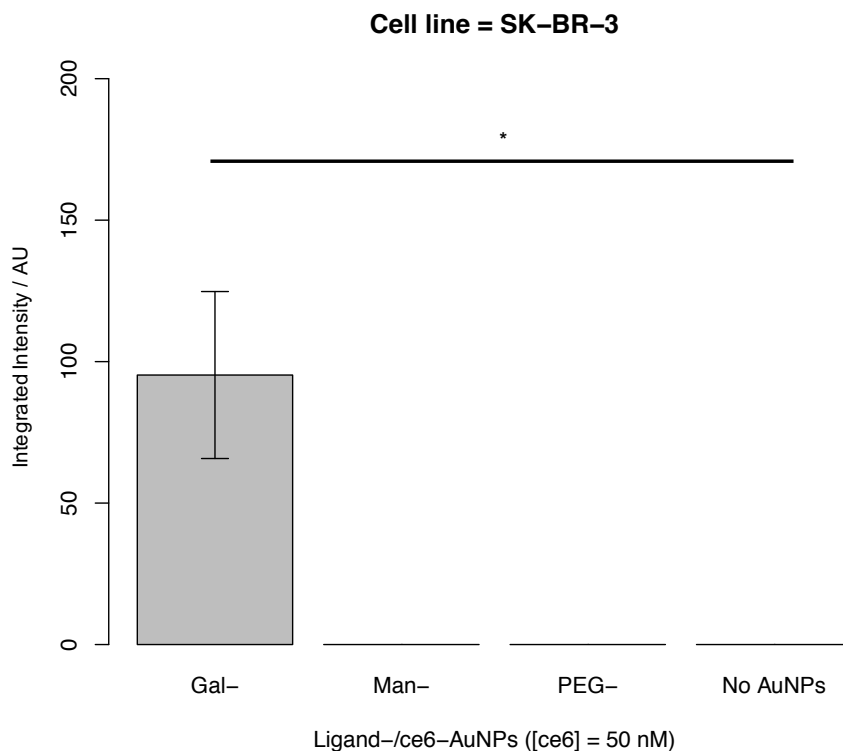
Figure 5.19: Quantitative analysis of confocal images from glycan-/ce6-AuNP binding to SK-BR-3, showing the integrated intensity for the different AuNPs: gal-/ce6-, man-/ce6-, PEG_3-/ce6 and no AuNPs, left to right. Error bars = +/- SEM, n=7 images. * = $p < 0.05$; ** = $p < 0.01$; *** = $p < 0.005$; ns = not significant.

The AuNP uptake studies by SK-BR-3 demonstrates that gal-/ce6-AuNPs had the strongest interaction with the SK-BR-3 cells. SK-BR-3 has been documented to overexpress galactose-binding cell surface proteins, such as galectins and GLUT receptors, which may account for the strong gal-/ce6-AuNP uptake under the conditions tested.

196

Non-cancer cell line: MCF-10A

To achieve selective targeting for drug delivery, the non-cancer cell line was assessed for interactions with the different glycan-/ce6-AuNPs. The processed confocal images of glycan-/ce6-AuNP uptake by the MCF-10A cell line is shown in Figure 5.20.

Ligand-/ce6-AuNPs

No AuNPs

PEG-

Man-

Gal-

DIC

DIC + *red filter*

DIC + *orange filter*

Composite

10 μm

10 μm

10 μm

10 μm
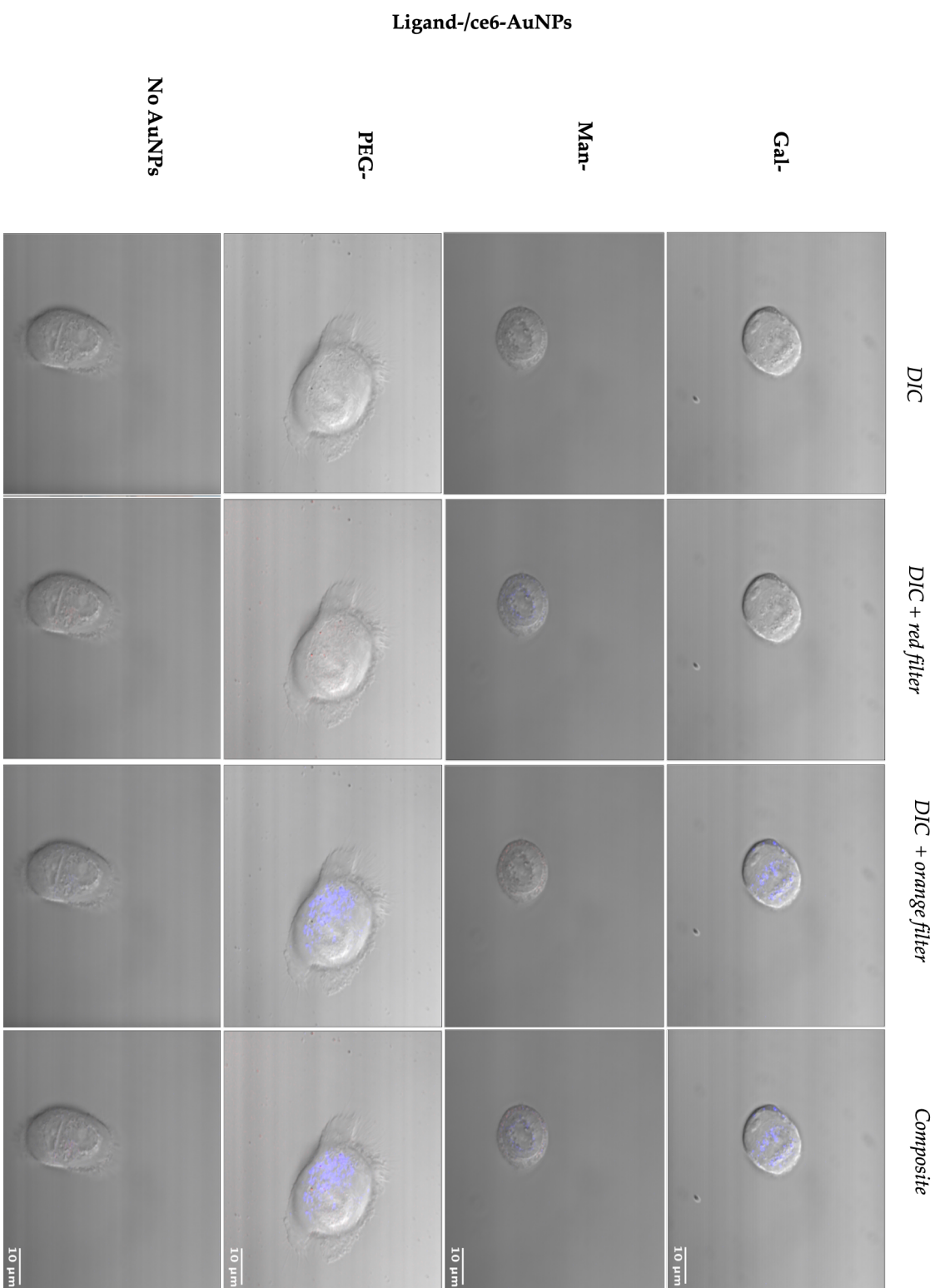
Figure 5.20: Example of processed confocal images from MCF-10A binding by AuNPs: gal-/ce6-, man-/ce6-, PEG3-/ce6- and no AuNPs, from top to bottom. Images are separated into no filter (DIC image), glycan-/ce6-AuNPs (red filter), BioTracker Orange dye (orange filter) and composite, from left to right. Red filter (ce6) represents glycan binding, and BioTracker Orange dye represents acidic organelles.

198

From Figure 5.20, neither the gal-/ce6-AuNPs or the man-/ce6-AuNPs showed cellular interaction or uptake with the non-cancer cell line. Figure 5.20 shows the MCF-10A and the PEG$_3$-/ce6-AuNPs when interaction was observed. The PEG$_{33}$-/ce6-AuNPs had mixed results, and showed low binding that was variable between images, where some of the images had no binding at all, suggesting that the interaction was non-selective. The quantified results from the MCF-10A cell line are shown in Figure 5.21.
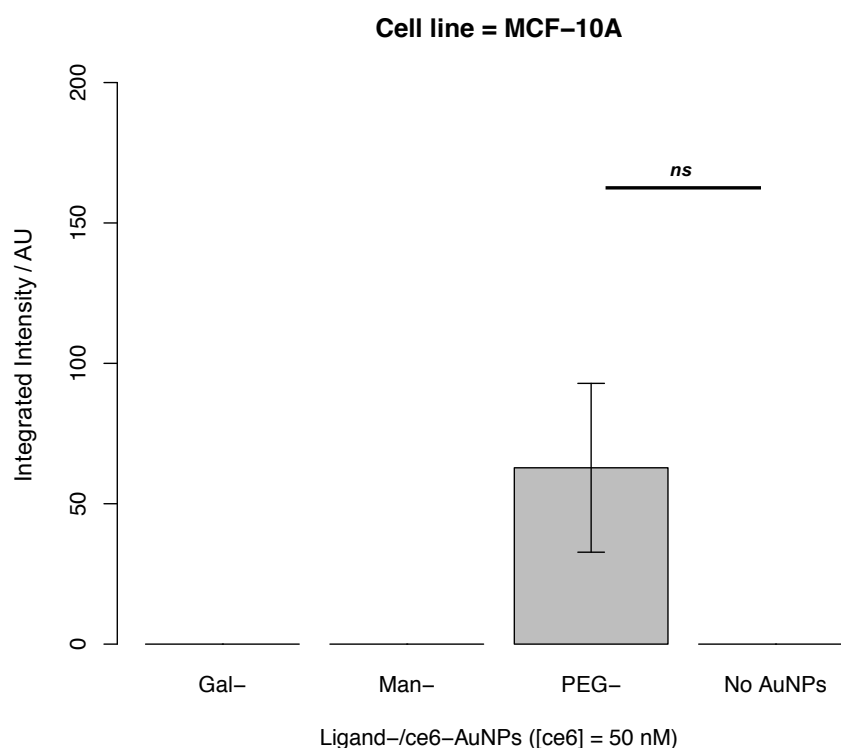
Figure 5.21: Quantitative analysis of confocal images from glycan-/ce6-AuNP binding to MCF-10A, showing the integrated intensity for the different AuNPs: gal-/ce6-, man-/ce6-, PEG$_3$-/ce6 and no AuNPs, left to right. Error bars = +/- SEM, n=7 images. * = p < 0.05; ** = p < 0.01; *** = p < 0.005; ns = not significant.

From Figure 5.21, no interaction was detected between MCF-10A and gal- or man-/ce6-AuNPs (Figure 5.21), which reflects the images seen in Figure 5.20. The interaction between the PEG$_3$-AuNPs and MCF-10A was determined as not statistically significant (p value = 0.09103). Importantly, the findings demonstrated that neither glycan-/ce6-AuNPs were taken up by the non-cancer

cell line, at the concentration tested (50 nM).

A summary of the glycan-/ce6-AuNP interactions with each cell line are shown in Table 5.3. Blue cell shading represents a statistically significant inter-action observed between the AuNPs and the cell line; and black cell shading represents no statistically significant interaction between the AuNPs and the cell line. Dark blue cell shading represents the greatest interaction observed between each cell line and AuNPs.

Table 5.3: Summary of statistically significant interactions observed between glycan-AuNPs and each cell line.

Ligand-/ce6-AuNPs	Cell line		
	MDA-MB-231	SK-BR-3	MCF-10A
Gal-			
Man-			
PEG$_3$-			

From comparing all the interactions of the AuNPs with the cell lines in Table 5.3, gal-/ce6-AuNPs provide the greatest selectivity of both cancer cell lines, as there was no significant interaction between the gal-/ce6-AuNPs and MCF-10A. Considering both the PAA and AuNP interaction results, galactose consistently gave selective, significant interaction with the cancer cell lines. The singlet oxygen results also demonstrated gal-/ce6-AuNPs generated singlet oxygen to a greater extent, as they demonstrated the most quenching of ABMA fluorescence signal with light treatment (Figure 5.14). Therefore, gal-/ce6-AuNPs were chosen for the PDT studies.

5.3.4 Receptor uptake of gal-/ce6-AuNPs by breast cancer cell lines

Before the PDT studies, the receptors involved in binding the AuNPs and their cellular uptake were assessed. In Garcia-Calavia *et al.*[47], lactose-/phthalocyanin-AuNPs (4 nm) were used to target the same cell lines used in this PhD research.

The lactose was aimed at targeting overexpressed galectin on both breast cancer cell lines. From an ELISA based approach, galectin protein was detected at higher levels on the MDA-MB-231 cell line over the SK-BR-3 cell line. However, upon PDT treatment of the two breast cancer cell lines, only cell death was observed for the SK-BR-3 cell line after three hours. The authors proposed that different receptors may be involved in the uptake of the particles. Consequently, in this research, the receptors involved in binding and uptake of the gal-/ce6-AuNPs was assessed, in hope of understanding the selective mechanism in which the particles are taken up by the cell lines, and to provide further confidence in the ability of both breast cancer cell lines to take up the gal-/ce6-AuNPs.

GLUT receptors and galectins are both overexpressed on the breast cancer cell lines. The SGLT (Sodium-dependent glucose cotransporter) receptor expression levels are yet to be compared between cancer and non-cancer breast cell lines, however a relationship between SGLT inhibitors and increased breast cancer risk has been documented[52]. As SGLT receptors can bind and transport galactose, SGLT receptors were also assessed for uptake of the gal-/ce6-AuNPs. To determine the proteins involved in gal-/ce6-AuNP binding and uptake, inhibitors of GLUTs (WZB117), galectins (33DFTG) and SGLTs (canagliflozin) were used (see Table 5.4). The cancer cell lines were incubated with 50 μM of each inhibitor for one hour before addition of the particles, and imaged by confocal microscopy. Full experimental method is detailed in Chapter 2.5.2.

Table 5.4: Inhibitors of galactose binding protein expressed on breast cancer cell lines.

Inhibitor	Target receptors
Canagliflozin	SGLT-1, -2
33DFTG	Galectin-1, -3
WZB117	GLUT-1, -3, -4

Cancer cell line: MDA-MB-231

Figure 5.22 shows the confocal images of gal-/ce6-AuNP binding in the presence of different galactose-binding protein inhibitors. All conditions show some level of binding of the gal-/ce6-AuNPs to the MDA-MB-231 cell line. However, when the galectin inhibitor was present (33DFTG), the fluorescent spots were reduced. The gal-/ce6-AuNPs were predominantly localised in the acidic organelles, as seen by colocalisation between the gal-/ce6-AuNPs and the BioTracker Orange dye. The quantified images are shown in Figure 5.23.
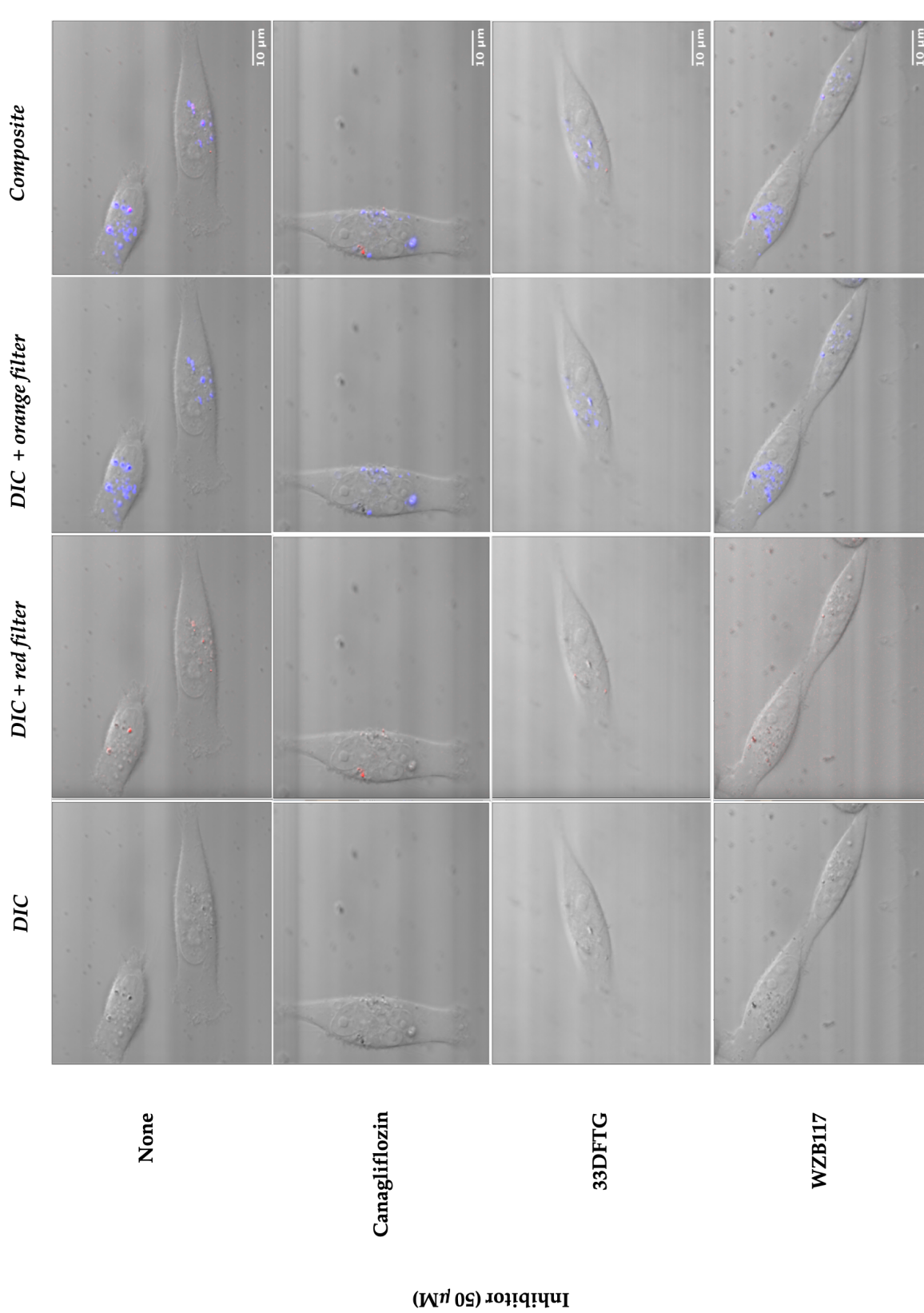
Figure 5.22: Example of processed confocal images for MDA-MB-231 protein binding inhibition to gal-/ce6-AuNPs. No inhibitor, and presence of SGLT (canagliflozin), galectin (33DFTG), and GLUT (WZB117) inhibitors (top to bottom). Images are separated into no filter (DIC image), glycan-/ce6-AuNPs (red filter), BioTracker Orange dye (orange filter) and composite, from left to right. Red filter (ce6) represents glycan binding, and BioTracker Orange dye represents acidic organelles.

From Figure 5.23, the gal-/ce6-AuNP interaction was inhibited in the presence of the galectin inhibitor, to high significance (p<0.005). The SGLT and GLUT inhibitors did not show any significant inhibition for gal-/ce6-AuNP interaction with the MDA-MB-231 cell line. Although there appeared to be a reduction in mean integrated intensity upon addition of WZB117, compared to no inhibitor, the reduction was not statistically significant (p = 0.1229).
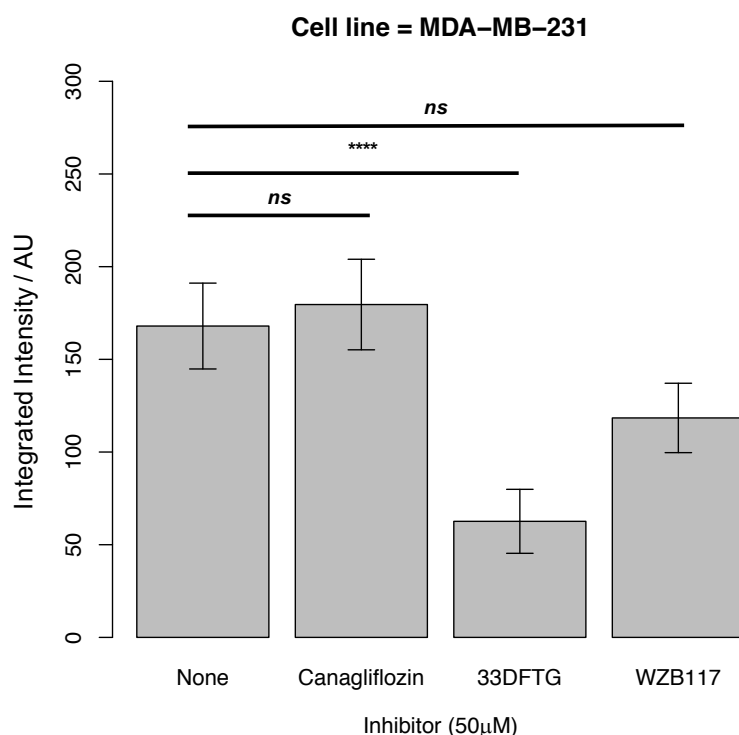
Figure 5.23: Quantitative analysis of confocal images from glycan-/ce6-AuNP binding inhibition to MDA-MB-231 glycan-binding proteins, showing the integrated intensity with the different inhibitors present: no inhibitor, SGLT (canagliflozin), galectin (33DFTG), and GLUT (WZB117) inhibitors, from left to right. Error bars = +/- SEM, n=7 images. * = p < 0.05; ** = p < 0.01; *** = p < 0.005; ns = not significant.

Cancer cell line: SK-BR-3

Figure 5.24 shows the confocal images of gal-/ce6-AuNP binding inhibition to the SK-BR-3 cell line. All conditions show some level of binding between the gal-/ce6-AuNPs and SK-BR-3 cell line. When the GLUT receptor inhibitor WZB117 was present (50 μM), there was a reduction in the interaction, as can

be seen by the lack of fluorescent spots. From comparing the localisation of the gal-/ce6-AuNPs and BioTracker dye, there were some areas of colocalisation but predominantly the particles were located elsewhere in the cell.
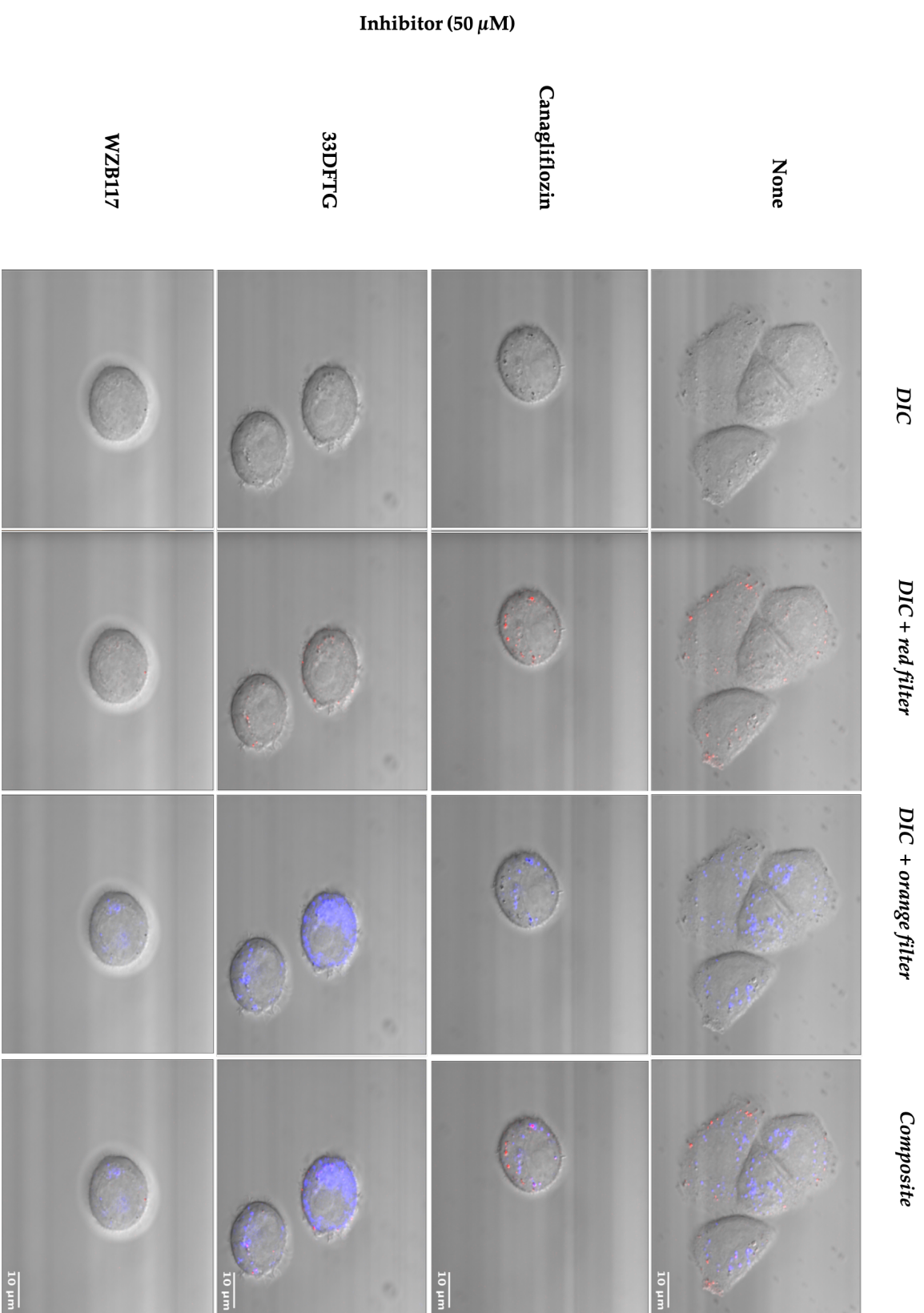
Figure 5.24: Example of processed confocal images for SK-BR-3 protein binding inhibition to gal-/ce6-AuNPs. No inhibitor, and presence of SGLT (canagliflozin), galectin (33DFTG), and GLUT (WZB117) inhibitors (top to bottom). Images are separated into no filter (DIC image), glycan-/ce6-AuNPs (red filter), BioTracker Orange dye (orange filter) and composite, from left to right. Red filter (ce6) represents glycan binding, and BioTracker Orange dye represents acidic organelles.

206

Figure 5.25 shows the quantification of the confocal images assessing gal-/ce6-AuNP interaction with SK-BR-3, in the presence of different inhibitors. The GLUT receptor inhibitor (WZB117) showed significant inhibition of the gal-/ce6-AuNP interaction with SK-BR-3. There was no significant inhibition with the SGLT or galectin inhibitors.
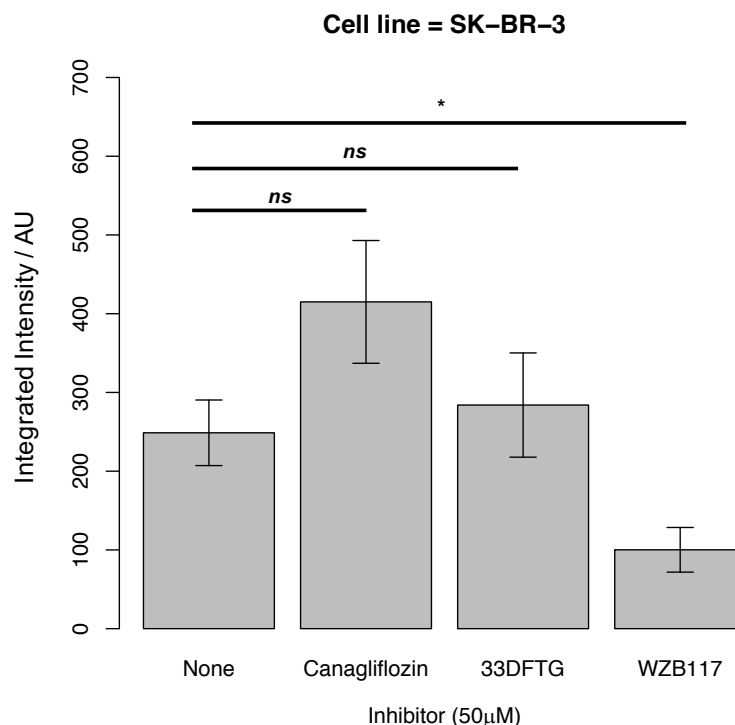
Figure 5.25: Quantitative analysis of confocal images from glycan-/ce6-AuNP binding inhibition to SK-BR-3 glycan-binding proteins, showing the integrated intensity with the different inhibitors present: no inhibitor, SGLT (canagliflozin), galectin (33DFTG), and GLUT (WZB117) inhibitors, from left to right. Error bars = +/- SEM, n=7 images. * = p < 0.05; ** = p < 0.01; *** = p < 0.005; ns = not significant.

A summary of the inhibition of the gal-/ce6-AuNP interaction with the cancer cell lines, in the presence of SGLT, galectin and GLUT inhibitors is shown in Table 5.5. Dark blue cell shading represents significant inhibition of gal-/ce6-AuNP interaction to the cell lines; and black cell shading represents no significant inhibition between the gal-/ce6-AuNPs and the cell lines.

Table 5.5: Summary of statistically significant inhibition of gal-/ce6-AuNP binding to cancer cell line galactose-binding proteins.

Inhibitor	Target receptors	Cancer cell line	
		MDA-MB-231	SK-BR-3
Canagliflozin	SGLT-1, -2	(black)	(black)
33DFTG	Galectin-1, -3	(blue)	(black)
WZB117	GLUT-1, -3, -4	(black)	(blue)

From Table 5.5, the interaction of the cancer cell lines with gal-/ce6-AuNPs is inhibited by different galactose-binding protein inhibitors, suggesting uptake of the particles is determined by different receptors on the cells. For the MDA-MB-231 cell line, the gal-/ce6-AuNPs interact with galectins; whereas the gal-/ce6-AuNPs interact with GLUT receptors on the SK-BR-3 cell line. These findings would explain why Garcia-Calavia *et al.* [47] still observed cell death with SK-BR-3, even though it had lower galectin expression than MDA-MB-231. The different galactose-binding proteins also effect the localisation of the gal-/ce6-AuNPs. For the MDA-MB-231 cell line, the AuNPs were predominantly localised in acidic organelles but this is not the case for SK-BR-3, where the gal-/ce6-AuNPs were mainly localised elsewhere in the cell.

The gal-/ce6-AuNPs have been shown to interact selectively for both cancer cell lines, and through galectin or GLUT receptors for MDA-MB-231 and SK-BR-3, respectively. The gal-/ce6-AuNPs were consequently then assessed for cell toxicity against the breast cancer cell lines through PDT.

5.3.5 Targeted PDT against breast cancer cell lines using gal-/ce6-AuNPs, *in vitro*

The gal-/ce6-AuNPs were taken forward for PDT studies against the breast cancer cell lines: MDA-MB-231 and SK-BR-3. The non-cancer breast cell line MCF-10A, was used as a control cell line to assess selective toxicity of the particles. For the PDT studies, 20 µM of staurosporine (st) was used as a positive

control, as st is toxic to cells at this concentration. Different concentrations of the gal-/ce6-AuNPs were used, based on the ce6 concentration of the particle solution (0, 25 or 50 nM). For each set of conditions, the studies were performed in duplicate to have one set of conditions exposed to irradiation (irradiated), and a corresponding control set of conditions that were not exposed to any light (non-irradiated). Using a commercially available cell viability kit (CellTitre Blue Cell Viability Assay, Promega), a fluorescent signal was produced when viable cells were present. The kit relies on the compound resazurin which is converted to the fluorescent compound resorufin, likely through reductase enzymes present in viable cells (see Figure 5.26)[53].
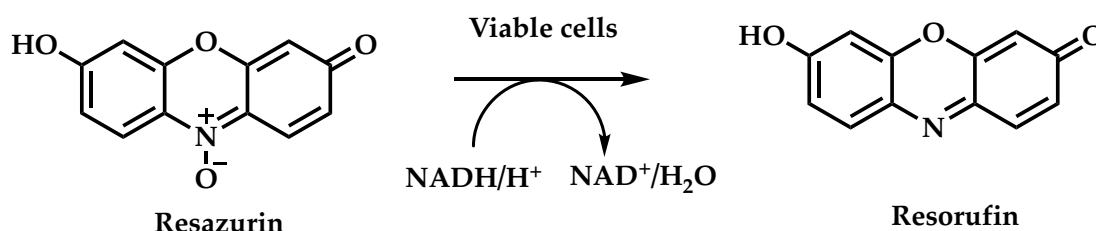
Figure 5.26: CellTitre Blue Cell Viability Assay non-fluorescent reagent (resazurin, left) is converted to a fluorescent reagent (resorufin, right) in the presence of viable cells.

The data will be represented as a percentage of cell viability, normalised to the non-irradiated, non-treated cells (0 nM of particles). Consequently, the lower the cell viability percentage, the more cell death was achieved through PDT. Full experimental detail can be found in Chapter 2.5. The processed results from the PDT studies are shown in Figure 5.27.
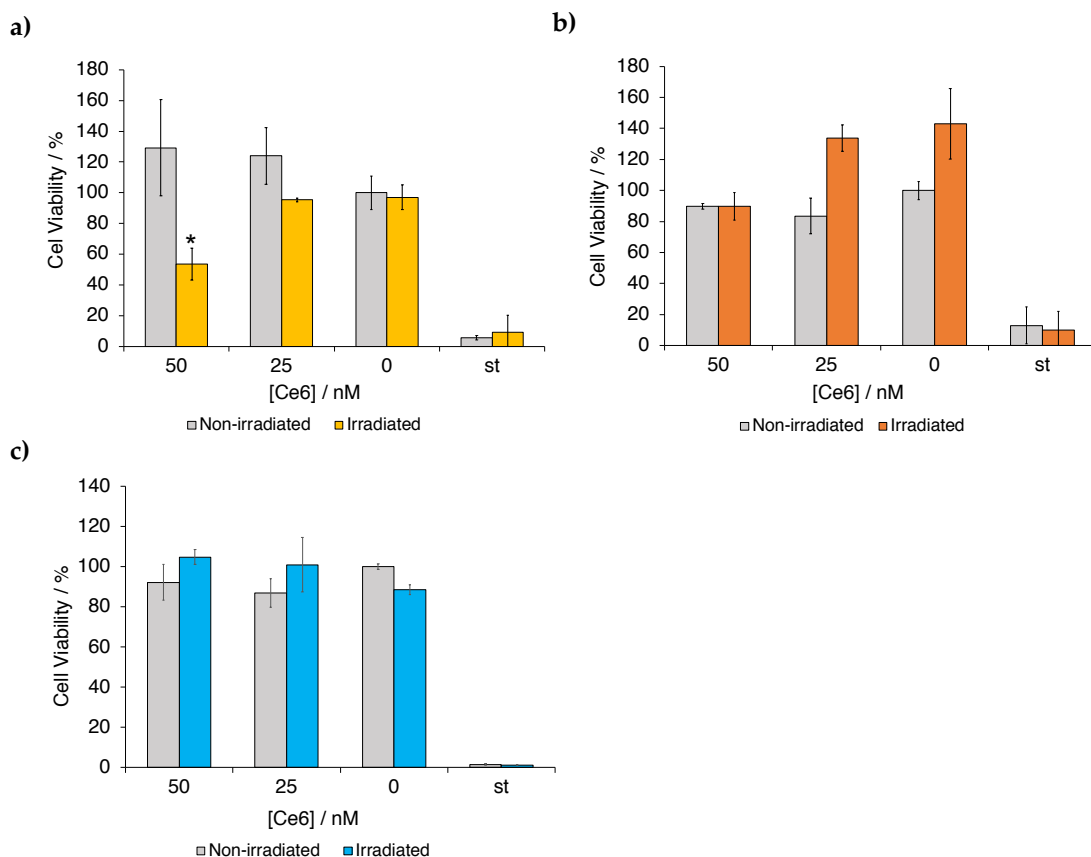
Figure 5.27: CellTitre Blue cell viability results after PDT treatment using gal-/ce6-AuNPs against a) SK-BR-3; b) MDA-MB-231; and c) MCF-10A. Different concentrations of gal-/ce6-AuNPs were tested (50, 25 and 0 nM, left to right), with 20 μM staurosporine (st) as a positive control for cell death. Error bars represent 95% confidence interval, n = 3.

From Figure 5.27, the processed cell viability for SK-BR-3 (Figure 5.27a), MDA-MB-231 (Figure 5.27b) and MCF-10A (Figure 5.27c) can be seen. Cell killing of the breast cancer cell line: SK-BR-3 was achieved using 50 nM ce6, with a 46.3 % reduction in cell viability compared to the control cells upon irradiation (yellow bars). Cell killing was only achieved upon irradiation with 633 nm He/Ne laser, as no reduction in cell viability was observed for the non-irradiated (grey bars) SK-BR-3 cells at 50 nM. No cell death of the non-cancer breast cell line (MCF-10A) was detected at 50 nM, demonstrating selective killing of the SK-BR-3 cells by 50 nM gal-/ce6-AuNPs.

However, there was no detectable cell killing of the MDA-MB-231 cell line at 50 nM of gal-/ce6-AuNPs. The reasons behind the lack of cell death are not

clear, as the previous work demonstrated successful interaction between the gal-/ce6-AuNPs and the MDA-MB-231 cell line.

One possibility for the results was the localisation of the particles in the MDA-MB-231 cells. As seen in the confocal work, the gal-/ce6-AuNPs reside predominantly in the acidic organelles after 3 hours; whereas the gal-/ce6-AuNPs appear elsewhere in the SK-BR-3 cells. Even though both cells appear to take up the gal-/ce6-AuNPs, the localisation of the PS has been shown important for the efficiency of cell death. As reactive oxygen species have a short lifetime, their location can be critical for achieving effective cell death. Although localisation in acidic organelles such as lysosomes has been shown effective for photoinduced cell death, organelles such as the mitochondria are widely superior for achieving efficient cell death[54][55]. One thought for the reason behind this improved efficiency is that the mitochondria directly induces apoptotic cell death, whereas lysosomes rely on indirect methods[55].

Due to time constraints, further investigation was not possible but if there was more time, a helpful next study would have been to use different subcellular localisation probes (mitochondria, cytoplasm, Golgi apparatus and plasma membrane). Determining the localisation for the ce6 in the SK-BR-3 may determine how to optimise the conditions for the MDA-MB-231 cell killing. This could be achieved by altering the incubation time and changing the concentrations, both can effect localisation of the PS in the cells but can be a complicated relationship. For example, if the PS localises in the plasma membrane, low concentrations can induce cell proliferation, and so require higher doses to induce damage to the plasma membrane[56]. Yet, high concentrations of PS in lysosomes can reduce the efficiency of photoinduced cell death, as they can form aggregates[57].

Increasing the incubation time may result in the gal-/ce6-AuNPs localised to different organelles, and improve the efficiency of the photoinduced cell damage from reactive oxygen species. Garcia-Calavia *et al.* [47], demonstrated cell killing of the MDA-MB-231 cell line after longer incubations (24 hours)

but at a reduced amount compared to the SK-BR-3. Furthermore, introducing additional ligands to the AuNP surface may improve subcellular localisation, such as the presence of cationic charges and amphiphilic ligands can promote localisation to the mitochondria[55][58][59].

Although, contrasting studies on localisation of PSs for most effective cell death have been published. Tsubone *et al.*[60] reported efficient autophagy-associated cell death of HeLa cells by targeting lysosomes with anionic porphyrins, which produced longer lasting and more effective reduction in cell growth. Interestingly this was achieved by lowering concentrations of the PS. Possibly this improved photodamage by targeting lysosomes with low concentrations, reduces aggregates of PS in the cell[61]. One way that may improve the system in this PhD research would be to lower the concentration of PS on the surface on the nanoparticles.

5.4   Conclusions

The research carried out in the chapter determined a suitable glycan to target breast cancer cells for PDT. Through confocal microscopy, two different scaffolds were employed to probe glycan binding by the cancer cell lines: MDA-MB-231 and SK-BR-3; and then compare their glycan binding to a non-cancer breast epithelial cell line: MCF-10A. A selection of PAA-glycans were selected for assessing glycan binding by the cell lines first. The PAA-glycans were commercially available and so were easily accessible to test an array of different glycans, including galactose, glucose, lactose and mannose. From the PAA-glycan analysis, the different cell lines interacted with different PAA-glycans, and to different levels. However, PAA-gal demonstrated selective interaction to both cancer cell lines, with no significant binding to the non-cancer cell line.

Next, a series of glycan-/ce6-AuNPs were prepared, to assess binding to the cell lines. The glycan-/ce6-AuNPs were prepared in the same format for the PDT studies. Galactose was selected as it had shown promising results

to achieve selective binding to the cancer cells from the PAA-glycan analysis. Mannose was also selected to functionalise AuNPs for binding analysis to the cell lines, as much literature has been developed on mannose to target MDA-MB-231, due the cell line's overexpression of mannose receptor. PEG_3-/ce6-AuNPs were prepared as a control to monitor non-selective binding. However, before assessing the binding selectivity of the particles to the different cell lines, the ability of the particles to function for the PDT assay were assessed. This involved testing the ability of the ce6 that was present on the AuNP surface to generate singlet oxygen, as conjugation of the dye to AuNPs can effect their properties. A probe (ABMA) was used to test singlet oxygen generation, as the ABMA fluorescence is quenched when singlet oxygen is produced. The process can be monitored using fluorimetry. The results demonstrated that all AuNPs that had ce6 present, generated singlet oxygen upon irradiation with 633 nm laser, as seen by a reduction in the fluorescence over time. The gal-/ce6-AuNPs were the most efficient at generating singlet oxygen as their presence resulted in the greatest reduction in fluorescence over 30 mins (-42.9%). Without light, quenching of the ABMA was of background level, suggesting the singlet oxygen generation was due to the activation of ce6 by irradiation *via* 633 nm laser.

Once the PS properties of the glycan-/ce6-AuNPs were confirmed, the interactions with the cell lines were monitored, using confocal microscopy. Consistent with the PAA-glycan analysis, the glycan-/ce6-AuNPs bearing galactose showed selective interactions with the cancer cell lines, with no significant interaction detected with the non-cancer cell line at 50 nM. Man-/ce6-AuNPs did show selective binding to MDA-MB-231, with no detectable binding interaction to the non-cancer cell line: MCF-10A, nor the second cancer cell line: SK-BR-3. Therefore, gal-/ce6-AuNPs were taken forward as they showed selective interactions to both cancer cell lines, with no detectable interaction to the non-cancer cell line.

Next, the galactose-binding proteins involved in cellular uptake of the gal-/ce6-AuNPs were assessed. Previous work by Garcia-Calavia *et al.*[47] used

lactose/PS based AuNPs (4 nm) to target galectins on MDA-MB-231 and SK-BR-3 cell lines for targeted PDT. The authors showed that the MDA-MB-231 had much higher levels of galectin expression, yet observed improved cell death with SK-BR-3, suggesting other receptors were involved with the uptake of the particles. Therefore, inhibitors of galectins, GLUT and SGLT receptors were used to probe the proteins involved with gal-/ce6-AuNP uptake by the cancer cell lines, and imaged using confocal microscopy. Interestingly, there was a difference between the proteins involved in cellular uptake of the particles between the two cancer cell lines. Gal-/ce6-AuNP interaction with MDA-MB-231 was inhibited by 33DFTG, an inhibitor of galectin-1 and -3, demonstrating that galectins were involved in cellular uptake of the gal-/ce6-AuNPs by MDA-MB-231. For SK-BR-3, gal-/ce6-AuNP was inhibited by WZB117, an inhibitor of GLUT-1, -3 and -4, and therefore particle uptake was regulated by GLUT receptors on SK-BR-3. The SGLT inhibitor did not effect the gal-/ce6-AuNP interaction with either cell line, showing that SGLT does not play a major role in particle uptake.

Finally, the gal-/ce6-AuNPs were assessed for their ability to induce targeted cell death of breast cancer cell lines through PDT studies. The results showed selective cell killing at 50 nM ce6 (concentration of gal-/ce6-AuNP solution) of the SK-BR-3 cell line, with a 46.3% reduction in cell viability upon irradiation. Without irradiation, no cell damage was detected. No detectable cell killing was observed for the control cell line MCF-10A, demonstrating selective cell killing of the SK-BR-3 cell line with 50 nM gal-/ce6-AuNPs. However, the MDA-MB-231 cell line did not show cell death with 50 nM of gal-/ce6-AuNPs, even though particle uptake at this concentration was demonstrated in the confocal microscopy studies. The inhibitory studies show differences in interactions with galactose-binding proteins between the two cancer cell lines. The confocal microscope images also revealed differences in subcellular localisation of the particles between the two cancer cell lines. For MDA-MB-231, the gal-/ce6-AuNPs were predominantly localised in acidic organelles, whereas this was not

the case for the SK-BR-3 cell line. If there was more time, further investigation into the localisation of the gal-/ce6-AuNPs in the SK-BR-3 cells may provide insight in how to optimise the gal-/ce6-AuNPs to effectively kill the MDA-MB-231 cell lines. Incubation time, concentration of ce6 and ligand properties can effect the subcellular localisation of the PS.

References

[1]   F. Bray, J. Ferlay, I. Soerjomataram, R. L. Siegel, L. A. Torre, and A. Jemal, "Global cancer statistics 2018: GLOBOCAN estimates of incidence and mortality worldwide for 36 cancers in 185 countries," *CA: A Cancer Journal for Clinicians*, vol. 68, no. 6, pp. 394–424, 2018. DOI: `10.3322/caac.21492`.

[2]   R. L. Siegel, K. D. Miller, and A. Jemal, "Cancer statistics, 2016," *CA: A Cancer Journal for Clinicians*, vol. 66, no. 1, pp. 7–30, 2016. DOI: `10.3322/caac.21332`.

[3]   J. Fang, T. Tao, Y. Zhang, and H. Lu, "A barcode mode based on glycosylation sites of membrane type mannose receptor as a new potential diagnostic marker for breast cancer," *Talanta*, vol. 191, pp. 21–26, 2019. DOI: `10.1016/J.TALANTA.2018.08.022`.

[4]   J. Makki, "Diversity of Breast Carcinoma: Histological Subtypes and Clinical Relevance.," *Clinical medicine insights. Pathology*, vol. 8, pp. 23–31, 2015. DOI: `10.4137/CPath.S31563`.

[5]   G. N. Sharma, R. Dave, J. Sanadya, P. Sharma, and K. K. Sharma, "Various types and management of breast cancer: an overview.," *Journal of advanced pharmaceutical technology & research*, vol. 1, no. 2, pp. 109–26, 2010.

[6]   K. A. Rygiel, M. Drozd, and L. Bułaś, "Care of cancer patients with liver and bone metastases - the place of pharmaceutical care in a balanced

plan, focused on the patient's needs and goals.," *Archives of medical science : AMS*, vol. 13, no. 6, pp. 1483–1492, 2017. DOI: `10.5114/aoms.2016.60509`.

[7] A. G. Waks and E. P. Winer, "Breast Cancer Treatment," *JAMA*, vol. 321, no. 3, p. 288, 2019. DOI: `10.1001/jama.2018.19323`.

[8] T. Ovcaricek, S. G. Frkovic, E. Matos, B. Mozina, and S. Borstnar, "Triple negative breast cancer - prognostic factors and survival.," *Radiology and oncology*, vol. 45, no. 1, pp. 46–52, 2011. DOI: `10.2478/v10019-010-0054-4`.

[9] M. Jiwa, A. Long, T. Shaw, G. Pagey, G. Halkett, V. Pillai, and X. Meng, "The management of acute adverse effects of breast cancer treatment in general practice: a video-vignette study.," *Journal of medical Internet research*, vol. 16, no. 9, e204, 2014. DOI: `10.2196/jmir.3585`.

[10] V. Masoud and G. Pagès, "Targeted therapies in breast cancer: New challenges to fight against resistance.," *World journal of clinical oncology*, vol. 8, no. 2, pp. 120–134, 2017. DOI: `10.5306/wjco.v8.i2.120`.

[11] A. H. Partridge, H. J. Burstein, and E. P. Winer, "Side Effects of Chemotherapy and Combined Chemohormonal Therapy in Women With Early-Stage Breast Cancer," *JNCI Monographs*, vol. 2001, no. 30, pp. 135–142, 2001. DOI: `10.1093/oxfordjournals.jncimonographs.a003451`.

[12] S. M. Motevalli, A. S. Eltahan, L. Liu, A. Magrini, N. Rosato, W. Guo, M. Bottini, and X.-J. Liang, "Co-encapsulation of curcumin and doxorubicin in albumin nanoparticles blocks the adaptive treatment tolerance of cancer cells," *Biophysics Reports*, vol. 5, no. 1, pp. 19–30, 2019. DOI: `10.1007/s41048-018-0079-6`.

[13] A. Varki and P. Gagneux, *Biological Functions of Glycans*. Cold Spring Harbor Laboratory Press, 2015. DOI: `10.1101/GLYCOBIOLOGY.3E.007`.

[14] J. M. Tarbell and L. M. Cancel, "The glycocalyx and its significance in human medicine," *Journal of Internal Medicine*, vol. 280, no. 1, pp. 97–113, 2016. DOI: `10.1111/joim.12465`.

[15] A. Krzeslak, K. Wojcik-Krowiranda, E. Forma, P. Jozwiak, H. Romanowicz, A. Bienkiewicz, and M. Brys, "Expression of GLUT1 and GLUT3 glucose transporters in endometrial and breast cancers.," *Pathology oncology research : POR*, vol. 18, no. 3, pp. 721–8, 2012. DOI: `10.1007/s12253-012-9500-5`.

[16] K. Nam, S.-h. Son, S. Oh, D. Jeon, H. Kim, D.-Y. Noh, S. Kim, and I. Shin, "Binding of galectin-1 to integrin β1 potentiates drug resistance by promoting survivin expression in breast cancer cells," *Oncotarget*, vol. 8, no. 22, 2017. DOI: `10.18632/oncotarget.16208`.

[17] D. Demydenko and I. Berest, "Expression of galectin-1 in malignant tumors.," *Experimental oncology*, vol. 31, no. 2, pp. 74–9, 2009.

[18] L. Venturelli, S. Nappini, M. Bulfoni, G. Gianfranceschi, S. Dal Zilio, G. Coceano, F. Del Ben, M. Turetta, G. Scoles, L. Vaccari, D. Cesselli, and D. Cojoc, "Glucose is a key driver for GLUT1-mediated nanoparticles internalization in breast cancer cells," *Scientific Reports*, vol. 6, 2016. DOI: `10.1038/srep21629`.

[19] Y. Deng, J. Zou, T. Deng, and J. Liu, *Clinicopathological and prognostic significance of GLUT1 in breast cancer A meta-analysis*, 2018. DOI: `10.1097/MD.0000000000012961`.

[20] E. Dalle Vedove, G. Costabile, and O. M. Merkel, "Mannose and Mannose-6-Phosphate Receptor–Targeted Drug Delivery Systems and Their Application in Cancer Therapy," *Advanced Healthcare Materials*, vol. 7, no. 14, 2018. DOI: `10.1002/adhm.201701398`.

[21] X. L. Hu, Q. Cai, J. Gao, R. A. Field, G. R. Chen, N. Jia, Y. Zang, J. Li, and X. P. He, "Self-Assembled 2D Glycoclusters for the Targeted Delivery of

Theranostic Agents to Triple-Negative Breast Cancer Cells," *ACS Applied Materials and Interfaces*, 2019. DOI: `10.1021/acsami.9b06016`.

[22] F.-C. Chou, H.-Y. Chen, C.-C. Kuo, and H.-K. Sytwu, "Role of Galectins in Tumors and in Clinical Immunotherapy.," *International journal of molecular sciences*, vol. 19, no. 2, 2018. DOI: `10.3390/ijms19020430`.

[23] K. Wdowiak, T. Francuz, E. Gallego-Colon, N. Ruiz-Agamez, M. Kubeczko, I. Grochoła, and J. Wojnar, "Galectin Targeted Therapy in Oncology: Current Knowledge and Perspectives," *International Journal of Molecular Sciences*, vol. 19, no. 1, p. 210, 2018. DOI: `10.3390/ijms19010210`.

[24] R. Dings, M. Miller, R. Griffin, and K. Mayo, "Galectins as Molecular Targets for Therapeutic Intervention," *International Journal of Molecular Sciences*, vol. 19, no. 3, p. 905, 2018. DOI: `10.3390/ijms19030905`.

[25] B. Birdsall, J. Feeney, I. D. Burdett, S. Bawumia, E. A. Barboni, and R. C. Hughes, "NMR solution studies of hamster galectin-3 and electron microscopic visualization of surface-adsorbed complexes: Evidence for interactions between the N- and C-terminal domains," *Biochemistry*, vol. 40, no. 15, pp. 4859–4866, 2001. DOI: `10.1021/bi002907f`.

[26] R. D. Cummings, F.-T. Liu, and G. R. Vasta, *Galectins*. Cold Spring Harbor Laboratory Press, 2015. DOI: `10.1101/GLYCOBIOLOGY.3E.036`.

[27] M. F. Brinchmann, D. M. Patel, and M. H. Iversen, *The role of galectins as modulators of metabolism and inflammation*, 2018. DOI: `10.1155/2018/9186940`.

[28] I. Camby, M. Le Mercier, F. Lefranc, and R. Kiss, *Galectin-1: A small protein with major functions*, 2006. DOI: `10.1093/glycob/cwl025`.

[29] A. H. Ebrahim, Z. Alalawi, L. Mirandola, R. Rakhshanda, S. Dahlbeck, D. Nguyen, M. Jenkins, F. Grizzi, E. Cobos, J. A. Figueroa, and M. Chiriva-Internati, "Galectins in cancer: carcinogenesis, diagnosis and therapy," *Annals of Translational Medicine*, vol. 2, no. 9, 2014. DOI: `10.21037/4775`.

[30] M. Ilmer, N. Mazurek, M. Z. Gilcrease, J. C. Byrd, W. A. Woodward, T. A. Buchholz, K. Acklin, K. Ramirez, M. Hafley, E. Alt, J. Vykoukal, and R. S. Bresalier, "Low expression of galectin-3 is associated with poor survival in node-positive breast cancers and mesenchymal phenotype in breast cancer stem cells," *Breast Cancer Research*, vol. 18, no. 1, p. 97, 2016. DOI: `10.1186/s13058-016-0757-6`.

[31] H. Zhang, X. Liang, C. Duan, C. Liu, and Z. Zhao, "Galectin-3 as a Marker and Potential Therapeutic Target in Breast Cancer," *PLOS ONE*, vol. 9, no. 9, e103482, 2014. DOI: `10.1371/JOURNAL.PONE.0103482`.

[32] M. J. V. White, D. Roife, and R. H. Gomer, "Galectin-3 Binding Protein Secreted by Breast Cancer Cells Inhibits Monocyte-Derived Fibrocyte Differentiation.," *Journal of immunology (Baltimore, Md. : 1950)*, vol. 195, no. 4, pp. 1858–67, 2015. DOI: `10.4049/jimmunol.1500365`.

[33] M. L. Macheda, S. Rogers, and J. D. Best, "Molecular and cellular regulation of glucose transporter (GLUT) proteins in cancer," *Journal of Cellular Physiology*, vol. 202, no. 3, pp. 654–662, 2005. DOI: `10.1002/jcp.20166`.

[34] A. Godoy, V. Ulloa, F. Rodrí´guez, R. Rodrí´guez, K. Reinicke, A. J. Yan~ez, Y. Yan~ez, M. Mari´, M. De Los, A. Garci´a, G. Garci´a, R. A. Medina, M. Mo´, M. Carrasco, S. Sofi´, S. Barberis, T. Castro, F. Marti´nez, M. Marti´nez, X. Koch, J. C. Vera, M. M. Mari´a, T. Poblete, C. D. Figueroa, B. Peruzzo, F. P. Rez, and F. Nualart, "Differential Subcellular Distribution of Glucose Transporters GLUT1-6 and GLUT9 in Human Cancer: Ultrastructural Localization of GLUT1 and GLUT5 in Breast Tumor Tissues," *JOURNAL OF CELLULAR PHYSIOLOGY*, vol. 207, pp. 614–627, 2006. DOI: `10.1002/jcp.20606`.

[35] S. Rogers, S. E. Docherty, J. L. Slavin, M. A. Henderson, and J. D. Best, "Differential expression of GLUT12 in breast cancer and normal breast tissue," *Cancer Letters*, vol. 193, no. 2, pp. 225–233, 2003. DOI: `10.1016/S0304-3835(03)00010-7`.

[36] L. Martinez-Pomares, "The mannose receptor," *Journal of Leukocyte Biology*, vol. 92, no. 6, pp. 1177–1186, 2012. DOI: `10.1189/jlb.0512231`.

[37] V. Torchilin, *Tumor delivery of macromolecular drugs based on the EPR effect*, 2011. DOI: `10.1016/j.addr.2010.03.011`.

[38] S. K. Golombek, J.-N. May, B. Theek, L. Appold, N. Drude, F. Kiessling, and T. Lammers, "Tumor targeting via EPR: Strategies to enhance patient responses.," *Advanced drug delivery reviews*, vol. 130, pp. 17–38, 2018. DOI: `10.1016/j.addr.2018.07.007`.

[39] R. Bazak, M. Houri, S. E. Achy, W. Hussein, and T. Refaat, "Passive targeting of nanoparticles to cancer: A comprehensive review of the literature.," *Molecular and clinical oncology*, vol. 2, no. 6, pp. 904–908, 2014. DOI: `10.3892/mco.2014.356`.

[40] G. Chen, I. Roy, C. Yang, and P. N. Prasad, *Nanochemistry and Nanomedicine for Nanoparticle-based Diagnostics and Therapy*, 2016. DOI: `10.1021/acs.chemrev.5b00148`.

[41] B. Timko, K. Whitehead, W. Gao, D. Kohane, O. Farokhzad, D. Anderson, and R. Langer, "Advances in drug delivery.," *Annual review of materials research*, vol. 41, no. 1, pp. 1–20, 2011. DOI: `10.1146/annurev-matsci-062910-100359`.

[42] K. Jain, "Drug delivery systems – an overview.," in *Drug delivery systems*, vol. 437, Humana Press, 2008, ch. 1, pp. 1–50.

[43] T. C. Zhu and J. C. Finlay, "The role of photodynamic therapy (PDT) physics.," *Medical physics*, vol. 35, no. 7, pp. 3127–36, 2008. DOI: `10.1118/1.2937440`.

[44] S.-R. Lee and Y.-J. Kim, "Hydrophilic Chlorin e6-Poly(amidoamine) Dendrimer Nanoconjugates for Enhanced Photodynamic Therapy.," *Nanomaterials (Basel, Switzerland)*, vol. 8, no. 6, 2018. DOI: `10.3390/nano8060445`.

[45] L. V. Kostryukova, V. N. Prozorovskiy, N. V. Medvedeva, and O. M. Ipatova, "Comparison of a new nanoform of the photosensitizer chlorin e6, based on plant phospholipids, with its free form.," *FEBS open bio*, vol. 8, no. 2, pp. 201–210, 2018. DOI: 10.1002/2211-5463.12359.

[46] T. Stuchinskaya, M. Moreno, M. J. Cook, D. R. Edwards, and D. A. Russell, "Targeted photodynamic therapy of breast cancer cells using antibody–phthalocyanine–gold nanoparticle conjugates," *Photochemical & Photobiological Sciences*, vol. 10, no. 5, p. 822, 2011. DOI: 10.1039/c1pp05014a.

[47] P. García Calavia, I. Chambrier, M. J. Cook, A. H. Haines, R. A. Field, and D. A. Russell, "Targeted photodynamic therapy of breast cancer cells using lactose-phthalocyanine functionalized gold nanoparticles," *Journal of Colloid and Interface Science*, vol. 512, pp. 249–259, 2018. DOI: 10.1016/J.JCIS.2017.10.030.

[48] Y. Shan, S. Ma, L. Nie, X. Shang, X. Hao, Z. Tang, and H. Wang, "Size-dependent endocytosis of single gold nanoparticles," *Chemical Communications*, vol. 47, no. 28, p. 8091, 2011. DOI: 10.1039/c1cc11453k.

[49] D. Ye, H.-Y. Chen, Y. Shen, A. J. Shuhendler, and J.-J. Xu, "Chem Soc Rev Two-photon excitation nanoparticles for photodynamic therapy Two-photon excitation nanoparticles for photodynamic therapy," *Chem. Soc. Rev. Chem. Soc. Rev*, vol. 45, no. 45, pp. 6659–6890, 2016.

[50] M. Gary-Bobo, Y. Mir, C. Rouxel, D. Brevet, I. Basile, M. Maynadier, O. Vaillant, O. Mongin, M. Blanchard-Desce, A. Morère, M. Garcia, J.-O. Durand, and L. Raehm, "Mannose-Functionalized Mesoporous Silica Nanoparticles for Efficient Two-Photon Photodynamic Therapy of Solid Tumors," *Angewandte Chemie International Edition*, vol. 50, no. 48, pp. 11 425–11 429, 2011. DOI: 10.1002/anie.201104765.

[51] M. Wang, L. Huang, S. K. Sharma, S. Jeon, S. Thota, F. F. Sperandio, S. Nayka, J. Chang, M. R. Hamblin, and L. Y. Chiang, "Synthesis and Photodynamic Effect of New Highly Photostable Decacationically Armed [60]-and [70]Fullerene Decaiodide Monoadducts to Target Pathogenic Bacteria and Cancer Cells NIH Public Access," *J Med Chem*, vol. 55, no. 9, pp. 4274–4285, 2012. DOI: 10.1021/jm3000664.

[52] H. W. Lin and C. H. Tseng, *A review on the relationship between SGLT2 inhibitors and cancer*, 2014. DOI: 10.1155/2014/719578.

[53] R. Csepregi, B. Lemli, S. Kunsági-Máté, L. Szente, T. Kőszegi, B. Németi, M. Poór, R. Csepregi, B. Lemli, S. Kunsági-Máté, L. Szente, T. Kőszegi, B. Németi, and M. Poór, "Complex Formation of Resorufin and Resazurin with B-Cyclodextrins: Can Cyclodextrins Interfere with a Resazurin Cell Viability Assay?" *Molecules*, vol. 23, no. 2, p. 382, 2018. DOI: 10.3390/molecules23020382.

[54] I. J. MacDonald, J. Morgan, D. A. Bellnier, G. M. Paszkiewicz, J. E. Whitaker, D. J. Litchfield, and T. J. Dougherty, "Subcellular Localization Patterns and Their Relationship to Photodynamic Activity of Pyropheophorbide-a Derivatives," *Photochemistry and Photobiology*, vol. 70, no. 5, pp. 789–797, 1999. DOI: 10.1111/j.1751-1097.1999.tb08284.x.

[55] D. Kessel, R. Luguya, and M. G. H. Vicente, "Localization and Photodynamic Efficacy of Two Cationic Porphyrins Varying in Charge Distribution¶," *Photochemistry and Photobiology*, vol. 78, no. 5, p. 431, 2003. DOI: 10.1562/0031-8655(2003)078<0431:LAPEOT>2.0.CO;2.

[56] Y.-J. Hsieh, C.-C. Wu, C.-J. Chang, and J.-S. Yu, "Subcellular Localization of Photofrin 1 Determines the Death Phenotype of Human Epidermoid Carcinoma A431 Cells Triggered by Photodynamic Therapy: When Plasma Membranes Are the Main Targets," *JOURNAL OF CELLULAR PHYSIOLOGY*, vol. 194, pp. 363–375, 2003. DOI: 10.1002/jcp.10273.

[57] A. P. Castano, T. N. Demidova, and M. R. Hamblin, "Mechanisms in photodynamic therapy: part one-photosensitizers, photochemistry and cellular localization.," *Photodiagnosis and photodynamic therapy*, vol. 1, no. 4, pp. 279–93, 2004. DOI: `10.1016/S1572-1000(05)00007-4`.

[58] H. Dummin, T. Cernay, and H. Zimmermann, "Selective photosensitization of mitochondria in HeLa cells by cationic Zn(II)phthalocyanines with lipophilic side-chains," *Journal of Photochemistry and Photobiology B: Biology*, vol. 37, no. 3, pp. 219–229, 1997. DOI: `10.1016/S1011-1344(96)07416-7`.

[59] E. J. Ngen, P. Rajaputra, and Y. You, "Evaluation of delocalized lipophilic cationic dyes as delivery vehicles for photosensitizers to mitochondria," *Bioorganic & Medicinal Chemistry*, vol. 17, no. 18, pp. 6631–6640, 2009. DOI: `10.1016/J.BMC.2009.07.074`.

[60] T. M. Tsubone, W. K. Martins, C. Pavani, H. C. Junqueira, R. Itri, and M. S. Baptista, "Enhanced efficiency of cell death by lysosome-specific photodamage.," *Scientific reports*, vol. 7, no. 1, p. 6734, 2017. DOI: `10.1038/s41598-017-06788-7`.

[61] D. B. Tada and M. S. Baptista, "Photosensitizing nanoparticles and the modulation of ROS generation," *Frontiers in Chemistry*, vol. 3, p. 33, 2015. DOI: `10.3389/fchem.2015.00033`.

Chapter 6

Conclusions

The aims of this PhD research were to develop targeted PDT against bacterial and cancer cells, through the use of glycoAuNPs, which would deliver PS to the target cells by selectively binding to cell-surface lectins. Two different approaches were required for targeted PDT against the different types of cells. For the bacterial cells, the aim was to deliver the PS to the outer membrane; whereas for the cancer cells, the PS needed to be localised intracellularly for effective cell killing. Consequently, for the bacterial cell targeting, focus was placed on optimising the glycan-lectin cell surface interaction, and the unique optical properties of AuNPs allowed for this interaction to be probed through colorimetric techniques. For the cancer cells, focus was placed on assessing selective cellular uptake of the PS. With respect to the initial aims, the following discusses the overall findings and conclusions.

6.1   Technical achievements

Through copper (I)-catalysed azide-alkyne cycloaddition click chemistry, one known galactose-based lectin inhibitor was synthesised, along with two novel glycan ligands: galactose-PEG$_3$-SH and mannose-PEG$_6$-SH (Figure 6.1). A thiol based tether was needed to form strong, covalent interaction with the surface

of the AuNPs. Spacing between the AuNP surface and the monosaccharide is important to allow accessibility for binding by the lectin carbohydrate recognition domain. Therefore, the synthesised glycan ligands had a PEGylated tether, terminated by a thiol. The PEG also provides further advantages, such as enhanced aqueous solubility, and steric stability of the particles. In a biological setting, PEG has also shown reduced clearance from the body.
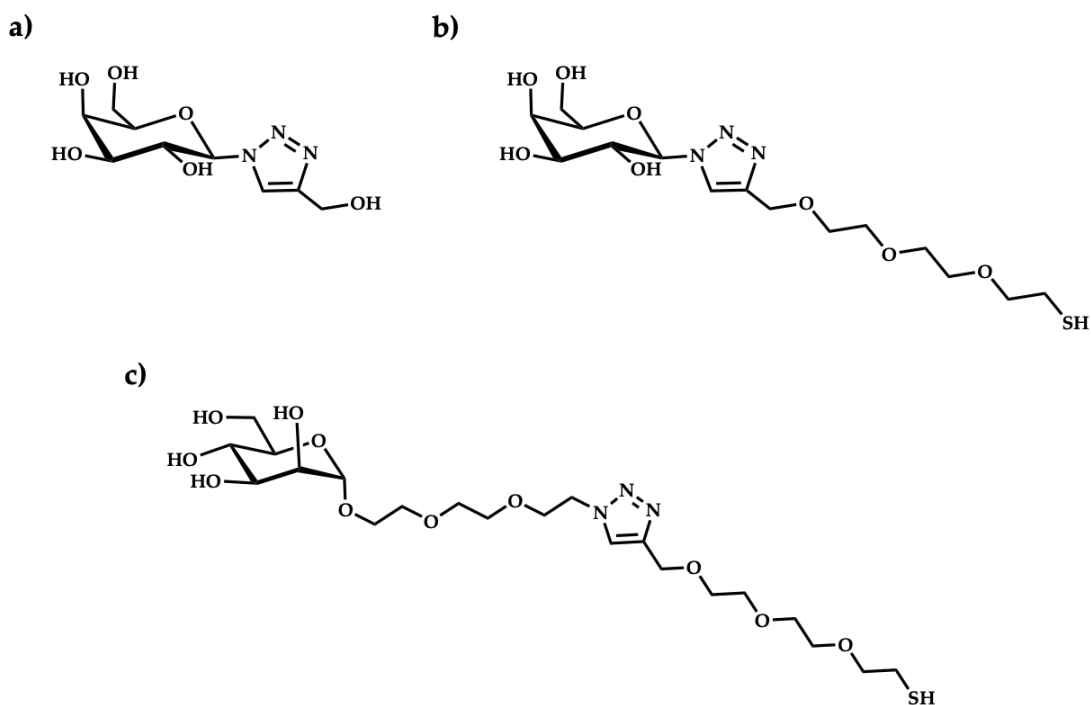
Figure 6.1: Synthesised glycan structures: a) galactose-based lectin inhibitor; b) galactose-PEG$_3$-SH; and c) mannose-PEG$_6$-SH.

Chapter 3 demonstrated successful generation of 16 nm citrate-stabilised AuNPs (citrate-AuNPs), functionalised with homogeneous monolayers of galactose-PEG$_3$-SH (gal-AuNPs), or with the cationic ligand TMAC (TMAC-AuNPs). For the gal-AuNPs, functionalisation was achieved by displacement of the citrate ions on the citrate-AuNPs with the galactose-PEG$_3$-SH. In contrast, the cationic TMAC needed a different method to achieve functionalisation, as the positively charged ligand causes irreversible aggregation upon addition to the negatively charged citrate-AuNPs, due to electrostatic interactions. Therefore, the citrate

ions are not displaced before aggregation and precipitation. Different addition techniques were attempted, such as addition of ligand in methanol, or through dropwise addition, but stable particles were not produced. By exploring a new two-phase transfer approach, developed by Hassinen *et al.* [1], the TMAC was functionalised onto the NP surface. Briefly, the method involves displacement of citrate ions with a neutrally-charged, organic soluble amine derivative: octadecylamine (ODA-AuNPs). The amine forms stronger interactions with the gold surface than the citrate, and so citrate displacement is achieved. The organic soluble ODA-AuNPs transfer into the organic phase from the aqueous phase. The ODA is then displaced by the water soluble ligand: TMAC (TMAC-AuNPs), and consequently the TMAC-AuNPs transfer into the aqueous phase (see Figure 6.2 for ligand structures). These functionalised AuNPs were used for lectin or bacterial binding, in **Chapter 4**.

a)

b)

c)
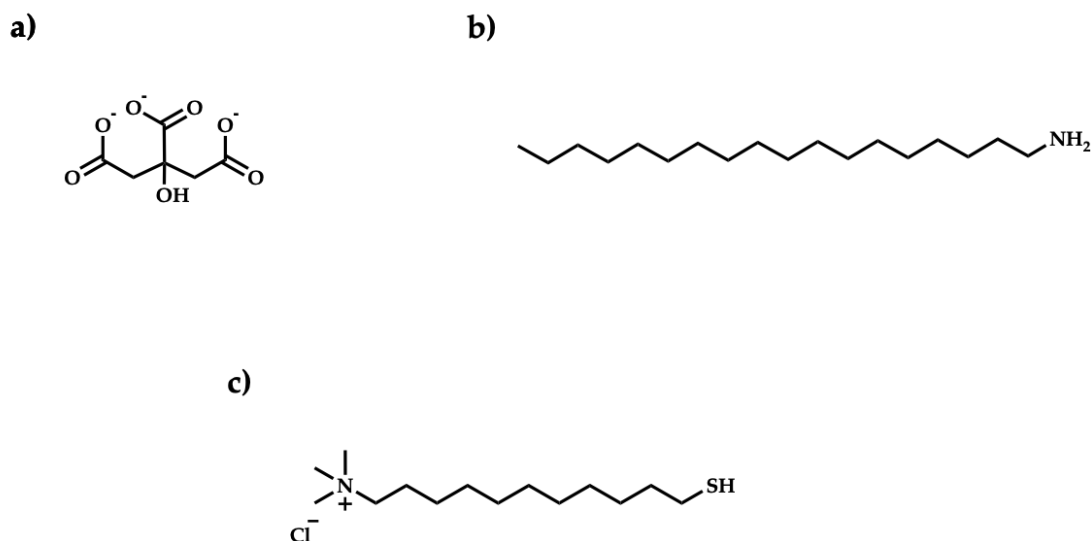
Figure 6.2: Ligands used in two-step phase transfer, for functionalising AuNPs with cationic ligand TMAC: a) citrate ion; b) ODA; and c) TMAC.

Heterogeneous monolayer functionalisation of the citrate-AuNPs was achieved using chlorin e6, and either a control PEG$_3$-SH ligand (PEG-/ce6-AuNPs), or with the novel synthesised glycan ligands: galactose-PEG$_3$-SH (gal-/ce6-AuNPs) or mannose-PEG$_6$-SH (man-/ce6-AuNPs). For ce6, an amine deriva-

tive was used for EDC conjugation to the AuNPs that were functionalised with a carboxylate ligand (COOH-PEG$_4$-SH). See Figure 6.3 for ligand structures. These particles were used for photodynamic therapy studies in **Chapter 5**.
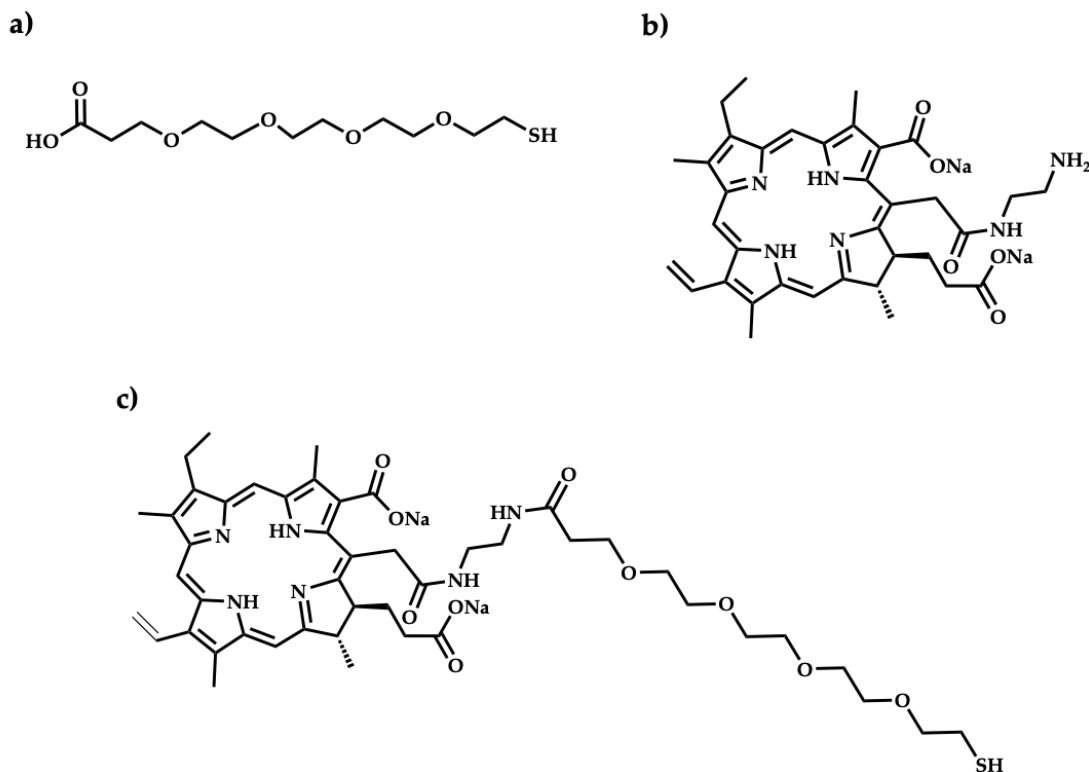
Figure 6.3: Ligands used in ce6 conjugation to AuNP surface: a) COOH-PEG$_4$-SH; b) ce6 amine derivative; and c) ce6-PEG$_4$-SH.

Chapter 4 documents the first experiments using a new filtration technique developed at Iceni Diagnostics. The technique relies on AuNP aggregates formed by lectin binding, or through bacterial binding, to be larger than the pores on a 384-well filter plate. The aggregates consequently cannot pass through the filter, and upon vacuum, solution passes through the filter and the aggregates remain on the filter surface; resulting in a red-to-blue colouration (dependent on sample) on the filter surface, which was observed by eye. The technique was shown successful at detecting both soluble lectin (LecA) and bacterial (*Pseudomonas aeruginosa* and *Escherichia coli*) samples. The technique also had similar sensitivity to the UV-Vis plate assay (64 nM LecA).

In **Chapter 5**, glycan binding to two breast cancer cell lines, and to a non-cancer breast epithelial cell line, was assessed through commercial polyacrylamide (PAA) probes. The PAA was modified with biotin, along with one of the following glycans (PAA-glycans): galactose (PAA-gal), glucose (PAA-glc), lactose (PAA-lac) or mannose (PAA-man). Binding between PAA-glycans and cells has predominantly been performed using flow cytometry[2][3][4][5] methods. Fluorescent imaging using PAA-glycans has been achieved using precomplexed PAA-glycan to streptavidin nanodiamonds[6]. The method used in this research was adapted from a combination of the different literature sources listed above, to achieve direct binding between PAA-glycan to the breast cell lines using confocal microscopy. The cell lines were cultured on glass cover slips, and their glycan binding probed using fluorescently labelled streptavidin, and detected by confocal microscopy.

6.2 Scientific achievements

In **Chapter 4**, 16 nm AuNPs were shown to successfully bind to two bacterial pathogens: *Escherichia coli* (*E. coli*) and *Pseudomonas aeruginosa* (*P. aeruginosa*), using the novel filtration technique listed in **Section 6.1**. At first, proof-of-principle was demonstrated using TMAC-AuNPs and *E. coli*, where binding occurs through electrostatic interactions, in a wide-spread manner, across the bacterial cell surface. The cationic charge on the TMAC-AuNPs interact with negatively charged groups on the Gram-negative bacterial cell surface, such as phosphates (LPS and phospholipids) or carboxylates (acidic sugars)[7].

Once the filtration technique demonstrated its capability of detecting bacterial binding by 16 nm AuNPs, investigation of target pathogen (*P. aeruginosa*) binding through glycan-lectin interactions was performed. The target lectin was LecA; a virulence factor expressed on the cell surface of *P. aeruginosa*. First, LecA expression by the *P. aeruginosa* strain was tested through Western blot analysis, and expression was detected during late-log and stationary phases.

Gal-AuNP binding to the target lectin LecA was then optimised. The initial studies were performed with soluble LecA, to remove the complex environment of bacteria. From these studies, higher galactose-PEG$_3$-SH (200 μm) concentrations for AuNP functionalisation were shown to improve the sensitivity of the LecA binding. Optimal binding to LecA was shown in the presence of CaCl$_2$, and at room temperature. Through UV-Vis and filtration-based plate assays, LecA was detected at 64 nM. The gal-AuNP binding by LecA was shown to be a selective interaction, as presence of galactose inhibitor resulted in loss of binding.

Finally, the gal-AuNPs were shown to detect *P. aeruginosa* at cultures with an optical density of 0.4 in the filter plate assay. The binding was inhibited in the presence of galactose inhibitor, suggesting a selective glycan-lectin interaction. The experiments were subsequently repeated and unfortunately, the results were not reproducible. Similar conclusions were drawn by Donnier-Marechal *et al.*[8], where glycoconjugates showed high affinity LecA binding but they could not show bacterial binding. Due to time constraints further investigation was not possible, and consequently, the *P. aeruginosa* was not taken forward for antimicrobial PDT studies.

In **Chapter 5**, investigation into 16 nm AuNPs for glycan targeted PDT was assessed. Previous work by Garcia-Calavia *et al.* assessed 4 nm AuNPs functionalised with lactose and phthalocyanine (lactose-C3Pc-AuNPs) for targeted PDT against breast cancer cell lines (SK-BR-3 and MDA-MB-231). By ELISA, MDA-MB-231 demonstrated increased expression of galectin-1 compared to SK-BR-3, suggesting lactose-C3Pc-AuNPs should be most effective against MDA-MB-231. However, cell death was only observed against SK-BR-3, when the particles were incubated for 3 hours. Although the authors speculated other lectins or receptors may be involved, time constraints restricted any further investigation. With this in mind, the research in this PhD focused on assessing glycan binding by the cancer cell lines and comparing them against a non-cancer breast epithelial cell line (MCF-10A). The aim was to gain information on the most suitable

glycan for targeted PDT, in hope of selective eradication of the cancer cell lines.

At first, commercially available PAA-glycans were used to compare binding by the different cell lines by confocal microscopy. The results demonstrated differential binding between the cell lines, with galactose showing statistically significant binding to both cancer cell lines, but not to the non-cancer cell line.

Next, glycan-/ce6-AuNP uptake by the different cell lines was assessed using confocal microscopy. Galactose and mannose were taken forward from the PAA-glycan binding studies, and PEG-/ce6-AuNPs were used as a control. These studies showed selective uptake of the gal-/ce6-AuNPs by both cancer cell lines, and no detectable interaction by the non-cancer cell line. Man-/ce6-AuNPs were only shown to interact with the MDA-MB-231 cell line, which was as expected as MDA-MB-231 overexpress mannose receptor.

As the gal-/ce6-AuNPs demonstrated selective uptake by both cancer cell lines, these were taken forward for future experiments. As mentioned previously, Garcia-Calavia *et al*[9] observed better particle uptake by the cell line that had lower galectin-1 expression (SK-BR-3). This suggested other receptors were involved, or possibly that galectin is not responsible for AuNP uptake. Consequently, an inhibitor experiment was designed, with inhibitors for the following galactose-binding proteins: galectins, GLUT receptors, and SGLT receptors. The cancer cells were incubated with inhibitor before gal-/ce6-AuNP addition, and effects on NP uptake were analysed by confocal microscopy. The results demonstrated that the cell lines used different proteins for gal-/ce6-AuNP uptake. For MDA-MB-231 (high expression of galectin-1), galectin inhibitor significantly reduced NP uptake by the cell line. Whereas for SK-BR-3, the GLUT inhibitor significantly reduced NP uptake. Consequently, cellular uptake of the gal-/ce6-AuNPs by the cancer cell lines were both galactose-selective interactions.

Finally, as cellular uptake of gal-/ce6-AuNPs by both cancer cell lines had been demonstrated, the particles were taken forward for PDT studies. The non-cancer cell line was used as a control. Different concentrations of ce6 were used

for the experiments, and selective cell death was observed for SK-BR-3, at 50 nM ce6. These results were consistent with the findings from Garcia-Calavia *et al.*, as no selective cell death was observed for MDA-MB-231, even though in this PhD research, cellular uptake of the particles was seen by confocal microscopy. Due to time constraints, further investigation was not possible. However, what was clear from the microscopy results was that the two cancer cell lines rely on different proteins for NP uptake. Consequently, this could mean different rates of uptake, or cellular processing once taken up by the cells, which could both effect cell eradication as localisation of the PS is key to effective PDT treatment.

6.3 Future work

The promising binding results between the gal-AuNPs and *P. aeruginosa* shown in **Chapter 4**, would be investigated further if there was more time. The first step would be to test binding with cultures from different time points. As LecA expression is associated with higher density cultures, possibly the LecA is more consistently expressed on the cell surface when cultures are allowed to grow for longer time periods.

Another set of experiments that may provide information on the low reproducibility, would be to test binding through different detection systems, such as SPR or TEM. This may provide information on whether it is a limitation of the experimental technique (filter plate), or whether there is inconsistency from the bacterial strain. Alternatively, as effective antimicrobial PDT requires the PS to be localised to the target cell, the *P. aeruginosa* could be taken forward for PDT studies to assess binding indirectly through viability studies. By comparing gal-/ce6-AuNPs with control particles (other glycans or PEG), and with galactose inhibitors or LecA mutant strains, selectively of the binding could be assessed.

Another avenue to explore would be *P. aeruginosa* biofilm cultures. LecA expression is associated with biofilm formation, and is needed on the *P. aerug-*

inosa cell surface for attachment. It may be worth comparing binding between planktonic and biofilm cultures, to see whether the gal-AuNPs are effective at biofilm binding and provide more consistent results.

In **Chapter 5**, selective cellular uptake of the gal-/ce6-AuNPs were observed for both cancer cell lines, yet only selective cell death was observed for SK-BR-3 cell line. Possibly, the different proteins involved in cellular uptake were effecting cellular localisation of the particles. Consequently, it would be informative to have further specific localisation data for the gal-/ce6-AuNPs in the cancer cell lines. This could be achieved by using dyes that localise in the various organelles, cytosol, and cellular membrane. First, this experimental layout would be performed using conditions the same as in the PDT studies in **Chapter 5** (3 hours incubation with particles before irradiation). Subsequently, monitoring the localisation through different time points could provide information on cellular processing of the particles. The hope would be that increasing incubation time would yield more effective cell eradication of the MDA-MB-231 cell line, as the particles would move through the cell to different compartments.

If there was more time, the glycan density would have been tested to see if differential glycan densities could improve uptake and cell death. This would be in form of either: 1) altering the galactose-PEG$_3$-SH to PS ratio; or 2) functionalising the particle surface with PS, and both galactose and mannose. The theory behind the latter experiment is that the mannose-/ce6-AuNPs showed selective uptake for only the MDA-MB-231 cell line; and neither galactose or mannose particles were taken up by the non-cancer cell line. Possibly by introducing both mannose and galactose onto the cell surface, the particles could target both galactose (galectins, GLUTs) and mannose (mannose receptor) binding proteins that are overexpressed on the cancer cell lines, and are able to improve effectiveness of PDT against both cell lines.

References

[1] J. Hassinen, V. Liljeström, M. A. Kostiainen, and R. H. A. Ras, "Rapid Cationization of Gold Nanoparticles by Two-Step Phase Transfer," *Angewandte Chemie International Edition*, vol. 54, no. 27, pp. 7990–7993, 2015. DOI: `10.1002/anie.201503655`.

[2] D. M. E. Otto, M. A. Campanero-Rhodes, R. Karamanska, A. K. Powell, N. Bovin, J. E. Turnbull, R. A. Field, J. Blackburn, T. Feizi, and P. R. Crocker, "An expression system for screening of proteins for glycan and protein interactions.," *Analytical biochemistry*, vol. 411, no. 2, pp. 261–70, 2011. DOI: `10.1016/j.ab.2010.12.036`.

[3] F. Alisson-Silva, D. De Carvalho Rodrigues, L. Vairo, K. D. Asensi, A. Vasconcelos-Dos-Santos, N. R. Mantuano, W. B. Dias, E. Rondinelli, R. C. D. S. Goldenberg, T. P. Urmenyi, and A. R. Todeschini, "Evidences for the involvement of cell surface glycans in stem cell pluripotency and differentiation," *Glycobiology*, vol. 24, no. 5, pp. 458–468, 2014. DOI: `10.1093/glycob/cwu012`.

[4] K. Bloem, I. M. Vuist, A. J. van der Plas, L. M. Knippels, J. Garssen, J. J. García-Vallejo, S. J. van Vliet, and Y. van Kooyk, "Ligand Binding and Signaling of Dendritic Cell Immunoreceptor (DCIR) Is Modulated by the Glycosylation of the Carbohydrate Recognition Domain," *PLoS ONE*, vol. 8, no. 6, 2013. DOI: `10.1371/journal.pone.0066266`.

[5] O. A. Vokhmyanina, E. M. Rapoport, S. André, V. V. Severov, I. Ryzhov, G. V. Pazynina, E. Korchagina, H. J. Gabius, and N. V. Bovin, "Com-

parative study of the glycan specificities of cell-bound human tandem-repeat-type galectin-4,-8 and-9," *Glycobiology*, vol. 22, no. 9, pp. 1207–1217, 2012. DOI: `10.1093/glycob/cws079`.

[6]   N. M. Cordina, N. Sayyadi, L. M. Parker, A. Everest-Dass, L. J. Brown, and N. H. Packer, "Reduced background autofluorescence for cell imaging using nanodiamonds and lanthanide chelates," *Scientific Reports*, vol. 8, no. 1, 2018. DOI: `10.1038/s41598-018-22702-1`.

[7]   Z. V. Feng, I. L. Gunsolus, T. A. Qiu, K. R. Hurley, L. H. Nyberg, H. Frew, K. P. Johnson, A. M. Vartanian, L. M. Jacob, S. E. Lohse, M. D. Torelli, R. J. Hamers, C. J. Murphy, and C. L. Haynes, "Impacts of gold nanoparticle charge and ligand type on surface binding and toxicity to Gram-negative and Gram-positive bacteria," *Chemical Science*, vol. 6, no. 9, pp. 5186–5196, 2015. DOI: `10.1039/C5SC00792E`.

[8]   M. Donnier-Maréchal, S. Abdullayev, M. Bauduin, Y. Pascal, M.-Q. Fu, X.-P. He, E. Gillon, A. Imberty, E. Kipnis, R. Dessein, and S. Vidal, "Tetraphenylethylene-based glycoclusters with aggregation-induced emission (AIE) properties as high-affinity ligands of bacterial lectins," *Organic & Biomolecular Chemistry*, vol. 16, no. 45, pp. 8804–8809, 2018. DOI: `10.1039/C8OB02035C`.

[9]   P. García Calavia, I. Chambrier, M. J. Cook, A. H. Haines, R. A. Field, and D. A. Russell, "Targeted photodynamic therapy of breast cancer cells using lactose-phthalocyanine functionalized gold nanoparticles," *Journal of Colloid and Interface Science*, vol. 512, pp. 249–259, 2018. DOI: `10.1016/J.JCIS.2017.10.030`.